A CRYSTALLOGRAPHIC STUDY OF GROUP I NIOBATE PEROVSKITES

Martin Daniel Peel

A Thesis Submitted for the Degree of PhD
at the
University of St Andrews

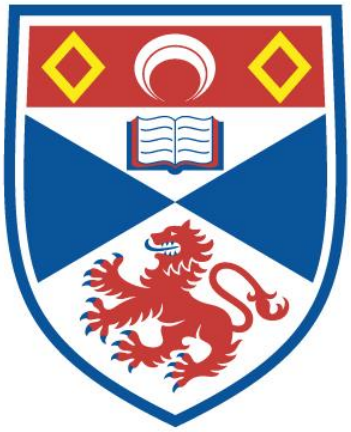

2014

A Crystallographic Study of Group I Niobate Perovskites

Martin Daniel Peel

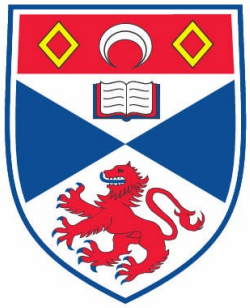

This thesis is submitted in partial fulfilment for the degree of PhD at the University of St Andrews

July 2014

I, Martin Daniel Peel, hereby certify that this thesis, which is approximately 50,000 words in length, has been written by me, that it is the record of work carried out by me and that it has not been submitted in any previous application for a higher degree.

I was admitted as a research student in June, 2010 and as a candidate for the degree of PhD in June, 2011; the higher study for which this is a record was carried out in the University of St Andrews between 2010 and 2014.

Date …… Signature of candidate ……

I hereby certify that the candidate has fulfilled the conditions of the Resolution and Regulations appropriate for the degree of PhD in the University of St Andrews and that the candidate is qualified to submit this thesis in application for that degree.

Date …… Signature of supervisor …… (Philip Lightfoot)

Signature of supervisor …… (Sharon Ashbrook)

In submitting this thesis to the University of St Andrews I understand that I am giving permission for it to be made available for use in accordance with the regulations of the University Library for the time being in force, subject to any copyright vested in the work not being affected thereby. I also understand that the title and the abstract will be published, and that a copy of the work may be made and supplied to any bona fide library or research worker, that my thesis will be electronically accessible for personal or research use unless exempt by award of an embargo as requested below, and that the library has the right to migrate my thesis into new electronic forms as required to ensure continued access to the thesis. I have obtained any third-party copyright permissions that may be required in order to allow such access and migration, or have requested the appropriate embargo below.

The following is an agreed request by candidate and supervisor regarding the electronic publication of this thesis:

Access to printed copy and electronic publication of thesis through the University of St Andrews.

Date …… Signature of candidate …… Signature of supervisor ……

Signature of supervisor ……

Abstract

In this work, X-ray and neutron powder diffraction experiments and complementary solid-state NMR spectroscopy are used to characterise $NaNbO_3$-based perovskite phases. Samples of $NaNbO_3$, $K_xNa_{1-x}NbO_3$ and $Li_xNa_{1-x}NbO_3$ are synthesised using a variety of techniques and subsequently characterised. For $NaNbO_3$, it is observed that at least two room temperature perovskite phases can co-exist, P and Q, and that each phase can be formed exclusively by manipulating the synthetic approach utilised. Phase Q can also be formed by the substitution of a small amount of K^+ or Li^+ for Na^+. The room temperature phases of these materials are also analysed using NMR spectroscopy and X-ray diffraction. It is found that, for $K_xNa_{1-x}NbO_3$, preferential A-site substitution of K^+ for Na^+ may occur, and this observation is supported using a range of NMR techniques and density functional theory calculations. The high-temperature phase behaviour of $NaNbO_3$ and $K_xNa_{1-x}NbO_3$ ($x = 0.03$ to 0.08) is analysed using high-resolution neutron and X-ray powder diffraction to determine when phase changes occur and to characterise each phase. Characterisation of these materials is supported used complementary symmetry mode analysis. For the $Li_xNa_{1-x}NbO_3$ perovskite system, complex phase behaviour is observed at room temperature. High-resolution neutron powder diffraction data shows that, over the range $0.08 < x < 0.20$, phase Q may co-exist with a rhombohedral phase, with the proportions of the two highly dependent upon the synthetic conditions used. Furthermore, using X-ray diffraction and NMR spectroscopy, phase Q is shown to undergo a crystal-to-crystal transition to the rhombohedral phase. For higher values of x, two compositionally-distinct rhombohedral phases are formed, termed Na-*R*3*c* and Li-*R*3*c*, as determined from neutron powder diffraction data.

Thesis Overview

The work presented in this thesis will show how $NaNbO_3$-based perovskites may be synthesised using different conditions and techniques to control which products are formed. At least two ambient-temperature perovskite polymorphs of $NaNbO_3$ are known, one of which belongs to the centrosymmetric space group (*Pbcm*), while the other ($P2_1ma$), is polar and potentially ferroelectric. The latter is considered the more commercially desirable of the two, yet it appears to be the least thermodynamically stable. Synthetic strategies are discussed to show how this latter phase may be formed preferentially. Alternatively, this phase may be formed *via* chemical doping, *i.e.*, substituting sodium for other group I metals, such as lithium and potassium. The phases formed are characterised using complementary combinations of X-ray and neutron powder diffraction and solid-state NMR spectroscopy. The former are used to provide information pertaining to the periodic structure and long-range order, whereas the latter is used to provide information on the local structure and disorder, and conclusions can often be supported using periodic DFT calculations. The temperature-dependent phases of $NaNbO_3$ are examined, and high-resolution neutron powder diffraction experiments are used to propose likely structures. This thesis is divided into six chapters, as described below.

In Chapter 1, an overview of perovskites is given, with a discussion on how the original $CaTiO_3$ perovskite lent its name to hundreds of structurally-similar materials. The general features of perovskites are discussed, of which distortions, such as octahedral tilting and cation displacements are very important. The physical properties of some perovskites are also discussed, including their roles as functional materials in dielectrics. Other properties of some perovskites are also detailed, including piezo- and ferroelectricity.

In Chapter 2, a theoretical background is given which, in the interest of space and time, considers only the concepts directly relevant to the work presented in this

thesis. An overview of crystallography is given, including crystal structures and symmetry, before a discussion of X-ray and neutron diffraction. This is followed by a brief overview of basic NMR theory and the interactions between nuclei. To complement this, an overview of the two-dimensional NMR experiments used is also given at the end of the chapter.

Chapter 3 is divided into two distinct sections. Firstly, a synthesis and characterisation of the room-temperature polymorphs of $NaNbO_3$ using both X-ray diffraction and solid-state NMR spectroscopy. Synthetic strategies to produce either one of the two polymorphs exclusively, and the conditions under which phase mixtures are formed are also discussed.. Both techniques will show how structurally similar the two polymorphs are, yet will also show how they can be readily identified. In the second part of the chapter, the high-temperature phases of $NaNbO_3$ will be considered. Firstly, neutron powder diffraction data is used to determine possible structural models for each of the high-temperature phases. These models are analysed using density functional theory to see if any of the proposed structures are energetically favoured. Complementary NMR data is also obtained to determine how the structures change as a function of temperature. This chapter will highlight how a combination of diffraction, NMR and computation can be used to propose structures for high-temperature phases, and also show the difficulties associated with such an approach.

Chapter 4 is also divided into two distinct sections. Firstly, strategies for synthesising the room temperature polar phase of $NaNbO_3$ are given by use of chemical substitution, with potassium and lithium. Interestingly, the two do not give the same results – low-level lithium-substituted $NaNbO_3$ is believed to form to one specific phase (space group $P2_1ma$), whereas potassium-substitution appears to give to a mixture of phases. Additionally, the two do not show the same dielectric behaviour as a function of temperature. Information on the structures is obtained from solid-state NMR spectroscopy and X-ray diffraction. In the second section, the high-temperature phase behaviour of potassium-substituted $NaNbO_3$ is explored using high-resolution

X-ray and neutron powder diffraction. Beyond the room-temperature polar phase, it is shown that a transition to a tetragonal structure occurs before a second transition back to an orthorhombic phase.

In Chapter 5, the $Li_xNa_{1-x}NbO_3$ perovskite system is discussed. The work presented in this chapter will show how the synthetic approach may be manipulated to alter the outcome of the products formed, by using X-ray and neutron powder diffraction and solid-state NMR spectroscopy. Additionally, it is found that one of the observed phases may only be metastable with respect to the other, as it is shown to convert into a different structure under ambient conditions. The entire 'compositional diagram' of $Li_xNa_{1-x}NbO_3$ is considered in this chapter. It will also be shown, that for values of x > 0.25, that a two-phase mixture is observed, where one phase is isostructural with the low temperature polymorph of $NaNbO_3$ and the other with $LiNbO_3$. These phases are formed independent of reaction conditions and reactant stoichiometry.

This thesis will finish with a chapter describing final conclusions, in which the different synthetic strategies and room-temperature polymorphs are compared, along with a discussion of the temperature-dependent phase transitions. Finally, a discussion on possible future work is given.

Contents

Publications

M. D. Peel, S. P. Thompson, A. Daoud-Aladine, S. E. Ashbrook, P. Lightfoot, *Inorg. Chem.*, 2012, **51**, 6876.

M. D. Peel, S. E. Ashbrook, P. Lightfoot, *Inorg. Chem.*, 2013, **52**, 8872.

M. H. Harunsani, D. I. Woodward, M. D. Peel, S. E. Ashbrook, R. Walton, *J. Solid State Chem.*, 2013, **207**, 117.

Acknowledgements

First and foremost, I would like to thank my family for their support during my studies at the University of St Andrews, in particular my mother and grandmother, and also my brother, Jonathan, for our many future career discussions. I would like to say a big thank you to my two supervisors, Phil and Sharon, for all their help, guidance and their advice over the past three years, and also to past and present members of both research groups.

I would also like to say thank you to my friends for helping me get through this project, in particular two of those in the chemistry department, Siobhan Smith and Charlotte Dixon, whose endless advice and humour have been invaluable.

I would like to say thank you to a few other people, who helped with various parts of this work: Aziz Daoud-Aladine at ISIS, Chiu Tang and Stephen Thompson at DIAMOND, Dinu Iuga for his help with some of the high-field NMR measurements, Filip Wormald (St Andrews) for advice with NMR, and Frédéric Blanc (Cambridge) for help with the high-temperature NMR measurements.

I would also like to thank the EPSRC and the University of St Andrews for funding this work.

I would also like to say a final thank you to the University of St Andrews for everything it has given and taught me over the past seven years. It has been a truly invaluable experience where I have learned about life and succeeding, as well as allowing me to make some of the best friends I will ever have. The value of my obtaining both my degree and PhD. at this University have been truly priceless.

A house divided against itself cannot stand

Chapter 1
Background

1.1. Perovskites

1.1.1. Introduction

Russian mineralogists, Gustav and Perovski, first discovered perovskite, $CaTiO_3$,[1] in 1839. However, it was not until much later that Megaw published the first crystal structure of this mineral.[2] $CaTiO_3$ perovskite lends its name to hundreds of structurally-similar materials, known as perovskites. The general perovskite composition may be formulated as $^{XII}A^{VI}BX_3$, where the A-site cation, typically a Group I or II metal, is in a dodecahedrally-coordinated site, and the B-site cation, typically a transition metal, is octahedrally-coordinated and surrounded by X anions, typically oxygen or fluorine, located at the face corners of the octahedron. The A- and B-site cations are typically of very different sizes, with the A-site cation being the larger of the two.

Perovskites can be found naturally occurring in the Earth's mantle all around the world. They have a range of useful physical properties including superconductivity and magnetoresistance, and many show dielectric behaviour.[3,4] These properties aid in the utility of perovskites in electrical equipment such as telecommunications and sensors.[5] The perovskite structure may be regarded as a three-dimensional network of corner-sharing BX_6 octahedra, as shown in Fig. 1.1. However, as most perovskite structures are non-ideal, *i.e.*, distorted, the figure shows a distorted perovskite structure. All references to perovskites in this thesis are to the general class of materials, and not $CaTiO_3$, unless otherwise stated.

Most metals can be incorporated into the perovskite structure. Properties of perovskites can be altered or subtly modified to suit a specific application. For example, lithium niobate ($LiNbO_3$) has commercial applications in optical equipment

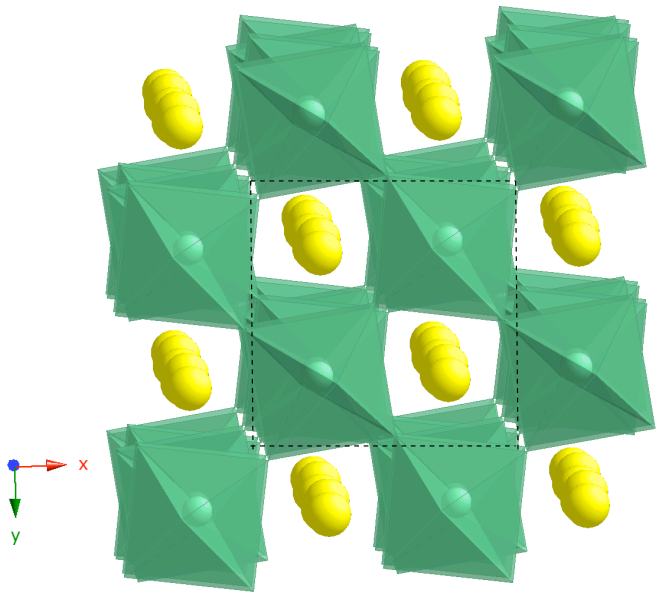

Figure. 1.1: Distorted perovskite (room temperature *Pbcm* polymorph of $NaNbO_3$), showing the repeat octahedral units in a typical perovskite structure. Yellow spheres are Na^+ cations, green are Nb^{5+}, and green octahedra represent NbO_6 units. The dashed line indicates the 2D unit cell edges.

and sensors, while barium titanate ($BaTiO_3$) has uses in multilayer ceramic capacitors and transducers.[6]

The 'ideal' perovskite structure is cubic, having no distortions or displacements of ions within the structure, and identical B-O bond lengths. The radii of the ions present are typically the most important factor when considering the stability of this ideal structure. It is observed that, for an ideal perovskite structure,

$$r_A + r_X = \sqrt{2}(r_B + r_X) \quad , \tag{1.1}$$

where r_A, r_B, and r_X are the Shannon radii[7] of the A, B and X ions, respectively. However, as most perovskites are distorted from an ideal structure,[8] a tolerance factor, t, has been introduced to describe this, and is given by

$$t = (r_A + r_X)/[(\sqrt{2})(r_B + r_X)] \quad . \tag{1.2}$$

The factor, proposed by Goldschmidt,[9] gives the range for which a perovskite phase is predicted to be stable. If the Goldschmidt tolerance factor lies in the region $0.85 < t < 1.06$, then the perovskite structure is stable and it may be adopted, with an ideal or suitably distorted structure. For $0.9 < t < 1.0$, the structure is most likely cubic and closer to ideal. As a consequence of Equation 1.2, if the atomic radii of A and B are poorly matched, then the value of t will be outwith the range for the structure to be stable, and as such, the resulting structure is not likely to be a perovskite, as it cannot meet the coordination requirements.[8] If the relative sizes of the A- and B-site cations are poorly matched, and do not fit well into their specific sites, then a strain is produced, forcing the BO_6 octahedra to adopt a distorted geometry or tilt to accommodate this. BO_6 distortions are a result of electronic effects resulting from the nature of the octahedral metal ion, discussed below.

1.1.2. Cation Displacements

Cation displacements are one of the most commonly observed deviations from the ideal perovskite structure, and may occur at either, or both, of the A- and B-sites. Examples include Ti^{4+} displacements in $BaTiO_3$ and Nb^{5+} displacements in low-temperature $NaNbO_3$ (Fig. 1.2), resulting in enhanced electrical properties. The most common displacement is, however, of the A-site. For example, perovskites with the $GdFeO_3$ structure show A-site cation displacements, but no B-site displacements are observed. In either case, the deviation from the average position is only small, owing to the size of the surrounding octahedron. Typically, these displacements will lead to very subtle changes in the geometry and bond lengths of the BO_6 octahedra. However, these displacements are key to the ferroelectric behavior of a material, and of considerable importance, yet are difficult to detect by most analytical techniques, such as X-ray diffraction and NMR spectroscopy.

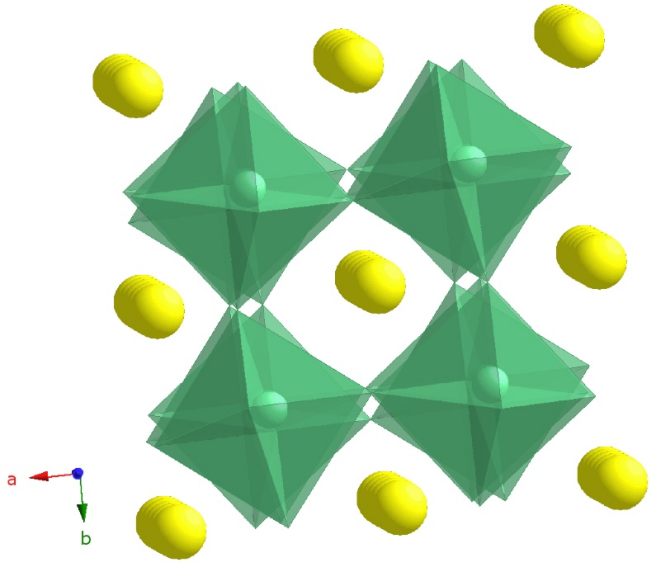

Figure. 1.2: *R*3*c* polymorph of $NaNbO_3$ showing subtle A-site (Na^+, yellow spheres) and B-site (Nb^{5+}, green spheres) displacements occurring simultaneously.

One of the principal reasons for the distortions observed in perovskites is the second-order Jahn-Teller (SOJT) effect. This effect can cause certain ions in the structure to displace from the centre of their coordinating polyhedra. Where the gap between the Highest Occupied Molecular Orbital (HOMO) and Lowest Unoccupied Molecular Orbital (LUMO) is small, and there is a symmetry-allowed distortion permitting the mixing of the two orbitals, then the two mix. This can be a favourable distortion because the result is an increased stabilisation of the HOMO and a destabilization of the LUMO. These SOJT effect distortions are typically observed for two different classes of cations. Firstly, high valent octahedrally-coordinated d^0 cations, such as Ti^{4+} or Nb^{5+}, and secondly, cations with stereoactive lone pairs, *i.e.*, containing a filled valence s shell, such as Bi^{3+}.[10] The cations shift from the centre of the their coordinating polyhedra, resulting in asymmetrical coordination environments.

BO_6 octahedral distortions and tilting are an intrinsic feature of perovskites, and can have great effects on the physical properties of a material.[11,12] This is because of the importance of octahedral tilting within a structure; two structurally-similar phases

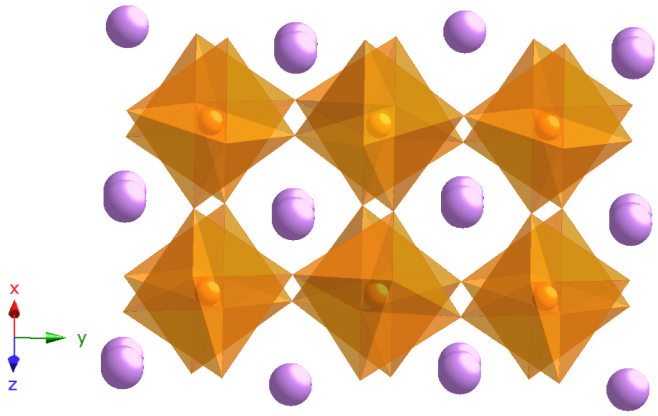

Figure. 1.3: Orthorhombic polymorph of $BiFeO_3$, with Bi^{3+} as purple and Fe^{3+} as orange spheres. The FeO_6 octahedral tilting (orange) is readily observed.

may exist, yet will show different dielectric properties and transition temperatures if different octahedral tilt systems are present. Octahedral tilting is, however, the most common mode of distortion within perovskites, and results in rigid BO_6 octahedra becoming tilted relative to one another but still maintaining their corner-sharing connectivity; examples of this are given in Figs. 1.1-1.3. This type of distortion is generally prevalent when the A-site cation is too small.[13] For example, extensive BO_6 octahedral tilting is observed in $NaNbO_3$, but substantially less is observed in $KNbO_3$, owing to the much smaller ionic radius of Na^+. Much work has focused on characterizing these tilt modes,[10-13] following on from the exhaustive and detailed original work carried out by Glazer in 1972.[14] Although later corrections to this work were made,[15] Glazer's initial classification in the field of octahedral tilting, produced the standard notation still used today. Using Glazer notation, the rotations of the octahedra about each Cartesian axis (describing the tilt system), are described by two parameters. A letter gives a 'non-specified' magnitude of the rotation about an axis, and is given relative to the rotations about the other axes. A negative superscript indicates that rotations of two adjoining octahedra along the specified tilt axis are in opposite directions, and a positive superscript indicates the same direction, as shown in Fig. 1.4. A zero superscript is used when there is no rotation about the tilt axis.

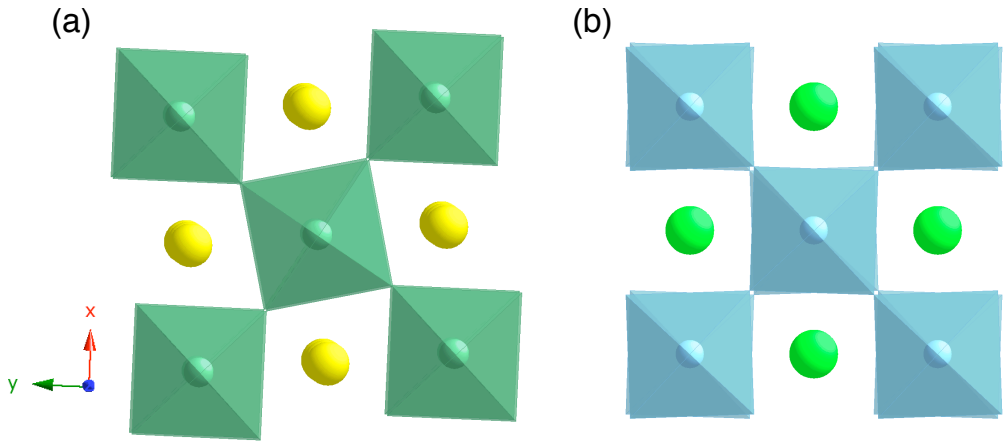

Figure. 1.4: The two different one-tilt systems listed in Table 1.1. (a) shows the $a^0a^0c^+$ tilt system of the *P*4/*mbm* polymorph of $NaNbO_3$, and (b) shows the $a^0a^0c^-$ tilt system of the *I*4/*mcm* polymorph of $SrTiO_3$. Figures are shown looking along the z direction, as no tilts are present along x and y, as denoted by the Glazer notation.

The publication by Glazer, and a detailed review by Woodward,[16] give some excellent examples of this. For example, the Glazer notation $a^+a^+a^+$ indicates that the rotation angle is the same about all axes and that the rotations of adjoining octahedra are in the same direction. For the system $a^+a^+c^+$, the rotation about the z-axis is different from that about the x- and y-axes. Fig. 1.5 shows the most commonly encountered Glazer tilt system ($a^-a^-b^+$). Table 1.1 shows the possible 23 tilt systems that Glazer deduced, along with the corresponding space group determinations.

The space group assignments for tilt systems 5 and 7 were later contested by Liebenweber and Parise,[14] and determined to belong to space group $P4_2/nmc$ as opposed to *Pmmn*, proposed by Glazer. These space groups are particularly relevant when considering work described later in Chapter 4. The new assignment is equally justifiable (if not perhaps more likely), owing to the higher symmetry of the space group. Additionally, it was noted that the original study did not consider the complications arising from simultaneous octahedral tilting and cation displacements. Woodward expanded on this work to include both of these effects and how they may affect space group assignments. It was noted that octahedral tilting cannot only cause

Table 1.1: Glazer tilt systems and corresponding space group determination. The table is adapted from the initial work of Glazer, listed in Ref. 14. n_p (n = a, b or c) denotes the cell lengths of the aristotype 'parent' structure.

Serial Number	Tilt Notation	Cell Multiplicity	Space Group
3-tilt systems		$2a_p \times 2b_p \times 2c_p$	
1	$a^+b^+c^+$		*Immm*
2	$a^+b^+b^+$		*Immm*
3	$a^+a^+a^+$		*Im*3
4	$a^+b^+c^-$		*Pmmn*
5	$a^+a^+c^-$		*Pmmn*
6	$a^+b^+b^-$		*Pmmn*
7	$a^+a^+a^-$		*Pmmn*
8	$a^+b^-c^-$		$A2_1/m11$
9	$a^+a^-c^-$		$A2_1/m11$
10	$a^+b^-b^-$		*Pnma*
11	$a^+a^-a^-$		*Pnma*
12	$a^-b^-c^-$		*F*-1
13	$a^-b^-b^-$		*I*2/*a*
14	$a^-a^-a^-$		*R*-3*c*
2-tilt systems		$2a_p \times 2b_p \times 2c_p$	
15	$a^0b^+c^+$		*Immm*
16	$a^0b^+b^+$		*I*4/*m*
17	$a^0b^+c^-$		*Bmmb*
18	$a^0b^+b^+$		*Bmmb*
19	$a^0b^-c^-$		*F*2/*m*11
20	$a^0b^-b^-$		*Imcm*
1-tilt system			
21	$a^0a^0c^+$	$2a_p \times 2b_p \times c_p$	*C*4/*mmb*
22	$a^0a^0c^-$	$2a_p \times 2b_p \times 2c_p$	*F*4/*mmc*
0-tilt system		$a_p \times b_p \times c_p$	
23	$a^0a^0a^0$		*Pm*3*m*

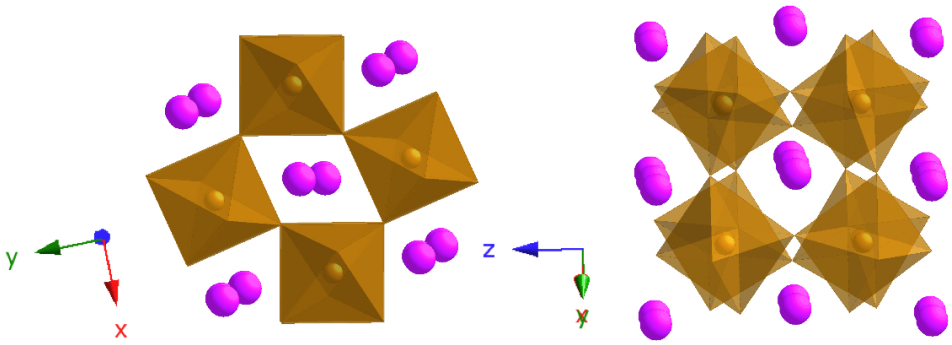

Figure. 1.5: The most commonly encountered Glazer tilt system, $a^{-}a^{-}b^{+}$, observed along different axes, for the crystal structure of $GdFeO_3$, where pink spheres are Gd^{3+}, brown spheres are Fe^{3+}, and brown octahedra represent FeO_6 units.

a doubling of the unit cell, but can accompany cation ordering, and as such, ordering and tilting were jointly considered. By doing so, Woodward was able to propose a list of space groups for each of the possible 23 tilt modes, including those assigned when no ordering was present, and when 1:1 cation ordering was observed. It is important to note, however, that Glazer considered only 2 × 2 × 2 blocks of octahedra, which do not fully account for the more complex tilt systems. For example, the *Pbcm* phase of room temperature $NaNbO_3$ has a four-fold repeat unit along the c-axis, and this was not considered in the original notation scheme.

1.1.3. Cation Substitution

Deviations from structural ideality, such as cation displacements and octahedral tilting, are found to sometimes enhance the physical properties observed. Due to the ease with which these deviations occur, structural modifications can be used to 'fine-tune' the desired physical properties. For example, $PbTiO_3$ and $PbZrO_3$ were combined to produce lead zirconium titanate (PZT), renowned for its high piezoelectric responses. However, in more recent times, health and safety, and environmental concerns, have led to the search for alternatives to this material, to produce a lead-free piezoelectric substitute, and the most effective way of enhancing

this property in perovskites is by cation substitution. Substitution may occur at either the A or B-site, or both, and is usually with a metal from the same group. For example, lithium may be substituted for sodium in $NaNbO_3$, to produce lithium sodium niobate, $Li_xNa_{1-x}NbO_3$. Such modifications are prevalent throughout the perovskite literature, and will form the basis of the materials studied in this work. By taking $BaTiO_3$ as an example, it is apparent why cation substitution is desirable for enhancing the physical properties of perovskites. $BaTiO_3$ is considered to be a lead-free alternative to PZT, owing to its high piezoelectric responses and, as such, has been the subject of a vast number of studies.[4] The highest piezoelectric coefficients are observed for the orthorhombic and rhombohedral phases, with values of 420 and 300 pC/N, respectively. Rehrig found that substituting small amounts of Zr onto the B-site led to the observation of greater piezoelectric responses at room temperature.[5] By varying the amount of B-site cation substitution, either the rhombohedral or orthorhombic phases could be stabilized at room temperature, thereby increasing the piezoelectric responses under these conditions.

Perovskites may sometimes possess defects, such as cation (*e.g.*, Na^+) or anion (*e.g.*, O^{2-}) deficiencies. Na^+ has been well documented as being volatile at higher temperatures,[17,18]. Other group I cations behave similarly.[19] Fang *et al.*[19] showed the variation of metal concentration across individual grains of $K_xNa_{1-x}NbO_3$ perovskite, and concluded that Na^+ and K^+ show significant variation in concentration across the grain at high temperatures. They showed that, for example, the Na^+ content at the centre of a grain was stoichiometric, but nearly entirely deficient at the grain boundaries, with the proportion falling near-linearly over a 400 nm range. This research shows the existence of concentration gradients along a grain and confirms the volatile nature of Na^+ at higher temperatures, especially at grain boundaries. Interestingly, similar results were observed for K^+, although to a lesser extent, indicating less volatility. The results also highlight the effects of grain size, whereby smaller grains will exhibit higher proportions of Na^+ volatility. Samples were heated to temperatures around 1100 K, similar to samples made in this work, and so it is possible that similar levels of volatility would be observed from the pellets. To counter this cation deficiency, perovskites may often exhibit anion deficiency, to ensure charge balancing throughout the crystal. Such an observation is the basis for the use of a sacrificial powder in all samples made during this work. A sacrificial

powder, covering the pellet during heating, will often display the Na^+ volatility previously discussed, while acting to reduce the amount of volatility in the pellet itself. As the work by Fang[19] showed, Na^+ volatisation towards the centre of grains (and, therefore, sample pellets) is much lower, and so the use of such powder should help mimimise concentration gradients in the samples.

Non-stoichiometry in the samples, caused by cation/anion vacancies, is difficult to detect using diffraction techniques. These methods identify the long-range structure, and so such defects, in the short-range structure, may go undetected. The use of solid-state NMR spectroscopy could be used to detect these defects. However, given the relatively small chemical shift ranges of the group I cations analysed in the thesis (^{23}Na and ^{7}Li), and the peak broadening observed in all samples (refer to Chapters 3 and 4), no defects were detected during the course of this work. However, it may be possible to detect the influence of these using higher fields (*e.g.*, 850 MHz) and longer acquisition times, to increase the signal-to-noise ratio.

1.2. Properties

1.2.1. Dielectric Materials

Dielectric materials are electrical insulators, and possess a high dielectric strength, allowing them to withstand high voltages without degrading. Additionally, they have a low dielectric loss, ensuring that loss of electrical energy is minimal. Additional properties of some dielectric materials include ferroelectricity and piezoelectricity, which are discussed in the sections below. In dielectric materials, such as $CaTiO_3$ and $SrTiO_3$, a polarisation of charge develops when a voltage is applied, with the polarisation being removed when the voltage falls to zero, making the dielectric effect reversible. The properties of dielectric materials are observed when placed in a capacitor, where the capacitance, C_0, is defined by

$$C_0 = \varepsilon_0 A / d \ . \qquad (1.3)$$

Here, ε_0 is the permittivity of free space in a vacuum, A is the area of the capacitor plates and d the separation between the plates. When a potential difference, V, is applied, a charge, Q_0, is stored in the plates, given by

$$Q_0 = C_0 V \quad . \tag{1.4}$$

However, adding a dielectric material between the plates increases the total charge stored to Q_1 and the capacitance to C_1, where the dielectric constant, ε', is related to the increased charge and capacitance by

$$\varepsilon' = C_1 / C_0 \quad . \tag{1.5}$$

The dielectric constant depends upon the polarisability, α, of the material and the amount of charge it is able to store. The polarisability is proportional to the induced dipole moment, P, created by the electric field, E, and is expressed as

$$P = \alpha E \quad . \tag{1.6}$$

There are three further classes of dielectric materials, each having their own unique characteristics and properties, increasing their commercial desirability.

1.2.2. Piezoelectricity

A material is termed piezoelectric if an applied mechanical stress results in the (proportional) development of electrical charges on opposite faces of the crystal. Piezoelectric materials must have a non-centrosymmetric crystal structure. Piezoelectric crystals have applications as transducers, as they are able to convert a mechanical stress into electrical energy.

1.2.3. Pyroelectricity

In a pyroelectric material, heating changes the magnitude of the dipoles, and as such, P_S is temperature dependent, as shown in Equation 1.7, where T is the temperature and π is the pyroelectric coefficient,

$$\Delta P_S = \pi \Delta T \quad . \tag{1.7}$$

As a result, measurements at constant temperature do not result in a change in P_S.

1.2.4. Ferroelectricity

Ferroelectric materials typically have much larger dielectric constants than normal dielectric materials, and they are fundamentally different as a result of their ability to retain some remnant polarisation, P_R, when an applied voltage is removed. This effect is shown schematically in Fig. 1.6. As the figure shows, the polarisation behavior when a potential difference is applied is not reproduced when the voltage is decreased, and the result is a hysteresis loop. When reducing the voltage to zero, a remnant, or residual, polarisation remains, which can only be removed by application of a reverse, or coercive, field. The relationship between di-, piezo-, pyro- and ferroelectric materials is not straightforward, and is best illustrated using a Venn diagram, as shown in Fig. 1.7. As the figure shows, all ferroelectric materials are pyroelectric and piezoelectric and all pyroelectric materials are piezoelectric, but not all piezoelectric materials are ferroelectric or pyroelectric.

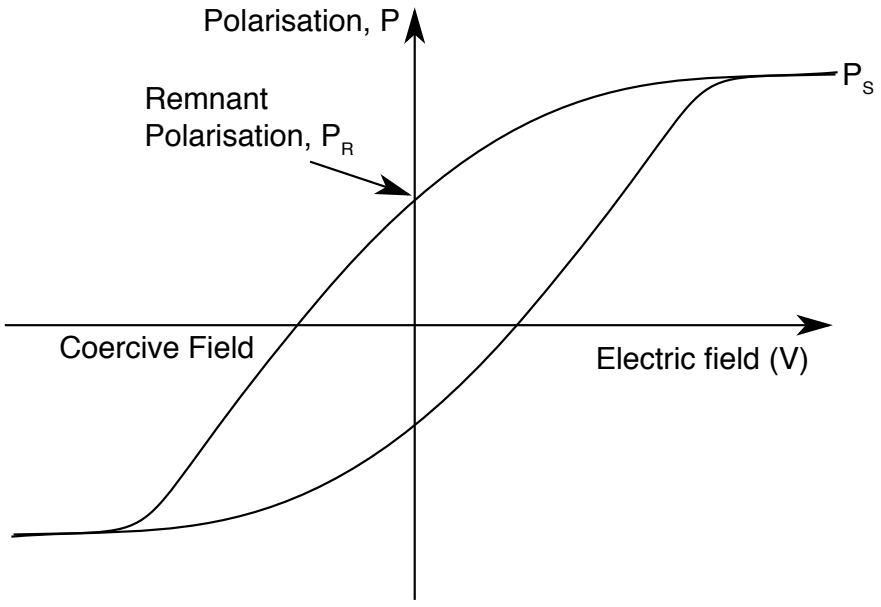

Figure. 1.6: Schematic representation of ferroelectric behaviour.

Cation displacements are the most common origin of the ferroelectric effect because they result in the formation of local dipoles, which, if aligned in the same direction, result in large net dipoles. This in turn results in the saturation polarisation being reached, *i.e.*, a greater degree of polarisation cannot be achieved simply by increasing the amount of internal dipole alignment. This can be exemplified by considering ferroelectric $BaTiO_3$ at room temperature. The Ti^{4+} cations within the TiO_6 octahedra are all displaced from their position by about 0.1 Å in the direction of an oxygen atom,[20] resulting in the formation of a large net dipole. Another example of this effect is ferroelectric $NaNbO_3$ at –100 °C. At this temperature, the Nb^{5+} cations are displaced from the centre of the octahedra, along the same direction, resulting in the formation of a large net dipole. The temperature at which the maximum dielectric constant is observed is termed the Curie temperature, T_C. Above T_C, the material is no longer ferroelectric, and is referred to as paraelectric. A material undergoing a ferroelectric-paraelectric phase transition may still be useful however, as it can have a dielectric constant higher than, or similar to, that before the transition.[7] Structural flexibility enables a structure to be exploited to alter T_C, so that it is closer to room temperature, or the temperature at which it will be used in an application, thereby producing higher dielectric constants.

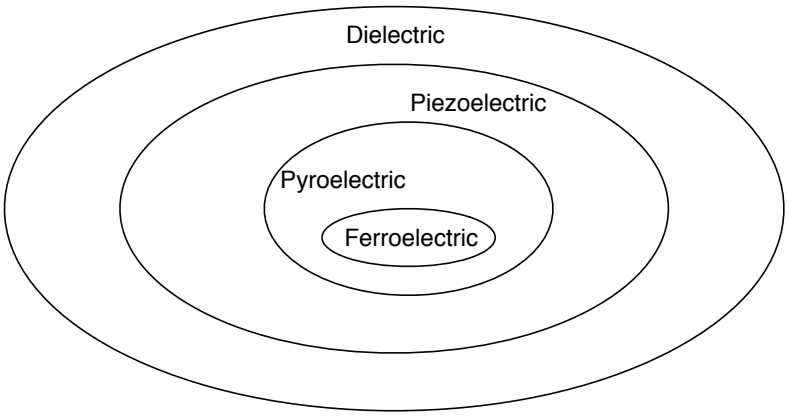

Figure. 1.7: Venn diagram showing the relationship between di-, piezo-, pyro- and ferroelectric materials.

1.3. The History of $NaNbO_3$

$NaNbO_3$ has been the subject of many studies over the last 70 years, with an increasing interest recently, due to its potential use as a lead-free alternative to PZT. Much of the key crystallographic work was carried out by Megaw *et al.*,[21,22] and they reported that there were seven phases of $NaNbO_3$.[23,24] However, these phases made reference only to a series of sequential transitions as a function of temperature, and the series does not include the second polymorph now known to often present at ambient temperature. The presence of this second polymorph was found to be dependent upon the synthetic route employed.[18] The original seven phases that Megaw reported are labeled N (rhombohedral, stable below –100 °C), P (orthorhombic, –100 - 360 °C), R (orthorhombic, 360 - 480 °C), S (orthorhombic, 480 - 520 °C), T1 (orthorhombic, 520 - 575 °C), T2 (tetragonal, 575 - 640 °C) and U (cubic, stable above 640 °C). Ahtee and Glazer[25] subsequently developed this phase diagram, as shown in Fig. 1.8. (Note the figure represents the potassium sodium niobate system (KNN); the left-hand axis of the diagram represents pure $NaNbO_3$). As the figure shows, only phase P is present for $NaNbO_3$ at ambient temperature (although this was later shown to possibly be incorrect), and the first higher temperature phase transition occurs at 360 °C, with the subsequent temperature-dependent transitions occurring at the aforementioned temperatures. The detailed and well-cited work carried out by Megaw, Ahtee and Glazer has since been used as the basis for nearly all further work into the temperature-dependent phase transitions. Crystallographic data for each phase is not given here, as the proposed structure for each has been subsequently 'improved upon' by the development of better diffraction techniques.

The ambient temperature polymorph P has a well-characterised structure. Recent work by Johnston *et al.* has confirmed that phase P can be formed alongside a second polymorph, Q, under certain synthetic conditions,[26,27] and a number of different characterisation techniques, including neutron powder diffraction and solid-state NMR spectroscopy, were used to confirm this. Such work, however, casts doubt on previous studies, as many of the temperature-dependent phases of $NaNbO_3$ had been determined from subtle peak splittings in diffraction data, with the underlying assumption that the starting material was exclusively phase P. However, due to the

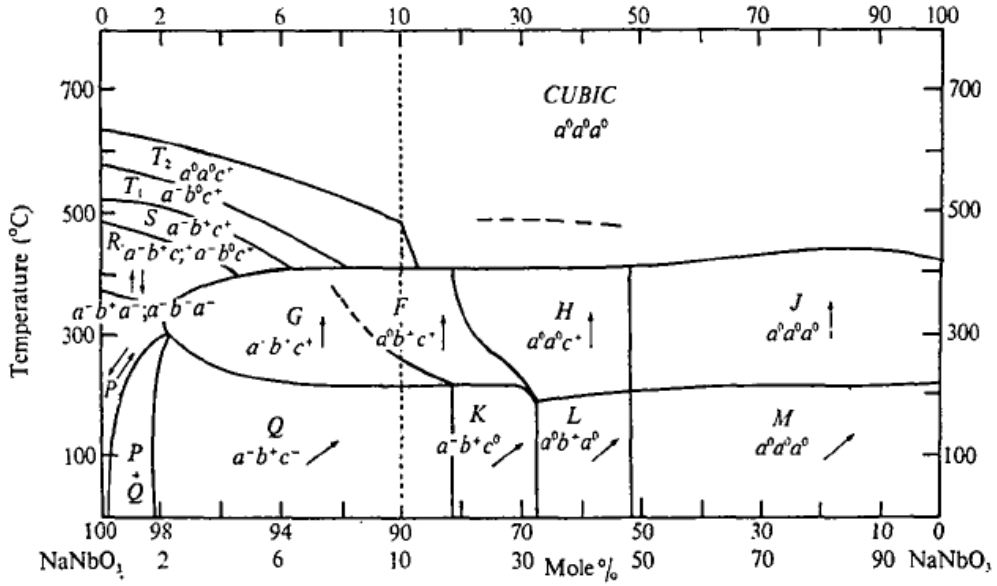

Figure 1.8: A copy of the KNN phase diagram proposed by Ahtee and Glazer (Ref. 25). The figure is taken directly from the publication.

very similar diffraction patterns of phases P and Q of $NaNbO_3$ (see Chapter 3), the presence of Q may have gone undetected in some previous work. As such, any temperature-dependent structures proposed may have been based on two-phase samples, and so care must be taken when interpreting previous work.

Phases P and Q have been the subject of many studies, and as such, there are several proposed crystallographic structures for each. The crystallographic structures for phases P and Q, proposed by Mishra[28] and Johnston[26], respectively, represent some of the more recent work on $NaNbO_3$. In all relevant prior literature, phase P is reported to be non-polar and phase Q to be polar. There is agreement in the prior literature that phase P possesses a $4a_p$ repeat unit along the *c*-axis and phase Q a $2a_p$ repeat unit along the *b*-axis. An investigation by Shuvaeva *et al.*[29] suggested that phase Q could be induced from phase P in the presence of an electric field. Mishra *et al.*[28] presented a neutron powder diffraction study, with supporting first-principles calculations and hysteresis measurements, to accurately characterise the transition from the low-temperature ferroelectric rhombohedral phase to the orthorhombic antiferroelectric phase P. Most interestingly, the study showed that the free energies of the two phases were extremely close, and that switching between the two may be relatively straightforward. The study highlights the utility of supporting diffraction-based

studies with first-principles calculations. These complementary techniques were also later used by Peel *et al*. to probe the temperature-dependent phase transitions of $NaNbO_3$.[37]

In addition to structural investigations using classic diffraction techniques, there have also been a number of solid-state NMR studies of $NaNbO_3$ reported. Wolf *et al.*[30] determined the quadrupolar interactions in $NaNbO_3$ using ^{23}Na and ^{93}Nb wide-line NMR. However, due to the relatively large quadrupolar interactions and the unavailability of high-resolution techniques until the late 1990's, very little additional structural information could be obtained. However, work by Blinc *et al.* focused on the possible diffusion of Na^+ in substituted $NaNbO_3$ using ^{23}Na NMR, by measuring the spin-lattice relaxation times of ^{23}Na over a range of temperatures.[31] Unfortunately, as high-resolution spectra were not available at the time, little support is given for the possibility of Na^+ diffusion, although the observations made in this thesis (Chapter 3) indicate some evidence for Na^+ diffusion at elevated temperatures. A further study by Blinc was presented in 1994, and focused on the possibility of Nb^{5+} defects, *i.e.*, non-stoichiometry.[32] Again, this was not possible to unambiguously prove as high-resolution techniques were not readily available at the time. As already discussed, such defects would be very challenging to detect using solid-state NMR owing to the higher fields and longer acquisition times needed, although understanding the nature of the defects in perovskites is very important due to their possible effects on electrical properties.

It wasn't until the introduction of high-resolution techniques (see Chapter 2), that detailed structural information could be gained from solid-state NMR. Detailed studies were performed by Walton and Ashbrook,[33,34] and subsequently Johnston,[26] in which solid-state NMR and X-ray and neutron diffraction techniques were used to understand the ambient-temperature phases of $NaNbO_3$, as well as how the synthetic approach may affect the ratio of the phases (see Chapter 3).

The 'seven phases' of $NaNbO_3$ (present as a function of temperature) reported by Megaw have been further investigated many times. Some of the more recent work was presented by Koruza (2010),[35] Mishra (2011)[36] and Peel (2012),[37] although this list is by no means exhaustive. For Refs. 35-37, there are some differences proposed

for each of the high temperature structures. It should be noted, however, that work by Peel (Ref 37) presents data for phases R and S only, and not T1, T2 and U. The work presented by Mishra in Ref. 36 is based on a detailed neutron powder diffraction study, with a brief consideration of phonon modes. However, details of the $NaNbO_3$ synthesis are not included, and so the exact phase composition of the starting material cannot be determined. Koruza *et al.*[35] suggested that the P-R transition temperature occurs at 359 °C and the S-T1 transition at 508 °C with the T1-T2 transition occurring at 557 °C. Using X-ray diffraction techniques, they suggested that both phases R and S belong to space group *Pnmm*. The transition temperatures given by Koruza (for S-T1 and T1-T2) are not in agreement with those given by Megaw. Mishra *et al.* reported that phases T1 and T2 possessed the *Cmcm* and *P*4/*mbm* space groups, respectively, in agreement with previous work by Darlington and Knight.[38] Mishra also reported that phases R and S possessed orthorhombic space group *Pbnm*, with $6a_p$ and $12a_p$ c-axis lengths, respectively, although only lower resolution diffraction data were provided. The space group assignment is in contrast to prior work and is not supported subsequently (Peel *et al*.).[37] In the work presented by Mishra and Koruza, however, there is no consideration of whether the starting material used was solely phase P, or a mixture of P and Q. Such consideration was given in the work by Peel, where the phase exclusivity of the starting material was determined using high-resolution neutron powder diffraction.

Additionally, Darlington and Knight[38] corroborated earlier work, in that they reported phase P to belong to space group *Pbcm*. However, caution should be applied when interpreting analyses of refinements for phases P and/or Q. This is because the two can co-exist depending on the synthetic route employed, and determining which phase is present solely from diffraction data can be challenging (see Chapter 3). Results from the characterisation of high-temperature diffraction data is then made more ambiguous by the fact that the starting material may have been phase P exclusively, or a mixture of P and Q, where each phase undergoes a different series of temperature-dependent phase transitions (see Chapter 4). Peel *et al.*[37] performed the most detailed work to date regarding the structures of phases R and S, of which there is no agreed consensus in the prior literature. By using complementary combinations of neutron and synchrotron X-ray diffraction and symmetry mode analysis, phase R was found to possess a $6a_p$ repeat unit along the *c*-axis and $2 \times 2a_p$ in the *ab* plane, and belong to

one of two space groups: *Pmmn* or *Pnma*; phase S was found to possess a $4a_p$ repeat unit along the *c*-axis with space group *Pmmn*. In addition, the phase transition temperatures of R and S were found to be in agreement with those given by Megaw in Refs. 22 and 23. The structures of these phases will not be given here - instead, they can be found in Chapter 3, where Ref. 37 will form the basis for a large portion of the work presented.

With so many variations in the proposed structures of the high-temperature phases, a range of synthetic approaches used and disparity in the phase transition temperatures suggested, it is perhaps unsurprising that research into $NaNbO_3$ still continues. The work presented in this thesis builds on this existing knowledge by using X-ray and neutron diffraction, a range of high-resolution solid-state NMR experiments, first-principles calculations (DFT) and symmetry mode analysis (see Chapter 3), to be able to develop a more comprehensive understanding of $NaNbO_3$.

1.4. Brief Overview of the Symmetry Mode Analysis of $NaNbO_3$

The similarities of the different phases of $NaNbO_3$ make structural characterisation challenging, as the diffraction patterns contain many of the same pseudosymmetries, and consequently the same principal reflections are present. One method of identifying the symmetries present in the different polymorphs and those that are lost (*i.e.,* from a lowering of symmetry) is to use symmetry mode analysis.[39-41] The symmetry elements that remain upon lowering of the symmetry form the space group symmetry of the superstructure, and this is referred to as a distortion symmetry of the parent aristotype symmetry, *e.g.,* for $NaNbO_3$, these are the symmetry elements present in both the cubic parent polymorph and the lower-symmetry polymorphs, such as phases T1 and T2. Symmetry distortions which deviate from the aristotype unit cell can be converted into useful symmetry modes *via* irreducible representations.[40,41] A symmetry mode is simply a phonon mode at a specific point in the Brillouin zone. The irreducible representation, denoted in this thesis as a combination of letters, signs and numbers, is associated with a specific set of peaks/regions in the diffraction pattern, *i.e.,* some peaks arise from the presence of specific symmetry modes. This provides an invaluable tool for determining which symmetry modes are present in different phases. A recently developed free user-

friendly program, ISODISTORT,[39] allows the user to determine the symmetry modes present in different phases, determine how different symmetry modes affect the peaks in a diffraction pattern, and to construct a list of possible structures based on the likely distortion modes and determine if the required modes are present. Work by Peel *et al.*[37] provides a detailed overview of the modes related to $NaNbO_3$ (particularly phases R and S), as discussed in Chapter 3.

References

[1] Weller, M. T., *Inorganic Materials Chemistry*, p. 38-44, Oxford University Press, Oxford, 1994.

[2] Megaw, H., *Nature*, 1945, **155**, 484.

[3] Yashimo, M., Matsuyama, S., Sano, R., Itoh, M., Tsuda, M., Fu, Deshung., *Chem. Mater. Comm.*, 2011, **23**, 1643.

[4] Zeb, A., Milne, S. J., *J. Am. Ceram. Soc.*, 2013, **96**, 2887.

[5] Wilkinson, A. P., Cheetham, A. K., *J. Appl. Phys.,* 1993, **74**, 3080.

[6] Rehrig, P. W., Park, S. E., Trolier-McKinstry, S., Messing, G. L., Jones, B., *J. Appl. Phys.,* 1999, **86**, 1657.

[7] Shannon, R. D., *Acta Cryst.,* 1976, **A-32**, 751.

[8] West, A. R., *Solid State Chemistry and its Applications*, p. 204-207, Wiley, Chichester, 1984.

[9] Goldschmidt, V. M., *Naturwissenschafen*, 1926, **14**, 477.

[10] King, G., Woodward, P. M., *J. Mater. Chem.*, 2010, **20**, 5785.

[11] Ahtee, A., Glazer, A. M., *Acta Cryst.,* 1976, **B32**, 3243.

[12] Woodward, P. M., *Acta Cryst.,* 1997, **B53**, 32.

[13] Howard, C. J., *Acta Cryst.,* 2005, **A61**, 93.

[14] Glazer, A. M., *Acta Cryst.,* 1972, **B28**, 3384.

[15] Liebenweber, K., Parise, J., *J. Solid State Chem.,* 1995, **114**, 277.

[16] Woodward, P. M., *Acta Cryst.,* 1997, **B-53**, 44.

[17] Liu, L., Fan, H., Fang, L., Chen, X., Dammak, H., Thi, M. D., *J. Mater. Chem. Soc.*, 2009, **117**, 138.

[18] Wang, Y., Damjanovic, D., Klein, N., Setter, N., *J. Am. Ceram. Soc.*, 2008, **91**, 1962.

[19] Fang, J., Wang, X., Zuo, R., Tian, Z., Zhong, C., Li. L., *Phys. Status Solidi*, 2011, **208**, 791.

[20] Holterman, J., Groen, P., *An Introduction to Piezoelectric Materials and Components*, Stichting Applied Piezo, Netherlands, 2012.

[21] Lefkowitz, I., Lukaszewicz, K., Megaw, H. D., *Acta Cryst*., 1966, **20**, 670.

[22] Megaw, H. D., *Acta Cryst.,* 1968, **A24**, 589.

[23] Glazer, A. M., Megaw, H. D., *Acta Cryst*., 1973, **A29**, 489.

[24] Megaw, H. D., *Ferroelectrics*, 1974, **7**, 87.

[25] Ahtee, M., Glazer, A. M., *Acta Cryst.,* 1976, **A32**, 434.

[26] Johnston, K. E., Tang, C. C., Parker, J. E., Knight, K. S., Lightfoot, P., Ashbrook, S. E., *J. Am. Chem. Soc*., 2010, **132**, 8732.

[27] Johnston, K. E., Griffin, J. M., Walton, R. I., Dawson, D. M., Lightfoot, P., Ashbrook, S. E., *Phys. Chem. Chem. Phys*., 2011, **13**, 7565.

[28] Mishra, S. K., Choudhury, N., Chaplot, S. L., Krishna, P. S. R., Mittal, R., *Phys. Rev. B.*, 2007, **76**, 024110.

[29] Shuvaeva, V. A., *Ferroelectrics,* 1993, **141**, 307.

[30] Wolf, F., Kline, D., Story, H. S., *J. Chem. Phys.*, 1970, **53**, 3538.

[31] Dolinsek, J., Blinc, R., *Solid State Communications,* 1989, **70**, 1077.

[32] Norcross, J. A., Ailion, D. C., Blinc, R., Dolinsek, J., Apih, T., Slak, J., *Phys. Rev. B.*, 1994, **50**, 3625.

[33] Ashbrook, S. E., Le Polles, L., Gautier, R., Pickard, C. J., Walton, R. I., *Phys. Chem. Chem. Phys.,* 2006, **8**, 3423.

[34] Modeshia, D. R., Darton, R. J., Ashbrook, S. E., Walton, R. I., *Chem. Comm.,* 2009, **1**, 68.

[35] Koruza, J., Tellier, J., Malic, B., Bobnar, V., Kosec, M., *J. Appl. Phys.,* 2010, **108**, 113509.

[36] Mishra, S. K., Mittal, R., Pomjakushin, V. Y., Chaplot, S. L., *Phys. Rev. B.,* 2011, **83**, 134105.

[37] Peel, M. D., Thompson, S. P., Daoud-Aladine, A., Ashbrook, S. E., Lightfoot, P., *J. Inorg. Chem.,* 2012, **51**, 6876.

[38] Darlington, C. N. W., Knight, K. S., *Physica B*, 1999, **266**, 368.

[39] ISODISTORT website: http://stokes.byu.edu/iso/isodistorthelp.php

[40] Orobengoa, D., Capillas, C., Aroyo, M. I., Perez-Mato, J. M., *J. Appl. Crystallogr*. 2009, **42**, 820.

[41] Campbell, B. J., Stokes, H. T., Tanner, D. E., Hatch, D. M., *J. Appl. Crystallogr.* 2006, **39**, 607.

Chapter 2
Theoretical Background

2.1. Crystal Symmetry

2.1.1. Introduction

There are many different types of crystal structures, each having specific characteristics, physical and chemical properties, and commercial applications. Crystals are built up of a regular arrangement of atoms, where the smallest unit that can be repeated to reproduce the crystal structure is called the unit cell.[1] As the unit cell represents the symmetry of the crystal structure, and also the spatial arrangement of atoms, it must be three dimensional and, as such, can be described using six parameters – three lengths (a, b and c) and three internal angles (α, β and γ). There are seven distinct and independent unit cell geometries, referred to as the seven crystal systems, and these are defined by the minimum elements of symmetry unique to each. The seven crystal systems are triclinic, monoclinic, orthorhombic, tetragonal, trigonal, hexagonal and cubic.

2.1.2. Crystal Systems[2]

The seven unique crystal systems are shown in Table 2.1, alongside the corresponding minimum symmetry requirements for each, and Fig. 2.1 shows the geometries of each. When characterising a crystal system it is important to identify elements of symmetry, or more accurately, point symmetry. The Hermann-Mauguin nomenclature system states the way in which symmetry elements are noted. There are four distinct elements of point symmetry – a mirror plane, *m*, a rotation axis, *n*, a roto-inversion axis, $\bar{n}$, and a centre of symmetry, $\bar{1}$, where *n* is substituted for a number and is equal to 360 / angle of rotation, and is therefore limited to values of 1, 2, 3, 4 and 6. It is important to note that these elements of point symmetry, and not the lattice

Table 2.1: The seven crystal systems and their corresponding minimum symmetry requirements.

Crystal System	Unit Cell Parameters	Symmetry Requirements
Triclinic	$a \neq b \neq c$	None. Lengths are not co-
	$\alpha \neq \beta \neq \gamma$	planar
Monoclinic	$a \neq b \neq c$	One two-fold axis or
	$\alpha = \gamma = 90°, \beta \neq 90°$	mirror plane
Orthorhombic	$a \neq b \neq c$	Three two-fold axes or
	$\alpha = \beta = \gamma = 90°$	mirror planes
Tetragonal	$a = b \neq c$	One four-fold axis
	$\alpha = \beta = \gamma = 90°$	
Trigonal	$a = b = c$	One three-fold axis
	$\alpha = \beta = \gamma \neq 90°$	
Hexagonal	$a = b \neq c$	One six-fold axis
	$\alpha = \beta = 90°, \gamma = 120°$	
Cubic	$a = b = c$	Four three-fold axes
	$\alpha = \beta = \gamma = 90°$	

parameters, define a crystal system. For example, a tetragonal unit cell must have a four-fold axis, and the corresponding lattice parameters are simply a consequence of the symmetry imposed on it. In addition, the symmetry elements listed in Table 2.1 are merely the minimum required symmetry elements for a unit cell geometry.

2.1.3. Point Groups[1,2,3]

The elements of point symmetry may occur on their own, or as a combination of symmetry types, such as n-fold axes and mirror planes. The combinations of point symmetry elements and crystal systems are called point groups, of which 32 are allowed combinations, and are given in Table 2.2. It should be noted that not all combinations of point symmetry elements exist. For example, point groups for the orthorhombic crystal system may be 222, *mm*2 or *mmm*, but *m*22 does not exist.

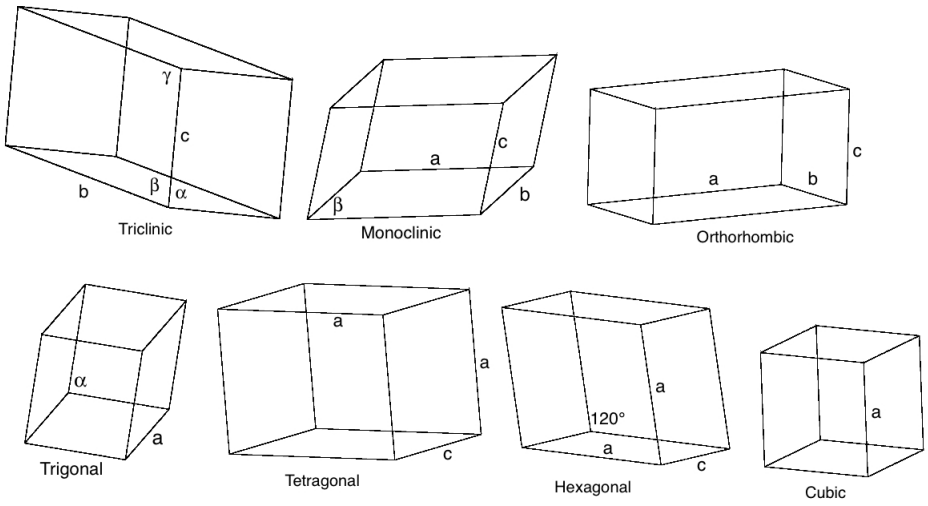

Figure 2.1: The seven distinct crystal systems.[1] Note, 90° angles are omitted for clarity and only independent parameters are shown.

Table 2.2: 32 possible crystallographic point groups arising from combinations of point symmetry elements for the conventional seven crystal systems, along with allowed lattice types.

Crystal System	Point Groups	Allowed Lattice Type
Triclinic	1, $\bar{1}$	*P*
Monoclinic	2, *m*, 2/*m*	*P* and *C*
Orthorhombic	222, *mm*2, *mmm*	*P, C, I* and *F*
Tetragonal	4, $\bar{4}$, 4/*m*, 422, 4*mm*, $\bar{4}$2*m*, 4/*mmm*	*P* and *I*
Trigonal	3, $\bar{3}$, 32, 3*m,* $\bar{3}$*m*	*P*
Hexagonal	6, $\bar{6}$, 6/*m*, 622, 6*mm*, $\bar{6}$*m*2, 6/*mmm*	*P*
Cubic	23, *m*3, 432, $\bar{4}$3m, *m*3*m*	*P, F* and *I*

2.1.4. Lattice Types and Symmetry[1]

When considering a periodic array of atoms, there is often more than one way to define the unit cell, and this gives rise to different lattice types. Fig. 2.2 shows a two-dimensional array of lattice points for cubic potassium bromide salt, where each point represents an alternating K and Br atom. There are two distinct ways to define the unit cell, whereby each possibility represents the smallest repeat unit within the crystal structure. It can be seen that the unit cell can be drawn by having four atoms positioned on the edges of the cell only. This is called a primitive lattice type, *P*, and occurs where no atoms are 'centred' within the unit cell. However, it also possible to define the unit cell by having an atom, or lattice point, centred within it, to give rise to a centred lattice type, of which there are three distinct types: side-centred, *A*, *B* or *C*, body-centred, *I*, and face-centred, *F*. The four distinct lattice types are shown in Fig. 2.3.

The seven crystal systems may be combined with the different lattice types, both primitive and centred, to give rise to the 14 unique Bravais lattices. Table 2.2 shows the allowed combinations of crystal system and lattice type, which give rise to the 14 Bravais lattices. Bravais lattices may be likened to unit cells, in that they can be repeated in all three dimensions to reproduce the crystal structure and they are the smallest possible unit that represents the full symmetry of the crystal.

In a crystal system, there may also be translational symmetry, or space symmetry, which involves two different symmetry elements occurring simultaneously, to produce a symmetry operation which cannot be found in finite molecules. The two translational symmetry elements are screw axes and glide planes. A screw axis is a simultaneous translation and rotation, and is denoted X_Y, where a Y/X translation occurs in the direction of the screw axis, coupled with a rotation by X.

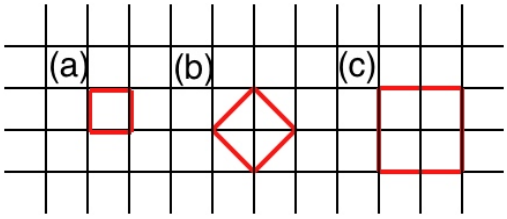

Figure 2.2: Two-dimensional array of a lattice to illustrate (a) a primitive unit cell, (b) a body-centred unit cell and (c) a supercell, *i.e.*, comprised of multiple unit cells. The primitive and body-centred unit cells can easily be defined from the same array of lattice points.

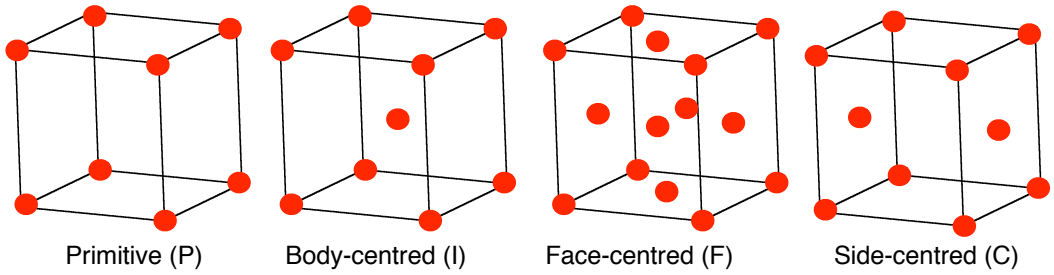

Figure 2.3: The four distinct lattice types.

A glide plane is a combined translation and reflection. The translation is either parallel to a unit cell axis, (*a, b* or *c*) or face diagonal (*n*), and is by a 1/2 in that direction. In addition, a translation may be parallel to a body diagonal (*d*) and have a translation of 1/4 of the body to which it is diagonal. For example, consider the space group (Section 2.1.5) *Pbcm*. There is a *b* glide-plane perpendicular to the *a*-axis, a *c* glide-plane perpendicular to the *b*-axis, and a mirror plane perpendicular to the *c*-axis. If the gliding direction is parallel to the *b*-axis, then the glide plane is denoted as *b*, and represents a reflection in the *a*-plane followed by a translation parallel to the *b*-axis by *b*/2. The *c* glide is a reflection in the *c*-plane followed by a translation parallel to the *c*-axis by *c*/2.

2.1.5. Space Groups[1,2]

Space groups are a method of notation to describe the lattice type and symmetry operations present within a crystal structure. By combining the 14 Bravais lattices, 32 point groups and elements of translational symmetry, there are a total of 230 unique space groups available. All commensurate crystal structures belong to one of these space groups. A full list of these space groups is not shown here but is given in the *International Tables for X-ray Crystallography,* Vol. A. The first letter in a space group symbol is the lattice type – *P, C, I, F*, *etc*., and this is followed by the symmetry elements present. If a unique principal axis exists then this is denoted immediately after the lattice type. The remaining letters in a space group refer to the symmetry elements (both point and translational) present.

2.2. Bragg's Law[2,4]

X-rays are appropriate for diffraction by crystalline materials as they have a wavelength close to the interatomic separation of atoms in the crystal. Diffraction effects are greatest when the wavelength equals, or is close to, the atomic separation distance in the material. The interatomic separation is referred to as the d-spacing, d.

Bragg's law[4] governs diffraction of incident radiation (X-rays) from a crystal, or, more specifically, from Miller planes within the crystal. Bragg's law is given by

$$n\lambda = 2d \sin\theta \quad , \tag{2.1}$$

where λ is the wavelength of the incident radiation, n is an integer, and θ is the angle between the incident beam and the plane. This is illustrated schematically in Fig. 2.4.

Bragg's law, proposed in 1913 by W. H. Bragg and W. L. Bragg, places very strict conditions upon when constructive interference can occur in a diffraction experiment.

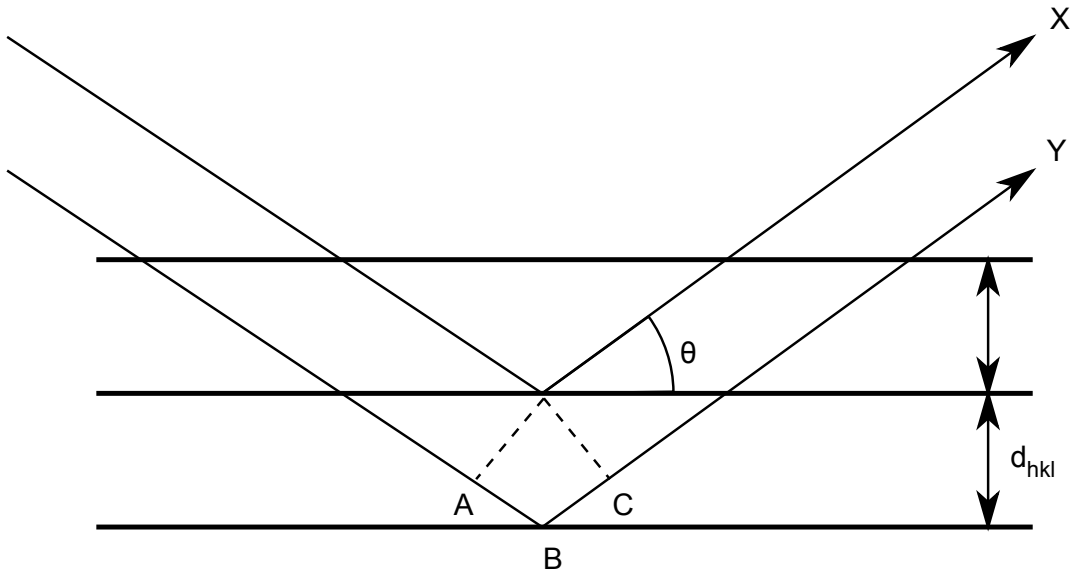

Figure 2.4: Schematic (not to scale) diagram showing Bragg diffraction of waves from Miller planes, showing the d-spacing between the planes, angle of reflection and the additional path difference (AB + BC) that wave Y must travel.

By considering Fig. 2.4 it can be seen that, for the lower of the three planes, the incident radiation travels an additional distance (AB + BC) to that scattered from the plane above it. This additional distance the incident radiation must travel is called the path difference. Bragg's law is satisfied when this path difference is an integer number of wavelengths (nλ) and, therefore, constructive interference will occur.

Bragg's law is a crude approach to understanding how diffraction works, and is an inaccurate tool in describing the process. The Laue equations,[1] however, provide a detailed and mathematically accurate way of describing the process, and consider the stringent diffraction conditions needed for all the planes in all three dimensions. As the Laue approach is not utilised in this work, no further discussion will be given here.

2.3.1. Miller Indices[1,5,6]

During an X-ray diffraction experiment (Section 2.4), it can be considered that X-rays diffract off planes within the crystal structure. These lattice planes are imaginary and do not necessarily pass through lattice points or atoms. They provide a simple way of visualising Bragg's law but are not responsible for the diffraction of X-rays. In a three-dimensional structure, lattice points can be considered to be divided up into many planes, separated by the interatomic d-spacing, d. Each lattice plane is assigned three letters, *h*, *k* and *l*, known as the Miller indices, describing a so-called Miller plane. Each plane is expressed as (*hkl*), where *h*, *k* and *l* are integers.

As Miller indices are used to specify planes and directions, they represent a vector, r, passing from the origin to any lattice point, is related to the three individual vectors in the unit cell, and is given by

$$\mathrm{r} = \mathrm{r}_1 a + \mathrm{r}_2 b + \mathrm{r}_3 c \quad , \tag{2.2}$$

where the basis vectors are *a*, *b* and *c* and represent the three dimensions in the cell, and r_1, r_2 and r_3 are the individual vectors which are expressed as Miller indices (*hkl*).

The relationship between Miller indices and the interatomic d-spacing is often straightforward for crystal structures with higher symmetry. Some examples can be found in Fig. 2.5. It can be seen from this that the higher the integer value of *h*, *k* or *l*, the smaller the d-spacing. For orthogonal crystals, *i.e.*, orthorhombic, tetragonal and cubic, the relationship between d-spacing and Miller plane is given by Equations 2.3-2.5. For non-orthogonal crystal systems, the calculations become increasingly more complex as the symmetry is lowered.

$$\frac{1}{\mathrm{d}^2} = \frac{h^2}{a^2} + \frac{k^2}{b^2} + \frac{l^2}{c^2} \tag{2.3}$$

$$\frac{1}{d^2} = \frac{h^2+k^2}{a^2} + \frac{l^2}{c^2} \quad (2.4)$$

$$\frac{1}{d^2} = \frac{h^2+k^2+l^2}{a^2} \quad (2.5)$$

By using these equations, a d-spacing can be calculated for any set of Miller planes, as long as the crystal system and lattice parameters are known. Again, this knowledge can also be used to assign Bragg peaks in an X-ray diffraction pattern to a set of Miller indices. Typically, X-ray diffraction patterns are plotted as a function of 2θ. Use of the Bragg equation allows this value to be converted into a d-spacing. By using Equations 2.2-2.4, the d-spacing and the lattice parameters, *a*, *b* and *c*, possible Miller indices may be proposed for each Bragg reflection.

2.3.2. Systematic Absences[1,2,4,5,6]

Not all Miller indices result in constructive interference, and consequently, not all are observed in a diffraction pattern. For centred lattice types, there are rules for reflections to be present. Determination of the Miller indices present, and those absent, allows the lattice centring to be determined, along with information regarding the symmetry elements present. As systematic absences are not considered further in this thesis, no further discussion is given.

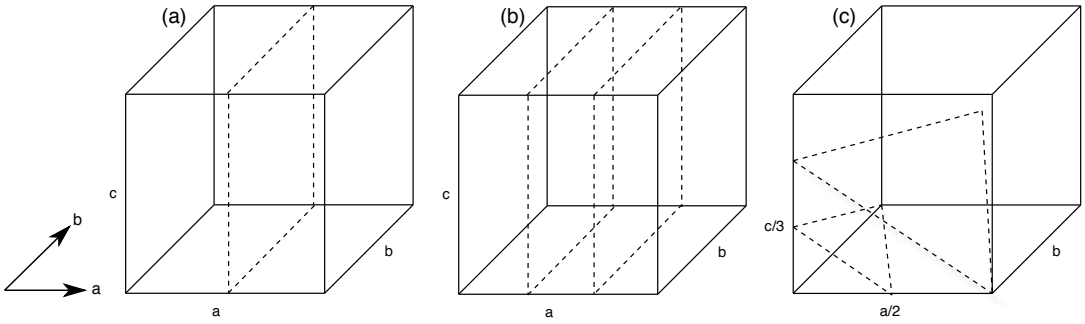

Figure 2.5: Examples of Miller indices showing the (a) 200, (b) (300) and (c) (213) planes.

2.4. X-ray Diffraction Experiments

2.4.1. Introduction

Solid matter can be broken down into two broad categories – amorphous and crystalline. Amorphous materials account for approximately 5% of solids and crystalline materials about 95%. Diffraction patterns of thousands of inorganic materials are now in databases, and, therefore, carrying out diffraction experiments on unknown samples allows a search-and-match to be performed, to identify the unknown crystalline material. The distinction between amorphous and crystalline materials is highly important – amorphous materials have a more random arrangement of atoms and are not periodic structures like crystals. X-ray diffraction experiments work by exploiting the inherent periodicity of crystals.

2.4.2. Generation of X-rays

Electrons are accelerated through high voltages in an electron gun, where they collide with a metal, typically copper. Upon collision, the electrons are slowed or stopped, with the subsequent release of energy with a range of wavelengths, sometimes referred to as 'white,' or Bremsstrahlung radiation. When the collision occurs, the incident high-energy electrons are able to ionise an electron from the 1s subshell of the metal (Cu) target. An outer electron will 'drop down' from the 2p or 3p subshell to fill this vacancy. This causes the release of energy corresponding to an X-ray. However, the 2p → 1s and 3p → 1s transitions result in the generation of X-rays with

different wavelengths. The 3p → 1s transition results in a X-ray wavelength of 1.3922 Å, whereas the 2p → 1s transition results in wavelengths of 1.54059 and 1.54433 Å, with an average value of 1.5418 Å. Note, this wavelength is that of X-rays commonly used in "laboratory" X-ray diffraction, used in this thesis. These emissions give rise to an X-ray emission spectrum, as shown in Fig. 2.6. Ideally, only one wavelength of radiation is used in the experiment, and for a Cu source, Ni metal is used as a filter. Alternatively, a monochromator may be used to provide radiation of one wavelength.

2.4.3. Scattering of X-rays[1,2]

X-ray diffraction experiments may be performed using a powdered sample or a single crystal. All diffraction work presented in this thesis will focus on powder diffraction, and as such, single crystal diffraction methods will not be discussed. In powder diffraction, millions of small crystals are present, and each of these has a slightly different orientation, resulting in a full range of orientations being observed relative to the incident X-ray beam. For some, the angle of orientation will be equal to the Bragg angle, resulting in Bragg's law being satisfied and constructive interference in the diffraction experiment being observed. A moving detector is able to detect the diffracted X-rays and record these digitally.

The X-rays can be envisaged as diffracting in a cone-like shape, *i.e.*, they are divergent. Each of these cones will have some intensity, I, of X-rays hitting the detector, and this signal is recorded as a Bragg peak in the diffraction pattern, of intensity, I. Sometimes, these cones will have some degree of overlap due to their close proximity and the result is partially resolved peaks being present in the pattern.

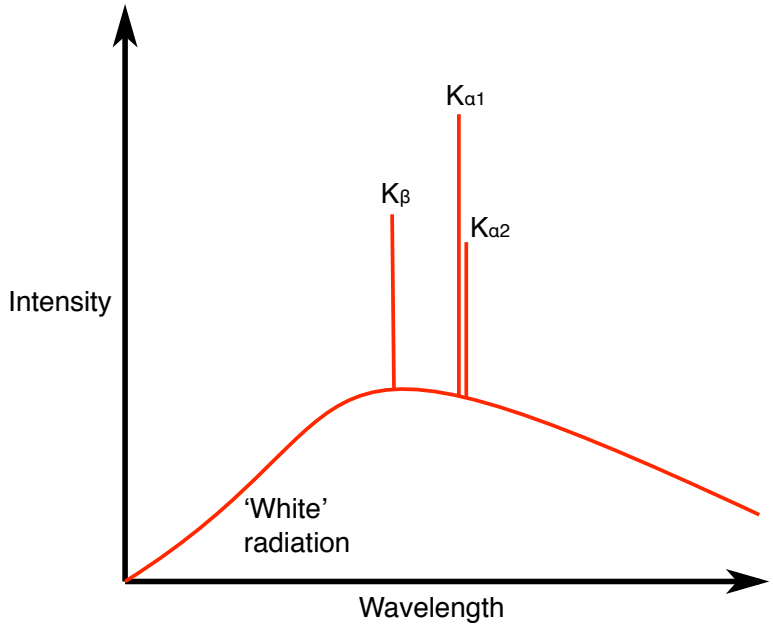

Figure 2.6: Schematic (not to scale) representation of an X-ray emission spectrum from an electron gun with a Cu target showing 'white' radiation where low intensity X-rays of many wavelengths are produced, along with higher intensity X-rays of specific wavelengths, denoted K_{β}, $K_{\alpha 1}$ and $K_{\alpha 2}$.

In diffraction patterns, two physical properties are of particular importance. Firstly, the d-spacing, obtained from the position of the Bragg peak, and secondly, the intensities of the peaks. In similar samples, similar d-spacings may be observed and, therefore, peaks may appear in similar places in the diffraction patterns but nonetheless, the intensities of the peaks may be different. Quantitative measurements of peak intensities can aid in the determination of unknown crystal structures.

The total intensity scattered is equal to the sum of all the individual intensities of the peaks: $I_1 + I_2 + I_3 \ldots$. The scattering factor, or form factor, f_n, of an atom is proportional to the atomic/electron number of the atom, and as such, heavier elements have greater scattering factors. As a result, light atoms, such as H and Li, do not scatter X-rays well, and X-ray diffraction patterns are typically 'dominated' by heavier elements when they are present, making light atom location difficult to determine. Additionally, atoms with *similar* atomic number are also difficult to distinguish as they have similar scattering factors and therefore result in peaks with similar intensities. The atoms in the sample will only scatter quite weakly at high

angles, and as such, the intensities of these peaks are poor. Important structural information, such as anisotropic displacement parameters, is often obtained from the high-angle region, and as such, this information cannot be accurately determined if the intensities are weak. Fig. 2.7 shows the scattering factors of two nuclei as a function of λ/2θ. These specific problems associated with using X-rays can be readily overcome by using neutron diffraction, as outlined in Section 2.6.

For each observed reflection in the diffraction pattern, which corresponds to a particular set of (*hkl*) values, a structure factor, F_{hkl}, is calculated to describe how the plane diffracted the incident X-rays. It describes both the amplitude and phase of the diffracted wave. The structure factor may also be used to determine if a reflection will be systematically absent, *i.e.*, it has a value of zero. The amplitude of the diffracted wave has both sine and cosine components. The structure factor is given by,

$$F_{hkl} = \sum_n f_n \cos\{2\pi(hx + ky + lz)\} + i\sum_n f_n \sin\{2\pi(hx + ky + lz)\}, \qquad (2.6)$$

where f_n is the form factor of atom n, and F_{hkl} is the structure factor for a particular plane.

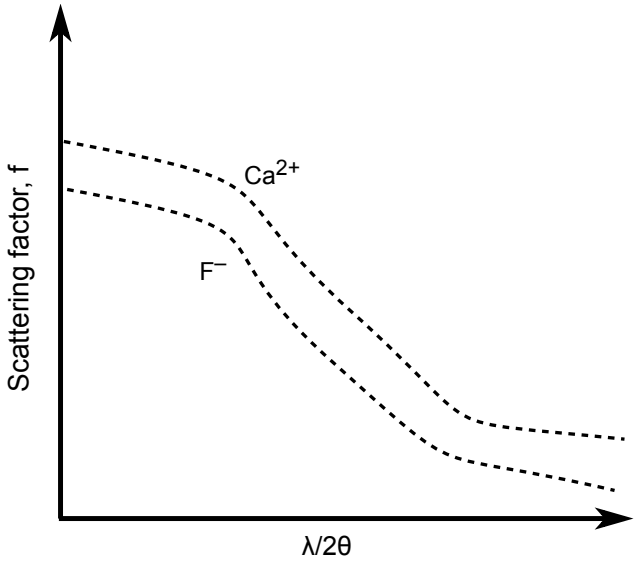

Figure 2.7: Schematic representation of the change in scattering factors for two nuclei over a range of incident angles.

The sine and cosine parts may be combined to derive the simplified expression

$$F_{hkl} = \sum_{n} f_n \exp i\{2\pi(hx + ky + lz)\} \ . \tag{2.7}$$

By using Equations 2.2-2.4, d_{hkl} may be calculated from the lattice parameters, which in turn, can be used to calculate sin θ/λ by using Bragg's law. The form factor for a given atom, f_n, may then be determined using the value of sin (θ/λ) - the form factors for all atoms at different values of sin θ/λ are given in the *International Crystallography Tables.*[7] The value of F_{hkl} is summed over all the atoms in the unit cell to obtain the final structure factor. The structure factor is closely related to the intensity of the observed reflection, as given by

$$F_{hkl}^2 \propto I_{hkl} \ . \tag{2.8}$$

This is an abbreviated term, used for convenience.

2.5. Synchrotron X-rays

2.5.1. Introduction

Synchrotron X-rays may have a much shorter wavelength than the X-rays used in standard laboratory experiments (1.5418 Å for Cu $K_{\alpha 1}$). Shorter wavelengths allow additional structural information to be gained and often provide a much higher resolution diffraction pattern. Additionally, the beam intensity is substantially higher, increasing peak-to-background signal and often decreasing the acquisition time needed for each experiment. One drawback of using synchrotron X-rays in diffraction experiments is the specialist equipment needed – a large synchrotron is required for this, and time and access to these national facilities is limited.

2.5.2. Synchrotron X-ray Generation[8]

In a synchrotron, electrons are generated in an electron gun, and accelerated through three particle accelerators – a linear accelerator, a booster synchrotron and a large storage ring. The storage ring is composed of dipole magnets, which are used to steer the electrons around the ring at very high velocities. When the electrons pass between the magnets, they lose energy in the form of waves, and these pass out of the storage ring and are directed towards the diffractometers for use in experiments.

The synchrotron diffraction work within this thesis was carried out at the DIAMOND Light Source in Didcot, Oxford.[9] At DIAMOND, the electron beam is accelerated up to energies of 90 keV before entering the linear accelerator (linac). In the linac, the electrons are then accelerated up to energies of 100 MeV using small radiofrequency cavities. They then enter the booster synchrotron where 36 dipole bending magnets accelerate them to energies of 3 GeV before they enter the storage ring. This is composed of 24 straight sections angled together to form a closed loop of 562 m. The electrons generate synchrotron light through their motion around the ring, which is filtered off to the separate beamlines. The average life span of the electron beam is approximately 20 hours, and 'new' electrons top this up twice daily.

All of the synchrotron diffraction data presented in this thesis was obtained on beamline I-11 - High-Resolution Powder Diffraction (HRPD). The energy of X-rays used is approximately 15 keV, corresponding to a wavelength of typically 0.826 Å. Multi-analysing crystal (MAC) detector banks are used with cover a 2θ range of 0 - 120°. Alternatively, position sensitive detector (PSD) banks may be used with a 2θ range of 0 - 90°. MAC detectors typically require 30 minute experiments for sufficient signal-to-background to be obtained, whereas those that use PSDs require only seconds. This beamline allows for a hot air blower to be used to obtain high temperature diffraction data (up to 1200 K, although there is up to a 100 K difference between actual and target temperature, which increases as the target is raised), although this severely limits the upper 2θ range (70°) that can be obtained using PSDs. This is not affected when MAC detectors are used. Fig. 2.8 shows a figure of the diffractometer and typical experimental setup used in this work.

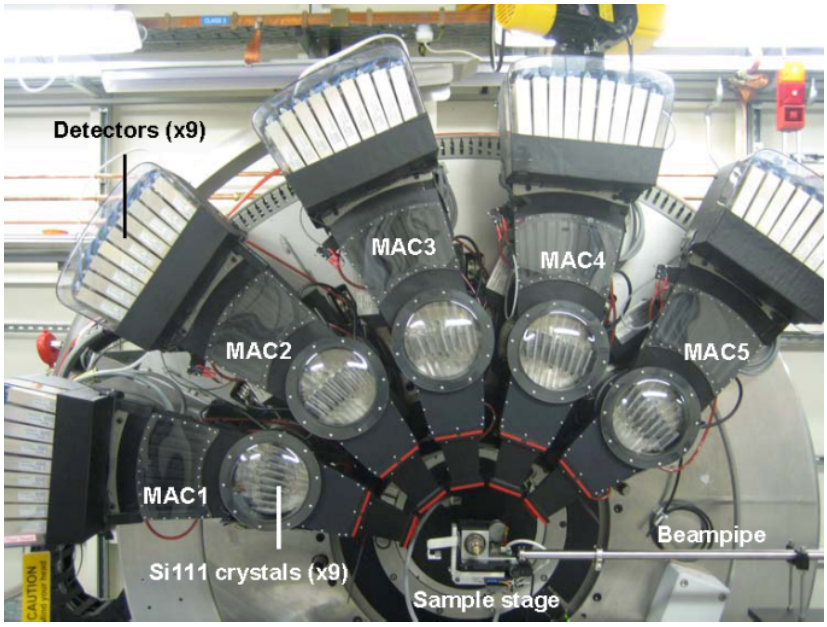

Figure 2.8: The I-11 (High-Resolution Powder Diffraction) diffractometer at DIAMOND.[9]

2.6. Neutron Diffraction

2.6.1. Introduction

Whilst neutrons have a mass, and may therefore be considered a particle, they also have a wavelength on the order of atomic spacings and are, therefore, ideal for probing structure in solids. Neutrons are diffracted by solid material, in particular, they are diffracted by the nucleus directly and not by surrounding electron clouds, like X-rays. Whilst the drawbacks of X-ray diffraction are that light atom location is poor and atoms of similar atomic number are difficult to distinguish, this is not the case in neutron diffraction. Light nuclei, such as ^{2}H and ^{7}Li, can be readily observed in diffraction patterns, and are in fact, good neutron scatterers. Neutron diffraction is seen as a complementary technique to (synchrotron) X-ray diffraction as each has its advantages and disadvantages, as discussed in the relevant sections. The neutron diffraction work in this thesis was carried out at the ISIS spallation neutron source, in Didcot, UK.[12]

2.6.2. Generation of Neutrons

ISIS is a spallation neutron source (rather than a reactor source),[10, 11] where neutrons are generated and used in diffraction experiments. At the start of an accelerator, H^- ions are produced using an electric discharge. These charged ions leave the ion source (typically NaH) in pulses, typically on the microsecond timescale, where they form pulsed beams that are accelerated towards a linear accelerator. In the linear accelerator, the beam is accelerated to around 70 MeV, and then passes into a synchrotron. Upon entering the synchrotron, the beam passes through a target, typically aluminium oxide or gold foil, where the electrons are stripped off. This results in the formation of a pulsed proton beam, which is accelerated around the synchrotron at a rate of 30-70 times per second. The beam is then diverted into a heavy-metal target, where a collision results in spallation, and the heavy-metal atoms break down into smaller ones, with the release of neutrons. The heavy metal is placed in the target station, to which a number of diffractometers and spectrometers are linked. The pulsed neutrons are then slowed down toward the desired diffractometer, as lower speeds are required for the experiments.

2.6.3. Neutron Diffraction and Scattering

Neutron diffraction experiments often make use of time-of-flight (TOF) techniques[12] - a form of elastic neutron scattering that requires the starting position of the neutrons to be fixed. Additionally, the time between the pulse being fired, collision and detection must also be recorded. Controlling the initial time of the neutron pulse is simple for spallation sources, as is recording the time the scattered neutrons hit the detector. Recording the time a neutron takes to travel any fixed distance allows its wavelength to be calculated by combining the de Broglie wavelength (Equation 2.9) with the Bragg equation, as shown in Equation 2.10, where λ is the wavelength, h is Plank's constant, v and m are the speed and mass of the neutron, respectively, L is the path length the neutron travels and t is the time of flight.

$$\lambda = \frac{h}{mv} \tag{2.9}$$

$$\lambda = 2d \sin\theta = \frac{ht}{mL} \tag{2.10}$$

By using this method, the time-of-flight, *t*, is utilized in calculating the wavelength of the neutron, which in turn, is used to calculate the d-spacings.

The scattering properties of an incident neutron by an atom are determined by the spin state of the nucleus and the interaction it has with the spin (I = 1/2) of the neutron. The interaction of these spin states results in two observations – firstly, coherent, or in-phase, scattering occurs and Bragg reflections can then be observed, and secondly, incoherent, or out-of-phase, scattering occurs, resulting in background signal. Note, incoherent scattering results in increased background signal for TOF neutron scattering experiments but destructive interference observed in X-ray diffraction experiments does not. When neutrons are diffracted by the target sample they are detected by detector banks, which generally occupy fixed positions. The low-angle detectors will measure the intensities of peaks with higher d-spacings, the high-angle detectors measure the intensities of peaks with lower d-spacings, and the back scattering detector banks provide data with the highest resolution over a range of d-spacings.

The neutron data presented in this work were obtained on two beamlines - High-Resolution Powder Diffraction (HRPD) and General Materials (GEM), with the specific features of each making it ideally suited to specific materials or experiments. HRPD is the highest resolution powder diffractometer of its type in the world.[11] At GEM, neutrons have a much shorter flight path of approximately 17 m (distance between the source and sample), where the scattered flight path (distance from sample to the detector) of the neutron is between 1 and 2.9 m, with detectors covering a 2θ range of 1.1 - 169.3°, whereby 'portions' of this range are covered from different detector banks, of which there are six in total.

2.6.4. Comparison of Neutron and X-ray Diffraction

Neutron scattering is sensitive to isotope effects, so that high scattering contrast can be observed between, for example, ^{1}H and ^{2}H. These isotopes have substantially different neutron scattering lengths: –3.74 and 6.67 fm,[13] respectively, and as such, their scattering effects can be readily distinguished. The neutron scattering lengths are a measure of the strength of the interaction between the neutron and the specified nucleus. Light atom determination in the presence of heavier atoms is much more readily achieved with neutron diffraction methods. For example, in a sample of $Li_xNa_{1-x}NbO_3$, the lighter ^{7}Li, ^{16}O and ^{23}Na nuclei may have positions difficult to determine in the presence of heavier ^{93}Nb. However, their respective neutron scattering lengths are –2.22, 5.80, 3.63 and 7.05 fm, which allows their scattering effects to be readily distinguished.

Spallation neutron sources, however, are inherently weak, unlike synchrotron X-ray sources. The weak nature of the source means that less signal is observed, good quality diffraction patterns typically take longer to acquire, and substantially larger volumes of sample are required. The latter, in particular, is a major disadvantage of neutron diffraction techniques compared with X-rays diffraction. Neutrons, are non-destructive, and as such, 'delicate' material, such as organic molecules and biological samples, can be readily investigated, whereas sample degradation is more likely to occur when exposed to X-rays, and particularly the higher energy synchrotron X-rays. Fig. 2.9 shows a comparison of the three types of powder diffraction used in this thesis - neutron, synchrotron X-ray and "laboratory" X-ray, denoted NPD, s-PXRD and l-PXRD, respectively, for $Li_{0.1}Na_{0.9}NbO_3$.

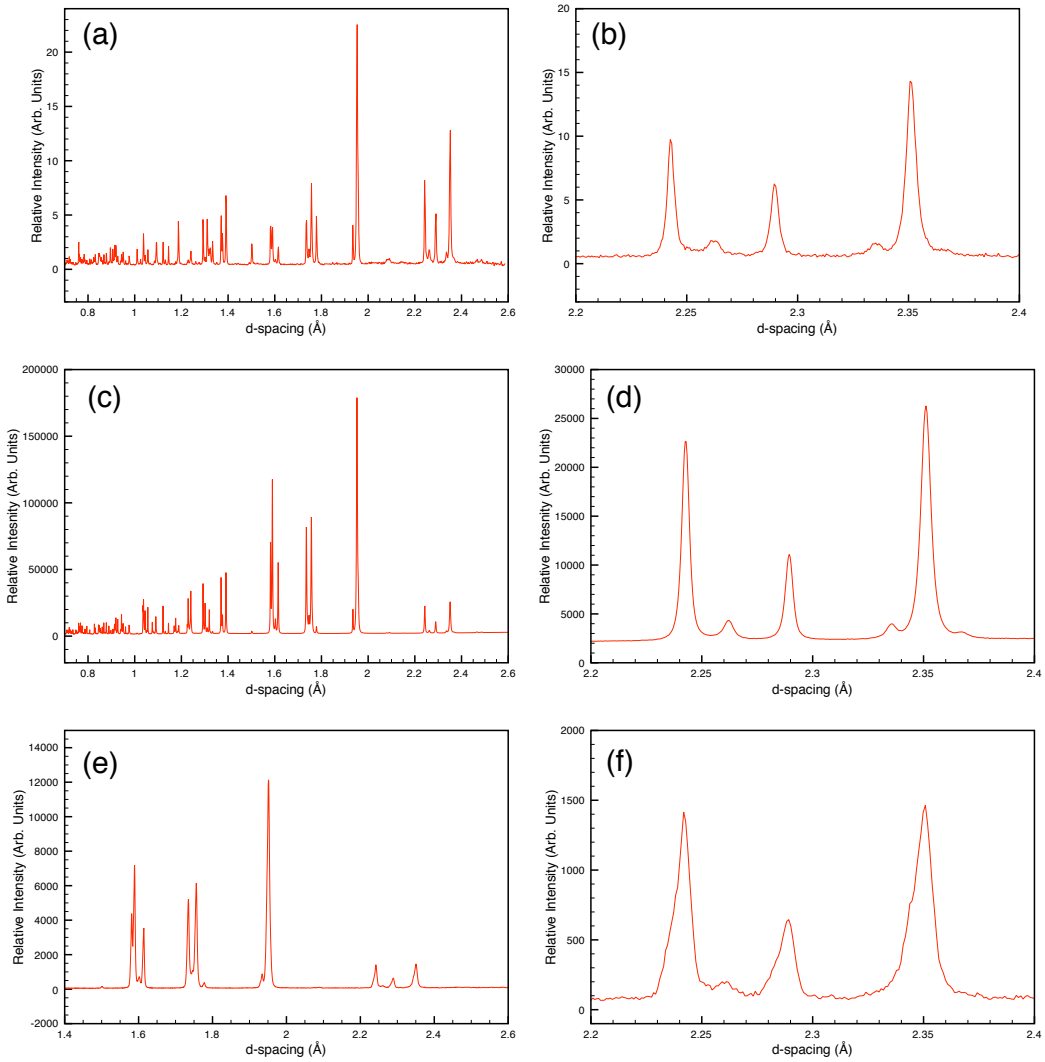

Figure 2.9: Diffraction patterns of a sample of $Li_{0.1}Na_{0.9}NbO_3$, along with corresponding expansions of the higher d-spacing regions. (a) and (b) are NPD data, (c) and (d) are s-PXRD data and (e) and (f) are l-PXRD data. For ease of comparison, all diffraction patterns are plotted using d-spacing. Note, the d-spacing lower limit of the l-PXRD diffraction pattern is greater than for the other methods.

2.7. Rietveld Analysis[14]

In any X-ray or neutron diffraction powder pattern a large number of Bragg peaks are observed, particularly in the region of low d-spacing (0.7 - 2.5 Å). Most crystalline materials will give rise to a high number of peaks in the diffraction pattern, and it is common for some of these peaks to overlap. As a consequence, it is difficult to determine the intensities, peak width and structure factors for each individual peak. Rietveld refinement, named after the inventor Hugo Rietveld,[15] provides an approach that allows an observed diffraction pattern to be compared to a known, or calculated, diffraction pattern by line fitting using the least squares method. This method, however, requires some prior structural knowledge, as an initial calculated pattern is needed, and approximate values of the crystallographic parameters (*i.e.*, unit cell, space group and atomic coordinates) are needed as initial input. The refined parameters include background coefficients, a zero-point error correction, lattice parameters, peak profile functions (*e.g.*, using Gaussian and Lorrentzian-based functions), isotropic and anisotropic displacement parameters, fractional coordinates of the atoms and fractional site occupancies.

The overall level of fit in a Rietveld refinement is given by the R-factor, where lower values represent better fits. Two factors are used - R_p and wR_p - where the latter represents the weighted R-factor. The weighted R-factor value fits all peaks with equal importance and assumes that fitting peaks with more intensity should not be prioritized. The factors are calculated as

$$R_p = \frac{\sum |y_{obs} - y_{calc}|}{\sum y_{obs}} \tag{2.11}$$

$$wR_p = \left(\frac{\sum_i w (y_{obs} - y_{calc})^2}{\sum_i w (y_{obs})^2} \right)^{1/2} \tag{2.12}$$

In this thesis, all structural refinements were carried out using the General Structure Analysis System[16,17] (GSAS), where an additional goodness of fit parameter is also

calculated, with best possible fits having a value of, or close to, one. This goodness of fit parameter, χ^2, is defined in Equation 2.13, where N_{con} is the number of system constraints, N_{obs} is the number of observations and N_{ref} is the number of parameters refined.

$$\chi^2 = \frac{\sum_i w(y_{obs} - y_{calc})^2}{N_{obs} - N_{ref} + N_{con}} \quad (2.13)$$

The weighting factor, w, is equal to the inverse of the square of the standard deviation ($1/\sigma^2$). Where standard counting measurements are made, *e.g.*, for laboratory X-ray diffraction experiments, this is simply equal to $1/y_i$. This term prevents peaks of greater intensity from dominating the refinement. This simplified term may not be used for neutron and synchrotron diffraction due to beam flux.

2.8. Introduction to Solid-State NMR

2.8.1. Introduction

In 1946, Bloch and Purcell [18] found that nuclei could absorb radiofrequency electromagnetic radiation when placed in a magnetic field. This phenomenon has been investigated and experiments adapted and refined over the past half century in order to obtain detailed chemical and structural information. Despite the challenges associated with solids, with the appropriate experimental parameters and conditions, high-resolution spectra can be obtained, where the subtle differences in the electronic environments of the nuclei give rise to different resonant frequencies. NMR experiments probe the local structure (on the atomic scale) and disorder of a material and, therefore, provide a complementary approach to both X-ray and neutron diffraction experiments that typically probe the longer-range periodicity of crystal systems. Additionally, solid-state NMR experiments may yield useful structural information when performed on amorphous solids, where it can often be more difficult to use experiments based on Bragg diffraction.

2.9. Theory of Solid-State NMR

2.9.1. Theory of Magnetic Resonance[19,20]

Nuclei possess an intrinsic angular momentum called spin, **I**, (where the bold typeface indicates a vector), with a magnitude quantised in units of ħ,

$$\mathbf{I} = \hbar [I (I + 1)]^{1/2} \quad . \tag{2.13}$$

The spin quantum number (I) is determined by the nucleus composition, *i.e.*, different numbers of protons and neutrons give rise to different values. When the numbers of protons and neutrons in a nucleus are both even, then the nucleus/isotope has I = 0 and is, therefore, NMR inactive. The angular momentum vector for NMR-active (I > 0) nuclei has 2I + 1 projections onto an arbitrary axis. For example, the z-component of the angular momentum is quantised as

$$\mathbf{I_z} = m_I \hbar \quad , \tag{2.14}$$

where m_I is the magnetic spin quantum number, ranging from –I to +I. From this it is clear that for nuclei, when I = 1/2, there exist two possible orientations, where both have the same energy (*i.e.*, are degenerate), in the absence of a magnetic field. However, when placed in an external magnetic field, B_0, the degeneracy is lifted and the two energy levels are separated by the Zeeman interaction. Fig. 2.10 illustrates the energy level separation in an external magnetic field, for nuclei with I = 1/2, 1 and 3/2. The magnitude of the separation of the states depends upon B_0 and the gyromagnetic ratio, γ. Spins also exhibit a magnetic dipole moment, **μ**, that is proportional to the angular momentum, and given by

$$\boldsymbol{\mu} = \gamma \mathbf{I} \quad . \tag{2.15}$$

The Zeeman energy, E, is given by

$$E = -\mu_z B_0 \quad , \tag{2.16}$$

where μ_z represents the component of μ along the field direction. By combining Equations 2.14-2.16, it can be seen that the energy of a particular spin state is now given by

$$E = -m_I \hbar \gamma B_0 \quad . \tag{2.17}$$

All observable transitions are governed by the selection rule, $\Delta m_I = \pm 1$, and therefore only transitions between adjacent energy levels are observed in the spectrum. Substitution of spin states for spin I = 1/2 nuclei into Equation 2.17 reveal the energy change for the NMR-observable transition is given by

$$\Delta E = (-\tfrac{1}{2} \hbar \gamma B_0) - (\tfrac{1}{2} \hbar \gamma B_0) \quad , \tag{2.18}$$

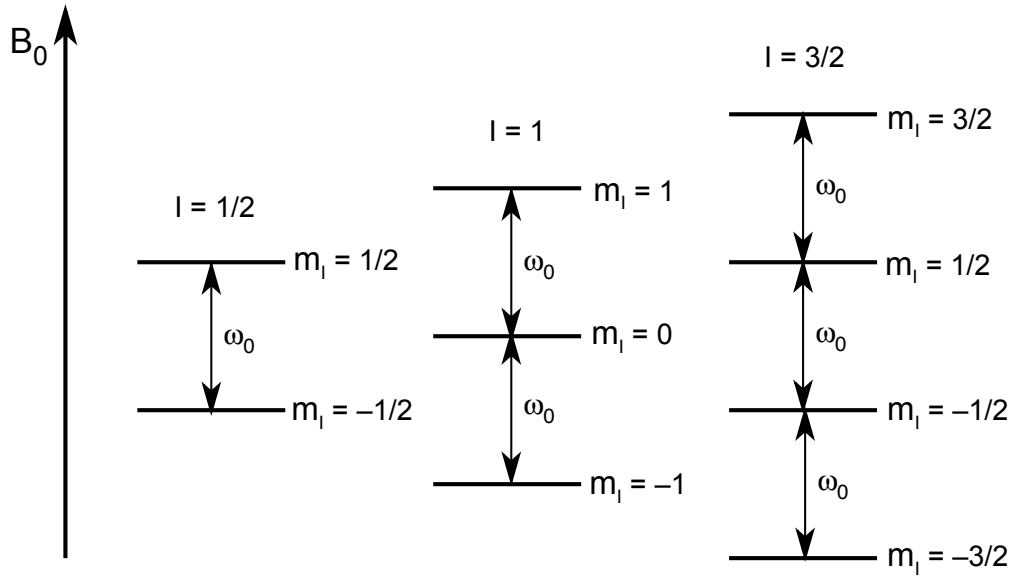

Figure 2.10: Zeeman energy levels for different spin values in the presence of an external magnetic field.

which, in turn simplifies, to

$$\Delta E = -\hbar \gamma B_0 \quad . \tag{2.19}$$

The frequency at which these transitions occur is called the Larmor frequency, ω_0 (in rad s^{-1}), and is given by

$$\omega_0 = \frac{\Delta E}{\hbar} = -\gamma B_0 \quad . \tag{2.20}$$

Equation 2.20 shows that each nuclear isotope has a unique Larmor frequency, which varies with the external field strength. For I = 1/2 nuclei, the nuclear spin magnetic moments align either parallel (α-state) or antiparallel (β-state) to B_0, and the population difference between the two states is given by the Boltzmann distribution

$$\Delta n_0 = \frac{n_{upper}}{n_{lower}} = \exp\left(\frac{-\Delta E}{kT}\right) \quad , \tag{2.21}$$

where n_{upper} and n_{lower} refer to the β-state and α-state populations for a spin I = 1/2 nucleus, respectively, k is the Boltzmann constant and T is the temperature. Very small population differences are observed, and since the magnitude of the NMR signal is proportional to the population difference, it is beneficial to increase Δn_0. This is achieved by the application of a stronger magnetic field or by exploiting nuclei with higher gyromagnetic ratios.

2.9.2. Chemical Shift[21,21]

The local field experienced by a particular nucleus, B, in an atom is typically slightly less than the external field. Theoretically, B_0 is the field that would be felt by a nucleus surrounded by no electrons, *i.e.*, a bare atom. In reality, however, the electrons precess in their orbitals and this generates a small magnetic field, B', which opposes B_0. The field experienced by the nucleus is given by

$$B = B_0 - B' = B_0 (1 - \sigma) \quad , \tag{2.22}$$

where σ is referred to as the shielding constant. The resonance frequency, ω, of the nucleus can be defined in terms of the shielding constant and is expressed as

$$\omega = -\gamma B_0 (1 - \sigma) \quad , \tag{2.23}$$

although it is often difficult to measure σ directly. It is more common to report the chemical shift, δ, of a nucleus, quoted in ppm, relative to a reference compound is given by

$$\delta = 10^6 \frac{\omega - \omega_{ref}}{\omega_{ref}} \quad , \tag{2.24}$$

where ω is the resonant frequency of the specific nucleus and ω_{ref} is the resonant frequency of a reference nucleus. Equation 2.24 can be expanded to become

$$\delta = 10^6 \frac{\sigma_{ref} - \sigma}{1 - \sigma_{ref}} \approx 10^6 (\sigma_{ref} - \sigma) \quad . \tag{2.25}$$

2.9.3. The Rotating Frame

As described earlier, when a nucleus is placed into an external magnetic field, the magnetic dipole moments will align either parallel or antiparallel to the direction of the field. As there is typically an excess number of spins in the parallel (α-state), a net, or bulk magnetisation exists, represented by a bulk magnetisation vector, $\mathbf{M_0}$, proportional to the population difference and gyromagnetic ratios of the nuclei, and given by

$$\mathbf{M_0} = \frac{1}{2} \gamma \hbar \Delta n_0 \quad . \tag{2.26}$$

The effect of radiofrequency (rf) pulses (short bursts of intense radiation) upon this magnetisation vector can be conveniently described using the vector model.[21] If $\mathbf{M_0}$ is tipped away from the z-axis it will precess around B_0 at an angular frequency, ω_0. To manipulate the magnetisation vector, rf pulses are usually applied in the xy plane. A pulse is composed of an oscillating magnetic field and it can be difficult to understand its effect in the fixed, or 'laboratory' frame. It is more useful to transform to a frame of reference termed the 'rotating frame' that is itself rotating at an angular frequency, ω_{rf}, resulting in an effective field, B_{eff}. The pulse can now be described as a fixed field, B_1 applied usually along the x or y axes. Upon application of the pulse, the magnetisation vector nutates around the direction of B_1 towards the xy plane. The angle of nutation is termed the flip angle, β, and is given by

$$\beta = \gamma B_1 \tau_p \ , \tag{2.27}$$

where τ_p is the duration of the pulse. If $\beta = 90°$ then the magnetisation vector will be rotated to lie in the xy plane. If the pulse is applied along the x-axis, the vector will lie

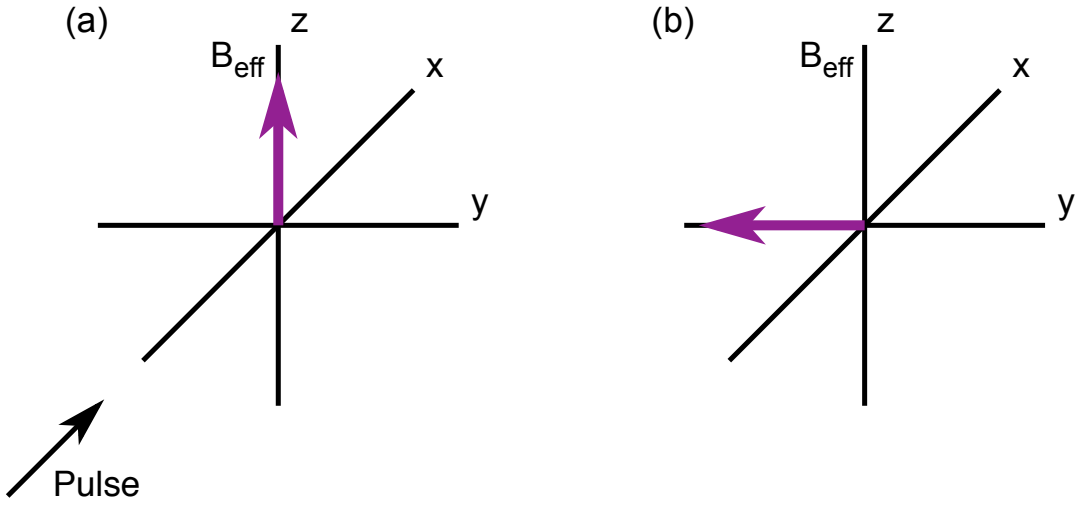

Figure 2.11: (a) Alignment of the bulk magnetisation vector, $\mathbf{M_0}$, (purple arrow) with B_{eff} along the z direction and application of a pulse along x, (b) magnetisation is nutated into the xy plane after the pulse is applied, where they precesses about B_{eff}.

along the –y-axis, as shown in Fig. 2.11. After the application of the pulse, the magnetisation vector will then precess around B_{eff} at a frequency

$$\Omega = \omega_0 - \omega_{rf} \quad . \tag{2.28}$$

It is this precession, or free induction decay (FID), that is detected (as an oscillating magnetic field) by a detector coil as the signal in a NMR experiment. Conventionally, two detectors (usually along x and y axes) are used in an approach termed 'quadrature' detection, to ensure that the sense of precession can be determined.

2.9.4. Relaxation

The oscillating signal detected in a NMR experiment is damped by relaxation processes. There are two distinct types of relaxation. Firstly, the bulk magnetization has a tendency to return to its equilibrium state, parallel to the z axis, and this process is referred to as longitudinal, spin-lattice, or "T_1" relaxation. This relaxation is described by an exponential term and expressed as

$$M_z(t) = M_0 [1 - \exp(\frac{-t}{T_1})] \quad , \tag{2.29}$$

where $M_z(t)$ is the z-component of the bulk magnetisation at time, t, and T_1 is the relaxation time constant. The rate of longitudinal relaxation is dependent upon the nucleus and its environment, and may range from seconds to hours for solids. For example, ^{23}Na (I = 3/2), ^{17}O (I = 5/2) and ^{89}Y (I = 1/2) have typical longitudinal relaxation times* on the order of seconds, minutes and hours, respectively.

In addition to longitudinal relaxation, transverse, spin-spin, or "T_2" relaxation also occurs simultaneously, but is independent of longitudinal relaxation. After an rf pulse is applied along x or y axes, the bulk magnetization nutates towards the xy plane, to give M_{xy}. The magnetization subsequently precesses in the xy plane but the net coherent magnetization is eventually lost from this plane and becomes dephased. Individual spins will precess at different rates – some faster and some slower than others. Over time, the precession of each spin becomes sufficiently different such that no bulk magnetization is observed. This is shown in Fig. 2.12, which shows a simplified case where three spins, a, b and c, are present.

2.9.5. Free Induction Decay and Fourier Transformation[22,23]

In an NMR experiment, the magnetization aligned along the z direction, parallel to B_0, is perturbed when a pulse is applied, such that the magnetization nutates from the z-axis into the xy plane. In the xy plane, precession then occurs (ignoring the effects of relaxation outlined in Section 2.9.5) and can be detected as a time-domain signal. This signal (the FID) can be difficult to interpret for complex systems. A Fourier transform is typically used to convert the FID into a frequency-domain signal, or a spectrum, where the FT is expressed as

* The timescales given are very general, and are dependent upon the surrounding environment. Additionally, these time constants may be reduced if paramagnetic ions are present in the sample.

$$S_{spec}(f) = \int_{0}^{+\infty} S_{FID}(t) \cos(2\pi ft)\, dt \ , \tag{2.30}$$

where $S_{spec}(f)$ is the intensity of the spectrum at frequency f and $S_{FID}(t)$ is the amplitude of the FID at time t. The upper limit of the integral is defined as being infinite, but in practice, the calculation is only performed on data points with a magnitude greater than the noise, *i.e.*, the FID is damped and decays over time due to the effects of relaxation, and as such, only a finite number of data points are collected.

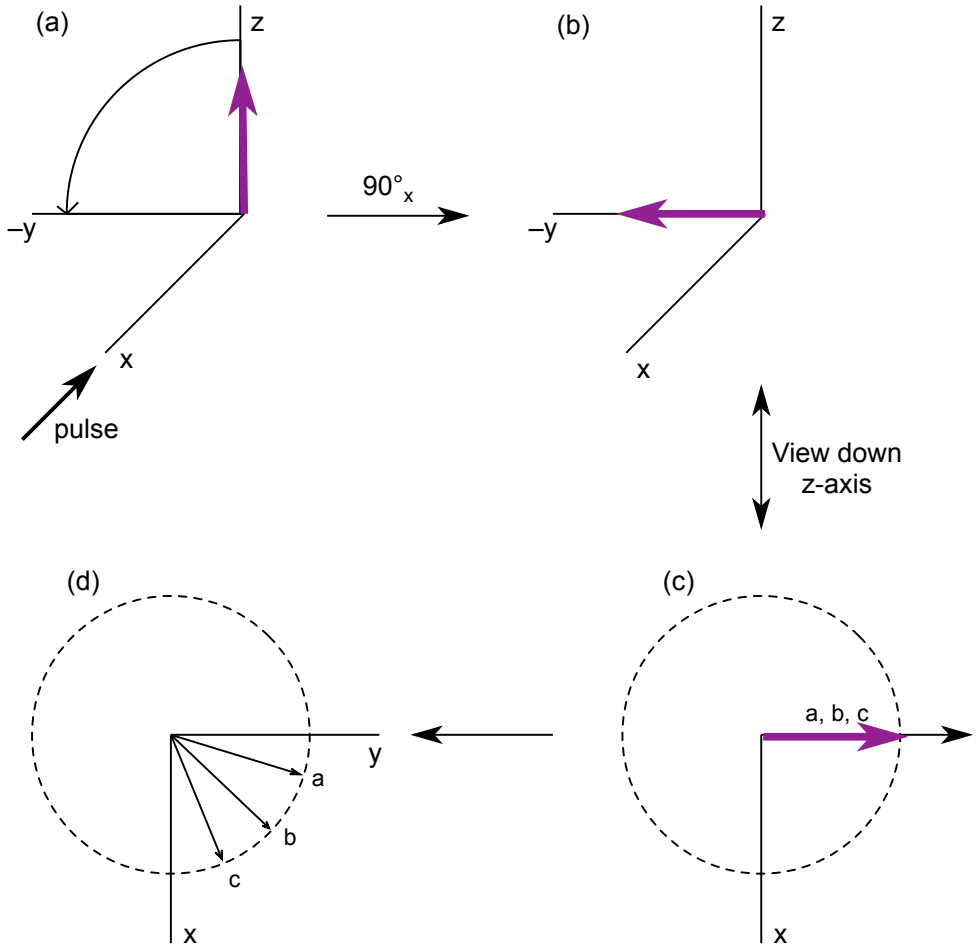

Figure 2.12: (a) Alignment of the bulk magnetisation vector (purple arrow) with B_0 along the z axis, (b) application of a pulse along x to nutate the spins into the xy plane, (c) spins (a, b and c) in the xy plane immediately after the pulse and (d) dephasing of spins in the xy planes (T_2 relaxation) over time.

2.10. Solid-State NMR Interactions

2.10.1. Introduction

Interactions in solid-state NMR can cause broadening of lineshapes, making the extraction of NMR parameters, and even determining the number of resonances present, difficult. These interactions, such as dipolar (Section 2.10.3) and quadrupolar couplings (Section 2.12), have an orientation dependence, and unless all molecules/crystals in the sample have the same orientation, will result in line broadening. In solution-state NMR, however, the rapid molecular motion and tumbling means that the anisotropic parts of these interactions are 'averaged out' to zero, and acquired spectra often have sharp, narrow lineshapes, reflecting just the isotropic or averaged components of the interactions. Whilst lineshape broadening may be problematic in the acquisition of solid-state NMR spectra (in particular, those with spin $I > 1/2$ having quadrupolar coupling contributions), several techniques may be employed to remove the anisotropic broadenings caused by these interactions by averaging their orientation dependence to zero. Such techniques include magic-angle spinning (MAS), double rotation (DOR) NMR and multiple-quantum (MQ) MAS experiments, outlined in Sections 2.11, 2.13 and 2.14, respectively.

The interactions that affect solid-state NMR spectra can be described by a Hamiltonian, H, expressed for general interactions as

$$H = \mathbf{I} \,.\, \mathbf{R} \,.\, \mathbf{X} \ , \tag{2.31}$$

where **I** is a spin angular momentum operator, **R** is a second-rank Cartesian tensor describing the interaction and **X** is an additional spin operator or the magnetic field. Each of the terms may be expanded in matrix form

$$H = (I_x I_y I_z) \begin{pmatrix} R_{xx} & R_{xy} & R_{xz} \\ R_{yx} & R_{yy} & R_{yz} \\ R_{zx} & R_{zy} & R_{zz} \end{pmatrix} \begin{pmatrix} X_x \\ X_y \\ X_z \end{pmatrix} \ . \tag{2.32}$$

The total Hamiltonian may be expressed as the sum of the individual Hamiltonians for each interaction, such that

$$H = H_Z + H_{rf} + H_Q + H_{CS} + H_D + H_J \quad , \tag{2.33}$$

where H_Z is the Hamiltonian of the Zeeman interaction, H_{rf} the radiofrequency pulse, H_{CS} the chemical shielding, H_Q is the quadrupolar coupling, H_D the dipolar coupling and H_J the scalar coupling. It is worth noting that the interactions above can be divided into two distinct categories: external (H_Z and H_{rf}) and internal (H_Q, H_{CS}, H_D and H_J), where it is the internal interactions that contribute to the observed line broadening in NMR spectrum. It can be difficult to express this easily for a powder distribution of crystallites, where all possible crystallite orientations are simultaneously present. Interactions are usually expressed in the principal axis system (PAS) - a frame where the interaction tensor is diagonal, as shown schematically in Fig. 2.13. This allows us to define the magnitude and asymmetry of the interaction, while the rotation back to the laboratory frame provides the orientation dependence for each individual crystallite.

Much of the work in this thesis will focus on the study of quadrupolar nuclei ($I > 1/2$) where the quadrupolar coupling will have the largest effect on the spectral lineshapes (after the Zeeman interaction). Whilst other interactions also contribute to lineshape broadening, their effects are substantially smaller, and as such, only a brief overview of these interactions will be given in this thesis.

2.10.2. Chemical Shift Anisotropy

As described previously, in an NMR experiment, the field experienced by a spin is not the same as the applied field, B_0, as the electrons around the nucleus generate their own small electric field. The shielding constant, σ, was previously introduced as an isotropic scalar component. However, for solids, σ is anisotropic and, therefore, represented by a tensor (*i.e.*, it is orientation dependent), and described in the PAS by

$$\begin{pmatrix} \sigma_{11} & 0 & 0 \\ 0 & \sigma_{22} & 0 \\ 0 & 0 & \sigma_{33} \end{pmatrix} . \tag{2.34}$$

This shielding is usually described in terms of three parameters, the isotropic shielding, σ_{iso}, the shielding anisotropy, $\Delta\sigma_{CS}$ and asymmetry, η_{CS}, where each is given by

$$\sigma_{iso} = \frac{1}{3}(\sigma_{11} + \sigma_{22} + \sigma_{33}) \tag{2.35a}$$

$$\Delta\sigma_{CS} = \sigma_{33} - \sigma_{iso} \tag{2.35b}$$

$$\eta_{CS} = \frac{\sigma_{11} - \sigma_{22}}{\sigma_{33} - \sigma_{iso}} \quad , \tag{2.35c}$$

such that $0 \leq \eta_{CS} \leq 1$.In the laboratory frame, with B_0 defined along the z axis, the secular approximation can be applied and the chemical shift Hamiltonian reduces to

$$H_{CS} = \gamma B_0 \sigma_{33} I_z \quad , \tag{2.36}$$

i.e., dependent upon the σ_{33} component of the laboratory frame tensor. This can be determined by considering a rotation from the PAS

$$\sigma_{33} = \sigma_{iso} + (\frac{\Delta\sigma_{CS}}{2}) [(3\cos^2\theta - 1)\eta_{CS}(\sin^2\theta \cos 2\varphi)] \quad , \tag{2.37}$$

where θ and φ specify the crystallite orientation. The different crystallites will, therefore, have a different σ_{33} and, therefore, ultimately a different chemical shift, resulting in broadened lineshapes. In solution, rapid tumbling motion averages the anisotropy, leaving just the isotropic component, σ_{iso}.

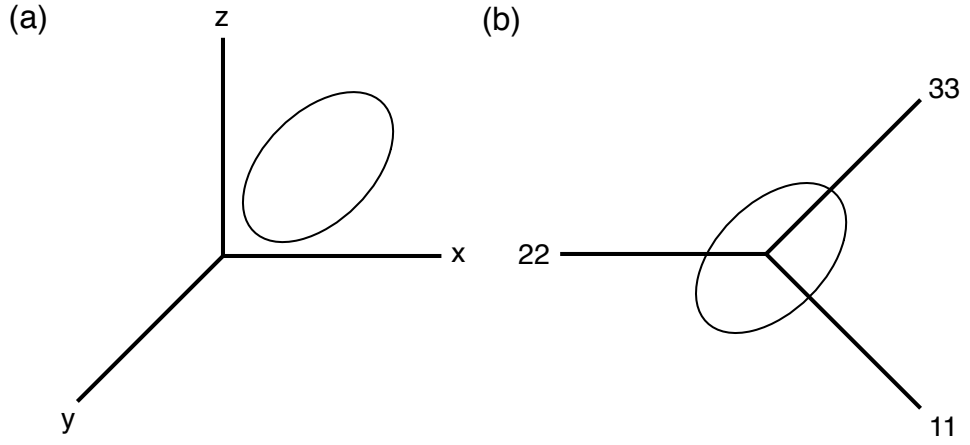

Figure 2.13: (a) Crystallite in the standard laboratory frame of reference and (b) crystalline in the PAS.

2.10.3. Dipolar Coupling

The dipolar interaction is a through-space magnetic spin-spin coupling, decreasing in magnitude with the cube of the inverse distance between the spins. Each nucleus produces a small localised magnetic field which can interact with the dipole moments of other nearby nuclei. The dipolar coupling interaction is orientation dependent, and is therefore anisotropic. Similar to the CSA, this interaction is averaged to zero in solutions due to rapid molecular tumbling.

For two spins, j and k, separated by a distance, r_{jk}, the dipolar coupling constant in the PAS, ω_D^{PAS}, is given by

$$\omega_D^{PAS} = \frac{-\mu_0}{4\pi} \cdot \frac{\gamma_j \gamma_k \hbar}{r_{jk}^3} \quad , \tag{2.38}$$

where μ_0 is the permittivity of free space. It can be seen that ω_D^{PAS} is inversely proportional to the separation cubed, and this coupling constant (in the PAS) is used to determine the magnitude of the dipolar interaction for a crystallite/molecule included at an angle θ_{jk} to B_0 by

$$\omega_D = \omega_D^{PAS} (3 \cos^2 \theta_{jk} - 1) \quad , \tag{2.39}$$

where θ describes the orientation of the internuclear vector to B_0. Not only, therefore, is the dipolar coupling constant, ω_D, dependent upon the spin-spin separation, it is also has an orientation dependence proportional to $3\cos^2 \theta - 1$. It is important to remember, however, that the dipolar interaction is not only present between two spins, but between many more spins in a sample, and this contributes significantly to the line broadening observed in NMR spectra, especially for nuclei with high γ and high abundance.

2.10.4. Scalar Coupling

The scalar (or J) coupling is a through-bond electron-mediated spin-spin coupling on the order of $1 - 10^3$ Hz, making this a relatively small interaction. The interaction is described by a tensor with both isotropic and anisotropic components, where the latter is orientation dependent. The magnitude of the coupling depends upon the number of bonds between the two spins, and generally decreases with distance. Experimentally, the anisotropy of the J coupling is not normally observed directly since it cannot be distinguished from the substantially larger dipolar coupling. Isotropic J couplings can be resolved if they are greater than the inherent linewidths.

2.11. Magic-Angle Spinning

In any powdered sample there are many crystallites, each having a slightly different orientation, and therefore contributing to anisotropic broadening of the lineshapes in the spectrum. Whilst anisotropic line broadening interactions, such as the CSA and dipolar coupling, can provide useful chemical information, they can also hinder the extraction of other information, such as the number of crystallographically-distinct sites present. The impact these anisotropic interactions have on an NMR spectrum can be reduced by using a technique called magic-angle spinning (MAS), in which the sample is rotated about an axis inclined at an angle of 54.736° - the so-called magic-

angle.[24,25] If the sample is rotated sufficiently rapidly, then the average orientation of all crystallites is 54.736°.

MAS is now commonplace in solid-state NMR experiments as it removes the effects of many line broadening interactions to provide high-resolution spectra. Most probes have MAS capability built into them, making spectral acquisition relatively straightforward. MAS rates of up to 80 kHz are achievable on commercial hardware, although in general terms, higher spinning rates require more costly probes. Fig. 2.14 shows a schematic of the experimental implementation of MAS, where θ is the angle between the crystallite (the principal z axis of the interaction tensor) and B_0, θ_R is the angle between B_0 and the spinning axis, and β is the angle between the spinning axis and the principal z axis of the tensor. The CSA and dipolar coupling (anisotropic interactions) both contain orientation-dependent terms, proportional to $3\cos^2\theta - 1$. If the sample is rotated rapidly, it can be shown that

$$\frac{1}{2}\langle 3\cos^2\theta - 1\rangle = \frac{1}{2}(3\cos^2\theta_R - 1)\frac{1}{2}(3\cos^2\beta - 1) \quad , \tag{2.40}$$

where $\langle\ \rangle$ equals zero if θ_R is set to 54.736°. If the MAS rate is too slow, then spinning sidebands will be present in the NMR spectrum. These sidebands are additional peaks, separated from the isotropic centreband by the spinning frequency (MAS rate). Using different MAS rates, the spinning sidebands will 'move' and remain separated according to the MAS rate, whilst the position of the centreband will remain unchanged, as shown in Fig. 2.15.

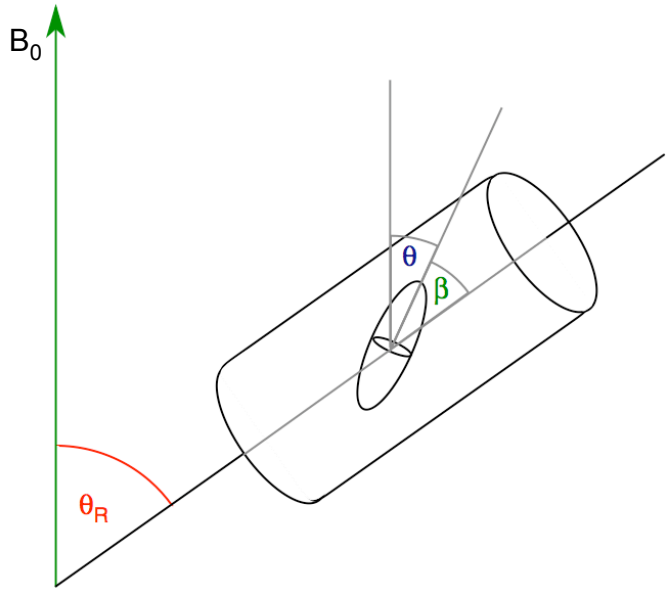

Figure 2.14: Schematic representation of magic-angle spinning where the rotor spins at an angle θ_R of 54.736° to B_0. All terms in the figure are discussed in the main text.

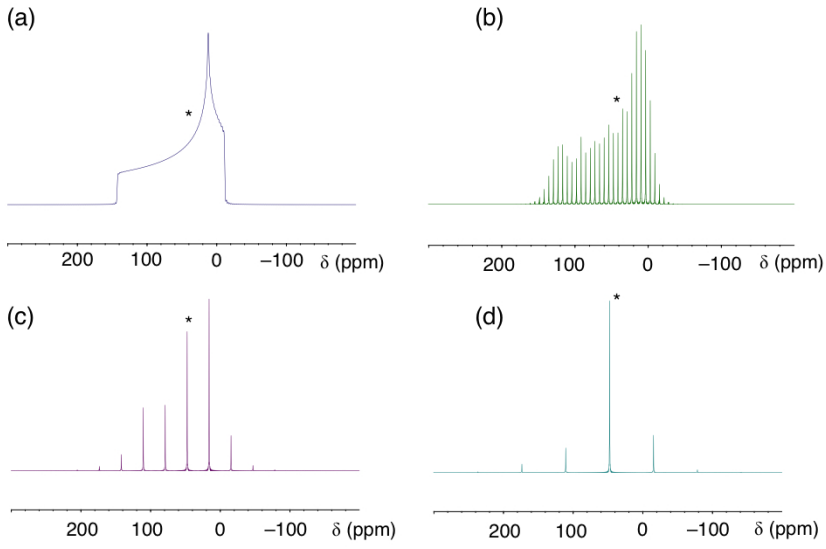

Figure 2.15: Simulated spectra for a spin I = 1/2 nucleus with MAS rates of (a) 0 kHz, (b) 1 kHz, (c) 5 kHz and (d) 10 kHz. An η_{CS} of 0.25 is used, and a * is used to denote the isotropic chemical shift (50 ppm).

2.12. Quadrupolar Nuclei

2.12.1. Quadrupolar Coupling under MAS Conditions

Nuclei with spin values greater than 1/2 are termed quadrupolar, and account for approximately 75% of all NMR-active nuclei. In a sample, an electric field gradient (EFG) is generated at the nucleus, which can interact with any electric nuclear quadrupole moment, eq, which arises from charge asymmetry in the nucleus, *i.e.* a non-symmetrical distribution of charge.[26] This interaction is called the quadrupolar interaction, or quadrupolar coupling, and is often very large and on the order of MHz, resulting in broadened lineshapes. This interaction inhomogeneously broadens lineshapes in solid-state NMR spectra, often making extraction of useful information difficult. The EFG, when described in the PAS, is described by three principal components, V_{xx}, V_{yy} and V_{zz}. Conventionally, the components are ordered such that $|V_{zz}| \geq |V_{yy}| \geq |V_{xx}|$, and the magnitude of the EFG is given by

$$eQ = V_{zz} \quad . \tag{2.41}$$

The quadrupolar Hamiltonian, H_Q,[27] is given by

$$H_Q = \frac{eQ}{2I\,(2I-1)\,\hbar}\,\mathbf{I.\,V.\,I} \quad , \tag{2.42}$$

where **I** is the spin operator and **V** is the tensor describing the EFG. The magnitude of the quadrupolar tensor is given by the quadrupolar coupling constant, C_Q, and is given by

$$C_Q = \frac{eQV_{zz}}{h} \quad , \tag{2.43}$$

and the shape of its cross-section is conveniently described using the quadrupolar asymmetry parameter, η_Q, which is given by

$$\eta_Q = \frac{V_{xx} - V_{yy}}{V_{zz}} \quad , \tag{2.44}$$

where $0 \leq \eta_Q \leq 1$. Although typically large, the quadrupolar interaction is usually smaller than the Zeeman interaction, and can usually be described by a perturbation to the Zeeman levels. However, the simple perturbation used to describe quadrupolar effects is sometimes an insufficient description when larger quadrupolar interactions are present, and a second-order perturbation is required.

All subsequent information and equations given regarding quadrupolar nuclei will be treated as though they are under MAS conditions and are for nuclei with half-integer spin only. Integer spin quadrupolar nuclei and static experiments are not relevant to the work presented in this thesis.

2.12.2. First- and Second-Order Quadrupolar Effects

The effect of the quadrupolar interaction on all energy levels may be described using perturbation theory.[28] The Zeeman energy levels are perturbed to a first-order approximation, as shown in Fig. 2.16 for the case of I = 3/2 nuclei. The degenerate Zeeman levels become split, such that the central transition (CT), arising from the $m_I = 1/2 \leftrightarrow -1/2$ transition, is unaffected by the quadrupolar interaction, but the satellite transitions (ST), dependent upon ω_Q, are affected. The transitions are equally spaced in the spectrum by $2\,\omega_Q$, where ω_Q, the quadrupolar frequency, is given by

$$\omega_Q = \omega_Q^{PAS} \frac{1}{2} [(3\cos^2\theta - 1) + \eta_Q(\sin^2\theta \cos 2\varphi)] \quad , \tag{2.45}$$

where ω_Q^{PAS} is given by (in rad s^{-1})

$$\omega_Q^{PAS} = \frac{3\pi C_Q}{2I(2I-1)} \quad , \tag{2.46}$$

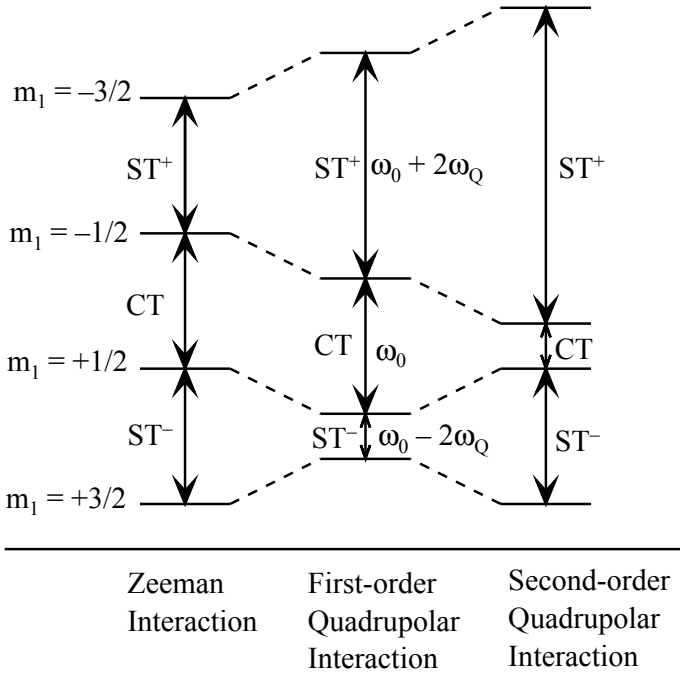

Figure 2.16: Schematic representation of the effect of the Zeeman and first- and second-order quadrupolar interactions upon the energy levels and observable transitions for a spin I = 3/2 nucleus.

where η_Q is the quadrupolar asymmetry parameter with a value between 0 and 1, and the angles, θ and φ, define the orientation of the EFG PAS to B_0. The effect of the quadrupolar asymmetry parameter on NMR lineshapes for a I = 3/2 nucleus under MAS is shown in Fig. 2.17.

The linewidth in a spectrum is dependent upon C_Q and, as such, can provide information on the magnitude of the interaction. However, as the quadrupolar interaction is often very large, first order perturbation theory is insufficient to describe the interaction, and as such, second-order perturbation is needed to describe the effects of the interaction on the Zeeman levels.

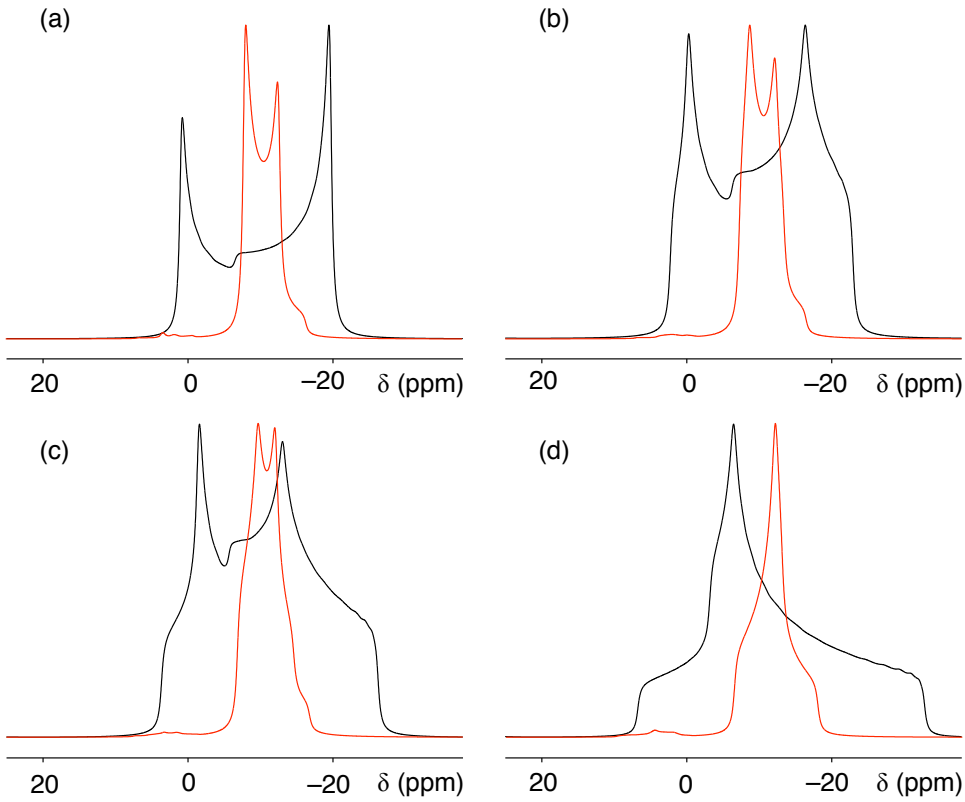

Figure 2.17: Simulated powder pattern lineshapes for a spin I = 3/2 nucleus at 9.4 T with C_Q = 2 MHz for static (black) and MAS (12.5 kHz, red) conditions, with η_Q of (a) 0, (b) 0.25, (c) 0.5 and (d) 1.

As shown in Fig. 2.16, the first-order quadrupolar interaction does not affect the CT. However, second-order effects affect both the central and satellite transitions. The second-order perturbation (assuming $\eta_Q = 0$ for simplicity) for a symmetrical transition $m_1 \leftrightarrow m_{-1}$ is expressed as

$$E^2_{(m_1)} - E^2_{(-m_1)} = \frac{(\omega_Q^{PAS})^2}{\omega_0} [A^0(I, m_1) + A^2(I, m_1)\, d^2_{00}(\theta_R)\, d^2_{00}(\beta) + A^4(I, m_1)\, d^4_{00}(\theta_R)\, d^4_{00}(\beta)] \quad , \qquad (2.47)$$

where

$$d^2_{00}(\chi) = \frac{1}{2}(3\cos^2\chi - 1) \quad , \qquad (2.48a)$$

$$d^4_{00}(\chi) = \frac{1}{8}(35\cos^4\chi - 30\cos^2(\chi) + 3) \quad , \tag{2.48b}$$

and $A^n(I, m_I)$ are spin- and energy-dependent coefficients given in Table 2.3. A^0 describes an isotropic term and therefore has no orientation dependence; the A^2 component describes a second-rank second-order anisotropic term proportional to $(3\cos^2\theta - 1)$, and the A^4 component is a fourth-rank second-order anisotropic term with a more complicated angular dependence. As with the first-order quadrupolar interaction and dipolar coupling, MAS can completely remove the anisotropic broadening terms for the second-rank second-order component, but not the fourth-rank terms. Rotation around a different angle would be required to remove the fourth-rank broadening. Naturally, MAS alone is insufficient as only one axis of rotation (at any one time) may be employed using this technique.

To obtain high-resolution spectra of quadrupolar nuclei subject to second-order quadrupolar interactions, different techniques must be employed, such as DOR, which allows the sample to be rotated about two different angles at the same time, and MQMAS, which eliminates the need for spinning about a second angle by manipulation of the nuclear spins.

Table 2.3: List of $A^n(3/2\ m_I)$ coefficients.

	m_I	$A^0(3/2, m_I)$	$A^2(3/2, m_I)$	$A^4(3/2, m_I)$
I = 3/2	1/2	–2/5	–8/7	54/35
	3/2	6/5	0	–6/5

2.13. Double Rotation (DOR) NMR[29]

It was shown in Equation 2.47 that MAS was unable to completely remove second-order quadrupolar broadening. Instead, simultaneously spinning a sample at two specific angles may average the interaction to zero. The first angle is 54.736° and the second is either 30.56 or 70.12°, corresponding to averaging of $d^2_{00}(\chi)$ and $d^4_{00}(\chi)$ terms, respectively. Spinning at the magic angle will remove the first-order

quadrupolar and second-order second-rank broadening, as well as the CSA and dipolar coupling contributions to the NMR lineshapes. Spinning at two angles simultaneously is achieved by using a DOR experiment, in which one rotor spins inside another, where each is at a different angle. As such, the second-order quadrupolar broadening contributions can be both averaged to zero. However, while the concept may be straightforward, the experiment itself is difficult to perform and has limitations. Firstly, specialist DOR probes are required, which increases the cost of the approach. Secondly, the technical complexity means that only relatively slow MAS rates (up to 10 kHz for the inner rotor and 3 kHz for the outer) may be employed, meaning that spinning sidebands may be present and may be difficult to distinguish from the isotropic centreband. This is overcome by repeating the experiment with a different MAS rate, thereby separating the sidebands and centreband by a different amount, *i.e.,* the sidebands will appear to 'move' whilst the position of the centreband remains unchanged.

2.14. Multiple-Quantum Magic-Angle Spinning (MQMAS)

2.14.1. Introduction

In 1995, Frydman and Harwood[30] proposed the first MQMAS experiment, in which high-resolution two-dimensional spectra could be acquired directly. Unlike DOR experiments, no specialist equipment or probes are needed for MQMAS experiments and they may be performed simply using conventional MAS hardware. The initial MQMAS experiment involved a basic excitation/conversion sequence performed under MAS conditions to remove the effects of first-order and second-rank second-order quadrupolar broadening.

In the MQMAS experiment, a high-power rf pulse is used to excite symmetrical multiple-quantum (MQ) coherences. This is the triple-quantum, *i.e.*, a $m_I = +3/2 \leftrightarrow -3/2$ transition, for the case of a spin I = 3/2 nucleus. However, this change in coherence cannot be directly observed as a consequence of the observable selection rule. The MQ coherences are then allowed to evolve for a time period, t_1. At the end of this evolution period, a second, high-power rf pulse is applied to convert the MQ coherences (p = –3, not observable, where p is the coherence order) to single-quantum (1Q) (CT) coherences (p = –1, observable). If the sequence is repeated with increasing

t_1, a series of FIDs can be acquired. This two-dimensional data set can be Fourier transformed in both dimensions to give a two-dimensional NMR spectrum, where 1Q (CT) coherences (sometimes referred to as the MAS dimension) are correlated with MQ coherences. In the two-dimensional spectrum, ridges lie along a gradient equal to the MQMAS ratio. This is the ratio of the anisotropic broadening found for MQ and CT coherences, such that the ratio is given by $A^4(I, 3/2) / A^4(I, 1/2)$, where for a spin I = 3/2 nucleus the value is –7/9. The $A^4(3/2, m_I)$ values are given in Table 2.3. An isotropic spectrum, *i.e.*, free from quadrupolar broadening, is obtained from a projection orthogonal to this axis. An example of this MQMAS experiment is illustrated schematically in Fig. 2.18 for a spin I = 3/2 nucleus. By using a mathematical transformation, termed shearing, the ridges aligned about an axis described by the MQMAS ratio can be transformed into ones aligned parallel to δ_2, resulting in isotropic projections being obtained directly in δ_1, shown schematically in Fig. 2.19.

The relatively simple experiment proposed by Frydman and Harwood does not give rise to phase-pure lineshapes in both dimensions, *i.e.*, they are "phase-twist" lineshapes. More recently, however, this experiment has been modified to give pure absorption-mode lineshapes, and some of these modified approaches, termed shifted-echo and amplitude modulated experiments, are discussed below.

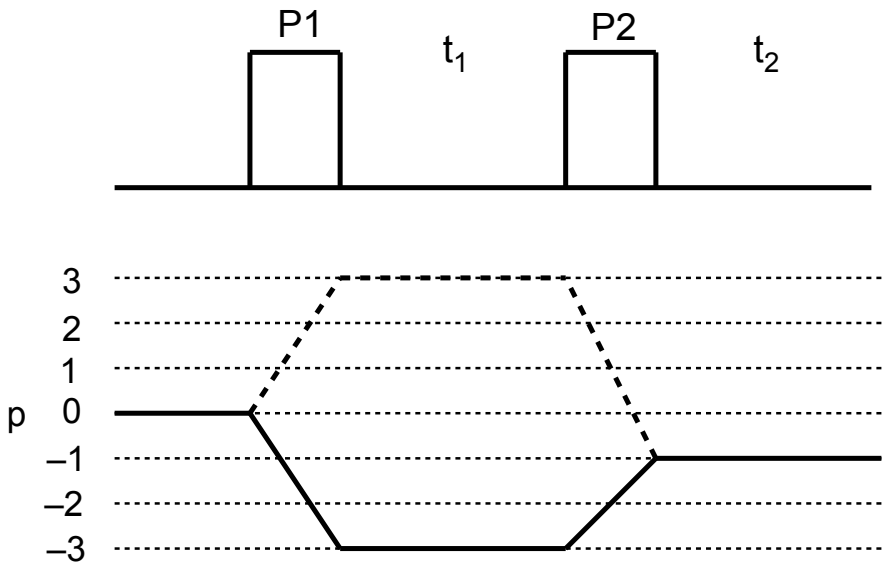

Figure 2.18: Schematic representation of the basic MQMAS experiment similar to that proposed by Frydman and Harwood, where P1 and P2 denote pulses. (NB, in the initial work a two-pulse sequence was used to excite MQ coherences). The corresponding coherence transfer pathway is shown, and for a spin I = 3/2 nucleus the p = –3 coherence path is followed (solid line). The dashed line represents the pathway taken for spins I = 5/2, 7/2 and 9/2 (see text for explanation).

2.14.2. Shifted-Echo MQMAS (I = 3/2)

Massiot *et al.*[31] proposed the first shifted-echo MQMAS experiment, for which the pulse sequence is shown in Fig. 2.20. In this experiment, a whole echo is acquired, resulting in pure absorption-mode lineshapes being observed. As the figure shows, a p = +1 coherence is obtained after the second high-power rf pulse has been applied, changing from p = +3 or –3 after the first high-power pulse. At this point, it can be seen that two transfer pathway options are available, involving either the transition from p = +3 to +1 or p = –3 to +1, where $\Delta p = -2$ and +4, respectively. For a spin I = 3/2 nucleus, the $\Delta p = +4$ pathway must be used, which is less efficient than the $\Delta p = -2$ pathway. For I = 5/2, 7/2 and 9/2 nuclei, however, the echo pathway involves the (more desirable) $\Delta p = -2$ coherence transfer, as the sign of the MQMAS ratio is different than for a spin I = 3/2 nucleus.

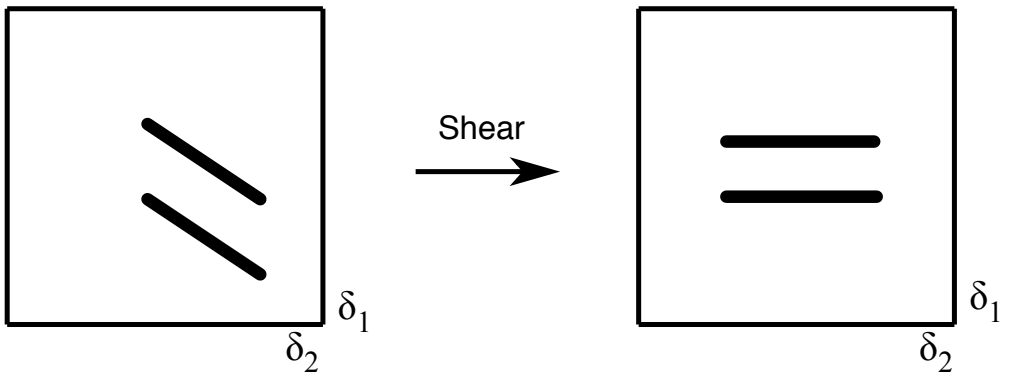

Figure 2.19: Schematic representation of an unsheared spectrum (left) with ridges lying along a gradient equal to the MQMAS ratio. A shearing transformation is used to obtain ridges orthogonal to the δ_1 axis, in which the isotropic projection can now be easily obtained.

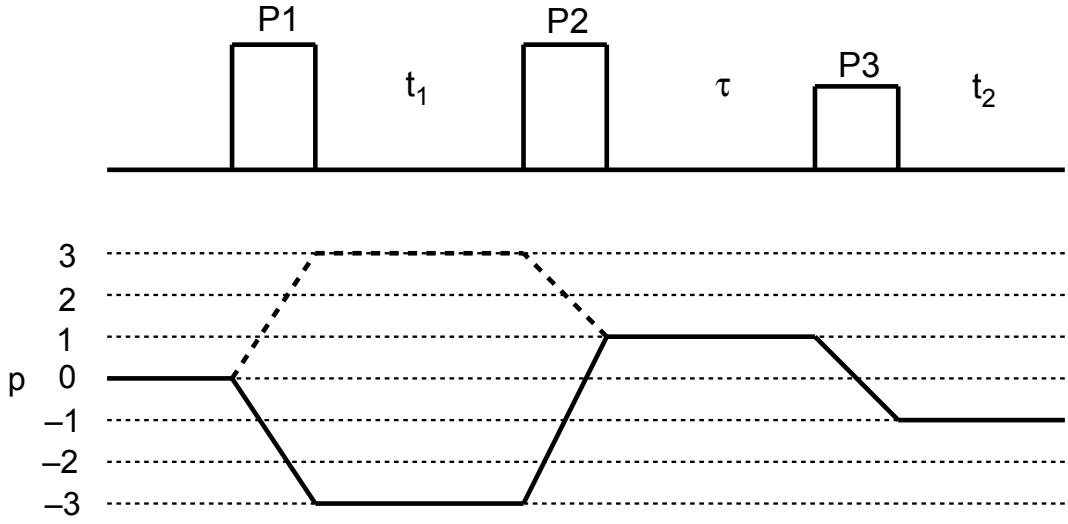

Figure 2.20: Schematic representation of the pulse sequence for a shifted-echo MQMAS pulse sequence and corresponding coherence transfer pathway, where the three pulses are denoted P1, P2 and P3 and the echo delay is shown as τ. The solid line in the coherence pathway diagram represents the (echo) pathway taken for a spin I = 3/2 nucleus. For spins I = 5/2, 7/2 and 9/2, the dashed line denotes the echo pathway.

The echo is shifted into the acquisition period, t_2 (hence the term shifted-echo), by increasing the delay, τ, and allowing the whole echo to be acquired. However,

increasing the delay by too much can cause distortions, owing to the effects of transverse relaxation. If T_2 (not to be confused with t_2) is short, then relaxation can become a limiting factor because little, or no signal may be present in the FID. If transverse relaxation is particularly fast, then it may be preferable to use a z-filtered NMR experiment.

2.14.3. Z-Filtered MQMAS

Amoureux *et al.* first proposed a z-filtered MQMAS NMR experiment in 1996,[32] which was amplitude modulated, inherently giving pure-phase two-dimensional lineshapes. Z-filtered MQMAS NMR experiments are some of the most convenient experiments for utilising amplitude modulation, in which the magnetisation is filtered though longitudinal magnetization prior to observation. The echo and antiecho pathways are combined (p = +3 *and* –3) with equal amplitude to give rise to pure absorption-mode lineshapes in the NMR spectrum. This method is straightforward to implement for all half-integer spin quadrupolar nuclei, making this a robust technique. A schematic representation of the pulse sequence is shown in Fig. 2.21. Similar to the shifted-echo MQMAS experiment, a high-power pulse is used to excite 3Q coherences, followed by a t_1 evolution period and a second hard pulse to create longitudinal magnetisation. A low-power CT-selective (soft) pulse is then used to convert the resulting population difference into observable p = –1 signal. As an echo is not recorded, transverse relaxation will be less of a concern. As a result, this robust technique is often utilised for experiments involving species with shorter relaxation times, which may be more challenging to observe in shifted-echo experiments.

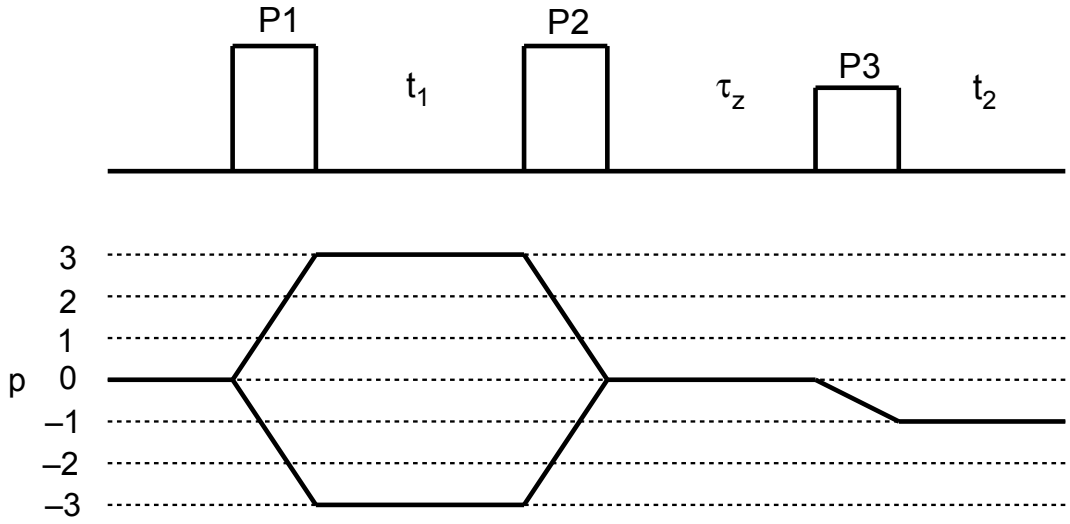

Figure 2.21: Schematic representation of a z-filtered MQMAS pulse sequence and corresponding coherence transfer pathway. The three pulses are denoted P1, P2 and P3, and τ_z is a short delay. As the coherence transfer pathway shows, both 3Q (p = +3 and –3) pathways are followed, and are combined with equal amplitude.

2.14.4. Split-t_1 MQMAS (I = 3/2)

It is possible to overcome the need for a shearing transformation in MQMAS by using a so-called 'split-t_1' approach, *i.e.*, splitting the t_1 evolution period into separate durations, which, in essence, is 'shearing' in the time domain. The split-t_1 methodology can be applied to either the shifted-echo or amplitude-modulated experiments.[33] However, the favourable coherence transfer pathway of the shifted-echo experiment (*i.e.*, the presence of +3 and +1 evolution periods in the original experiments) has ensured a more widespread application. In a split-t_1 shifted-echo sequence, shown in Fig. 2.22, the pulse sequence and coherence transfer pathway are identical to that used in the original experiment. However, the t_1 evolution period is split into MQ and 1Q evolution periods (hence the name split-t_1), denoted kt_1 and $k't_1$, as shown for I = 3/2 nuclei in Fig. 2.22, and are related to the MQMAS ratio. For a spin I = 3/2 nucleus, the MQ and 1Q fractions (k and k', respectively) are 9/16 and 7/16. In this way the second-order fourth-rank anisotropic broadening is refocused at the end of the t_1 period, resulting in ridges parallel to the δ_2 axis in the two-dimensional NMR spectrum. The ^{87}Rb split-t_1 3QMAS spectrum of $RbNO_3$ is shown

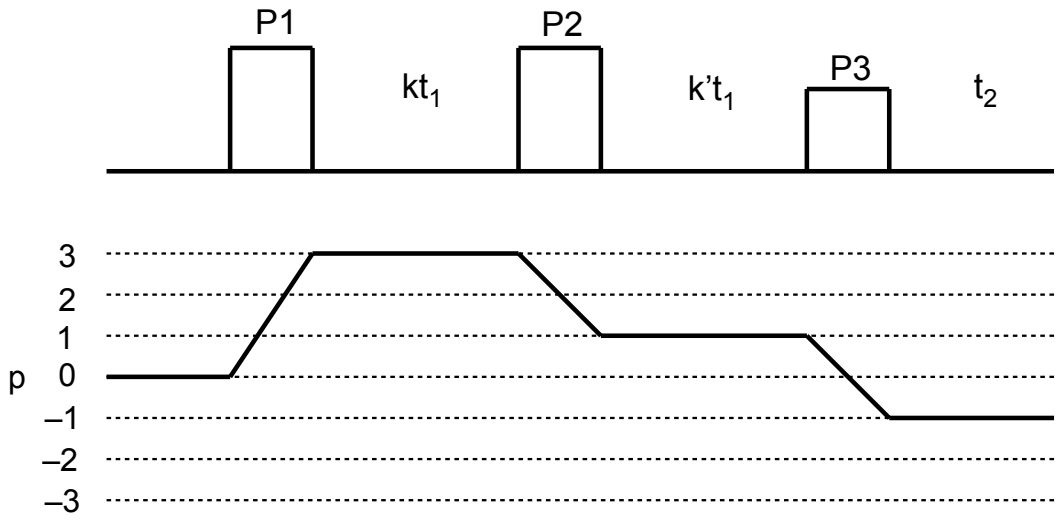

Figure 2.22: Schematic representation of the phase-modulated split-t_1 MQMAS pulse sequence and corresponding coherence transfer pathway for a spin I = 3/2 nucleus. The t_1 evolution period is split into a MQ and SQ component, denoted kt_1 and $k't_1$, respectively for a spin I = 3/2 nucleus. The three pulses are denoted P1, P2 and P3.

in Fig. 2.23, alongside the corresponding MAS spectrum. Additionally, the extracted lineshapes (cross-sections taken parallel to δ_2) are also shown for each resonance, along with a fit of the lineshapes shown, allowing one to determine useful NMR parameters, such as δ_{iso}, C_Q and η_Q. It should be noted that lineshape distortions can be observed in MQMAS spectra but nonetheless they provide an extremely useful tool.

2.14.5. Determination of NMR Parameters

Determination of NMR parameters, such as δ_{iso}, C_Q and η_Q, is sometimes possible by extracting the NMR lineshapes from MQMAS spectra, and 'fitting' them using an analytical lineshape fitting within the Topspin software. This, however, is only possible if the lineshapes are not overlapped or very distorted from multiple-quantum filtration. An alternative method to extract information on the NMR parameters is to determine the centre of gravity of the ridges (δ_1 and δ_2) in the MQMAS spectra.

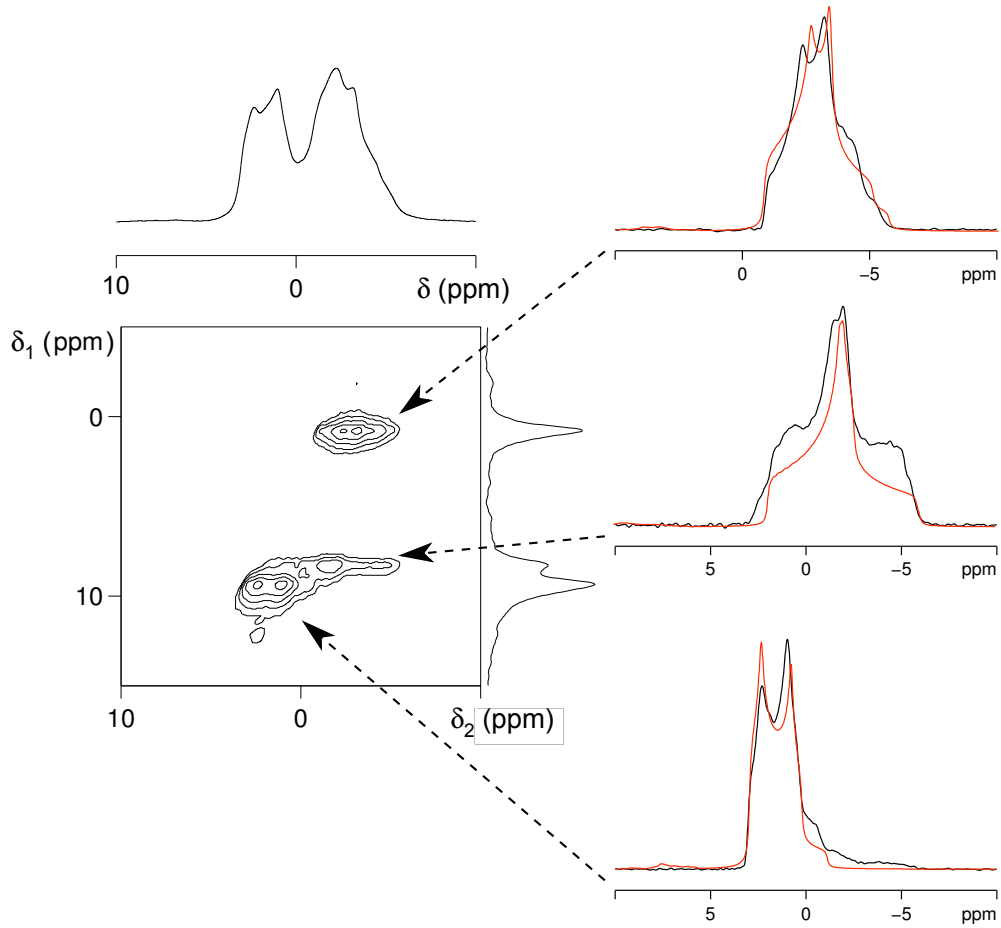

Figure 2.23: ^{87}Rb (14.1 T) split-t_1 shifted-echo MQMAS spectrum of $RbNO_3$ with the isotropic projection, obtained with an MAS rate of 12.5 kHz, with the corresponding MAS spectrum shown above. Also shown, are extracted cross-sections along the ridges orthogonal to δ_1 (black) with fits shown in red. The spectrum was recorded using 4.5 and 1.3 μs high-power pulses, with a CT-selective low-power 34 μs pulse.

From this, it is possible to calculate δ_Q (the isotropic quadrupolar shift) and, consequently the quadrupolar product, P_Q, can be determined. P_Q is related to C_Q and is given by[34]

$$P_Q = C_Q \left(1 + \frac{\eta_Q^2}{3}\right)^{\frac{1}{2}} \quad , \tag{2.49}$$

where C_Q and η_Q cannot be determined individually. The δ_1 and δ_2 positions can also be used to ultimately determine the isotropic shift, δ_{iso}. For a split-t_1 or sheared z-filtered MQMAS experiment, for I = 3/2 nuclei,

$$\delta_1 = \frac{17}{8}\,\delta_{iso} + \frac{1}{2}\,\delta_Q \tag{2.50a}$$

$$\delta_2 = \delta_{iso} - \frac{2}{5}\,\delta_Q \quad , \tag{2.50b}$$

where δ_Q and δ_{iso} may be determined by solving the simultaneous equations.

2.15. Density Functional Theory

2.15.1. Introduction

Density functional theory (DFT) provides a quantum mechanical (QM) framework for determining the electronic structure of a system, enabling the properties that depend upon it, such as NMR parameters or band gaps, to be determined. Whilst, in principle, energies can be determined using the Schrödinger equation,[35] this can be time consuming and costly for many electron systems. An alternative approach was proposed by Kohn and Sham,[36] who demonstrated that the energy could be written solely as a function of the electron density, ρ, providing a more cost-effective route to the calculation of electronic structure. The total energy, E, can be written as the sum of the number of contributions[37]

$$E = E[\rho(r)] \propto E_{Vext} + E_K[\rho(r)] + E_{HC}[\rho(r)] + E_{XC}[\rho(r)] \quad , \tag{2.51}$$

where E_K is the kinetic energy of non-interacting electrons, E_{Vext} is the energy of the electrons due to the external potential (generated by the nuclei), E_{HC} is the Coulombic-Hartree electron-electron repulsion and E_{XC} is the exchange-correlation energy (which can be associated with the interaction of the electrons). The forms of

most of the terms in Equation 2.51 are known and can be determined exactly; however, the form for the last term is not known exactly, although it can be proved that it is a functional of ρ. A number of approximate functionals have been developed to describe E_{XC}, although a detailed description is beyond the scope of this chapter. For the work presented in this thesis, the generalised gradient approximation (GGA)[38] Perdew-Burke-Ernzerhof (PBE) approximation has been used, as it has been demonstrated to provide an accurate and robust approach for periodic solids. In order to determine the contributions to the total energy the wavefunction of the system ψ(r) must be known. Wavefunctions are usually expanded in terms of a basis set, once again to minimise computational cost. For periodic systems, planewaves offer a natural choice (as they are inherently periodic functions). Although easy to compute, a large number of planewaves will be required for accurate calculations. The number of planewaves used is described in terms of cut-off energy, E_{cut}, the value of which can be increased until calculations are deemed sufficiently accurate.

Many properties of a system are determined by the valence electrons, and so calculation times may be reduced by using the 'frozen core' approximation. The core electrons are fixed during the calculation and their effect can be described by a contribution to the potential. A further approximation can also be made. The valence electrons experience only a weak effective potential in the core region, and the wavefunction here can be described more simply, using a pseudopotential (and producing a corresponding pseudowavefunction).[39] These two approximations, usually applied together, significantly reduce the computational time and cost. Neglecting the core electrons is a good approximation for total energies and forces, but for calculating other properties a full all-electron wavefunction is required. This can be generated using the projector-augmented wavefunction (PAW)[40] approach. Although this works well in many cases, in the presence of a magnetic field a more complex approach, the gauge-included (GI)PAW approach, is required.

2.15.2. CASTEP

First-principles calculations were carried out using the CASTEP DFT code,[41] a planewave pseudopotential method using the GIPAW formalism. The PBE parameterisation of GGA was employed and core-valence electron interactions were

described using ultrasoft pseudopotentials.[42] The accuracy of the calculations is controlled by two parameters, E_{cut} (described above) and the k-point spacing (determines the accuracy with which the Brillouin zone is sampled). The calculations are 'converged' as far as possible, (*i.e.*, increasing the value of the parameter does not result in any significant increase in accuracy) with respect to the two parameters.

2.15.3. Experimental Details for CASTEP Calculations

First-principles calculations were performed using the CASTEP DFT code[41] - a plane wave pseudopotential method using the gauge-including projector-augmented wave (GIPAW) formalism.[43] Crystallographic structures suitable for optimisation were obtained from the Inorganic Crystal Structure Database[44] and Rietveld refinement of data within this thesis. Geometry optimisation and NMR calculations were performed using a cut-off energy of 60 Ry and a k-point spacing of 0.04 $Å^{-1}$. These values were obtained from calculations on multiple structures, including $NaNbO_3$ and $KNbO_3$, for which the k-point spacing and cut-off energy were optimised. NMR calculations produce an absolute isotropic shielding value and not an isotropic chemical shift. As such, the shielding, σ_{iso}, is converted into a δ_{iso} value by determining a reference shielding, σ_{ref}, *via* $\delta_{iso} = \sigma_{ref} - \sigma_{iso}$. Calculations were performed on $NaNbO_3$ (phase P) to derive a σ_{ref} of 559.40 ppm for ^{23}Na, the average of both sites. Calculations were carried out at the University of St Andrews using CASTEP version 5.5.2 on a 198-node (2376 core) Intel Westmere cluster with 2 GB memory per core and QDR Infiniband Interconnect. Additional information concerning CASTEP calculations can be found in the relevant chapters.

2.16. Experimental Details

The following experimental details are applicable to all results presented in Chapters 3, 4 and 5. Any additional experimental details can be found in the relevant chapters.

2.16.1. Synthesis

Commercially-obtained samples of $NaNbO_3$ (Sigma-Aldrich, 99.9%) were used without further purification. Samples were also prepared using the traditional solid-

state route by mixing Na_2CO_3 (Sigma-Aldrich, 99.9%,) and Nb_2O_5 (Alfa Aesar, 99.9%) in acetone in an agate mortar and pestle for 10-20 minutes, pressing (5 tons/in^2) into pellets of 10 mm diameter and approximately 4 mm thickness, and annealing at temperatures between 500 and 1100 °C for periods of 12 to 24 hours, with use of a sacrificial powder, comprised of the unreacted reagents. For lithium or potassium doped niobates, Li_2CO_3 (Sigma-Aldrich, 99.9%) or K_2CO_3 (Sigma-Aldrich, 99.9%) were also incorporated into the reaction, using the above process.

Samples made using the sol-gel technique were prepared from the addition of sodium ethoxide (Sigma-Aldrich, 99.5%, 3.67 mmol) to niobium (V) ethoxide (Sigma-Aldrich, 99%, 2.9 mmol), refluxing in 1-methoxyethanol (10 ml) at 130 °C for 3 hours, cooling slowly to room-temperature, allowing to crystallise overnight and annealing at temperatures between 400 and 800 °C for 8 hours. In a modified sol-gel approach, the mixture was refluxed and crash-cooled in ice, with the resulting powder filtered off. Half the powder was dried at 90 °C, with the other half pressed into a pellet and annealed at 500 °C to improve crystallinity.

2.16.2. Neutron Powder Diffraction

Time-of-flight neutron powder diffraction was carried out at the ISIS neutron spallation source on the high-resolution powder diffractometer (HRPD).[45] The powdered samples (approximately 5 grams) were mounted into vanadium cans, with each scan being recorded for 20 μAhr of incident beam (approx. 30 minutes continuous beam). Data were collected from room-temperature to 530 °C (for $NaNbO_3$) or 660 °C (for KNN), with a 10 minute thermal equilibration period allowed between scans. All data for samples of LNN were acquired at ambient temperature.

2.16.3. Synchrotron X-ray Powder Diffraction

Synchrotron X-ray powder diffraction data were collected using the multianalysing crystal (MAC) detector system on beamline I-11 (High-Resolution Powder Diffraction) at Diamond[46] at a wavelength of 0.82503 Å. Samples were mounted in quartz capillaries (0.5 mm diameter), which were heated using a hot-air blower (with a heating rate of 10 °C min^{-1}) over the temperature range from 100 to 660 °C at 20 °C

intervals. Each scan was recorded for 15 minutes, with a temperature equilibration of 10 minutes allowed between scans.

2.16.4. Laboratory Powder X-ray Diffraction

Powdered samples were loaded into disks of 3 mm depth, and data were obtained using Cu $K_{\alpha 1}$ radiation (wavelength of 1.5406 Å). Diffraction patterns were obtained using a Panalytical EMPYREAN diffractometer with a 2θ step size of 0.017°. All diffraction patterns were recorded at room temperature with a 1 hour scan time.

2.16.5. Diffraction Data Analysis

All diffraction data were analysed by Rietveld refinement[15] using the General Structure Analysis System (GSAS) software package.[16,17] Parameters refined included background coefficients, profile coefficients, lattice parameters, atomic positional coordinates, isotropic atomic displacement parameters and phase fractions, where applicable. Any specific additional details can be found in the relevant chapters.

References

[1] West, A. R., *Solid State Chemistry and its Applications*, Chapter 5, Wiley, Chichester, 1984.

[2] West, A. R., *Basic Solid State Chemistry*, Chapter 1, Wiley, Chichester, 1991.

[3] Moulson, A. J., Herbert, J. M., *Electroceramics*, Second Edition, Chapter 1, Wiley, Chichester, 2003.

[4] Bragg, W. L., *Nature,* 1912, **90**, 410.

[5] Hammond, C., *The Basics of Crystallography and Diffraction*, OUP, Oxford, 2009.

[6] Sands, D. E., *Introduction to Crystallography*, Dover Publications Inc., Dover, 1994.

[7] International Tables for Crystallography, Vol. A, 4th Edition, 1995.

[8] DIAMOND Facility website: http://diamond.ac.uk/Home/About/Synchrotrons/Machine.html Access date: 05/06/13

[9] DIAMOND Light Source, Harwell Science and Innovation Campus, Didcot, Oxford, UK.

[10] ISIS Facility website: http://www.isis.stfc.ac.uk/about-isis/how-isis-works6313.html Access date: 05/06/13

[11] ISIS Facility website: http://www.isis.stfc.ac.uk/about-isis/what-is-a-neutron3855.html Access date: 05/06/13

[12] ISIS, Harwell Science and Innovation Campus, Didcot, Oxford, UK.

[13] NIST Centre for Neutron Research website: http://www.ncnr.nist.gov/resources/n-lengths/ Access date: 23/03/13

[14] Young, R. A., *The Rietveld Method*, OUP, Oxford, 1996.

[15] Rietveld, H. M., *Acta Cryst.,* 1966, **A-20**, 508.

[16] Larson A. C., Von Dreele, R. B., General Structure Analysis System (GSAS), Los Alamos National Laboratory, Report LAUR 86-748 (2000).

[17] Toby, B. H., *J. Appl. Cryst.,* 2001, **34**, 210.

[18] Bloch, F., *Phys. Rev.,* 1946, **70**, 460.

[19] Hore, P. J., *Nuclear Magnetic Resonance*, Chapter 2, OUP, Oxford, 1995.

[20] Keeler, J., *Understanding NMR Spectroscopy,* Chapter 4, Wiley, Chichester, 2005.

[21] Keeler, J., *Understanding NMR Spectroscopy,* Chapter 2, Wiley, Chichester, 2005.

[22] Hore, P. J., Jones, J. A., Wimperis, S., *NMR: The Toolkit,* Chapter 2, OUP, Oxford, 2000.

[23] Ernst R. R., Anderson, W. A., *Rev. Sci. Instr.,* 1996, **37**, 93.

[24] Andrew, E. R., Bradbury, A., Eades, R. G., *Nature,* 1958, **182**, 1659.

[25] Andrew, E. R.,Bradbury, A., Eades, R. G., *Nature,* 1959, **183**, 1802.

[26] Hore, P. J., *Nuclear Magnetic Resonance*, Chapter 5, OUP, Oxford, 1995.

[27] Abragam, A., *Principles of Nuclear Magnetism,* p. 232, OUP, Oxford, 1961.

[28] Simmonds, J. G., Mann Jr., J. E., *A First Look at Perturbation Theory,* Chapter 1, Dover Publications, Dover, 1998.

[29] Samoson, A., Lippmaa, E., *J. Magn. Reson.,* 1989, **84**, 410.

[30] Medek, A., Harwood, J. S., Frydman, L., *J. Am. Chem. Soc.,* 1995, **117**, 12779.

[31] Massiot, D., Touzo, B., Trumeau, D., Coutures, J. P., Virlet, J., Florian, P., Grandinetti, P. J., *Solid State Nucl. Magn. Reson,* 1996, **6**, 73.

[32] Amoureux, J. P., Fernandez, C., Steuernagel, S., *J. Magn. Reson.*, 1996, **123**, 116.

[33] Brown, S. P., Wimperis, S., *J. Magn. Reson.*, 1997, **128**, 42.

[34] Mueller, K. T., Wu, Y., Chmelka, B. F., Stebbins, J., Pines, A., *J. Am. Chem. Soc.,* 1991, **113**, 32.

[35] Jensen, F., *Introduction to Computational Chemistry*, Chapter 5, Wiley, Chichester, 2007.

[36] Hohenberg, P., Kohn, W., *Phys. Rev. B.,* 1964, **136**, 864.

[37] Born, M., Oppenheimer, R., *Annalen der Physik*, 1927, **389**, 457.

[38] Juan, Y. M., Kaxiras, E., *Phys. Rev. B.*, 1993, **48**, 14944.

[39] Walle, C. G., Blöch, P. E., *Phys. Rev. B.*, 1993, **47**, 4244.

[40] Pickard, C. J., Mauri, F., *Phys. Rev. B.*, 2001, **63**, 245101.

[41] Clark, S. J., Segall M. D., Pickard, C. J., Hasnip, P. J., Probert, M. J., Refson, K., Payne, M. C. *Z. Kristall.* 2005, **220**, 567.

[42] Yates, J. R., Pickard, C. J., Mauri, F. *Phys. Rev. B* 2007, **76**, 024401.

[43] Pickard, C. J., Mauri, F., *Phys. Rev. B,* 2001, **63**, 245101.

[44] ICSD website: cds.rsc.org

[45] ISIS, Harwell Science and Innovation Campus, Didcot, Oxford, UK.
Web address: http://www.isis.stfc.ac.uk/instruments/hrpd/hrpd.html.

[46] DIAMOND Light Source, Harwell Science and Innovation Campus, Didcot, Oxford, UK.
Web address: http://diamond.ac.uk/Home/Beamlines/I11.html.
Instrument paper: Tartoni, N., Thompson, S. P., Tang, C. C., Willis, B. L., Derbyshire, G. E., Wright, A. G., Jaye, S. C., Homer, J. M., Pizzey, J. D., Bell, A. M. T., *J. Synch. Rad.,* 2008, **15**, 43.

Chapter 3
The Rich Polymorphism of $NaNbO_3$

3.1. Introduction

Sodium niobate, $NaNbO_3$, has been studied extensively over the past half century and is one of the most complex ferroelectric perovskites, in terms of its rich polymorphism and crystal structures.[1] It offers highly promising piezoelectric responses and is known to have room-temperature polar polymorphs that are also potentially ferroelectric.[2] In part, the interest in $NaNbO_3$ is attributed to its potential use as a functional material, offering a replacement to the commercially-used $Pb(Zr,Ti)O_3$ as a lead-free alternative. A $NaNbO_3$-based piezoelectric material would allow the widely used PZT to be replaced with a material that is less detrimental to human and environmental health, and also easier to dispose of safely.

The phase diagram of $NaNbO_3$ is known to be highly complex,[3,4] owing to difficulty in accurately determining the structures of the polymorphs. To date, seven temperature-dependent phases have been identified, with much of the earlier work being carried out by Megaw, Glazer and Darlington.[4,5,6] There is much ambiguity over the exact structures of the phases, and consequently, the space groups that should be assigned. However, each polymorph has been denoted with a letter: N (stable below –100 °C), P (–100 to 360 °C), R (360 to 480 °C), S (480 to 520 °C), T1 (520 to 575 °C), T2 (575 to 640 °C) and U (above 640 °C). In addition to these phases, phase Q may also exist at room temperature, as discussed in Chapter 1. Phase P adopts the *Pbcm* space group (with unit cell metric $\sqrt{2}a_p \times \sqrt{2}a_p \times 4a_p$, where a_p denotes the parent aristotype cell metric) and is antiferroelectric (AFE).[7] Phase Q adopts the non-centrosymmetric $P2_1ma$ space group[8] (unit cell $\sqrt{2}a_p \times 2a_p \times \sqrt{2}a_p$) and is polar. Initially, this phase was reported to be present when induced in an electric field.[9] More recent work has shown (partly owing to the improvements in resolution in diffraction techniques) that the co-existence of phases P and Q is dependent upon the synthetic route employed.[10] More recently, it has been reported that this phase may be formed preferentially when using sol-gel synthesis techniques,[11] Reported Curie

temperatures for phase P range from 320 °C[12] to 400 °C,[13] with a range of dielectric constants observed. The differences may arise from differences in the phase composition studied, *i.e.,* samples could be phase P, a mixture of P and Q, or contain small amounts of impurity or other polymorphs.

There is much ambiguity in the literature over the unit cell and space group assignments for the high-temperature phases of $NaNbO_3$, in particular R and S. In part, this arises from their similar diffraction patterns and the very subtle structural differences between the different polymorphs. As discussed in Chapter 1, the most common perovskite distortions are cation displacements and octahedral tilting, of which the latter is crucial to understanding the polymorphism of $NaNbO_3$. Whilst Glazer developed a well-used notation scheme for octahedral tilting,[14] it is not ideally suited for application to $NaNbO_3$. This is because the original scheme, derived from a $2 \times 2 \times 2$ repeat unit of linked octahedra, does not necessarily apply to all polymorphs of $NaNbO_3$, *e.g.*, phase P has a four-fold repeat unit while for R and S longer repeat units have been suggested.

Typically, these phases are characterised by diffraction techniques, generally neutron powder diffraction, although much of the initial work relied on X-ray diffraction. One difficulty, however, is that several phases have very similar diffraction patterns, making accurate structure determination difficult. For example, Zhang proposed that phase Q has a subtle monoclinic distortion (space group *Pm*)[15] whereas other work suggests the phase is orthorhombic (space group $Pmc2_1$, or $P2_1ma$ in the alternate setting).[9] As such, additional methods for characterizing these phases have been considered, including DFT and symmetry mode analysis. DFT, whilst problematic when considering high-temperature structures (Section 3.4.2) has recently been shown to be an excellent technique for the study of octahedral tilting.[16] Symmetry mode analysis provides an alternative approach to structural analysis by determining the symmetry-allowed distortions that can arise from a parent aristotype structure (for $NaNbO_3$, it is the cubic polymorph). This method allows starting points for structural refinement to be readily determined, although Rietveld analysis is still needed. The symmetry modes specifically relevant to $NaNbO_3$ are discussed in more detail in section 3.4.2. Additional discussion can also be found in the recent publication by Peel.[17]

3.2. Experimental

3.2.1. Synthesis and Diffraction Techniques

Refer to Chapter 2 for an overview of the experimental techniques and conditions used.

3.2.2. Solid-state NMR

Solid-state ^{23}Na (I = 3/2) NMR spectra were acquired using Bruker Avance III spectrometers, equipped with wide-bore 14.1 or 9.4 T magnets, at Larmor frequencies of 158.746 and 105.842 MHz, respectively. Samples were packed into conventional ZrO_2 (4 mm) rotors and rotated at a MAS rate of 12.5 kHz. ^{23}Na chemical shifts were referenced to 1 M $NaCl_{(aq)}$ using a secondary reference of $NaCl_{(s)}$ (δ_{iso} = 7.8 ppm). Conventional ^{23}Na MAS NMR spectra were obtained using single-pulse experiments, with pulse lengths of 1.5 and 1.9 μs, at 14.1 and 9.4 T, respectively, with a recycle interval of 5 s. All MQMAS spectra were acquired using a split-t_1 shifted-echo pulse sequence (see Fig. 2.22). High power pulses (of 5 and 1.7 μs with $\omega_1/2\pi$ = 100 kHz at 14.1 T and 6 and 2 μs with $\omega_1/2\pi$ = 95 kHz at 9.4 T) were used for triple-quantum excitation and conversion, respectively. The final 180° pulse was applied with low power (~9 kHz at both fields) to be selective for the CT. Additional experimental details can be found in the relevant figure captions or sections.

High-temperature ^{23}Na MAS NMR spectra were acquired using a Bruker Avance III spectrometer, equipped with a wide-bore 9.4 T magnet. Temperatures were calibrated using $Pb(NO_3)_2$ and KBr, and thermal equilibration periods were at least 30 minutes. A 30 °C temperature gradient was present along the 4 mm ZrO_2 rotor. A MAS rate of 4 kHz was employed. All high-temperature experiments were performed by Dr. Frédéric Blanc at the University of Cambridge.

^{23}Na DOR NMR spectra were acquired using a Bruker Avance III spectrometer equipped with a wide-bore 20.0 T magnet and a Samoson DOR probe, at a Larmor frequency of 224.876 MHz, at the UK 850 Solid-State NMR Facility located at the University of Warwick. Spectra were referenced as for 9.4 and 14.1 T NMR

experiments. Typical rotor spinning speeds were 1200-1600 Hz for the outer rotor and 5000-7000 Hz for the inner rotor. Exact spinning speeds and additional experimental details can be found in the relevant figure captions. The spectra were obtained with the experimental assistance of Dr Dinu Iuga.

All simulated NMR spectra were obtained using SIMPSON - a general density matrix simulation program for solid-state NMR spectroscopy.[18]

3.3. Room-Temperature Experimental Results

3.3.1. Commercial Sample

Initial work focused on commercially-purchased $NaNbO_3$ (Sigma-Aldrich) characterising the sample through diffraction and solid-state NMR spectroscopy, and performing CASTEP calculations on the structure to compare the simulated and experimentally-obtained NMR spectra. The two room-temperature polymorphs (P and Q) have very similar diffraction patterns, and so a detailed analysis of their superstructure peaks is required, as this is where the key differences are found. PXRD data confirmed the sample to be composed solely of the phase P polymorph. As the diffraction patterns of phases P and Q are very similar, an overlay of the two showing their superlattice regions is given in Fig. 3.1.

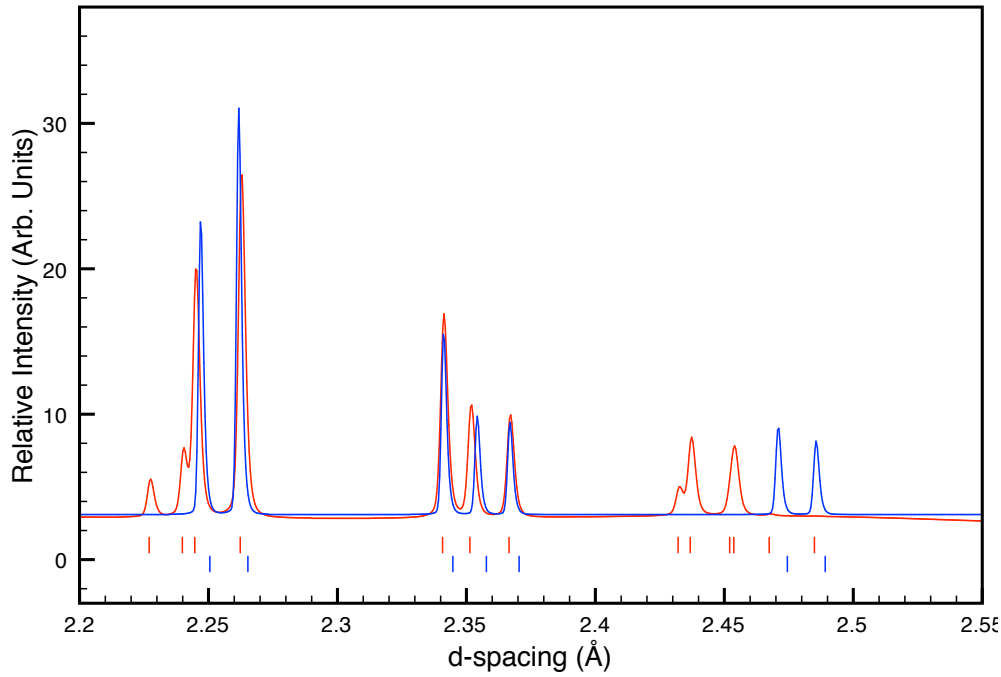

Figure. 3.1: Simulated diffraction patterns (NPD) of $NaNbO_3$ phase P (red) and phase Q (blue) showing their superlattice regions. Within this range, the key differences between the two patterns can be seen. This figure can be used as a point of reference for refinements presented within this chapter.

The presence of any additional $NaNbO_3$ polymorphs was ruled out by using NPD, as shown in Fig. 3.2, and ^{23}Na solid-state NMR spectroscopy. Corresponding crystallographic data obtained from Rietveld refinement are given in Appendix B. Data sets refined well to the *Pbcm* model, providing good levels of fit to the NPD data. Based on the refinements, it appears that phase P is formed exclusively, although given the level of noise in the superstructure region, it is possible that a small amount of phase Q may be formed.

^{23}Na (I = 3/2) is a quadrupolar nucleus and, as such, MAS spectra often show broadened lineshapes due to second-order quadrupolar coupling. Consequently, extraction of useful NMR parameters (δ_{iso}, C_Q and η_Q) is often hindered by the broadening, and ^{23}Na MAS NMR is therefore ineffective in determining the number of crystallographically-distinct sites. ^{23}Na MQMAS spectra, however, are free from second-order quadrupolar broadening and allow an isotropic spectrum to be obtained. ^{23}Na triple-quantum MAS spectra of $NaNbO_3$ are shown in Fig. 3.3. It can be seen that two sharp resonances are present in each isotropic spectrum, suggesting that two crystallographically-distinct ^{23}Na sites are present in the sample.

Note, a third resonance can also be observed, more so in the spectrum acquired at 9.4 T, and this is discussed in Section 3.3.3 in some detail. By considering the extracted ^{23}Na NMR parameters given in Table 3.1, it can be seen that one site has a much larger P_Q (and consequently C_Q) than the other. The site with the larger P_Q (Na2) is referred to as the 'broad' site, while the other (P_Q = 1.1 MHz, Na1) is the 'narrow' site.

CASTEP DFT calculations may be used to predict the NMR parameters of the *Pbcm* polymorph which can then be compared to those obtained from the ^{23}Na isotropic NMR spectra. By optimising the structure obtained from Rietveld refinement of NPD data (but fixing the unit cell size - see Section 3.4.2) and calculating the NMR parameters, the NMR spectrum can be simulated, as shown in Fig. 3.4. The calculated NMR parameters are in agreement with those obtained experimentally, as can be seen when comparing Figs. 3.3(a) (MAS spectrum) and 3.4.

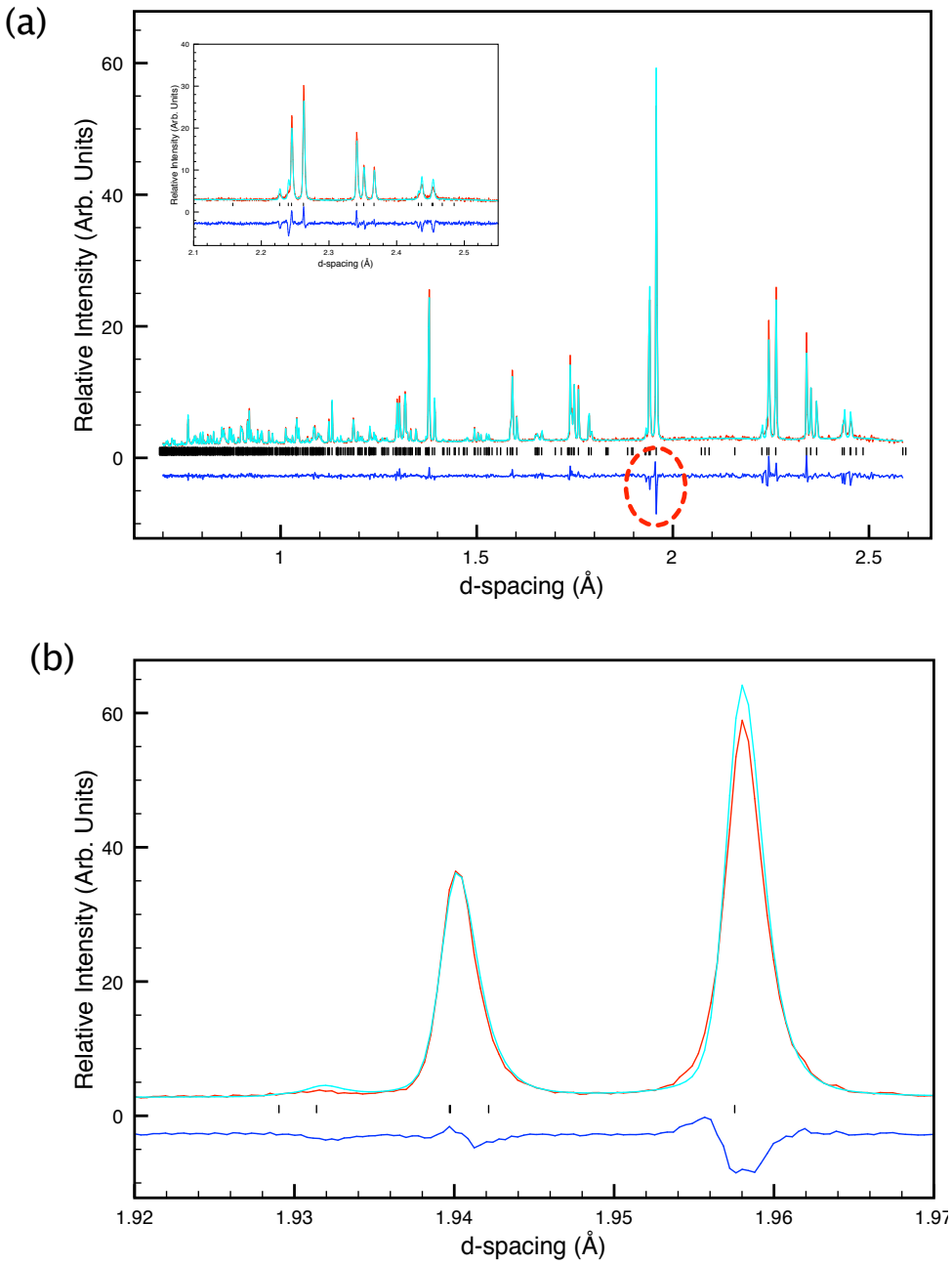

Figure. 3.2: NPD Rietveld profile of (a) commercial $NaNbO_3$ refined in space group *Pbcm* (phase P); a = 5.50437(3) Å, b = 5.56973(3) Å and c = 15.51759(7) Å. wRp = 6.14% and χ^2 = 4.14. An expansion of the region around 1.95 Å is given in (b), where it can be seen that the fit is satisfactory, and the difference plot in (a) appears to be an artefact of the graphics program used.

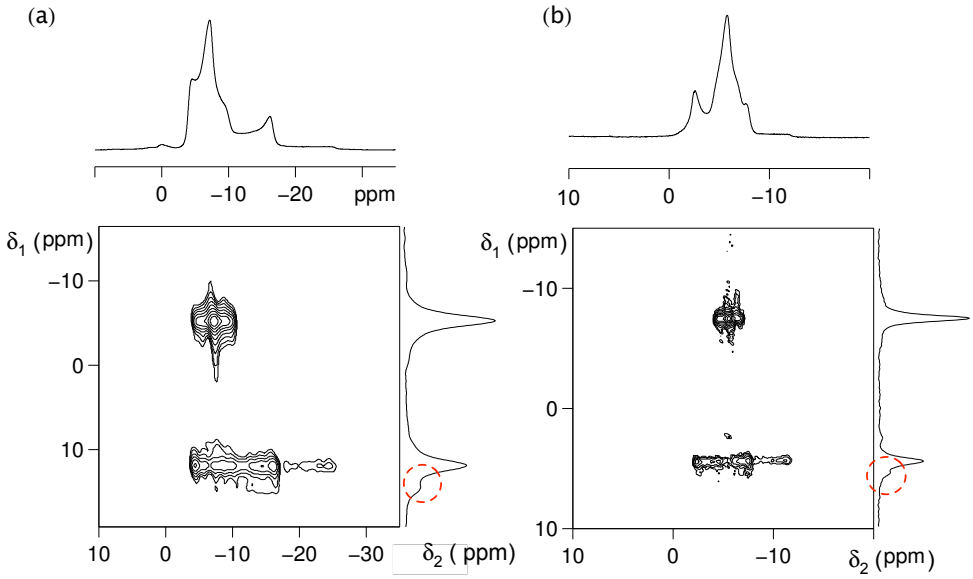

Figure. 3.3: ^{23}Na split-t_1 shifted-echo MQMAS spectra of $NaNbO_3$ (Aldrich) acquired at (a) 9.4 T and (b) 14.1 T, with corresponding MAS spectra shown above. At least two crystallographically-distinct sites are visible in each MQMAS spectrum, which is not immediately discernible from the MAS spectra. Extracted NMR parameters for both spectra can be found in Table 3.1. The spectra are the result of averaging 96 transients for each of 100 t_1 increments of 142.22 μs, with a 5 s recycle interval. The red circles highlight possible additional resonances, considered further in Section 3.3.3.

Table 3.1: Extracted ^{23}Na NMR parameters for $NaNbO_3$ (Aldrich) at 9.4 and 14.1 T. The corresponding spectra are shown in Fig. 3.3.

Field	Site	δ_{iso} (ppm)	P_Q / MHz
9.4 T	Na1	–4.3(5)	1.2(1)
	Na2	–0.6(5)	2.2(1)
14.1 T	Na1	–4.3(5)	1.1(1)
	Na2	–0.8(5)	2.1(1)

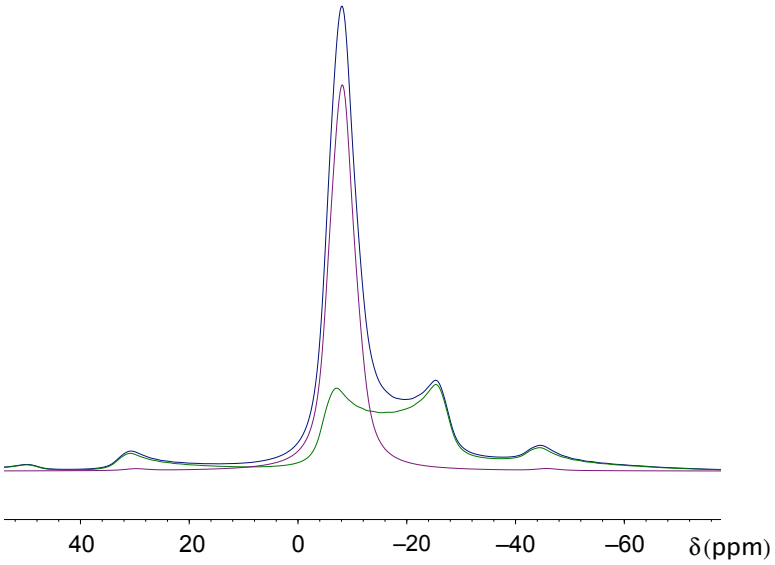

Figure. 3.4: Simulated ^{23}Na (9.4 T) MAS (12.5 kHz) NMR spectra of (blue) $NaNbO_3$ (phase P) and the two individual ^{23}Na sites (purple and green). The spectra were simulated using values obtained from CASTEP calculations. For the individual sites Na1 and Na2 (purple and green, respectively): δ_{iso} = –5.2 and 0.5 ppm, C_Q = 1.13 and 2.24 MHz and η_Q = 0.7 and 0.1, respectively.

3.3.2. Synthesis and Characterisation of Phase Q

Phase Q has a non-centrosymmetric polar space group, $P2_1ma$, and is therefore more commercially desirable than phase P. Additionally, it has been reported to be ferroelectric[2] and to exhibit good piezoelectric responses. $NaNbO_3$ samples were prepared using the traditional solid-state synthetic route, using annealing temperatures of 500 - 1100 °C. Samples annealed at the lower end of this temperature range often led to incomplete reactions, with sometimes large amounts of starting materials being observed in the diffraction data; those annealed at the higher end often led to a more complete reaction but with phase P formed preferentially, if not exclusively. $NaNbO_3$ samples annealed at 800 °C for 12 hours give rise to a mixture of phases P and Q, as determined using solid-state NMR, shown in Fig 3.5. Whilst higher fields in NMR typically provide higher resolution spectra, it is often useful to acquire spectra at

different fields as, for quadrupolar nuclei, resolution can sometimes be improved at lower fields. This is because both the chemical shift and quadrupolar coupling interaction are field dependent and, as such, overlapping resonances may better resolve at lower field as well as higher. This is readily observed in Fig. 3.5, where a ^{23}Na split-t_1 MQMAS spectrum is shown at 9.4 and 14.1 T. As the figure shows, the 'upper' ridge ($\delta_1 \approx -6$ ppm) comprises two distinct resonances at both 9.4 and 14.1 T. However, at 9.4 T, the lower ridge ($\delta_1 \approx 12$ ppm) shows two distinct resonances, but these remain overlapped at 14.1 T. Table 3.2 shows the extracted NMR parameters. Those from phase P are in excellent agreement with those from the commercially-purchased sample. It can be seen that phase P is present in the sample alongside a second phase, which can be shown to be Q. NMR calculations performed using CASTEP (similar to those for phase P) for phase Q show an excellent agreement with the experimentally-observed data. The calculations show that phases P and Q have very similar NMR parameters, with one sharp and one broader site, as observed experimentally. Calculated values of P_Q (from CASTEP optimisations) for phases P (Na1 and Na2) and Q (Na1 and Na2) are 1.2, 2.4, 1.1 and 2.5 MHz, respectively, which are in good agreement with experimentally-observed values given in Table 3.2. Similarly, δ_{iso} values of –5.2, –0.5, –6.1 and –1.6 ppm were obtained, which shows reasonable agreement to those obtained experimentally (Table 3.2).

By using quantitative analysis, it is possible to determine the relative proportions of phases P and Q from the NMR data. Rietveld refinement allows the phase fractions to be determined with a reasonable degree of accuracy, while isotropic NMR spectra may be integrated to quantify the proportions of the resonances. Integration of the isotropic spectrum suggests the value is approximately 50%, although no exact quantitative error can be given for integrating the peaks.

It has been well-reported that phase Q is polar and shows promising piezoelectric responses. A review of the literature shows that no dielectric measurements of phase Q have been reported, and where measurements are reported for $NaNbO_3$, this is most likely for the phase P polymorph, or at least, a mixture of the two. By considering the solid-state synthetic approach, it is highly likely that *lower* annealing temperatures

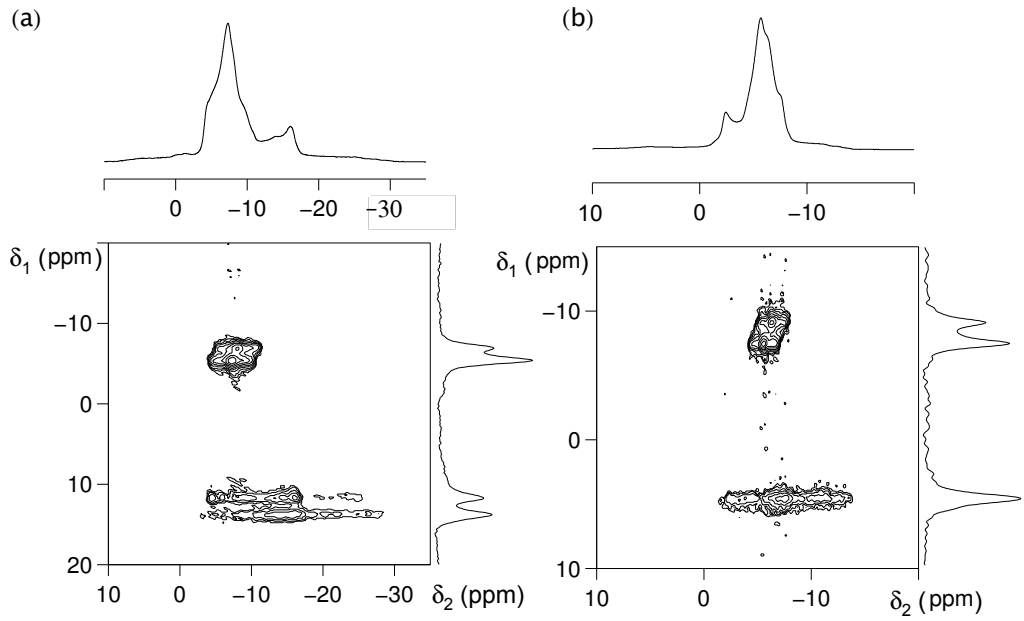

Figure. 3.5: ^{23}Na split-t_1 shifted-echo MQMAS spectra of $NaNbO_3$ (solid-state, annealed at 700 °C, mixed phase) acquired at (a) 9.4 T and (b) 14.1 T, with corresponding MAS spectra shown above. The spectra are the result of averaging 96 transients for each of 100 t_1 increments of 142.22 μs, with a 5 s recycle interval.

Table 3.2: Extracted ^{23}Na NMR parameters for $NaNbO_3$ (solid-state, annealed at 700 °C, mixed phase) at 9.4 and 14.1 T. The corresponding spectra are shown in Fig. 3.5.

Field	Phase	Site	δ_{iso} (ppm)	P_Q / MHz
9.4 T	P	Na1	–4.2(5)	1.1(1)
		Na2	–0.4(5)	2.2(1)
	Q	Na1	–5.0(5)	1.1(1)
		Na2	–1.1(5)	2.2(1)
14.1 T	P	Na1	–4.3(5)	1.2(1)
		Na2	–0.7(5)	2.2(1)
	Q	Na1	–5.0(5)	1.1(1)

favour formation of the phase Q polymorph, although incomplete reactions are observed if the annealing temperature is below 600 °C. Softer synthetic approaches, such as hydrothermal sol-gel syntheses, may be used instead, which allow the reaction to be completed at much lower temperatures. Hydrothermal synthesis of $NaNbO_3$, however, has been shown to result in the formation of the ilmenite polymorph,[19] as well as phases P and Q. Altering the pH, though, did change the relative fractions.[20] The sol-gel approach utilises much softer conditions, and is outlined in Chapter 2. The Rietveld profile of a sample synthesized using this approach is shown in Fig. 3.6, with the ^{23}Na MAS and MQMAS spectra shown in Fig. 3.7. The corresponding crystallographic data and NMR parameters are given in Appendix B and Table 3.3, respectively. As Fig. 3.6 shows, there are a number of impurity peaks in the diffraction pattern which are not attributed to phase Q. These peaks are not attributed to polymorphs of $NaNbO_3$ or the starting materials, sodium ethoxide and niobium ethoxide. Whilst unable to confirm the impurity present, based on the work presented within this chapter, the peaks are not attributed to phase P. However, closer inspection of the superlattice region (Fig. 3.6) reveals that there may be a peak at around 37° which is not accounted for in the refinement. Switching the focus to the NMR data (Fig. 3.7) reveals no evidence of phase P, although the broad nature of the resonances makes it impossible to confirm this absolutely. If phase P has been formed alongside phase Q, it is in a small quantity. When considering the NMR spectra of the samples, it is observed that the linewidths of the resonances are much greater for the sol-gel sample: for the sol-gel sample, peak width at half height in the isotropic projection is 300 Hz, whereas this is 140 Hz for the commercial (Aldrich) sample. Increases in linewidth often occur for one, or both, of two reasons: increased disorder and poorer crystallinity. As no additional disorder has been introduced (*i.e.,* cation substitution or atomic positional variation), it is most likely that the greater linewidth arises from the poorer crystallinity.

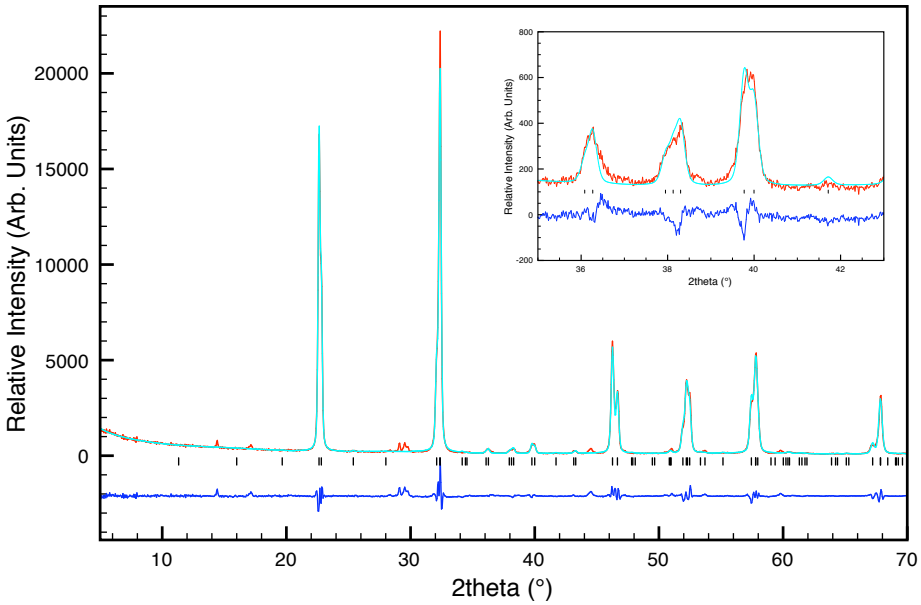

Figure 3.6: Rietveld profile and (inset) expansion of the superstructure region of l-PXRD data using the $P2_1ma$ model for $NaNbO_3$ (sol-gel). Small peaks unaccounted for in the refinement can be seen at approximately 14, 17 and 30°. wRp = 8.49%.

Table 3.3: Extracted ^{23}Na NMR parameters for $NaNbO_3$ (sol-gel) at 9.4 and 14.1 T. The corresponding spectra are shown in Fig. 3.7.

Field	Site	δ_{iso} (ppm)	P_Q / MHz
9.4 T	Na1	–5.0(5)	1.2(1)
	Na2	–1.0(5)	2.4(1)
14.1 T	Na1	–5.1(5)	1.1(1)
	Na2	–0.9(5)	2.3(1)

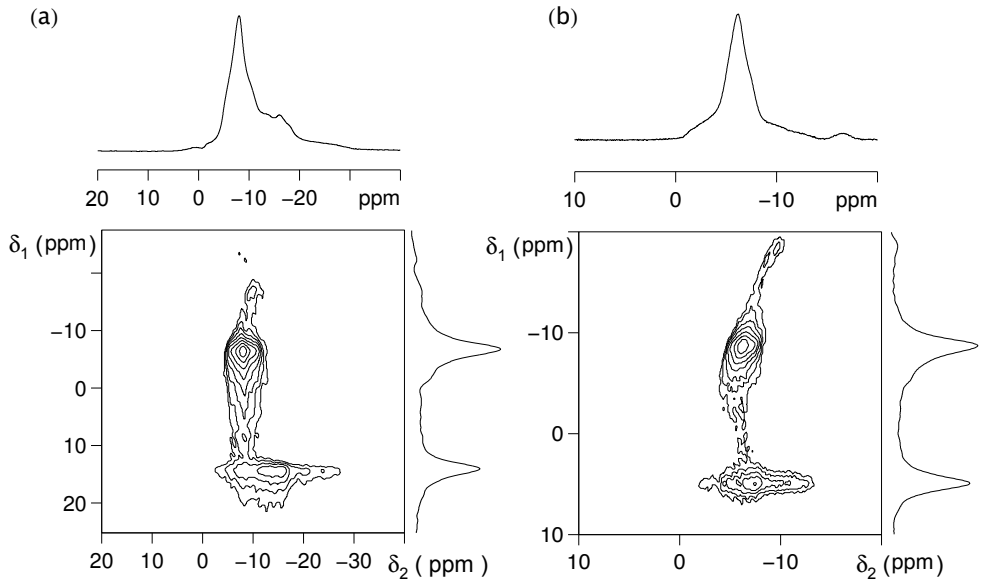

Figure 3.7: ^{23}Na split-t_1 shifted-echo MQMAS spectra of $NaNbO_3$ (sol-gel) acquired at (a) 9.4 T and (b) 14.1 T, with corresponding MAS spectra shown. The spectra are the result of averaging 96 transients for each of 100 t_1 increments of 142.22 μs, with a 5 s recycle interval.

3.3.3. An Additional Polymorph?

Alongside phase P in the commercially-obtained sample of $NaNbO_3$, there is evidence for a second phase or impurity also being present, as shown in Fig. 3.3. A small resonance can be seen in the isotropic spectra of $NaNbO_3$ recorded at 9.4 and 14.1 T, although it is better resolved at the lower field, as shown in Fig. 3.3. Data obtained from neutron diffraction experiments do not provide any reason to suggest that another phase/impurity is present. Three possible explanations for this are that (i) the phase/impurity is amorphous, and is therefore undetected using diffraction methods, although this is unlikely as a 'good' diffraction pattern would be expected to show 5 – 10% of an amorphous material; (ii) it is present in small regions of the sample and therefore has no/little long-range (periodic) structure, and/or (iii) it is a closely-related polymorph. This is best exemplified when considering the diffraction patterns for phases P and Q (Fig. 3.1) - differing only very slightly in their superlattice regions.

With such similar patterns, it is possible that an additional polymorph may go undetected (especially when only a small amount is present) using diffraction methods, *i.e.,* most of the peaks overlap with those from phase P. To investigate the nature of this additional resonance in the commercial sample (phase P), complementary ^{23}Na DOR NMR experiments were performed at 20.0 T, as shown in Fig. 3.8. As the figure shows, two 'principal' resonances are observed, corresponding to Na1 and Na2 in the MQMAS spectrum of phase P, with δ_{DOR} = –4.40 and –2.39 ppm, respectively. However, an additional resonance is observed in the DOR spectrum, with δ_{DOR} = –3.21 ppm. From MQMAS spectra acquired at two or more different fields, it is possible to predict the isotropic shift of the resonances in the DOR spectra, *i.e.*, a knowledge of the δ_1 line position in the MQMAS spectra at 9.4 and 14.1 T can be used to predict where the resonance will appear in the DOR spectrum at 20.0 T. The δ_1 line position is related to the isotropic chemical and quadrupolar shifts by

$$\delta_1^{14.1} = \frac{17}{8}\,\delta_{iso} + \frac{1}{2}\,\delta_Q^{14.1} \tag{3.1}$$

$$\delta_1^{9.4} = \frac{17}{8}\,\delta_{iso} + \frac{1}{2}\,\delta_Q^{9.4} \quad , \tag{3.2}$$

where 9.4 and 14.1 denote the respectively field strengths. Substitution of the MQMAS δ_1 line positions (14.6 and 5.3 ppm at 9.4 and 14.1 T, respectively) provides a set of simultaneous equations, where it is seen that

$$\frac{1}{2}\delta_Q^{9.4} - \frac{1}{2}\delta_Q^{14.1} = \delta_1^{9.4} - \delta_1^{14.1} \quad . \tag{3.3}$$

Substitution of

$$\delta_Q^{14.1} = \delta_Q^{9.4} \times \frac{4}{9} \tag{3.4}$$

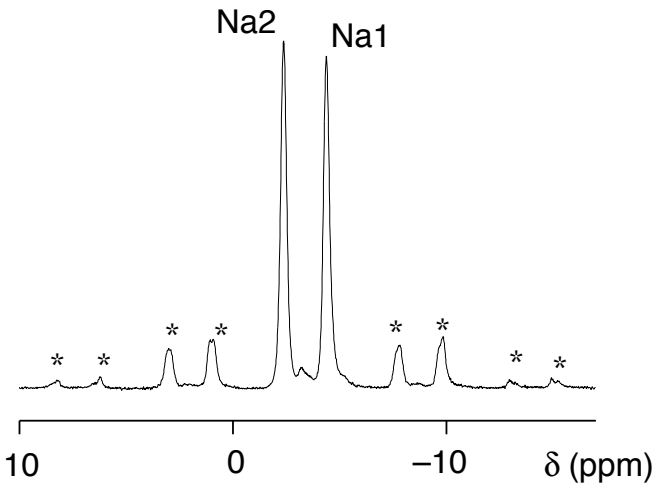

Figure 3.8: ^{23}Na (20.0 T) DOR NMR spectrum of $NaNbO_3$ (Aldrich), with a MAS rate of 1400 Hz (a second spectrum acquired at 1200 Hz is not shown but was used to determine which peaks were spinning sidebands, as denoted by *). Labels 'Na1' and 'Na2' correspond to phase P.

into Equation 3.3 gives a δ_Q value of 33.48 ppm at 9.4 T, corresponding to a P_Q of 2.4 MHz. The predicted resonance position in the DOR spectrum can then be calculated from

$$\delta_{DOR}^{20.0} = \delta_{iso} - \frac{2}{5}\,\delta_Q^{20.0} \quad , \tag{3.5}$$

where δ_{DOR} denotes the shift in the DOR spectrum at the specified field. Equation 3.5 gives a predicted ^{23}Na DOR shift of –3.47 ppm at 20.0 T (850 MHz). This predicted shift is in excellent agreement with the experimentally-obtained value of –3.21 ppm, where the small differences most likely arise owing to errors in the accuracy of determination of the δ_1 line position and subsequently P_Q.

As the shift of this resonance is very similar to that of the Na2 site in phase P, and has a very similar P_Q, it is likely that this resonance corresponds to a polymorph of $NaNbO_3$ with a similar structure to phase P. It is unknown if this additional phase is present in the mixed phase (P and Q) samples, as the peaks would most likely not be

sufficiently resolved to observe them. Integration of the resonances in the DOR spectrum allows the amount of the unknown phase to be determined. A value of between 5 and 10% is obtained, although there is an error in determining the exact areas over which to integrate. It is surprising that an 'impurity' with 5-10% abundance is not observed in the diffraction data. The presence of this phase contributes to uncertainties in previous work. For example, the presence of this phase may affect the dielectric constants of $NaNbO_3$, or affect the peaks observed in high-temperature diffraction patterns.

3.4. High-Temperature Study of $NaNbO_3$

3.4.1. Phase P

Initial[21] (and some recent)[10.24] attempts to determine the exact structure of phase P relied heavily on powder diffraction data. Diffraction experiments provide the best method for accurately determining the lattice parameters and symmetry of a structure, although determining precise fractional atomic coordinates is difficult from powder X-ray diffraction alone. DFT structural optimisations, however, provide an excellent complementary method for determining the atomic coordinates by calculating the small energy changes involved in the variation of the atomic coordinates, *i.e.,* an atom can 'move' around to find its lowest energy position. Several starting models (*i.e.,* unoptimised structures from refinement of diffraction data, all slightly different owing to differences in the refinement strategy employed, the technique used (s-PXRD or NPD) or subtle differences in the sample used) of phase P were analysed, and then optimised by allowing (a) fractional coordinates only to vary, and (b) fractional coordinates and lattice parameters to vary. Table 3.4 shows the forces acting on some of the atoms for two different phase P structures (one proposed by Sakowski-Cowley[21] and one from work presented in this thesis). As Table 3.4 shows, there are very high forces acting upon several of the atoms, particularly Nb^{5+}. In the Cowley model,[21] forces of up to 2.31 eV / Å are observed along the x axis, and up to 0.57 eV / Å in the model proposed in this work (Appendix B). This suggests that the atomic positions are most likely slightly incorrect for both, leading to high forces on the atoms. As such, geometry optimisations were performed to minimise the forces acting upon the atoms by allowing their positions to vary. As Table 3.5 shows, the forces acting on the atoms become substantially smaller, indicating that geometry optimisation is required to provide a lower energy structure. It is worth noting here that all DFT calculations are performed nominally at 0 K and not ambient temperature. Additionally, the total energy of the system was lowered after optimisation, as discussed and shown in Sections 3.4.2 - 3.4.4. It should be noted that for both models, both the octahedral tilt system and Na^+ cation displacements did not noticeably change after optimisation. The octahedral tilt systems, both prior to and after DFT optimisation, are given in Fig. 3.9, with the tabulated fractional coordinates given in Appendix B.

Table 3.4: Selection of atomic forces in phase P along each of the three crystallographic axes for two different models determined by Sakowski-Cowley[21] and work within this thesis (corresponding to Fig. 3.2 and Appendix B), prior to geometry optimisation.

		Atomic Forces		
	Site	x (eV / Å)	y (eV / Å)	z (eV / Å)
S-Cowley	Nb1	2.31128	0.27695	0.84666
	Nb2	2.31269	0.2752	0.84701
	Na1	0.14991	0.00017	0.00011
	Na2	0.14795	0.00026	0.00085
	O1	0.4413	0.34362	0.24051
	O2	0.44222	0.3435	0.24006
	O3	0.44218	0.34368	0.23968
This work	Nb1	0.57095	0.17986	0.5684
	Nb2	0.57214	0.18105	0.56405
	Na1	0.00577	0.00003	0.00171
	Na2	0.00652	0.00002	0.00135
	O1	0.23921	0.0722	0.19875
	O2	0.23876	0.07215	0.19661
	O3	0.23683	0.07119	0.20028

Table 3.5: Selection of atomic forces in phase P along each of the three crystallographic axes for two different models determined by Sakowski-Cowley[21] and work within this thesis (corresponding to Fig. 3.2 and Appendix B), after geometry optimisation using DFT.

		Atomic Forces		
	Site	x (eV / Å)	y (eV / Å)	z (eV / Å)
S-Cowley	Nb1	0.00712	0.00912	0.04065
	Nb2	0.00617	0.01456	0.03653
	Na1	0.00161	0.00038	0.00215
	Na2	0.00279	0.00062	0.00179
	O1	0.00295	0.01102	0.02607
	O2	0.00349	0.01223	0.0287
	O3	0.00358	0.01282	0.02068
This work	Nb1	0.00666	0.01701	0.02608
	Nb2	0.01764	0.01382	0.00147
	Na1	0.00264	0.00005	0.00057
	Na2	0.00295	0.00013	0.00006
	O1	0.00041	0.00254	0.0096
	O2	0.00083	0.00317	0.01237
	O3	0.00908	0.00369	0.00288

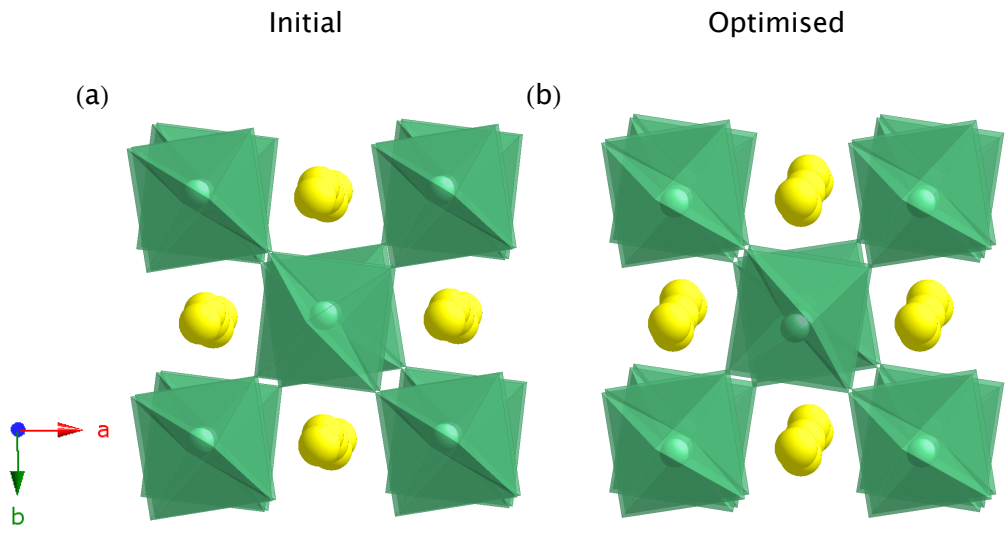

Figure 3.9: Crystal structures of $NaNbO_3$ for (a) initial and (b) geometry optimised (DFT) structures, where yellow spheres represent Na^+ cations and green polyhedra represent NbO_6 octahedra.

High-temperature s-PXRD experiments were carried out on a sample of commercial $NaNbO_3$ (phase P) from RT to 660 °C, including the phase P region (RT to 360 °C). Fig. 3.10 shows the variation in lattice parameters (normalised to the aristotype cell metric) over this region. It can be seen that the three pseudo-cubic axial lengths begin to converge toward each other, as is often observed upon heating. This correlates well with the changes observed in the distortion modes - the magnitude of the three modes decreases upon heating, which is compatible with the tendency of the three axial lengths to converge. Changes in the distortion modes as a function of temperature can be found in Appendix B, along with a brief discussion.

Complementary ^{23}Na MAS NMR spectra of phase P were acquired at 25 and 225 °C. The spectrum acquired at RT along with simulated lineshapes of the individual sites is shown in Fig. 3.11. This spectrum clearly illustrates the presence of two distinct ^{23}Na sites in the experimental spectrum, with NMR parameters given in Table 3.2.

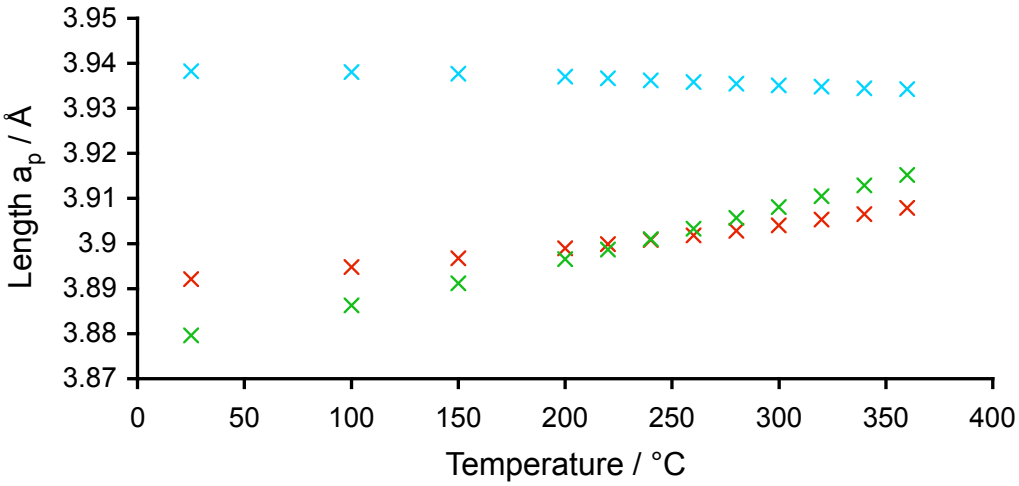

Figure 3.10: Lattice parameters obtained from a sample refined in space group *Pbcm* (phase P) over the temperature range 25 - 360 °C. Data are normalised to the aristotype cell metric. The *a*, *b* and *c* parameters are red, blue and green crosses, respectively. Error bars derived from GSAS are smaller than the data points and are therefore not shown.

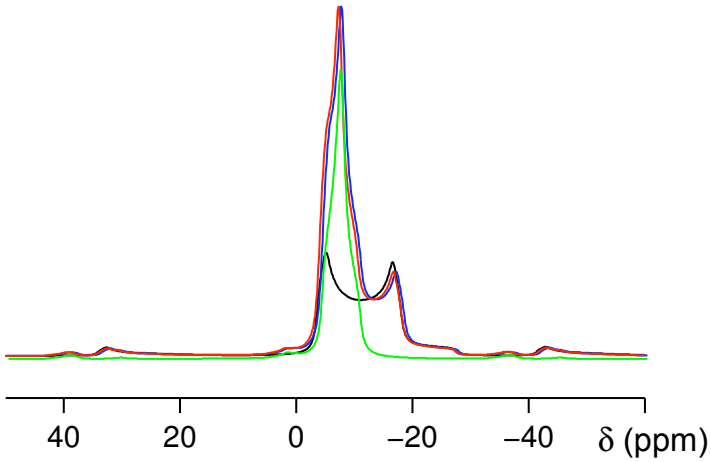

Figure 3.11: ^{23}Na (9.4 T) MAS (12.5 kHz) NMR spectrum of $NaNbO_3$ acquired at room temperature. The simulated spectrum (blue) compares well to the experimental lineshape (red), and simulations of the individual 'sharp' (green, Na1) and 'broad' (black, Na2) resonances are also shown. NMR parameters were obtained from CASTEP DFT calculations, with values given in the text and the caption to Fig. 3.3.

A similar spectrum was recorded at 225 °C and an overlay of the two is shown in Fig. 3.12. As the figure shows, the two spectra are noticeably different, with the principal change in lineshape occurring due to changes in the 'broad' resonance (Na2). The contribution of the narrow resonance (Na1) to the lineshape is similar in both cases. However, the broad resonance becomes noticeably sharper (as characterised by the increase in intensity and decrease in linewidth). This is an interesting result that suggests that the main structural changes that occur prior to the phase transition have greatest influence on the Na2 site. As the ^{23}Na MQMAS spectra have confirmed, this site has the greater C_Q, and therefore lower symmetry than Na1, and so it is logical that this site must undergo the greatest change since the symmetry increases due to an increase in temperature.

Complementary NPD data were also obtained for $NaNbO_3$ (phase P) to study the temperature-dependent phase transitions. Data were obtained for different temperatures within the phase P region (RT to 360 °C) and Rietveld refinements allowed crystallographic structures to be determined. The refinements and goodness of fit parameters can be found in Appendix B. The Na-O bond lengths within each structure were then extracted, and are shown in Table 3.6. The changes in Na-O bond lengths for the Na2 site are much more pronounced than for Na1, in particular for the Na2-O2 bond. This suggests that the Na2 cations displace by a much greater magnitude than those on the Na1 site as the temperature increases, in agreement with the NMR data (see Fig. 3.12). While an increase in symmetry is often expected upon heating, the data here suggest that one site undergoes a larger change than the other, most likely caused by the larger displacements of the Na2 cations. These displacements most likely result in the cations on the Na2 site being in a more symmetrical environment and therefore having a smaller C_Q, resulting, overall, in a more symmetric structure, as exemplified by the changes in the MAS NMR spectra. To support this assumption, NMR calculations were performed on structures obtained from Rietveld refinement of the NPD data (not DFT optimised) to determine if, and by how much, the magnitude of C_Q changed as a function of temperature. As the temperature increased from 25 to 200 to 340 °C, C_Q for Na2 fell from 2.8 to 2.1 to 1.8 MHz, respectively. ^{23}Na NMR spectra were simulated, as shown in Fig. 3.13, showing a pronounced change in the broad site. The simulated spectra show a similar

trend to that observed experimentally, and suggest that cations on the broad Na2 site are in a more symmetrical local environment as temperature increases.

Table 3.6: Na-O bond lengths for $NaNbO_3$ (phase P) at different temperatures. Data are obtained from refinement of NPD data. Only bond lengths less than 3 Å are shown, and * denotes that no bond shorter than 3 Å was present. In some cases, two bond lengths less than 3 Å occur. Numbers highlighted in red correspond to the bond length that showed the greatest change over the temperature range. Symmetry-equivalent bond lengths are not shown.

Temperature / °C	**Site**	**Na-O Bond Lengths / Å**			
		O1	**O2**	**O3**	**O4**
25	Na1	2.373(11), 2.800(10)	*	2.762(5)	2.405(5), 2.868(6)
	Na2	*	2.474(11), 2.518(7)	2.482(5), 2.632(7)	2.690(7)
200	Na1	2.359(10), 2.794(10)	*	2.767(5)	2.438(5), 2.873(6)
	Na2	*	2.526(10), 2.536(7)	2.515(5), 2.632(7)	2.688(5)
340	Na1	2.38(3), 2.79(3)	*	2.789(13)	2.460(13), 2.844(16)
	Na2	*	2.62(2), 2.54(6)	2.52(6), 2.68(7)	2.69(5)

In a subsequent step, the structures obtained from refinement of NPD data were geometry optimised to (a) find a lower-energy configuration of the atoms if possible, and (b) calculate the NMR parameters to determine if they support the experimentally-obtained spectra. Single-point energy calculations of the optimised structures confirm that there is a very small difference in energy between the optimised structures, as shown in Table 3.7. The table also shows the energies of the

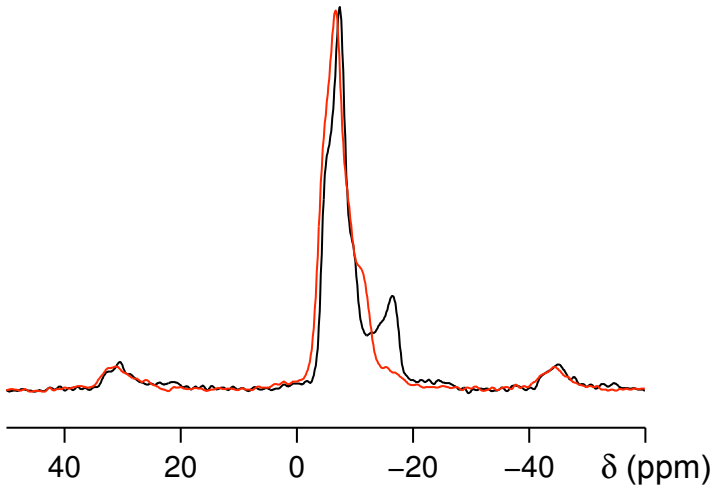

Figure 3.12: ^{23}Na (9.4 T) MAS (4 kHz) NMR spectra of $NaNbO_3$ acquired at (black) room-temperature and (red) 225 °C.

structures taken directly from refinement of NPD data (refinements shown in Appendix B), which shows a much more pronounced increase in energy as the temperature increases, compared to the energies obtained from DFT calculations. It is worth noting again that all DFT geometry optimisations are performed at 0 K, and so do not take into account entropy contributions or thermal vibrations (refer to Section 3.4.4). Nonetheless, DFT has been an invaluable tool to highlight the differences between starting models (this work compared to prior literature) and to understand the changes occurring at higher temperatures.

Table 3.7: Energies of the structures obtained from refinement of NPD data for both pre- and post-optimised structures. As temperature increases, the energies of the structures from NPD data change by a much greater amount than from DFT. Note, all DFT calculations are performed at 0 K, the temperature refers to the structure taken from high-temperature diffraction work.

Temperature / °C	Energy of NPD Structure / eV/f.u.	Energy of Optimised Structure / eV/f.u.
25	–4381.1770	–4381.1936
200	–4381.1639	–4381.1930
340	–4381.1529	–4381.1926

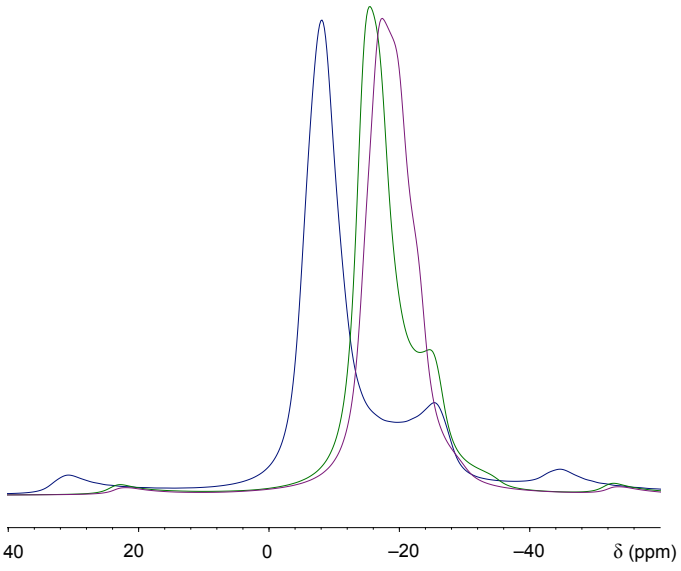

Figure 3.13: Simulated ^{23}Na (9.4 T) MAS (4 kHz) NMR spectra (normalised) of $NaNbO_3$, simulated from structures at RT (blue line), 200 °C (green line) and 340 °C (purple line). NMR parameters were obtained from DFT calculations of NPD data, which were not geometry optimised. It can be seen that the 'broad' component reduces in linewidth as the temperature increases.

3.4.2. Phases R and S

The series of temperature-dependent phase transitions of $NaNbO_3$ was discussed in Chapter 1, and some comparisons of the different structures proposed were given. However, the two phases causing the most ambiguity in the prior literature are R and S. Phases N, Q, T1, T2 and U are generally well characterised and there is significant agreement in the literature regarding their structures. Phases R and S, however, have been less well characterized, with several structures having been proposed for each. Much of the work presented in this section is based on symmetry mode analysis, neutron powder diffraction, solid-state NMR spectroscopy and DFT calculations. Some of the content is based on work presented by Peel *et al.*,[17] and parts of this publications will be replicated here.

Table 3.8 gives some of the previously proposed structures of phases R and S, including their unit cell metrics, space group assignments and the key distortion modes present. Before the reasoning behind why these assignments were incorrect is discussed (see Section 3.4.3), consideration should be given to the key distortion modes present in $NaNbO_3$. A 'revised' temperature-dependent series of phase transitions is presented in Section 3.4.3, and crystallographic data for each of the structures can be found in Appendix B. As discussed in Chapter 1, the key drivers for distortions in perovskites are octahedral tilt modes, ferroelectric cation displacements and Jahn-Teller distortions. Systematic and straightforward analysis of these modes has been made possible with the introduction of user-friendly software that can analyse the distortions away from the higher-symmetry parent structure *via* decomposition into symmetry modes.[22,23] Each distortion mode condenses at a specific point or line in the Brillouin zone of the parent (cubic) perovskite. The M point in the Brillouin zone is at the point k = (1/2, 1/2, 0) in reciprocal space, the R point is at k = (1/2, 1/2, 1/2) and the T line is at k = (1/2, 1/2, n), where n can equal 1/3, 1/4, 1/6 *etc*. The M point represents a doubling of the real-space unit cell in one plane, the R point causes a doubling of the unit cell in each direction, whereas any increase in unit cell size arising from the T line is dependent on the value on n. The distortions manifested at these points cause extra peaks to be present in the diffraction pattern compared to that of the parent structure. For each M, R and T point or line, there can be several distortion modes present in the structure, including octahedral

tilting and cation displacements. However, when using symmetry mode decomposition to aid in structure determination, only the *dominant* modes are considered in detail. For $NaNbO_3$, these dominant modes are those arising from octahedral tilting, although it should be stressed that additional modes are also present, *e.g.*, the Δ_5 mode corresponds to Na^+ displacements in phase P.

Howard and Stokes[24] carried out extensive work on symmetry mode decomposition, and determined that all the unique 'simple' octahedral tilt modes in perovskites could be described using one of 15 space groups, as opposed to the 23 tilt systems proposed by Glazer. However, there are exceptions for more complicated structures. As illustrated in Peel *et al.*,[17] it is possible for some modes to give rise to two, or more, distinct octahedral tilting systems. As the symmetry modes may be the same, but acting along different axes, the corresponding peaks in the powder diffraction pattern will be in a similar place for both, and only the intensity will differ.

The two *dominant* modes in $NaNbO_3$ are labelled M_3^+ and R_4^+, which specifically correspond to "in phase" and "out of phase" octahedral tilts, respectively, about one axis. The effects of each of these distortion modes on the $NaNbO_3$ structure are shown in Fig. 3.14, with additional figures given in Ref. 17.

Table 3.8: Some of the previously proposed models for phases R and S, showing the unit cell metrics, the space group assignments and the key distortion modes present. The axial directions of the tilt modes in the structure are given in brackets. The table is adapted from Ref. 17.

Phase	**Cell metrics, a_p**	**Space group assignment**	**Key distortion modes present**
R^{21}	$2a_p \times 6a_p \times 2a_p$	*Pmmn*	M_3^+ (*a,b*), T_4 (*b*), R_4^+ (*c*), Δ_5 (Na,Nb)
R^{25}	$2a_p \times 4a_p \times 6a_p$		
R^{26}	$2a_p \times 2a_p \times 2a_p$	*Pmmn*	M_3^+ (*a*), M_3^+ (*b*), R_4^+ (*c*)
R^{27}	$\sqrt{2}a_p \times \sqrt{2}a_p \times 6a_p$	*Pbnm*	M_3^+ (*c*), T_4 (*c*), R_4^+ (*ab*)
S^{28}	$2a_p \times 2a_p \times 2a_p$	*Pnmm*	R_4^+ (*a*), M_3^+ (*b*), M_3^+ (*c*)
S^{25}	$2a_p \times 4a_p \times 6a_p$		
S^{27}	$\sqrt{2}a_p \times \sqrt{2}a_p \times 12a_p$	*Pbnm*	M_3^+ (*c*), T_4 (*c*), R_4^+ (*c*)

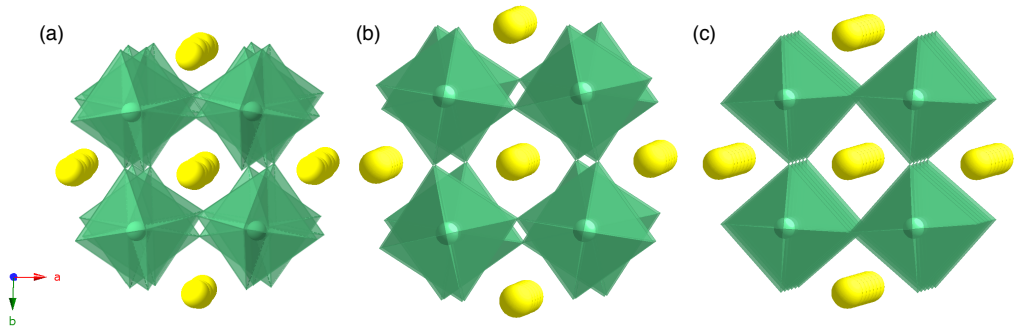

Figure 3.14: Crystal structures of $NaNbO_3$ with (a) the R_4^+ mode, (b) a T_4 mode, and (c) the M_3^+ mode. All figures are shown looking down the *c*-axis. The T_4 mode causes octahedra to tilt in opposite directions, resulting in the AACC tilt system observed in phase P, where A is an anticlockwise tilt and C is a clockwise tilt (0 describes no relative tilt); this nomenclature is used to avoid confusion with Glazer notation. The Δ_5 mode is not shown as this simply represents Na cation (yellow spheres) displacements.

NPD data were obtained over the temperature range 360 – 520 °C. Fig. 3.15 shows the diffraction patterns (over the d-spacing range 2 – 2.55 Å) obtained at 430 and 500 °C, corresponding to phases R and S, respectively. Phase S was first considered in detail. From Fig. 3.15 several key superlattice reflections can be seen, allowing the cell multiplicity to be determined. The peaks at 2.10, 2.37 and 2.49 Å are indexed by applying a $\sqrt{2}a_p \times \sqrt{2}a_p$ or $2a_p \times 2a_p$ cell metric in the *ab* plane, the peak at 2.27 Å is the (111) subcell peak, and the peaks at 2.45 and 2.24 Å require a $4a_p$ expansion along the *c*-axis to be indexed. The peaks at 2.24 and 2.45 Å, assigned to the T_4 mode, require a $4a_p$ cell metric along the *c*-axis, as this is the minimum value required to fully index the diffraction pattern. The simplest way to derive all possible starting models with these minimum cell metrics is the use of distortion mode analysis, using ISODISTORT. Based on the cubic parent structure, all distorted models could be derived with a specified unit cell size and symmetry. Based on the diffraction data above, the $\sqrt{2}a_p \times \sqrt{2}a_p \times 2a_p$ and $2a_p \times 2a_p \times 4a_p$ cell sizes were chosen with either primitive tetragonal symmetry or C-centered orthorhombic symmetry. However, the assumption that phase S is centrosymmetric is imposed, since the lower-temperature phase, P, is also centrosymmetric. By using these criteria, 140 possible structures were generated, although this list was significantly reduced by applying a further assumption that the dominant distortion modes are those derived from tilting of the

NbO_6 octahedra, as evidenced by analysis of other well-characterised polymorphs of $NaNbO_3$. Each distortion mode gives rise to peaks in the diffraction patterns: the M_3^+ mode observed has Miller indices (odd, odd, 4n), the R_4^+ mode (odd, odd, 2n) and the T_4 mode (odd, odd, odd). The peaks at 2.10 Å (134/314) and 2.49 Å (130/310), therefore, correspond to the presence of the M_3^+ mode, the peak at 2.37 Å (116/131/312) requires the R_4^+ mode to be present and the peaks at 2.24 and 2.45 Å (133/313 and 131/311, respectively) the T_4 mode. Analysis of the diffraction patterns in Fig. 3.15 confirms the need for the simultaneous presence of the M_3^+ and R_4^+ modes, resulting in only seven possible structures. Detailed Rietveld refinements were carried out for all possible structures, although none produced a sufficiently good fit with the simultaneous presence of the distortion modes along one axis. As such, models were then considered that allowed the distortion modes to be present along two or all three different axes, which required a lowering of the symmetry to $2a_p \times 2a_p \times 4a_p$ primitive orthorhombic cells. Again, a systematic search through the possible structures derived from ISODISTORT to show only those with the simultaneous presence of M_3^+ and R_4^+ modes, around two different axes, was undertaken. Detailed Rietveld refinements were performed on all options, with two producing excellent fits, with space groups *Cmmm* and *Pmmn*. Representations of the crystal structures of the two can be found in Fig. 3.16 along with portions of the Rietveld profiles. Close inspection of the superlattice peaks, however, confirmed that the latter showed the better fit. Rietveld profiles, expansions of the superlattice regions and crystallographic data can be found in Appendix B.

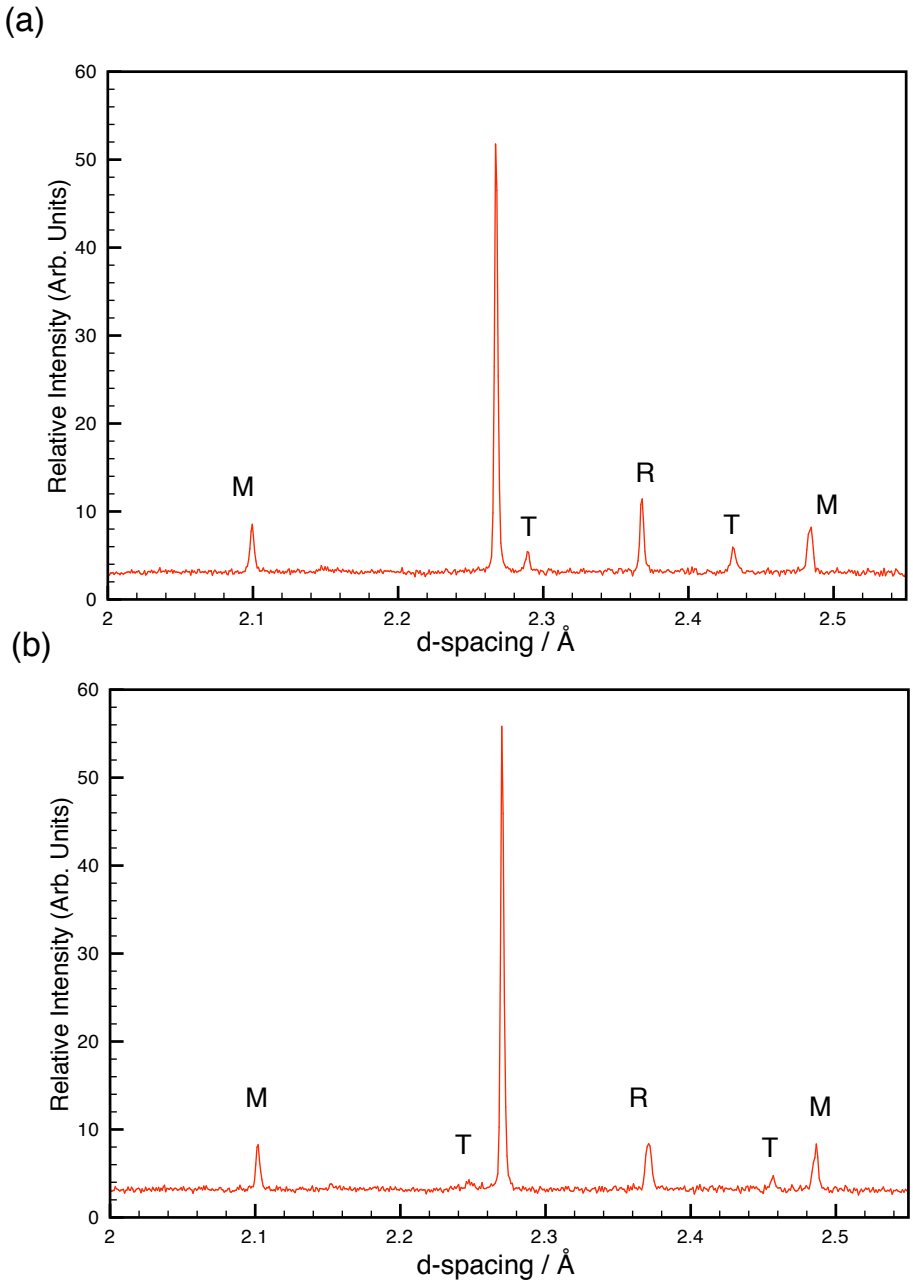

Figure 3.15: Portions of NPD data for (a) phase R at 430 °C and (b) phase S at 500 °C, with peaks resulting from the M, R and T points are labeled.

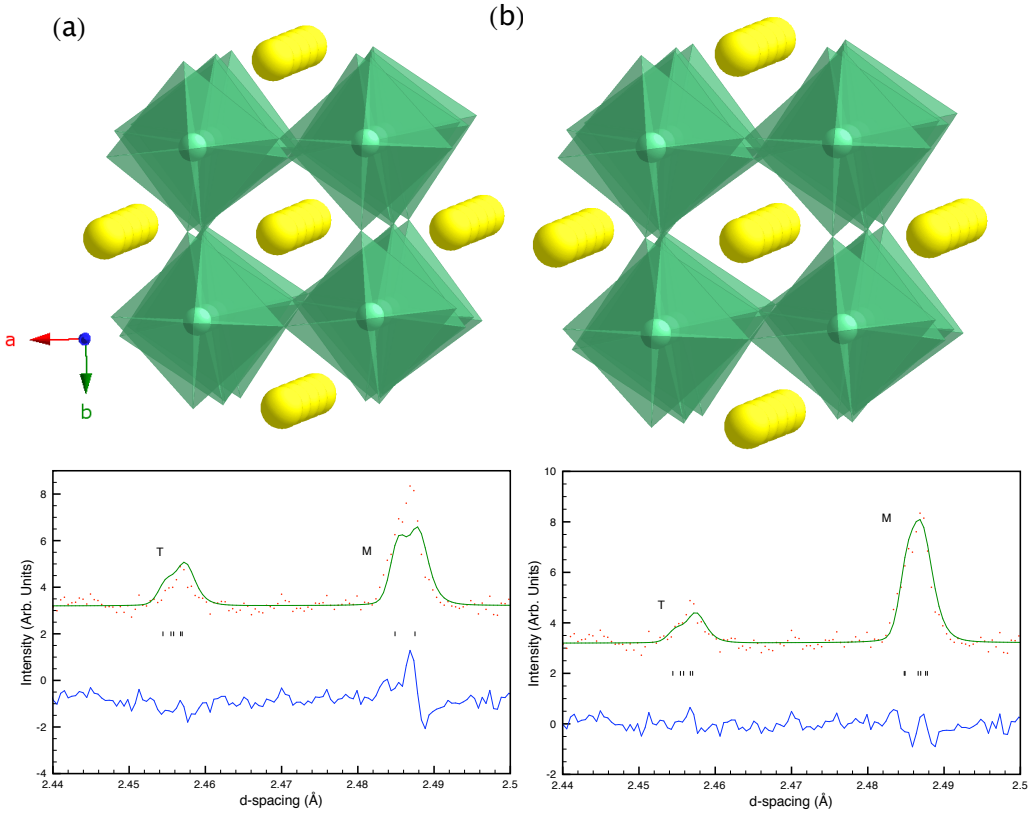

Figure 3.16: Representations of the crystal structures of phase S in space groups (a) *Cmmm* and (b) *Pmmn*. Both structures are viewed along the *c* axis. Corresponding expansions of the Rietveld profiles are shown under each, with the M- and T-point peaks labeled for clarification. For *Cmmm*, wRp = 5.4% and χ^2 = 2.28, and for *Pmmn*, wRp = 4.8% and χ^2 = 1.80, with the latter showing the better fit of the M-point peak. Additional details can be found in Appendix B.

When determining the structure of phase R, the same process was followed as for S. However, subtle differences are observed in the diffraction patterns for the two (Figs. 3.15(a) and 3.17). Most significantly, the positions of the T-point superlattice peaks are different, suggesting a $6a_p$ repeat unit along one axis and not $4a_p$. In such a unit cell, there are two distinct sets of T-points allowed, with *k* points (1/2, 1/2, 1/3) and (1/2, 1/2, 1/6), yet only the former are observed (with *l* = 2n peaks being present and *l* = 2n + 1 peaks being absent). With the T-point (1/2, 1/2, 1/3) being observable, there must be a simultaneous R_4^+ tilt mode to result in a further doubling of the cell (*i.e.,* give rise to a $6a_p$ unit).

Using symmetry mode decomposition (ISODISTORT), a number of possible structures were derived, being tetragonal $\sqrt{2}a_p \times \sqrt{2}a_p \times 6a_p$, primitive orthorhombic $\sqrt{2}a_p \times \sqrt{2}a_p \times 6a_p$, and C-centered orthorhombic $2a_p \times 2a_p \times 6a_p$. As with phase S, the simultaneous presence of both the M_3^+ and R_4^+ modes is required, and a systematic search through the possible options derived revealed that this was true for only two structures in each type of cell. As previously discussed, each of these options also included the $T_4(1/3)$ tilt modes and not the $T_4(1/6)$. An analysis of Fig. 3.17 confirms that phase R has peaks in the diffraction pattern corresponding to the $T_4(1/3)$ mode and not $T_4(1/6)$. All proposed models were refined and produced good levels of fit, but no one model gave a significantly better fit than the rest. However, close inspection of the M peak at d = 2.48 Å reveals a subtle peak splitting which was only accounted for in the C-centered orthorhombic $2a_p \times 2a_p \times 6a_p$ cells. However, these models produce a poorer fit of the T-point peaks, and so the logical conclusion was that the symmetry must be further lowered to the primitive $2a_p \times 2a_p \times 6a_p$ orthorhombic cell. Following a process similar to that used for phase S, two possible structures were proposed with space groups *Pmmn* and *Pnma*. Representations of the crystal structures of the two are shown in Fig 3.18, with corresponding crystallographic data in Appendix B. Unfortunately, it cannot be unambiguously stated that one structure is more likely to be correct than the other, based on diffraction data and symmetry mode analysis. Instead, attention was switched to first-principles calculations and solid-state NMR to determine if additional information could be obtained.

The forces acting upon individual atoms were also determined to gain insight into the stability of the phase (higher forces typically mean that atoms are not in the lowest energy position and structural optimisation may be required). It is worth noting again that all DFT structural optimisations are performed at 0 K and therefore do not include any temperature-dependent effects, such as thermal vibrations. Despite the shortcomings of the method when studying high-temperature structures, it has still been used as a complementary technique with the goal of providing additional insight, as most structures represent a local minimum on the potential energy surface and can

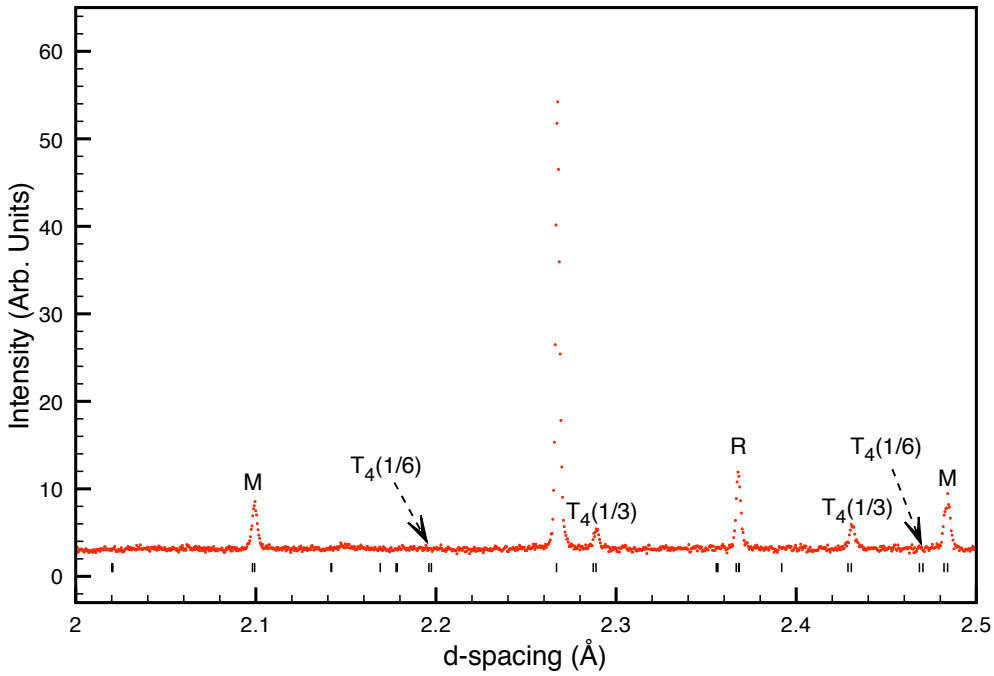

Figure 3.17: Portion of the NPD data obtained at 440 °C, showing the superlattice peaks at the M, R and T-points, as labelled, and it can be seen that the $T_4(1/6)$ peaks are absent. The figure is adapted from Ref. 17.

therefore be studied. It should be stressed that the DFT calculations alone are *not* used to form conclusions on the work presented. Single-point energy calculations showed two distinct trends, as shown in Table 3.9. Firstly, the five models proposed for phases R and S prior to DFT optimisation all had very similar energies, meaning that no one model seemed to be favoured significantly over another. Secondly, in all cases the energy of the structures was greater than that for phase T1. This was an unexpected result because the higher temperature phase (T1) might be expected to have the higher energy (a detailed discussion of this is given in Section 3.4.4). Analysis of the data shown in Table 3.9 shows that, while close in energy, the models proposed for phase R are generally lower in energy than those for phase S, as perhaps expected when considering the experimentally-observed series of phase transitions. However, it is difficult to say unambiguously which model for phases R and S is more favourable.

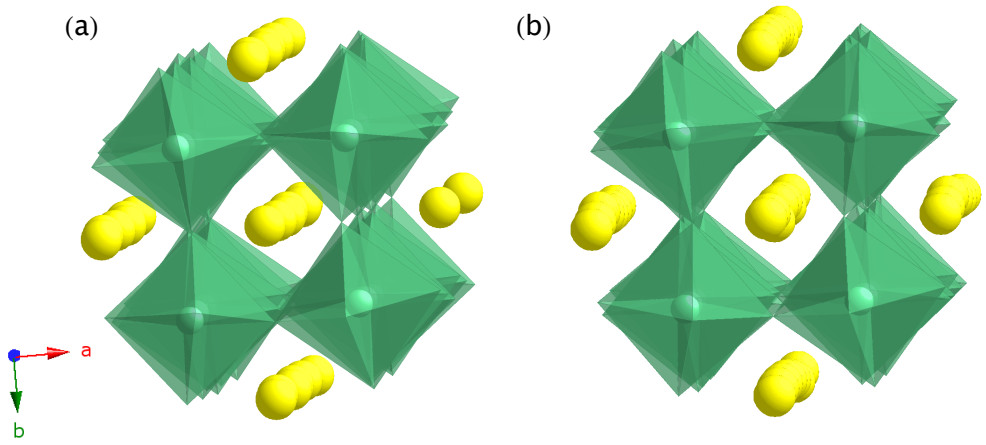

Figure 3.18: Crystal structures of phase R in space groups (a) *Pnma* and (b) *Pmmn*. Both structures are shown viewed down the *c*-axis. Yellow spheres represent Na^+ cations and green polyhedra represent NbO_6 octahedra. Differences in the octahedral tilting system can be seen, and the distortion modes present can be found in the main text and Ref. 17.

In a subsequent step, two sets of optimisations were performed on all 5 models - optimising just the fractional coordinates (Method 1) and both the fractional coordinates and lattice parameters (Method 2). As Table 3.9 shows, optimisation (Method 1) leads to lower energy structures for all models proposed, as expected, with full optimisations (Method 2) being even lower. When optimising the structures using Method 1, the forces acting upon the atoms are minimised, with all forces < 0.05 eV/Å. It should be noted that it is sometimes common to constrain the lattice parameters as inaccuracies in the GGA functional often lead to small overestimations in the unit cell lengths. The overall energy of the phases changed slightly, although energies for models for phase R are still lower energy than those for S. Interestingly, the models for phase R (*Pmmn* and *Pnma*), although very similar in energy, are now notably lower in energy (Method 1) than those for phase T1, in accordance with the order of phases observed experimentally as a function of temperature.

The proposed models retained the same octahedral tilting system along the *c*-axis (A0CA0C for phase R and A0C0 for S, where A is an anticlockwise tilt, 0 describes no relative tilt and C is a clockwise tilt). Crystallographic structures can be found in

Appendix B. Two exceptions to this can be found in Section 3.4.4. Re-analysis of the optimised models using ISODISTORT confirmed that there were no significant changes in the three distinct tilt modes – M_3^+, R_4^+ and T_4. The changes were extremely subtle but nonetheless sufficient to reduce the forces acting upon the atoms.

Table 3.9: Energies of the models proposed for phases R and S obtained from DFT energy calculations both pre- and post-optimisation. A * denotes that the model was obtained from the literature.[6] Data for phase T1 are shown solely for comparison to phases R and S.

Phase	Initial Energy / eV/f.u.	Optimised (Method 1) Energy / eV/f.u.	Optimised (Method 2) Energy / eV/f.u.
T1	–4381.12187	–4381.15174	–4381.15430
T1*	–4381.11988	–4381.15123	–4381.15478
S (*Pnma*)	–4381.08395	–4381.15867	–4381.16077
S (*Pmmn*)	–4381.08757	–4381.14632	–4381.14824
S (*Cmmm*)	–4381.09110	–4381.12916	–4381.14053
R (*Pmmn*)	–4381.10360	–4381.17750	–4381.18005
R (*Pnma*)	–4381.09806	–4381.17805	–4381.18305

Finally, all structures were optimised using Method 2 where both the unit cell parameters and atomic coordinates were allowed to vary. This allows any limitations of the refinement, such as inaccuracy in the unit cell parameters, to be overcome, *i.e.,* fixed unit cell parameters are no longer imposed on the DFT optimisation. It is worth noting, however, that in all cases, the unit cell volume increased (*i.e.,* overestimated relative to diffraction measurements) most likely due to inaccuracies in the GGA functional. Table 3.10 shows the unit cell volumes of the five models both before and after full optimisation using Method 2.

Table 3.10: Unit cell volumes of the initial and optimised (Method 2) models for phases R and S.

Phase and Model	Initial Cell Volume / Å^3	Optimised Cell Volume / Å^3	% Increase after Optimisation
R (*Pnma)*	1451.374	1463.728	0.85
R (*Pmmn)*	1451.374	1462.419	0.76
S (*Pnma*)	972.206	1032.442	6.20
S (*Pmmn*)	972.311	984.041	1.21
S (*Cmmm*)	972.208	973.874	0.18

As these optimisations are performed to lower the internal energy of the system, and not the Gibbs free energy, and no entropy effects or thermal vibrations are included, it is impossible to draw unambiguous conclusions from the data. Ideally, temperature and vibrational effects would be in included in the optimisations, but this requires specialist expertise in the field of DFT. This is considered further in Section 3.4.4. Additionally, the observation that some of the optimised structures (Method 2) have higher energies than phase T1 is unexpected, and is, again, most likely attributed to the absence of thermal and vibrational effects.

High-temperature ^{23}Na MAS NMR experiments were performed at 420 and 500 °C to obtain the spectra of phases R and S, respectively (spectra acquired over the full temperature range can be found at Fig. 3.19). DFT calculations of NMR parameters were performed on the optimised structures for each phase to simulate spectra and compare to those obtained experimentally. Unfortunately, there was little difference in the simulated spectra for models for phase R or S. This is most likely due to the slower spinning speeds used in the spectral simulation (4 kHz to match the experiment) and the high number of crystallographically-distinct Na sites causing multiple (6 or 8 distinct ^{23}Na sites, refer to Appendix B for crystallographic data of the structures) resonances to overlap. Unfortunately, ^{23}Na MQMAS experiments, needed to provide high-resolution spectra, could not be obtained experimentally at these temperatures. Figs. 3.19 and 3.20 show the experimentally-obtained and simulated NMR spectra, respectively, with corresponding NMR parameters for the

simulated spectra given in Appendix B. As Fig. 3.20 shows, the simulated spectra for phase R (*Pmmn* and *Pnma*) are very similar to one another and in reasonable agreement with the experimentally-obtained spectrum shown in Fig. 3.19 (red line). Both simulated spectra equally match the experimental spectrum, and so it cannot be said that one model is favoured over another. For phase S, the model favoured by Peel *et al.*[17] shows good agreement between the simulated and experimentally-observed NMR spectra, with a narrower linewidth being observed compared to phase R. Additionally, Fig. 3.19 (green line) shows that a broader resonance is present in the spectrum, and can be seen to the right-hand side of the peak. This is in excellent agreement with the calculated NMR parameters for the *Pmmn* model for phase S, which also shows that a broad resonance is present. Unfortunately, owing to the overlapping of the resonances in the experimentally-obtained spectrum, it is not possible to determine the isotropic shifts and quadrupolar couplings of the individual resonances, nor is it even possible to determine the number of crystallographically-distinct sites. To gain more insight into the structures, ^{23}Na high-resolution MQMAS spectra could be acquired at high-temperature in the future.

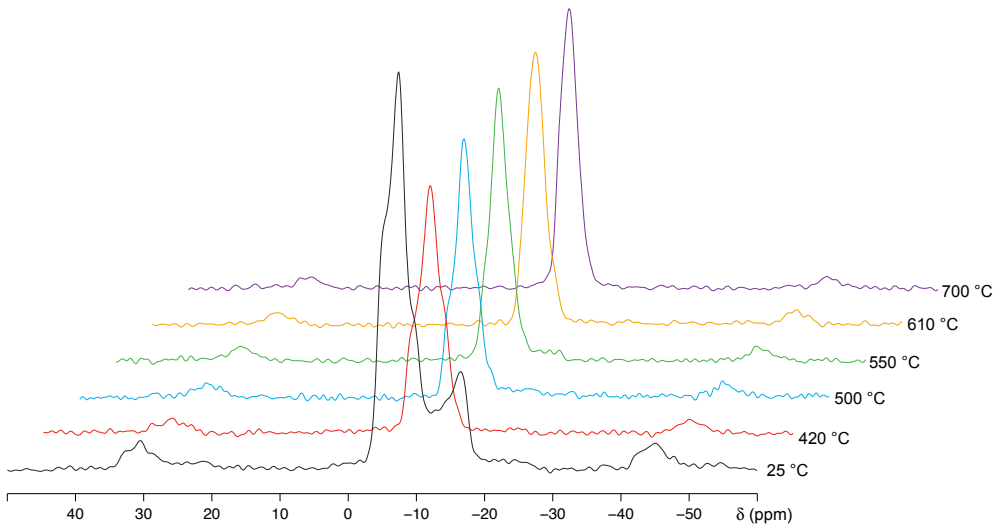

Figure 3.19: ^{23}Na (9.4 T) MAS NMR spectra of the different phases of $NaNbO_3$, with each spectrum obtained at a different temperature, labelled in the figure. Phase P is black, R is red, S is blue, T1 is green, T2 is yellow and U is purple.

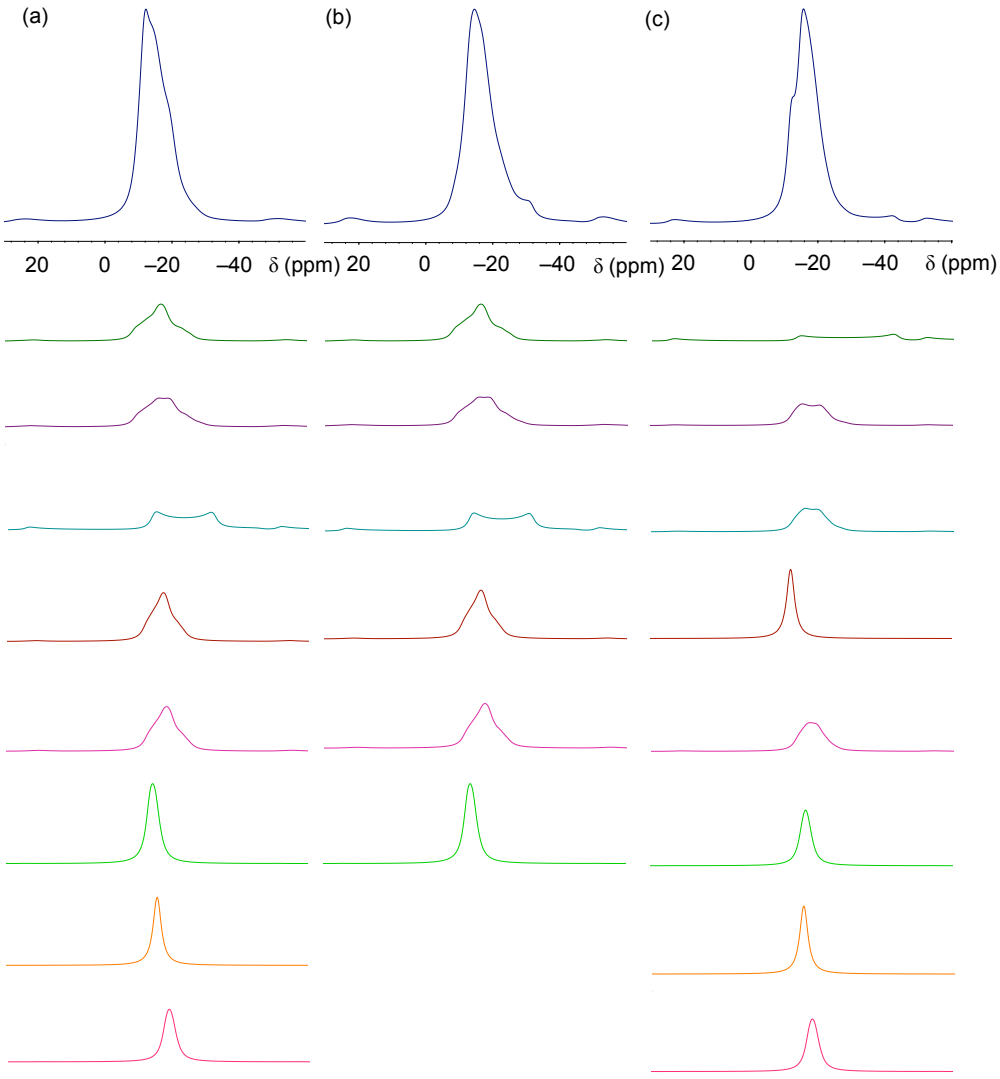

Figure 3.20: Simulated ^{23}Na (9.4 T) MAS (4 kHz) NMR spectra of (a) R-*Pmmn*, (b) R-*Pnma* and (c) S-*Pmmn*. Simulations of the individual sites are shown below each spectrum (not normalised) to show the 'broad' and 'sharp' sites. The site numbers increase from top-to-bottom, with corresponding NMR parameters given in Appendix B. The very broad resonance in S-*Pmmn* (site 1) is readily observed, with no evidence for this in the experimentally-obtained spectrum (Fig. 3.19).

3.4.3. Review of the temperature-dependent phase diagram

It was shown in Table 3.8 that various structures have been proposed for phases R and S, with work presented by Peel *et al*.[17] offering the most comprehensive crystallographic study to date. For phase S, proposed by Ahtee, a full refinement was not carried out and an assumption made that the Nb^{5+} cations did not displace from the centre of their octahedra. Whilst both the M- and R-modes were present, the subtle T_4 tilting mode was not included and consequently the additional expansion along the *c*-axis was not considered.[25] Work presented by Darlington and Knight[22] and by Mishra[24] suggested new structures for both phases R and S. The former presented much more complex supercells, attributed to weak reflections in the NPD data, which was possibly caused by the co-existence of phases P and Q in the starting material (*i.e.*, before heating). For the work presented by Mishra,[24] it can be seen that the diffraction patterns (NPD data) are much poorer resolution than those presented by Peel *et al*.,[17] and therefore some of the subtle distortions are missed from their proposed structures. By incorporating the work presented in this chapter with Ref. 17, a new temperature-dependent series of phase transitions is proposed, as shown in Table 3.12.

Table 3.12: Revised series of temperature-dependent phase transitions of $NaNbO_3$ based on the prior literature and the current work. Small, medium and large refer to the relative magnitudes of the pseudocubic subcell axes, *a, b* and *c* refer to the crystallographic axes. The Δ_5 and Γ_4^- modes are cation displacements. This table is adapted from Ref. 17, where additional information can be found. Crystallographic data for each of the phases can be found in Appendix B.

Phase	Space group	Small	Medium	Large
U	*Pm-3m*			
T2[29]	*P4/mbm*			*c* (M_3^+)
T1[25]	*Cmcm*	*a* 0	*b* (R_4^+)	*c* (M_3^+)
S (this work)	*Pmmn*	*a* (M_3^+)	*c* R_4^+ T_4	*b* (M_3^+)
R (this work)	*Pmmn*	*a* (M_3^+)	*b* T_4	*c* (R_4^+)
	Pnma	*b* (M_3^+)	*c* T_4	*a* (R_4^+)
P[8]	*Pbcm*	*a* (R_4^+), Δ_5(Na,Nb)	*c* T_4	*b* R_4^+, Δ_5 (Na,Nb)
N[30]	*R3c*	R_4^+ Γ_4^-	R_4^+ Γ_4^-	R_4^+ Γ_4^-

3.4.4. Discussion

The main purpose of performing DFT calculations and obtaining high-temperature NMR spectra of $NaNbO_3$ was to corroborate and expand on the previous work that focused primarily on results obtained from diffraction and symmetry mode analysis. Two unexpected observations were found with the DFT investigation of $NaNbO_3$: firstly, as discussed in Section 3.4.2, two of the models changed significantly upon optimisation using Method 1 and, secondly, the calculated order of the phases (*i.e.,* from low to high-temperature) is different from the experimental observation. Both of these findings are discussed below in detail. After geometry optimisation of the *Pmmn* models for phases R and S using Method 1, it was observed that a significant change in structure had occurred. In both cases, the structure optimised to one with a 2-repeat unit (instead of the 6- or 4-repeat), which adopted the clockwise-anticlockwise (CA)

tilt system, as shown in Fig. 3.21. In addition to the change in tilt system, pronounced distortions in the octahedra were also observed, as shown in Table 3.13, which compares the Nb-O bond lengths for the initial and optimised structures. It was observed that the initial Nb-O bond lengths were all relatively similar (1.984 – 1.992 Å for phase R and 1.968 – 1.981 Å for phase S), suggesting that the octahedra were not significantly distorted, compared to a value of 1.970 Å for the cubic phase. After optimisation (Method 1), however, the bond lengths changed significantly, resulting into two distinct 'groups' being formed. Three 'short' and three 'long' bonds were observed for each model, where phase R had Nb-O bond lengths of 1.871 – 1.912 Å and 2.084 – 2.162 Å, and phase S 1.883 – 1.905 Å and 2.079 – 2.138 Å. The resulting tilt systems were similar to that observed for the low-temperature $NaNbO_3$ rhombohedral phase N, having space group *R*3*c* (corresponding to Glazer tilt system $a^-a^-a^-$), as shown in Fig. 3.22. A model for this structure was optimised using Method 1, which gave 3 Nb-O bond lengths of 1.886 and 3 of 2.147 Å, which correspond to the 'short' and 'long' bonds observed for the *Pmmn* models. The distortion of the NbO_6 octahedra during optimisation is shown in Fig. 3.23 for the phase S model, which shows distinct changes in the geometry of the octahedra and significant changes in the Nb-O bond lengths. In addition, it can be seen that the three bonds that increase in length are all on the same face of the octahedron, *i.e.,* one axial and two equatorial bonds, similar to *fac*-isomerism. This most likely occurs due to a displacement of the Nb cations and not because of a unilateral expansion or contraction of the NbO_6 octahedra. This type of displacement is also observed in phase N.

When the optimised models for phases R and S resulted in a structure closely resembling the low-temperature phase N (*R*3*c*) it was an unexpected result. Intuitively, one may expect an energy barrier to be present, which would prevent such a transformation from one polymorph to another, as was the case for models with space groups *Cmmm* and *Pnma* (see earlier). This suggests that some models had a smaller energy barrier to phase interconversion than others, with models with space group *Pmmn* having a lower barrier. The changes in energy for the optimisation steps

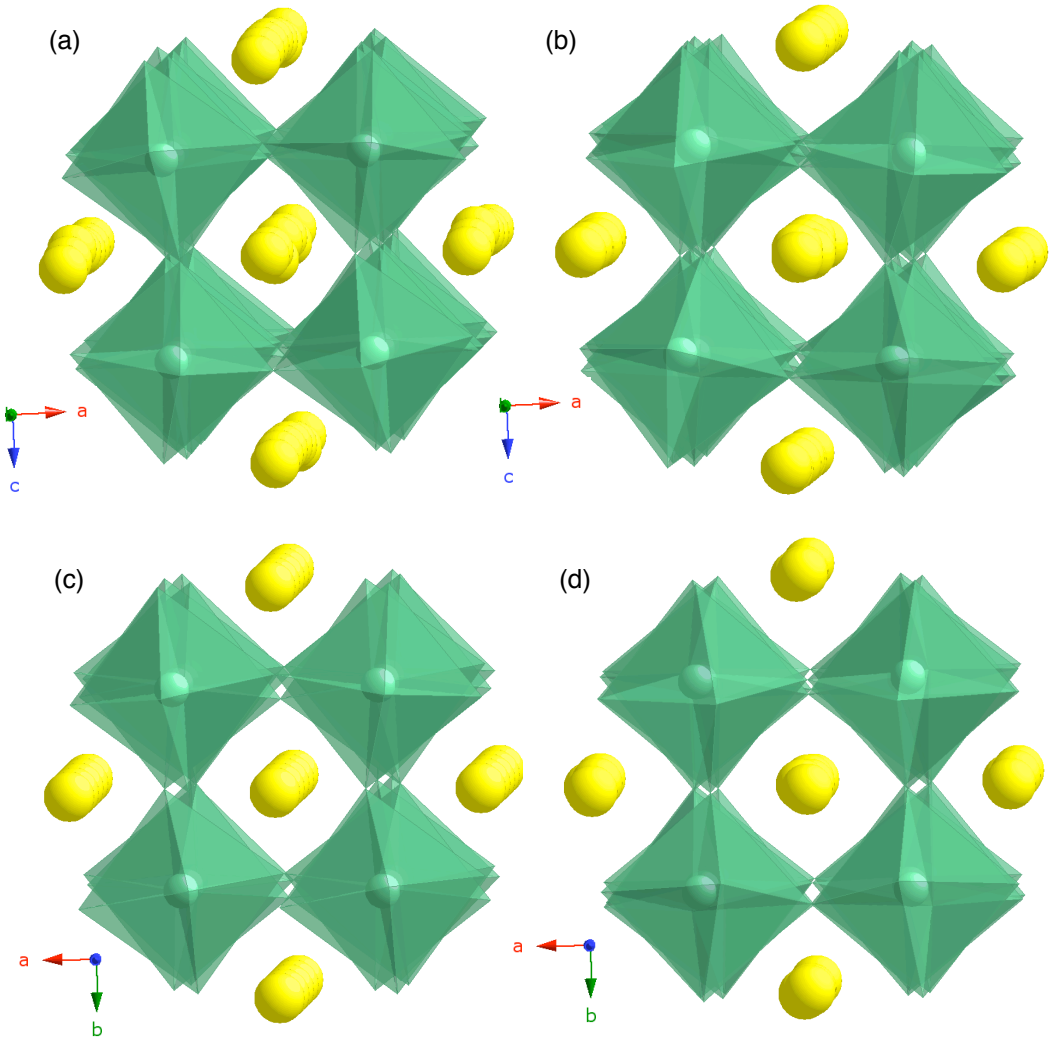

Figure 3.21: Crystal structures of (a) initial and (b) optimised (Method 1) models for phase R (space group *Pmmn*) and (c) initial and (d) optimised (Method 1) models for phase S (space group *Pmmn*). In both cases, the 4- or 6-repeat unit became a two-repeat unit.

Table 3.13: Nb-O bond lengths for the phase S (*Pmmn*) model before optimisation, mid-way through at the first plateau (see Fig. 3.24) and at the end of the optimisation (Method 1). For comparison, the Nb-O bond lengths for the rhombohedral *R*3*c* phase are also shown.

Nb-O Number	Initial / Å	First plateau / Å	Optimised / Å	*R*3*c* phase / Å
1	1.974	1.966	1.899	1.886
2	1.981	1.990	1.905	1.886
3	1.968	1.994	1.883	1.886
4	1.974	1.976	2.113	2.147
5	1.981	1.991	2.079	2.147
6	1.968	1.995	2.138	2.147

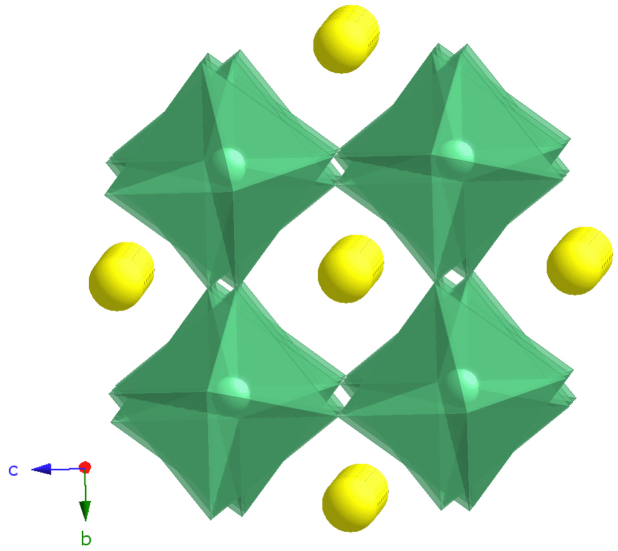

Figure 3.22: Crystal structure of phase N (*R*3*c*) of $NaNbO_3$, showing the AC tilt system (Glazer system $a^-a^-a^-$) as viewed down the a-axis. It can be seen that this tilt system is adopted for phases R and S (*Pmmn*) when optimised using Method 1.

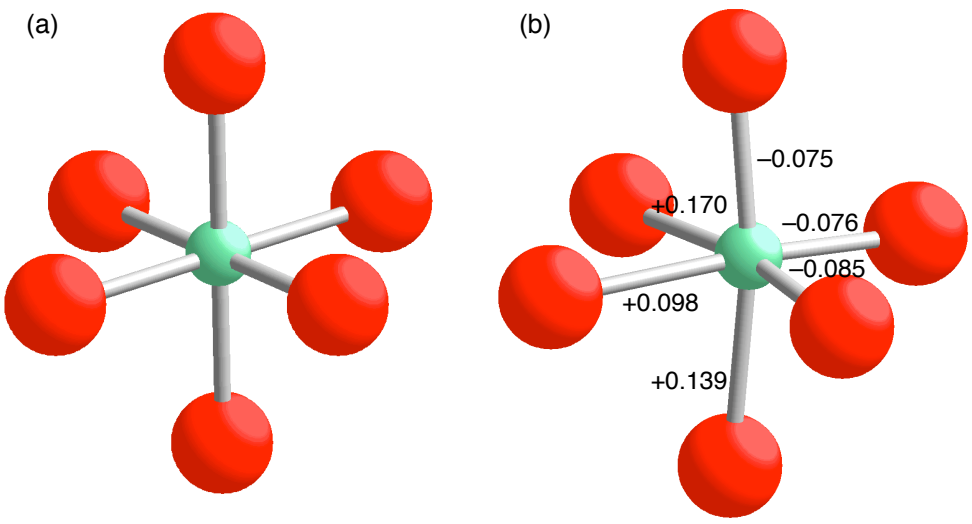

Figure 3.23: NbO_6 octahedra (green spheres are Nb^{5+} cations and red are O^{2-} anions) for phase S (*Pmmn*) (a) prior to optimisation and (b) following optimisation using Method 1. The Nb-O bond lengths have all changed after optimisation, and the magnitude of the change is labelled next to each bond. All values given are in Å.

(how the energy changes during each cycle of the optimisation) were then analysed. Fig. 3.24 shows the changes in energy during the optimisation, in which two distinct energy features can be seen. The first plateau (Region 1) corresponds to a local energy minimum, and the final minimum (Region 2), most likely to the global minimum at 0 K. The structure at this point corresponds to phase N (the lowest-energy phase of $NaNbO_3$). However, the first plateau corresponds to the optimised model (still *Pmmn*) where the 4- or 6-repeat unit is preserved, alongside the tilt system and uniform Nb-O bond lengths. The optimised bond lengths for the first plateau are given in Table 3.13, which show that they are very similar to the initial values and do not contain the 3 'short' and 'long' bonds which characterise phase N. Fig. 3.25 shows the optimised structures corresponding to a point in Region 1. These structures can be seen to be very similar to the initial ones, *i.e.*, there is no change in the observed octahedral tilting system. The very subtle differences in the energies of the phases and the apparent low-energy barrier to phase interconversion suggests that the different

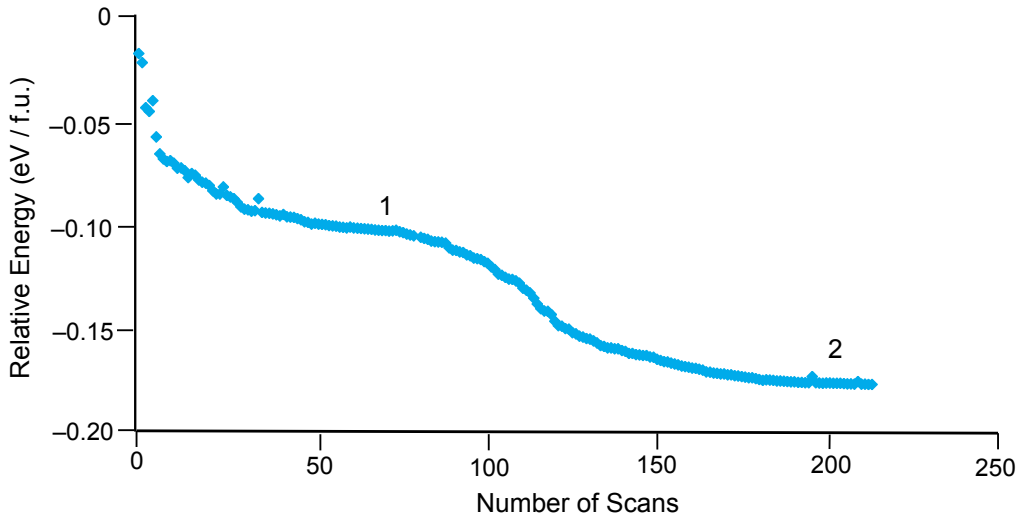

Figure 3.24: Profile following the energy for the DFT optimisation (Method 1) of phase S (space group *Pmmn*), showing an intermediate plateau (Region 1) where the initial tilt system is retained, followed by final convergence to a model isostructural with phase N of $NaNbO_3$ (Region 2).

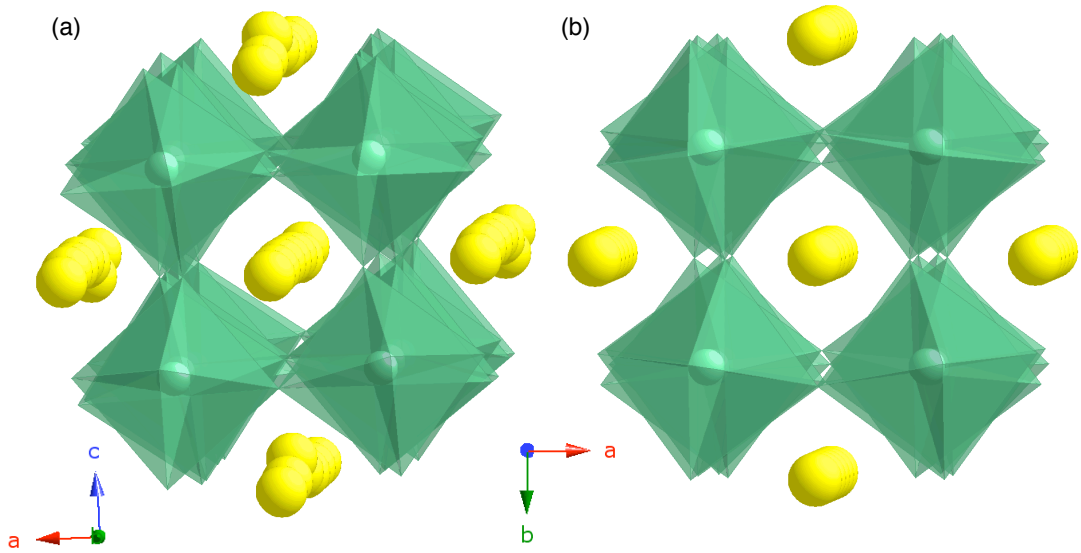

Figure 3.25: Crystal structure of (a) phase R (*Pmmn*) and (b) phase S (*Pmmn*) when optimised using Method 1. The structures correspond to the labelled intermediate plateau in the energy curve.

phases are inextricably linked, most likely attributed to the displacive nature of the phase transitions.

The experimentally-observed order of phases as a function of temperature does not match that from DFT optimisations (using both Methods 1 and 2). This is shown in Fig. 3.26, in which the energies of all the phases are shown prior to and after optimisation using both Methods 1 and 2. When considering the initial structures, it is immediately apparent that structural optimisation is required, given the high forces on the atoms, and the relatively high energy of phase Q, which upon optimisation significantly reduces to a value similar to that of phase P. Optimisation using Method 1 produces data more consistent with that observed experimentally. The energies of phase N, P and Q are the lowest, yet are so similar that it is not possible to say which is definitively the lower energy. However, after a full optimisation, phase N is noticeably the lowest, with phases P and Q higher, yet similar to one another. Both models for phase R have higher energies than phases P and Q, yet lower than phases S and T1, as observed experimentally. Unfortunately, the different models for this phase were still so similar in energy that no one could be said to be favoured over the other. It is when considering the energies of phases S, T1 and T2 that the main differences between the DFT and experimental results are noticeable. The proposed models for phase S differ significantly in energy, with *Pnma* being the lowest and *Cmmm* the highest (greater than phases T1 and T2). Whilst this may represent the true situation, it is also necessary to consider the importance of temperature in DFT calculations. DFT optimisations are principally based on reducing the internal energy, U, of the system, where U is not temperature dependent. However, the order of the phases observed experimentally is dependent upon the Gibbs free energy, ΔG, which contains the temperature-dependent term $T\Delta S$. At low temperatures, the effect of the $T\Delta S$ term is minimal and ΔG is dominated by ΔH (related to ΔU at constant pressure and volume). However, at high-temperature, this term becomes more dominant and has a larger effect on ΔG, which is not accounted for in simple DFT calculations. The

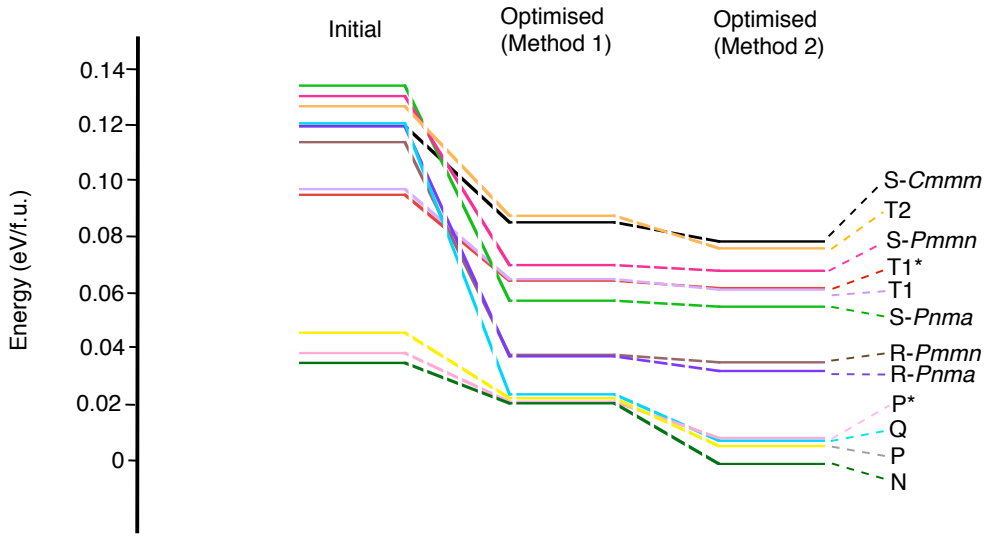

Figure 3.26: Initial and calculated energies of various phases of $NaNbO_3$. P* and T1* refer to literature-based models, given in Refs. 8 and 6, respectively. Dashed lines are a visual guide only.

structures may be stabilized by high temperature, low energy vibrations which are not included in the DFT optimisations. Consequently, it is difficult to compare DFT and experimentally-observed results for high temperature phases but it does help to understand the differences observed. Temperature and vibrational corrections could be incorporated into the optimisations of the high-temperature phases, although this would require significant computational cost, time and expertise. Although beyond the scope of the current work it presents an intriguing possibility for the future.

3.5. Conclusions

Using a combination of solid-state NMR and diffraction techniques, it has been shown that at least two phases of $NaNbO_3$ exist at room temperature, where the relative fractions of the two can be manipulated by modification of the synthetic route. Sol-gel techniques provide the best route to the synthesis of the polar phase Q, although additional heating has been shown to convert this into the centrosymmetric phase P, suggesting that the latter is the more thermodynamically stable of the two. In addition to phases P and Q, it has also been shown that a third polymorph may exist.

This polymorph is believed to be structurally similar to phases P and Q as there is no obvious evidence for its existence in diffraction data and its NMR parameters are very similar to those of the other two polymorphs.

The higher-temperature phases R and S have been suggested to possess 6- and 4-repeat units - these were the minimum cell metrics required to fully index the diffraction patterns. DFT calculations were performed on multiple models for each phase to determine which were the lowest energy, and to see if one model could be favoured over another. These high-temperature phases are most likely stabilised by thermal vibrations, although these effects are not included in DFT optimisations, which are all performed as though the structure were at 0 K. It is worth noting that for structures proposed at any one specific temperature (*e.g.,* models for phase R *or* phase S), the (lack of) inclusion of temperature-dependent effects, such as thermal vibrations, would have a much smaller effect than when comparing structures between different phases, *e.g.,* R-*Pmmn* and S-*Pmmn*. However, as each proposed structure would be affected differently (in terms of Gibbs energy) by the inclusion of temperature effects, it stands to reason that the order of these phases observed from DFT may not necessarily support the experimentally-observed phase diagram. While it is possible to include such corrections, it was beyond the scope, and expertise, of this work. Complementary ^{23}Na MAS NMR spectra of the phases of $NaNbO_3$ showed a reduction in linewidth as a function of temperature, most likely owing to an increase in the symmetry of the structures. Unfortunately, it was not possible to determine the number of crystallographically-distinct ^{23}Na sites from these spectra, owing to overlapping resonances. Whilst, theoretically, ^{23}Na MQMAS experiments would provide this information, these are difficult to obtain at high temperature. DFT optimisations of some structures led to a transition to the low-temperature phase N (or, at least, to something isostructural with the same tilt system and energy), which suggests that $NaNbO_3$ has very small energy barriers to phase interconversion, which in turn helps one to understand the temperature-dependent phase behaviour observed in $NaNbO_3$.

References

[1] Lines, M. E., Glass, A. M., Principles and applications of ferroelectrics and related materials, Oxford University Press, Oxford, 1977.

[2] Saito, Y., Takao, H., Tani, T., Nonoyama, T., Takatori, K., Homma, T., Nagaya, T., Nakamura, M., *Nature,* 2004, **432**, 84.

[3] Glazer, A. M., Megaw, H. D., *Acta Cryst.,* 1973, **A29**, 489.

[4] Glazer, A. M., Ahtee, M., Megaw, H. D., *Acta Cryst.,* 1972, **A28**, 179.

[5] Lefkowitz, I., Lukaszewicz, K., Megaw, H. D. *Acta Cryst*., 1966, **A20**, 670.

[6] Darlington, C. N. W., Knight, K. S., *Acta Cryst*., 1999, **B55**, 24.

[7] Rodel, J., Jo, W., Seifert, K. T. S., Anton, E. M., Granzow, T., Damjanovic, D., *J. Am. Ceram. Soc.,* 2009, **92**, 1153.

[8] Sakowski-Cowley, A. C., Lukaszewicz, K., Megaw, H. D. *Acta Cryst*., 1969, **B25**, 851.

[9] Shuvaeva, V. A., *Ferroelectrics,* 1993, **141**, 307.

[10] Ahtee, M.; Glazer, A. M., *Acta Cryst.,* 1976, **A32**, 434.

[11] Johnston, K. E., Tang, C. C., Parker, J. E., Knight, K. S., Lightfoot, P., Ashbrook, S. E., *J. Am. Chem. Soc.,* 2010, **132**, 8732.

[12] Konieczny, K., Śmiga, W., *Ferroelectrics,* 2011, **417**, 151.

[13] Atamanik, E., Thangadurai, V., *Mater. Res. Bull.,* 2009, **44**, 931.

[14] Glazer, A. M., *Acta Cryst.,* 1972, **B28**, 3384.

[15] Zhang, N., Glazer, A. M., Baker, D. W., Thomas, P. A., *Acta Cryst.,* 2009, **B65**, 291.

[16] García-Fernández, P., Ghosh, S., English, N. J., Aramburu, J. A., *Phys. Rev. B.,* 2012, **86**, 144107.

[17] Peel, M. D., Thompson, S. P., Dauod-Aladine, A., Ashbrook, S. E., Lightfoot, P., *J. Inorg. Chem.,* 2012, **51**, 6876.

[18] Bak, M., Rasmussen, J. T., Nielsen, N. C., *J. Mag. Res.*, 2000, **147**, 296.

[19] Ashbrook, S. E., Le Polles, L., Gautier, R., Pickard, C. J., Walton, R. I., *Phys. Chem. Chem. Phys.,* 2006, **8**, 3423.

[20] Modeshia, D. R., Darton, R. J., Ashbrook, S. E., Walton, R. I., *Chem. Comm.,* 2009, **1**, 68.

[21] Sakowski-Cowley, A. C., Ph.D. Thesis, University of Cambridge, 1967.

[22] Orobengoa, D., Capillas, C., Aroyo, M. I., Perez-Mato, J. M., *J. Appl. Crystallogr.* 2009, **42**, 820.

[23] Campbell, B. J., Stokes, H. T., Tanner, D. E., Hatch, D. M., *J. Appl. Crystallogr.* 2006, **39**, 607.

[24] Howard, C. J., Stokes, H. T., *Acta Crystallogr.*, 1998, **B54**, 782.

[25] Darlington, C. N. W., Knight, K. S., *Physica B.,* 1999, **266**, 368.

[26] Koruza, J., Tellier, J., Malic, B., Bobnar, V., Kosec, M. J., *Appl. Phys.*, 2010, **108**, 113509.

[27] Mishra, S. K., Mittal, R., Pomjakushin, V., Chaplot, S. L., *Phys. Rev. B.*, 2011, **83**, 134105.

[28] Ahtee, M., Glazer, A. M., Megaw, H. D., *Philos. Mag.*, 1972, **26**, 995.

[29] Glazer, A. M., Megaw, H. D., *Philos. Mag.*, 1972, **25**, 1119.

[30] Darlington, C. N. W., Megaw, H. D., *Acta Cryst.*, 1973, **B29**, 2171.

Chapter 4

The Phase Behaviour of K-Substituted $NaNbO_3$

4.1. Introduction

$NaNbO_3$ is one of the most complex perovskites known, in terms of its rich polymorphism and temperature-dependent phase transitions.[1] One of its room temperature polymorphs, phase P, belongs to the centrosymmetric space group *Pbcm,* which is not polar. Most of the initial work on $NaNbO_3$ has focused on characterising phase P and its phase transitions, using diffraction techniques.[2,3] Substitution of sodium for small amounts of other Group I metals, such as lithium or potassium, has been shown to result in the formation of phase Q - an orthorhombic polar phase, with non-centrosymmetric space group $P2_1ma$.[4,5] Additionally, this phase can be stabilised without chemical doping in the presence of a strong electric field.[6]

Potassium sodium niobate ($K_xNa_{1-x}NbO_3$, referred to as KNN) solid solutions have been well-studied in the literature, with the focus of research on materials with around 50% K^+ substitution, where a morphotropic phase boundary exists. Much of the work on the modification of $NaNbO_3$ to produce the polar phase has centred on the substitution of Na^+ for K^+,[7,8] and subsequent characterisation using diffraction techniques. However, much smaller amounts of substitution have been shown to produce materials with good piezoelectric properties which may make them suitable lead-free alternatives to the currently-available Pb($Zr_xTi_{1-x}NbO_3$), PZT.[9,10] More recent work, using a combination of diffraction and solid-state NMR spectroscopy[11] has shown that the presence of Phase Q in samples of pure $NaNbO_3$ is also influenced by the synthetic approach. Some recent work has shown that phase Q may actually belong to the monoclinic space group *Pm*, *via* the observation of a subtle distortion in the β angle.[12] Using Glazer notation,[13] the *Pm* monoclinic phase adopts the $a^-b^+c^-$ tilt system, compared with the $a^-b^+a^-$ tilt for the $P2_1ma$ space group. Work by Thomas,[12] however, has shown that there is a region of phase co-existence around RT for low-level doping ($x < 0.06$) whereby both monoclinic and rhombohedral phases have been

reported to exist. The rhombohedral phase (space group *R*3*c*) adopts the $a^-a^-a^-$ Glazer tilt system, and is isostructural with the low-temperature phase N of $NaNbO_3$.

Similar to $NaNbO_3$, KNN undergoes a series of complex temperature-dependent phase transitions, for which ambiguity exists in the literature regarding the different structures, regions of phase co-existence and temperatures of the phase transitions. There have been some attempts to fully characterise the phase diagram of KNN,[12,14] yet the series of different phases, as a function of composition, still appears to be relatively poorly understood. In the initial work by Ahtee and Glazer,[7] phase Q was reported to undergo a transition at approximately 270 °C to phase "G" and be stable up to 400 °C, varying slightly with the value of x ($0.02 \leq x \leq 0.10$). Above this temperature, transitions were observed between phases R, S, T1, T2 and U, which are analogous to the high-temperature phases of $NaNbO_3$ discussed in Chapter 3 of this work.[15,16] The phase diagram proposed by Ahtee and Glazer is given in Fig. 1.8. Thomas *et al.* provided a phase diagram showing that the structure may be tetragonal (space group *P*4*bm*) at around 400 °C before becoming cubic at approximately 520 °C (where $x < 0.10$). However, in both cases, it is reported that regions of phase co-existence occur, making accurate structural determination much more challenging.

Lithium sodium niobate ($Li_xNa_{1-x}NbO_3$, referred to as LNN) solid solutions have also been studied previously,[17] and it has been shown that small amounts of Li substitution ($0 < x < 0.08$) result in phase Q being observed, with space group $P2_1ma$.[18] Interestingly, no regions of phase co-existence have been reported for the LNN system where $0.01 < x < 0.08$ (although they have been observed for higher values of x - see Chapter 5).[19,20] High dielectric constants have been reported for phase Q of LNN,[21] dependent upon the value of x.

This chapter will be divided into two sections. Firstly, the characterisation of KNN phase Q will be discussed, showing the effects of K^+ substitution in $NaNbO_3$. Data will be contrasted with Li^+ substituted analogues, LNN, to show the different effects the two dopants have on the structure. The structures are characterised using complementary combinations of solid-state ^{23}Na and ^{39}K NMR, X-ray and neutron powder diffraction and DFT calculations. ^{23}Na MQMAS NMR spectra of LNN phase Q show two distinct resonances, as expected, whereas spectra of KNN suggest that at

least one additional resonance may also be present that is not attributed to phase Q. DFT calculations for disordered structural models are used to determine if there is a site preference for substitution, *i.e.*, if the cations preferentially dope onto Na site 1 or 2, and ^{39}K MAS NMR experiments were also performed to determine if a site preference is suggested. Secondly, the high-temperature behaviour of phase Q for samples of KNN (x = 0.03 and 0.05) will be explored using both synchrotron X-ray and neutron powder diffraction, which is complemented by symmetry mode analysis. An analysis of phase G is also undertaken and a new model for the structure is proposed. It is shown that this phase undergoes a transition at approximately 380 °C to an orthorhombic structure, where the minimum cell metric required to fully index the pattern is $2a_p \times 2a_p \times 6a_p$, similar to the structures discussed in Chapter 3 for $NaNbO_3$.

4.2. Solid-State NMR and Simulations

Solid-state ^{23}Na (I = 3/2) NMR spectra were acquired using Bruker Avance III spectrometers, equipped with wide-bore 14.1 or 9.4 T magnets, at Larmor frequencies of 158.746 and 105.842 MHz, respectively. Samples were packed into conventional ZrO_2 (4 mm) rotors and rotated at a MAS rate of 12.5 kHz. ^{23}Na chemical shifts were referenced to 1 M $NaCl_{(aq)}$ using a secondary reference of $NaCl_{(s)}$ (δ_{iso} = 7.8 ppm). Conventional ^{23}Na MAS NMR spectra were obtained using single-pulse experiments, with pulse lengths of 1.5 and 1.9 μs, at 14.1 and 9.4 T, respectively, with a recycle interval of 5 s. All MQMAS spectra were acquired using a z-filtered pulse sequence (see Fig. 2.21). High power pulses (of 5 and 1.5 μs with $\omega_1/2\pi$ = 100 kHz at 9.4 T and 6 and 1.9 μs with $\omega_1/2\pi$ = 95 kHz at 14.1 T) were used for triple-quantum excitation and conversion, respectively. The final 90° pulse was applied with low power ($\omega_1/2\pi \approx$ 9 kHz at both fields) to be selective for the CT. All z-filtered MQMAS NMR spectra are shown post shearing and are all the result of averaging 192 transients for each of 80 t_1 increments of 80 μs with a 5 s recycle interval. ^{39}K MAS NMR experiments were performed at 20.0 T, with a Larmor frequency of 39.670 MHz, at room temperature. Chemical shifts were referenced to 1 M $KCl_{(aq)}$ using a secondary reference of $KNbO_{3(s)}$ (δ_{iso} = 57.0 ppm). All spectra were recorded with a MAS rate of 12.5 kHz and a recycle interval of 30 s, with a pulse length of 10.0 μs ($\omega_1/2\pi \approx$ 40 kHz) used for conventional single-pulse experiments. Additional experimental details

can be found in the relevant figure captions or sections.

First-principles calculations were performed using the CASTEP DFT code[22] - a planewave pseudopotential method using the gauge-including projector-augmented wave (GIPAW) formalism.[23] Crystallographic structures suitable for optimisation were obtained from the Inorganic Crystal Structure Database[24] and Rietveld refinement of results within this thesis. Specific details of calculations can be found in Chapter 2.

4.3. Phase Q at Ambient Temperature

4.3.1. Solid-State NMR Results

Initial work focused on synthesising and characterising samples of $K_xNa_{1-x}NbO_3$, where x = 0.02 - 0.05 and 0.08 (denoted KNN-2, KNN-3, KNN-4, KNN-5 and KNN-8, respectively). For each sample, s-PXRD data were obtained and Rietveld refinements performed to try and determine the correct structural assignment. Unfortunately, it was not possible to reliably ascertain the correct space group or even if the structure is orthorhombic or monoclinic. Refinements in both $P2_1ma$ and Pm space groups were equally satisfactory. An overview of the work performed, along with the data, refinements, and goodness of fit parameters can be found in Appendix C.

To gain additional structural information regarding phase Q, complementary solid-state ^{23}Na NMR experiments were performed on the KNN samples. ^{23}Na z-filtered MQMAS NMR spectra were obtained for KNN-2 and KNN-3, as shown in Fig. 4.2. For KNN-2, two resonances can be observed, with $\langle\delta_{iso}\rangle$ = –5.0 and –1.3 ppm, and $\langle P_Q\rangle$ values of 1.1 and 2.4 MHz, respectively. These values are in excellent agreement with those obtained for phase Q of $NaNbO_3$, given in Chapter 3. Slight differences in the isotropic shifts between KNN and $NaNbO_3$ most likely arise from subtle changes in the local structure, *i.e.,* substitution of Na^+ for K^+ leads to small shift changes. For KNN-3, average isotropic shifts of –5.2 and –1.7 ppm are obtained, again with the small differences (compared to KNN-2) arising from changes in the nature of nearby atoms. The inclusion of a small amount of potassium appears to

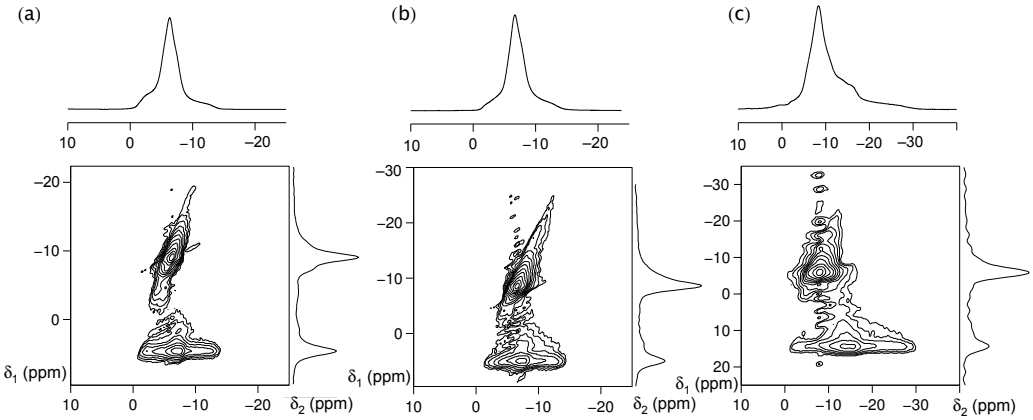

Figure 4.2: ^{23}Na z-filtered MQMAS NMR spectra of (a) KNN-2 at 14.1 T, (b) KNN-3 at 14.1 T and (c) KNN-3 at 9.4 T.

stabilise the polar $P2_1ma$ polymorph (assuming for now it is $P2_1ma$ and not $P1m1$ (*Pm*), where the latter option is discussed later) as opposed to phase P (*Pbcm*). The larger size of the K^+ cation (r_{K^+} = 1.51 Å and r_{Na^+} = 1.02 Å, for six-coordinate cations) may cause a change in the octahedral tilting system. The K^+ cation is sufficiently large as to be able to reduce the amount of tilting possible for the NbO_6 octahedra compared to Na^+, *i.e.,* the argument is one of steric hindrance. By preventing phase P from adopting the AACC (A = anticlockwise and C = clockwise tilt) tilt system, the tilt system of the $P2_1ma$ phase is instead adopted (AC, or $a^-b^+a^-$ in Glazer notation).

Additional z-filtered MQMAS NMR spectra were also obtained for KNN-4 and KNN-5 at 14.1 T, and as for KNN-3, two major resonances were observed, and a third broader 'resonance,' as shown in Fig. 4.3 (δ_1 = 1 ppm). The two major peaks were assigned to the $P2_1ma$ phase, owing to their very similar NMR parameters to the $P2_1ma$ phase of $NaNbO_3$, as shown in Table 4.1. However, there are two noticeable differences in the spectra as x increases from 0.02 to 0.05. Firstly, the intensity of the unassigned resonance increases with x, although it remains very broad. Even for KNN-4 and KNN-5, where the intensity of this resonance is greatest, it is still not possible to accurately determine the δ_1 line position, although a value of 1 ppm can be estimated from a projection onto the δ_1 axis. A z-filtered MQMAS NMR spectrum of

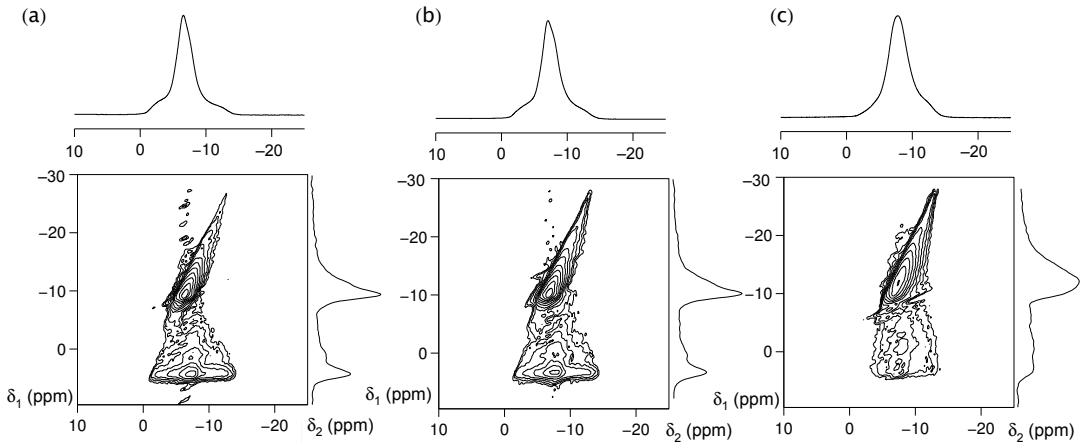

Figure 4.3: ^{23}Na (14.1 T) z-filtered MQMAS NMR spectra of (a) KNN-4, (b) KNN-5 and (c) KNN-8.

KNN-4 was also recorded at 20.0 T to improve sensitivity and resolution, with the hope that the unassigned resonance would have a more defined δ_1 projection. The spectrum is shown in Fig. 4.4(a), where it can be seen that greater intensity in the δ_1 projection is observed, and highlighted in red, with an approximate $<\delta_1>$ value of –0.3 ppm. It is not possible to accurately determine a value for δ_2. Secondly, the lineshapes become noticeably broader as x increases, perhaps as expected with increasing disorder. This increased broadening hinders the extraction of useful chemical information, *i.e.,* it becomes more difficult to observe peak splittings and low-intensity resonances, as they are more likely to overlap.

As the value of x increases from 0.02 to 0.08, it is observed that the broader Na2 resonance undergoes the greatest relative reduction in peak height intensity, as shown in Figs. 4.2 and 4.3, although both Na1 and Na2 resonances become noticeably broader. The relative reduction in peak height intensity on only one of the two sites may suggest there is a preferential site onto which K^+ dopes. The K^+ cations may substitute into the structure in one of three ways: (i) by clustering in a region, (ii) by substituting preferentially onto one site over the other, and (iii) randomly across both sites, *i.e.,* in a totally disordered manner. A detailed analysis of these options using

Table 4.1: ^{23}Na (14.1 T) NMR parameters for LNN-3 and samples of KNN, extracted from the MQMAS NMR spectra in Figs. 4.2, 4.3 and 4.5. The average quadrupolar product, $\langle P_Q \rangle$, is given, as the C_Q could not easily be determined owing to broadening of the resonances from disorder. A * denotes that a value could not be calculated owing to difficulties in determining the δ_1 and δ_2 line positions.

Sample	Site	$\langle \delta_{iso} \rangle$ (ppm)	$\langle P_Q \rangle$ / MHz
LNN-3	Na1	–4.6(5)	1.1(1)
	Na2	–0.6(5)	2.3(1)
KNN-2	Na1	–5.0(5)	1.1(1)
	Na2	–1.3(5)	2.4(1)
KNN-3	Na1	–5.2(5)	1.2(1)
	Na2	–1.7(5)	2.4(1)
KNN-4	Na1	–5.3(5)	1.1(1)
	Na2	–1.5(5)	2.4(1)
KNN-5	Na1	–5.3(5)	1.1(1)
	Na2	–1.8(5)	2.4(1)
KNN-8	Na1	–6.3(5)	1.1(1)
	Na2	*	*

DFT is given in Section 4.3.3, although a few comments are worth noting at this point. Firstly, clustering would not explain the relative reduction in intensity of the Na2 resonance. It is also unlikely because the NbO_6 octahedral tilt system of the 'bulk' structure, *i.e.,* not including the clustered region, would most likely retain the tilt system of the more thermodynamically-stable polymorph (space group *Pbcm* in the Na-rich region and *Amm*2 in the K-rich region). However, there is discussion in the prior literature that clustering may occur in these materials, and this might give rise to polar clusters/regions.[25] Secondly, substitution of K^+ preferentially onto the Na2 site would explain the changes in the MQMAS NMR spectra - less Na^+ on the

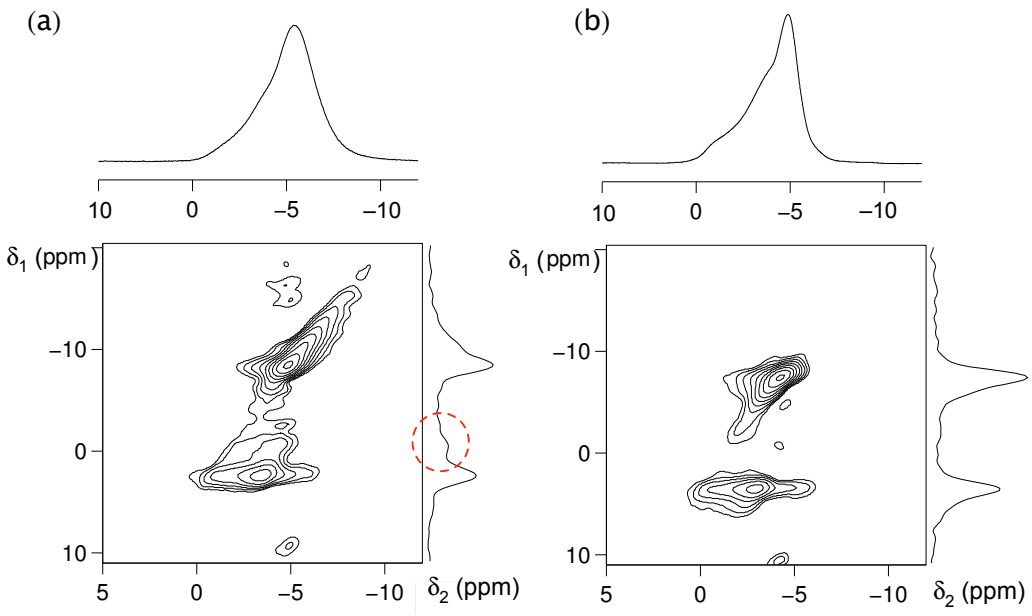

Figure 4.4: ^{23}Na (20.0 T) z-filtered MQMAS NMR spectra of (a) KNN-4 and (b) LNN-4. A red circle is used to highlight an additional resonance present in KNN-4 that is not present in LNN-4.

site would lead to a reduction in the relative intensity, and the Na1 resonance would become more broadened (with increasing x) due to the increased disorder on the nearby Na2 sites, *i.e.,* a change in the local structure. The nature of the Na1 and Na2 sites is discussed later, where it is shown that the Na2 site has longer Na-O bonds, and so may explain the preferential substitution of the larger K^+ cation.

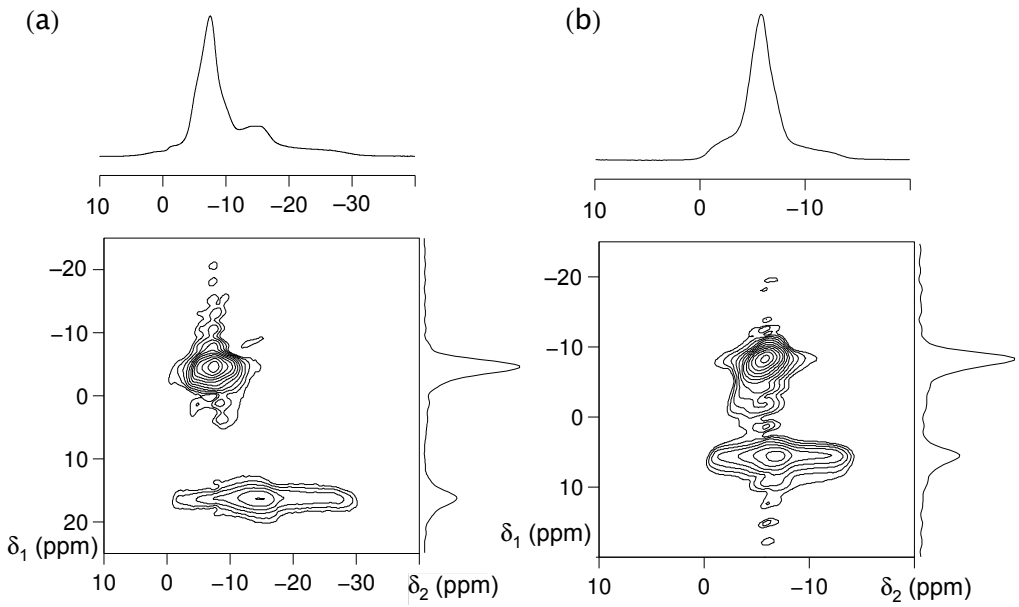

Figure 4.5: ^{23}Na z-filtered MQMAS NMR spectra of LNN-3 at (a) 9.4 T and (b) 14.1 T.

For samples of KNN-8, ^{23}Na MQMAS spectra show that the resonance corresponding to Na2 is of relatively low intensity (Fig. 4.3(c)), and it becomes difficult to accurately determine the δ_1 line position. It is also not possible to easily determine if the 'additional' resonance is present in the spectrum. This suggests that the Na2 site may be undergoing the largest structural change. Given the relatively small amount of K^+ substituted into the sample (8%), this is not sufficient to explain why the resonance is of such low intensity, *i.e.,* the Na2 site accounts for 50% of the total Na content, and even if all the K^+ doped onto the site, totalling 16%, there should still be sufficient Na content on the site to readily observe the resonance. This suggests that a phase change may perhaps be occurring, or at the very least, a significant structural re-arrangement. However, the relatively broad nature and low intensity of the resonance may be explained by the presence of a phase co-existence between the rhombohedral and monoclinic phases, as suggested by Thomas.[12]

In an attempt to assign the additional resonance (δ_1 = 1.2 ppm at 14.1 T), DFT calculations were performed for the monoclinic and rhombohedral phases of $NaNbO_3$, and their δ_1 positions determined to see if they matched the unassigned resonance. The ^{23}Na isotropic shielding, C_Q and η_Q were calculated using DFT, and the isotropic

shielding was then converted into an isotropic shift, as outlined in Chapter 2. The quadrupolar product can be determined from

$$P_Q = C_Q \times \sqrt{(1 + (\eta_Q^2 / 3))} \quad , \tag{4.1}$$

where C_Q and η_Q are obtained from the DFT calculation. The isotropic quadrupolar shift, δ_Q, is given by

$$\delta_Q = \left(\frac{3000\, P_Q}{12\, \nu_0}\right)^2 \quad , \tag{4.2}$$

where P_Q and ν_0 are both in MHz. The δ_1 line position is then given by

$$\delta_1 = \frac{17}{8}\delta_{iso} + \frac{1}{2}\delta_Q \quad . \tag{4.3}$$

For the rhombohedral *R*3*c* phase, a ^{23}Na δ_1 value of –4.27 ppm is obtained, and for the monoclinic *P*1*m*1 phase, four distinct values are given, the closest of which is –9.19 ppm (all values given calculated at 14.1 T). In a subsequent step, the experimental isotropic shift of the additional resonance was also calculated from knowledge of the δ_1 line positions at two different fields (14.1 and 20.0 T). The method used to calculate the isotropic shift is given in Section 3.3.3. A value of –0.33 ppm was obtained, which is in poor agreement with the values obtained from DFT for both phases (δ_{iso} = –4.27 ppm for the *R*3*c* phase and –9.19, –12.05, –17.84 and –18.21 ppm for the *P*1*m*1 phase). This could be due to difficulties in accurately determining the δ_1 line position at 14.1 T or, more likely, because neither of these phases are present in the samples.

Whilst the ^{23}Na isotropic shifts of the rhombohedral phase calculated from DFT are the closer match to that observed experimentally for KNN-4, there is still a large difference between the two values. This is most likely due to one of two reasons: firstly, neither of these phases are present in the sample (discussed above) and, secondly, because disorder has not been introduced into the calculated structures. In the experimentally-observed spectra, the line broadening on doping from KNN-2 to

KNN-5 is attributed to disorder, as are small changes in isotropic shifts. Any additional phase would most likely contain a mixture of Na^+ and K^+, and not necessarily in the stoichiometric ratio, *i.e.*, it is possible that an additional phase may contain a disproportionately large percentage of K^+. Consequently, the calculated δ_1 value is based on a $NaNbO_3$ structure with no potassium present, *i.e.,* no disorder. However, the experimentally-obtained values are affected by disorder, and this may account for any differences observed. However, the observed disorder *may* occur as a result of Na^+ volatisation during the heating process, although it is unlikely this would result in increased disorder as the amount of K^+ substitution is increased since the annealing temperature was constant across the series.

4.3.2. Comparison of KNN and LNN

To gain additional insight into the local structure and disorder in doped $NaNbO_3$, LNN samples were also synthesised and characterised using solid-state NMR. It is worth noting here that only samples of LNN-3 and LNN-4 can be included to serve as a comparison to the KNN analogues - this is due to very different phase behaviour being present where $x > 0.04$, as discussed in detail in Chapter 5. Using a combination of solid-state NMR and DFT, there are four principal differences between the data obtained for samples of KNN and LNN: (i) the presence of an additional resonance in MQMAS NMR spectra of KNN (not observed for LNN); (ii) a distribution of chemical shifts for KNN; (iii) the presence of *two* additional resonances in ^{23}Na DOR NMR spectra of KNN, and (iv) differences in the energies of structures from DFT when considering preferential site substitution of Li/K for Na. Each of these observations is discussed in more detail below.

In contrast to the observation of a third resonance in the ^{23}Na MQMAS spectra of KNN-3, 4 and 5, ^{23}Na MQMAS spectra of LNN-3 and LNN-4 contain only two resonances, as shown in Figs. 4.4 and 4.5. This suggests that any additional polymorph or clustering present in the KNN samples is not present in those in LNN. This is best exemplified at 20.0 T (Fig. 4.4) where the spectrum of KNN-4 clearly shows three resonances projected on the δ_1 axis, whereas only two are observed for LNN-4.

When analysing ^{23}Na MQMAS spectra (14.1 T) of KNN-2, 3, 4, 5 and 8, it is clear that the resonance attributed to site Na1 ($<\delta_1> \approx -10$ ppm) lies along a gradient, compared to the lower ridge which lies parallel to the δ_2 axis, as expected from a sheared spectrum. For KNN-5, this gradient is 2.12, where the value arises from $\Delta\delta_1/\Delta\delta_2$. For a I = 3/2 nucleus, a gradient of 17/8 (or 2.125) corresponds to a distribution of chemical shifts and –5/4 (or –1.25) is indicative of a distribution of quadrupolar parameters. This suggests that the upper ridge is primarily affected by a distribution of chemical shifts, whereas the lower ridge is notably less affected, as it lies parallel to the δ_2 axis. Neither resonance is broadened along a gradient close to –5/4, indicating that neither site is heavily affected by a distribution of quadrupolar couplings. By comparison, the ^{23}Na MQMAS spectrum of LNN-3 at 14.1 T, shown in Fig. 4.5, does not show similar results. The lower ridge lies parallel to the δ_1 axis and the upper ridge is not noticeably broadened along any other gradient. This suggests that samples with small amounts of Li^+ substitution are less affected by distributions of chemical shifts compared to those with K^+ substitution, perhaps due to smaller changes in the structure. Complementary ^{23}Na DOR NMR spectra were acquired for samples of KNN-4, 5 and 8 and LNN-3 and 4. The DOR spectrum of KNN-4 shows 4 resonances, while the spectrum of KNN-5 shows 3 (Fig. 4.6). In addition to the two principal resonances assigned to phase Q ($\delta \approx -3.7$ and –5.3 ppm), a small resonance at –2.3 ppm can be seen for KNN-4, and a shoulder at –6.2 ppm. By determining the δ_1 line positions in the MQMAS spectra at two different fields, it is possible to predict the corresponding shifts of resonances in the DOR spectra, as outlined in Section 3.3.3. From the ^{23}Na MQMAS spectra shown previously, the predicted ^{23}Na DOR shift can be calculated, giving a value of –0.41 ppm, where $\delta_{iso} = -0.33$ ppm and $\delta_Q =$ 0.20 ppm at 20.0 T. This value, however, does not correspond to any of the resonances in the ^{23}Na DOR spectra, shown in Fig. 4.6. Unfortunately, the region immediately around the predicted DOR shift has a spinning sideband present. Faster spinning speeds would have moved the sidebands away from this area, although difficulties in spinning stably at higher speeds prevented this. ^{23}Na DOR NMR spectra were also obtained for LNN-3 and LNN-4, for comparison to the spectra of KNN, as shown in Fig. 4.7. Similar to the ^{23}Na MQMAS spectra of these phases, only two resonances are observed - both assigned to phase Q.

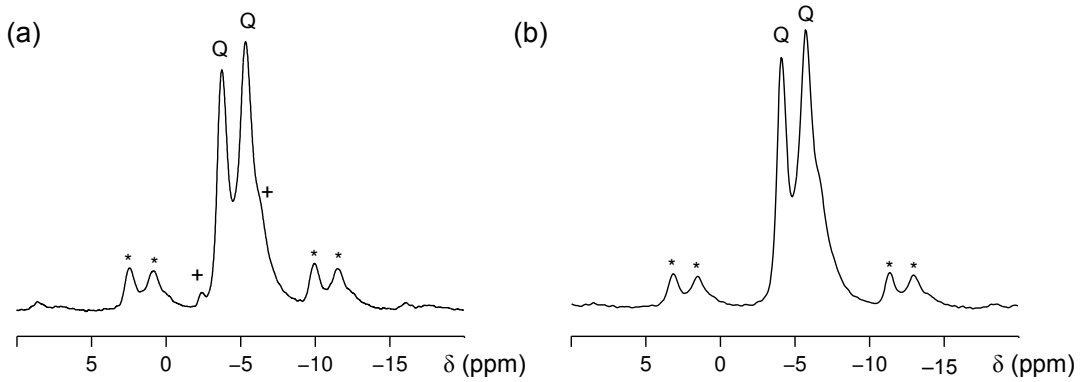

Figure 4.6: ^{23}Na (20.0 T) DOR NMR spectra of (a) KNN-4 and (b) KNN-5. Inner rotor spinning speeds of 1400 and 1650 Hz were used for KNN-4 and 5, respectively. All experiments were repeated with a second spinning speed to determine which peaks were spinning sidebands, denoted *. Q denotes resonances corresponding to phase Q and a + denotes additional resonances.

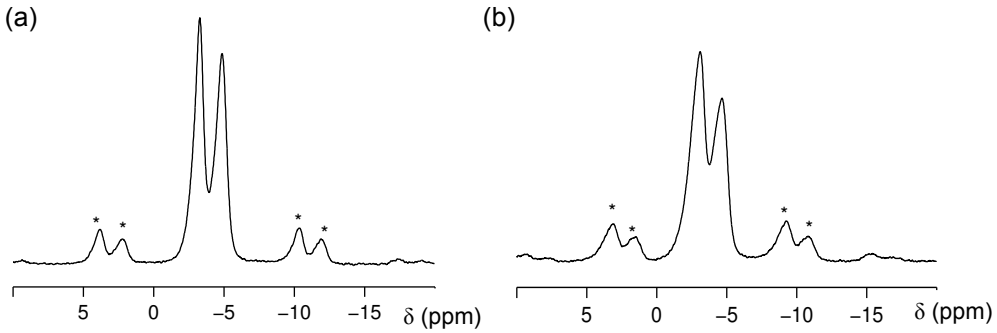

Figure 4.7: ^{23}Na (20.0 T) DOR NMR spectra of (a) LNN-3 and (b) LNN-4. Inner rotor spinning speeds of 1600 and 1400 Hz were used for LNN-3 and 4, respectively. All experiments were repeated with a second spinning speed to determine which peaks were spinning sidebands, denoted *.

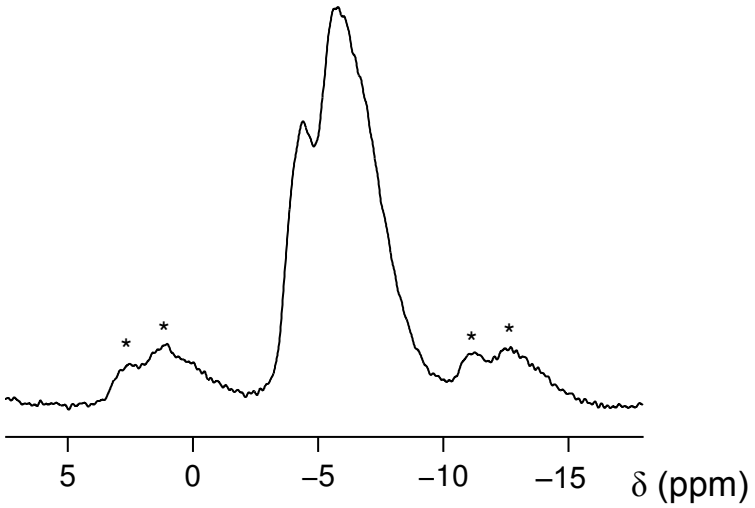

Figure 4.8: ^{23}Na (20.0 T) DOR NMR spectrum of KNN-8, obtained with an inner rotor spinning speed of 1400 Hz. Spinning sidebands are marked with a *.

The presence of the 'additional' resonances in the KNN spectra may suggest the formation of polar clusters/regions or the presence of an additional polymorph, neither of which there is evidence for in the spectra of LNN. In addition, a ^{23}Na DOR NMR spectrum of KNN-8 was also acquired, as shown in Fig. 4.8. As the spectrum shows, the isotropic peaks are now heavily broadened, compared to KNN-4 and 5, indicative of an increase in the amount of disorder present. However, two distinct isotropic peaks can be seen, attributed to the two crystallographically-distinct Na sites in phase Q. There is good agreement between the DOR shifts of these resonances for KNN-4, 5 and 8, with small differences most likely due to subtle changes in the local structure caused by increased levels of K^+ substitution. However, due to the breadth of the resonances it cannot be unambiguously stated that the other, low intensity resonances are not present, *i.e.,* they may be overlapped with this signal.

4.3.3. Is There a Site Preference for Substitution?

The orthorhombic $P2_1ma$ structure was geometry optimised using DFT, with the substitution of one Na^+ cation for one K^+ or Li^+ cation. However, this does still not represent the structures of KNN-3, 5 and 8. For example, a $P2_1ma$ supercell (*i.e.*, a 2 × 2 × 2 cell) contains 32 Na atoms, of which one is substituted for Li or K. This gives a substitution value of 1/32, or approximately 3%. It is not feasible, however, to model exactly 2, 3, 4 and 5% doping, as the size of cell needed would be too great to reasonably optimise, *i.e.*, computational cost precludes this. K^+ was substituted onto the Na1 and/or Na2 sites and the resulting model geometry optimised with both unit cell parameters and atomic positional coordinates allowed to vary. The same calculations were then performed by substituting Li^+ instead of K^+, to determine if any differences were observed.

Single-point energy calculations gave values of –4364.323 and –4364.333 eV/f.u., when one K^+ was substituted onto sites Na1 and Na2, respectively. Substitution onto the Na2 site results in the lower energy structure being formed. However, the difference in energy between the two is relatively small, compared to, for example, the high-temperature phases of $NaNbO_3$ discussed in Chapter 3. The difference in energies is approximately 0.01 eV/f.u., corresponding to approximately 1 kJ/mol. By contrast, values for the Li-substituted structure were –4364.2981 and –4364.2915 eV/f.u. for substitution onto the Na1 and Na2 sites, respectively. While substitution onto the Na1 site appears to be more energetically favourable than Na2, the difference between the two is still relatively small. It is not possible to unambiguously state that substitution onto one specific site is more favourable than the other, based solely on results obtained from DFT calculations. (It is worth noting here that the DFT geometry optimisations converge in energy to within a tolerance of 0.0001 eV). Additionally, NMR parameters were simulated for the Li- and K-substituted structures and were nearly identical; therefore comparison of simulated and experimentally-obtained spectra cannot be used to unequivocally state that one site is preferred to another for substitution.

To gain further insight into whether there is a site preference for substitution of K into $NaNbO_3$, ^{39}K MAS NMR spectra were recorded. ^{39}K (I = 3/2) is a challenging

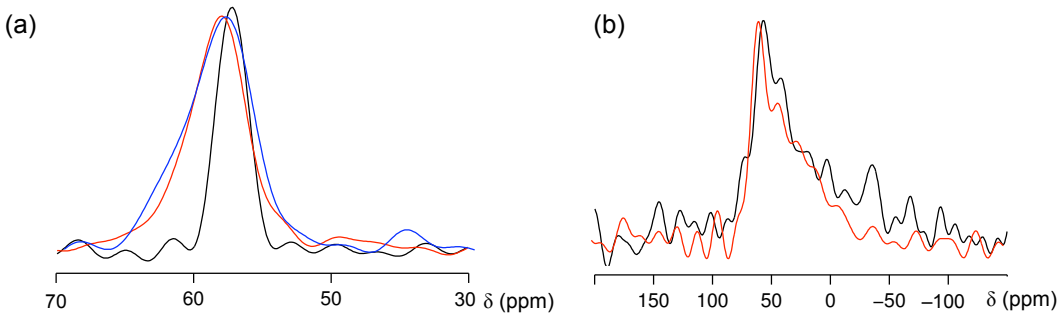

Figure 4.9: ^{39}K (20.0 T) MAS NMR spectra of (a) KNN-80 (black), KNN-30 (red), KNN-20 (blue) and (b) KNN-8 (black) and KNN-5 (red).

nucleus to study due to its low gyromagnetic ratio and poor receptivity to NMR. The MAS spectra for some KNN compounds are shown in Fig. 4.9, where some samples doped with higher levels of K^+ are shown for comparison. For samples with lower level doping (Fig. 4.9(b)), the spectra show a 'tail' in the upfield direction, whereby the broadening is predominantly towards lower chemical shifts. This 'tail' can be indicative of a distribution of chemical shifts and/or quadrupoles. However, interpretation of MAS spectra alone is not sufficient to determine which (or if both), and consequently, it can only be determined that these samples show a distribution of NMR parameters, indicative of disorder. Unfortunately, peak splittings, which may indicative that two or more ^{39}K environments are present, cannot be seen. Whilst this may indicate that only one chemically-distinct ^{39}K site is present, it is most likely due to the poor receptivity of ^{39}K to NMR and the low weight percentage of ^{39}K in the samples. As such, it is not possible to readily determine if there is a site preference for substitution by use of ^{39}K MAS NMR.

From DFT calculations, a ^{39}K σ_{ref} value of 1235.80 ppm was obtained by comparing experimentally-obtained δ_{iso} values to calculated σ_{iso} values for a series of 'simple' K-containing compounds,[26] shown in Fig. 4.10. The σ_{ref} value was then used to calculate an isotropic shift for the optimised KNN structures, where the calculated δ_{iso} was 92.74 and 85.46 ppm when K^+ was substituted onto sites Na1 and Na2, respectively. The spectra were simulated and then compared to the experimentally-

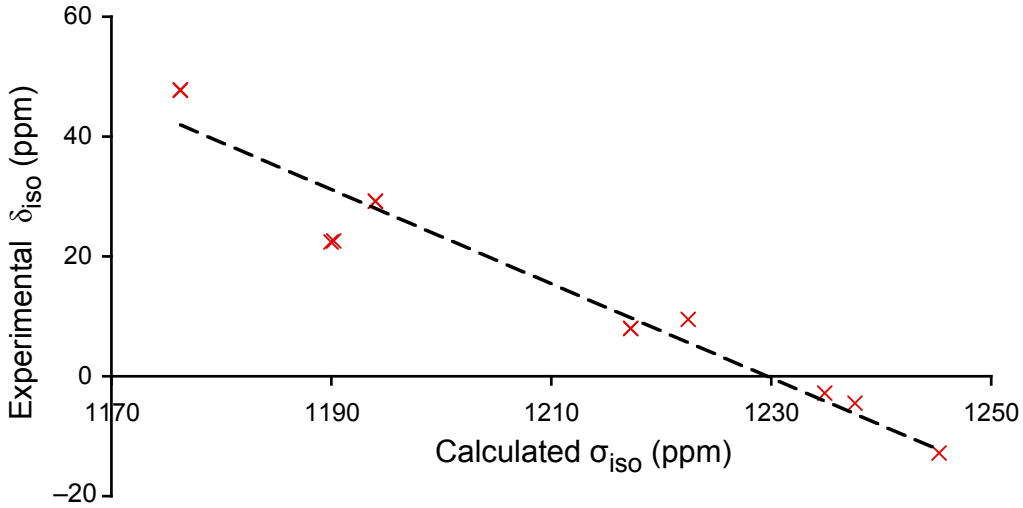

Figure 4.10: Plot of the calculated σ_{ref} and experimental δ_{iso} values[21] for a selection of K-containing compounds. Structures calculated include K_2SO_4, K_2CO_3, KNO_3, $KNbO_3$, KI, $KClO_3$, $KBrO_3$ and $KHSO_4$.

obtained spectrum, as shown in Fig. 4.11. The presence of a distribution of NMR parameters (either chemical shifts or quadrupoles) evident in the experimentally-obtained spectrum was not included in the (ordered) DFT calculations/simulations. The figure shows that the lineshape simulated for K^+ substituted onto Na1 agress well with the position of the experimental lineshape but is much narrower than the resonance observed. In contrast, the width of the simulated lineshape for K^+ substituted onto Na2 is perhaps in better agreement with the experimental lineshape, but is found at much lower shift. However, the experimentally-obtained spectrum could be envisaged as having two distinct components – a narrow (sharp) component and a much broader component, each consistent with simultaneous substitution onto both Na1 and Na2. The relative peak height of the Na2 resonance would be significantly reduced if the spectra were not normalized (as would occur experimentally), giving a much better fit with the experimentally-obtained spectrum. To further investigate this, additional DFT calculations were performed (primarily todetermine if the potassium is clustered or ordered in the sample) and further ^{39}K NMR spectra obtained. Each of these investigations is discussed below in detail.

To investigate the possible effects (*i.e.*, changes in isotropic chemical shift and C_Q) for potassium clustering in the $P2_1ma$ structure, further DFT calculations were performed using two different methods. Firstly, all but one of the Na^+ cations were replaced with K^+ atoms in the structure (Method A) to 'mimic' the effects of Na being surrounding by K atoms, *i.e.*, clustering, and secondly, two K^+ atoms were substituted into the $P2_1ma$ supercell but positioned next to one another (one each on Na1 and Na2), such that their separation was minimal (Method B) and the differences in isotropic shifts and C_Q for both the K^+ and surrounding Na^+ cations were compared to the initial calculations where one K^+ cation was substituted into the supercell. Using Method A, ^{39}K isotropic shifts of 114.31, 121.03 and 127.18 ppm were obtained, with C_Q values of 1.42, 4.02 and 4.05 MHz, respectively. The large C_Q values obtained from DFT calculations (Method A) are therefore in poor agreement with experiment (C_Q = 1.3 and 2.1 MHz for substitution onto sites Na1 and Na2, respectively), suggesting that clustering may not be prevalent. However, a small amount of clustering may still be present, but would be difficult to determine (owing to the broad lineshape as a result of the larger C_Q) if the majority of the substituted K^+ cations were disordered throughout the structure.

Using Method B, ^{39}K isotropic chemical shifts of 80.97 and 88.28 ppm were obtained with corresponding C_Q values of 1.40 and 1.96 MHz, and η_Q = 0.51 and 0.76, for sites Na1 and Na2, respectively. The differences between the calculated and experimentally-obtained values could be partially explained by the additional presence of a distribution of NMR parameters in the experimentally-obtained spectrum. It is worth noting, again, that it is not possible to determine if a distribution is caused by chemical shifts or quadrupoles solely from an MAS spectrum. From the DFT and NMR investigation, no evidence for significant potassium clustering is observed.

To complement the ^{39}K MAS NMR spectra and to provide additional information, ^{39}K quadrupolar CPMG (Carr-Purcell Meiboom-Gill) [27, 28] experiments were also performed. This approach is best utilised for nuclei with low gyromagnetic ratios and poor receptivity, as it provides an increase in the peak height (*i.e.*, not integrated) signal-to-noise ratio. Whilst the ^{39}K MAS spectrum (Fig. 4.9) of KNN-8 appears to

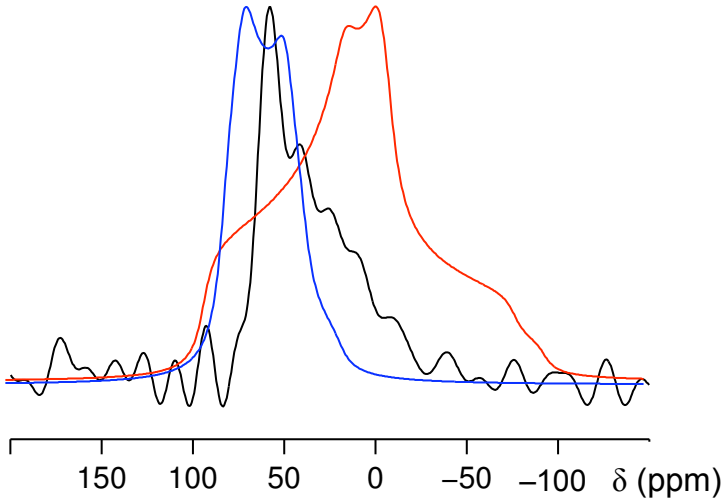

Figure 4.11: ^{39}K MAS NMR experimental spectrum of KNN-8 (black line) and normalised simulations of KNN, with data obtained from DFT calculations. The blue line is the simulated spectrum with K substituted onto the Na1 site (C_Q = 1.3 MHz), and the red line for the Na2 site (C_Q = 2.1 MHz). The principal difference between the experimental and simulated spectra is the lack of inclusion of a distribution of NMR parameters in the simulations, as the calculations are periodic.

show one broadened lineshape, the CPMG spectrum, shown in Fig. 4.12, does not. This may then allow additional chemical information to be obtained more easily, such as the number of chemically-distinct ^{39}K sites in the sample. Also shown in Fig. 4.12 is a 'guide-to-the-eye' simulated spectrum, in which two distinct ^{39}K sites were used, and the individual lineshapes are also shown. The 'sharp' (K1/Na1) resonance has δ_{iso} = 60.46 ppm, C_Q = 0.3 MHz and η_Q = 0.1, and the 'broad' (K2/Na2) resonance has δ_{iso} = 80.51 ppm, C_Q = 1.4 MHz and η_Q = 0.3 (these values provide a good 'fit' to the experimentally-obtained spectrum, but are a guide-to-the-eye only, *i.e.*, they did not come from DFT calculations). The resulting 'simulated' spectrum compares reasonably well with the experimental-obtained spectrum (Fig. 4.16(c)). It is worth noting that no distribution of parameters is included in the guide-to-the-eye spectrum. From the spectra though, it can be suggested that ^{39}K may well substitute onto both Na1 and Na2 sites, although the relative intensities of the two resonances suggests that preferential site substitution occurs on Na2 (experimentally, K2/Na2 has 8 times

more intensity than K1/Na1.)* This observation is in agreement with the results obtained from the ^{23}Na MQMAS spectra shown previously, in which it could be suggested that substitution occurs preferentially onto the Na2 site from the relative intensities of the ^{23}Na resonances.

* Additionally, a ^{39}K CPMG spectrum was also recorded for a sample of $RbNO_3$, to determine if there was any 'background' contribution to the observed signal, *e.g.*, from the rotor or probe. No signal was detected, and so it is assumed that all signal in the experimental spectrum of KNN-8 comes solely from the sample.

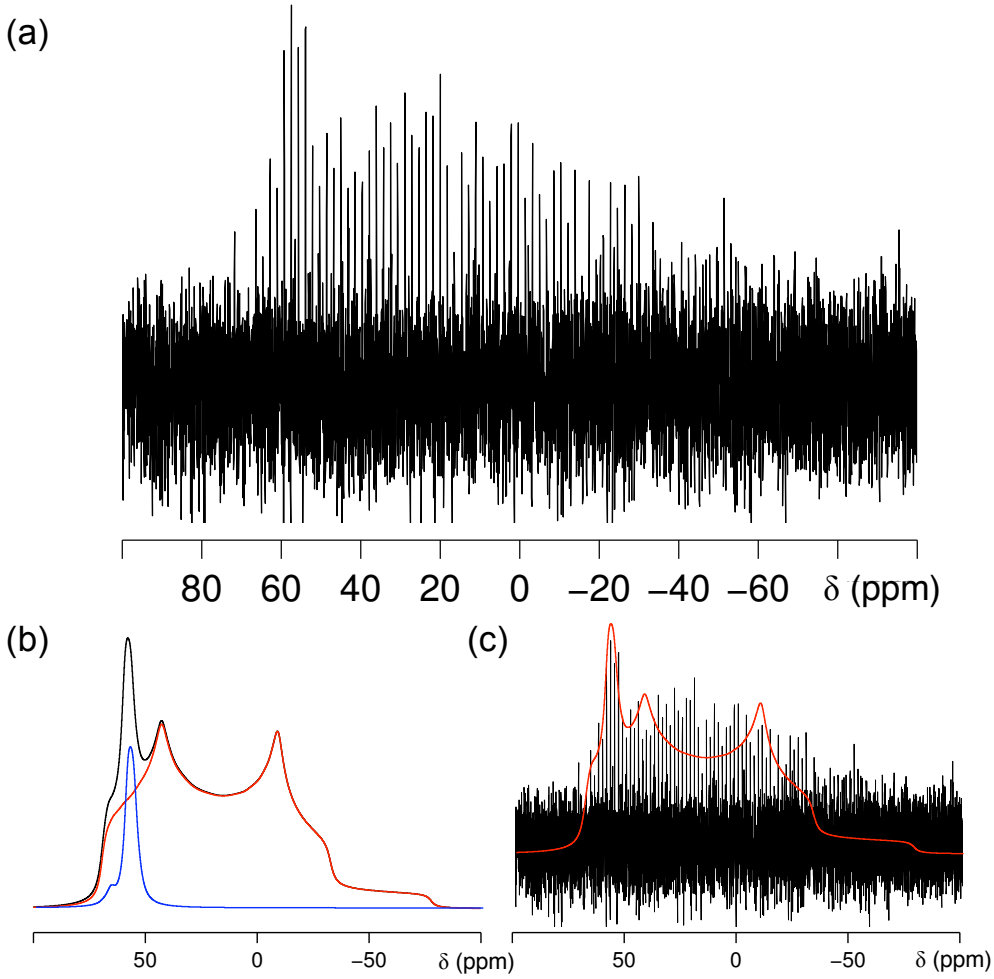

Figure 4.12: ^{39}K (14.1 T) quadrupolar CPMG MAS (12.5 kHz) spectrum of (a) KNN-8. A guide-to-the-eye spectrum (*i.e.*, not simulated from DFT) is shown in (b) where the broad (Na2) site is red, the sharp (Na1) site is blue and the sum of the two is in black. In (c), the spectra in (a) and (b) are overlaid, for comparison. Values used in the simulations are given in the main text. The experimental spectrum is the result of averaging 11956 transients with a 30 s recycle interval. High-power pulses of 8.0 and 28 μs duration were used, with a train of 50 echoes acquired with an echo delay of 20 ms, and spikelet spacing of 50 Hz.

4.4. The Temperature-Dependent Behaviour of KNN

4.4.1. Phase Q

High-resolution NPD data were obtained at HRPD for a sample of KNN-3, and s-PXRD data were obtained on beamline I11 at DIAMOND for samples of KNN-3 and KNN-5. NPD data for KNN-3 was obtained over the temperature range RT - 480 °C, with the intent of characterising the structures of phases G and T. Data were also obtained in the 'phase Q region' to determine if any unexpected phase behaviour or transitions occurred, as was shown to be the case for phase P of $NaNbO_3$, discussed in Chapter 3. Fig. 4.13 shows the variation in lattice parameters (normalised to the aristotype cell metric) as a function of temperature over the region 200 to 260 °C (a phase transition occurs at higher temperatures, as discussed later). As the figure shows, the three pseudo-cubic axial lengths begin to converge towards each other, as is often observed upon heating. These results correlate well with changes observed in the main distortion modes present in this phase – the M_3^+ and R_4^+ tilts and the Γ_4^- polar mode. Fig. 4.14 shows how the magnitude of these distortion modes decrease with increasing temperature, and Fig. 4.15 shows the corresponding Rietveld profiles. The observed decrease is compatible with the convergence of the three axial unit cell lengths. This result is similar to that observed for phase P of $NaNbO_3$, which adds further weight to the argument that the two phases are very structurally similar.

Average Na-O and Nb-O bond lengths for KNN-3 were determined from Rietveld refinement with the $P2_1ma$ space group for structures at RT, 200 and 240 °C, and are given in Tables 4.2 and 4.3, respectively. As the Na-O bond lengths show, there are no observable trends as function of temperature. Analysis of the Nb-O bond lengths as a function of temperature (Table 4.3) shows that three lengths increase with increasing temperature and three decrease. This is a similar observation to that for phase P of $NaNbO_3$, in which this distortion of the octahedra can be likened to *fac*-isomerism. It is possible to quantify the 'magnitude' of the polyhedral distortions for both NbO_6 and NaO_{12} polyhedra, to (a) compare the two directly, and (b) determine how they change as a function of temperature. To quantify the distortions of the polyhedra, a convenient parameter, Δ_d, can be calculated which is centred on the deviation of the Nb-O (or Na-O) bond lengths with respect to the

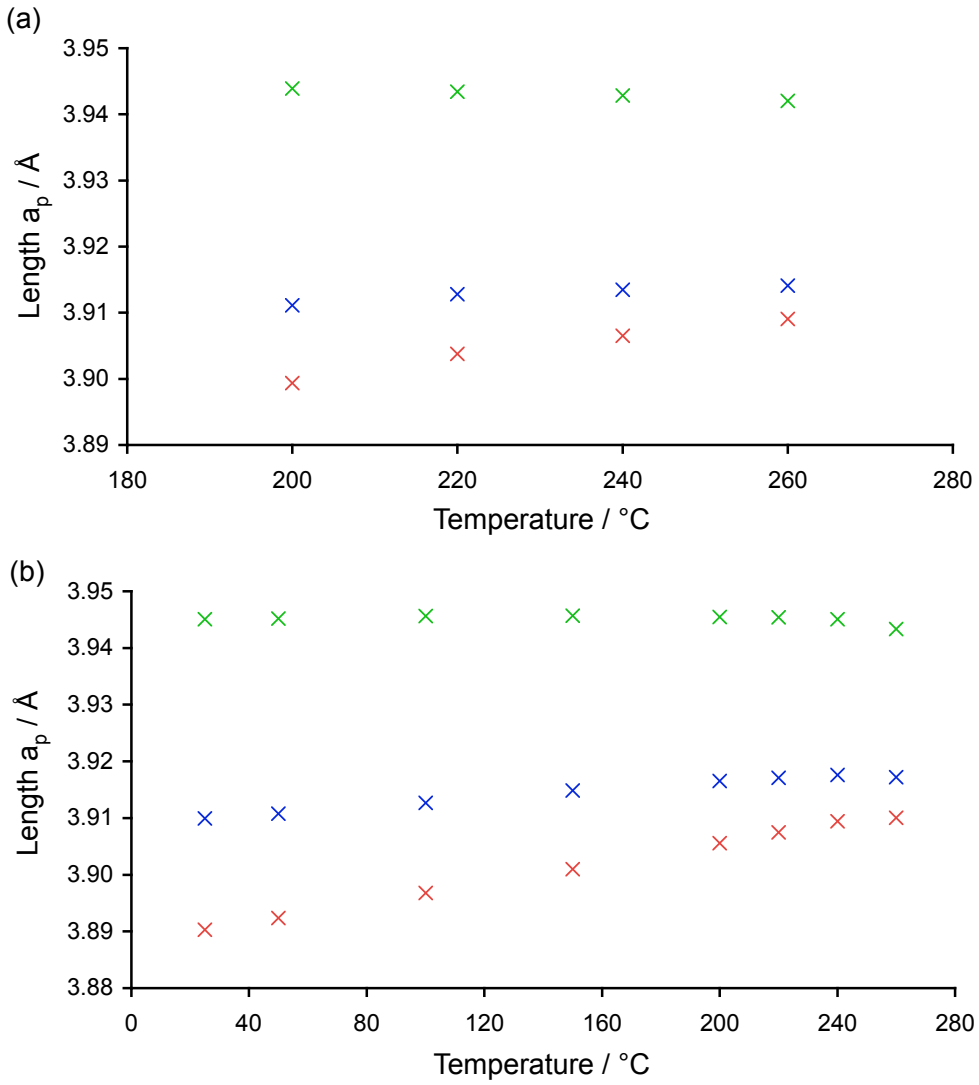

Figure 4.13: Lattice parameters as a function of temperature, normalised to the aristotype cell metric. Data are obtained from Rietveld refinement of (a) NPD data of KNN-5 and (b) s-PXRD data for KNN-5. The *a*, *b* and *c* parameters are shown in green, red and blue, respectively. Error bars are smaller than the data points and are therefore not shown.

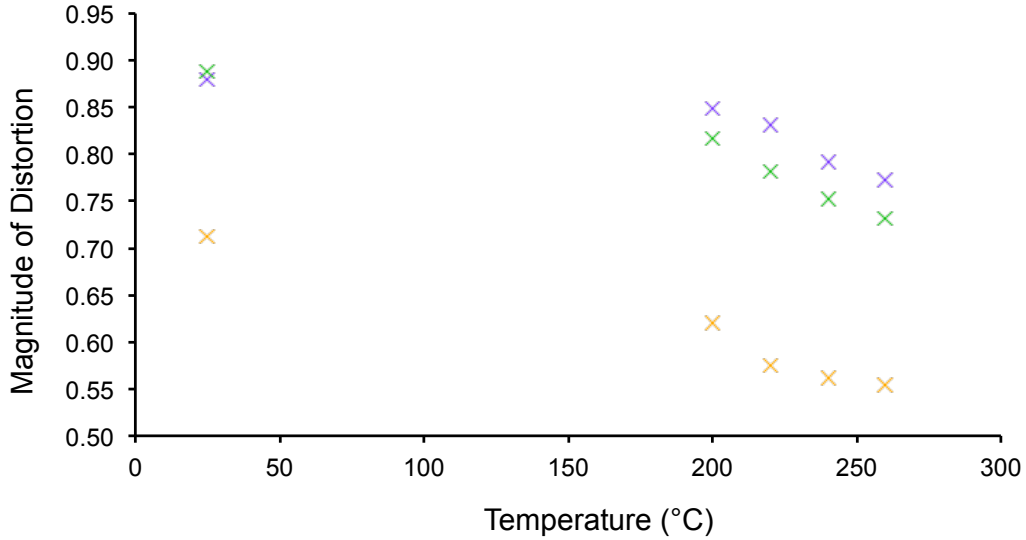

Figure 4.14: Magnitudes of the distortion modes for (KNN-3 obtained from NPD data. The M_3^+ (purple), R_4^+ (green) and Γ_4^- (yellow) modes are shown. Γ_4^- is the so-called polar mode, not present in the non-polar *Pbcm* polymorph of $NaNbO_3$. Error bars derived from ISODISTORT are shown. Error bars are smaller than the data points and so are not shown.

average Nb-O (or Na-O) bond length.[29,30] The magnitude of the distortion, Δ_d, is given by

$$\Delta_d = \frac{1}{n}\sum_{1}^{n}\left[\frac{(d_n - \langle d_0 \rangle)}{\langle d_0 \rangle}\right]^2 \quad , \tag{4.4}$$

where d_n is the bond length of Nb-O (or Na-O), $\langle d_0 \rangle$ is the *average bond length*, and n is the number of bonds (6 for Nb-O and 12 for Na-O[†]). By using Equation 4.4, Δ_d can be calculated for the polyhedra, and these values are given in Table 4.4. From these results, three conclusions can be made. Firstly, the NaO_{12} polyhedra show much greater distortion than the NbO_6 octahedra, as expected. Secondly, the magnitude of

[†] It is assumed that the A-site is twelve-coordinate.

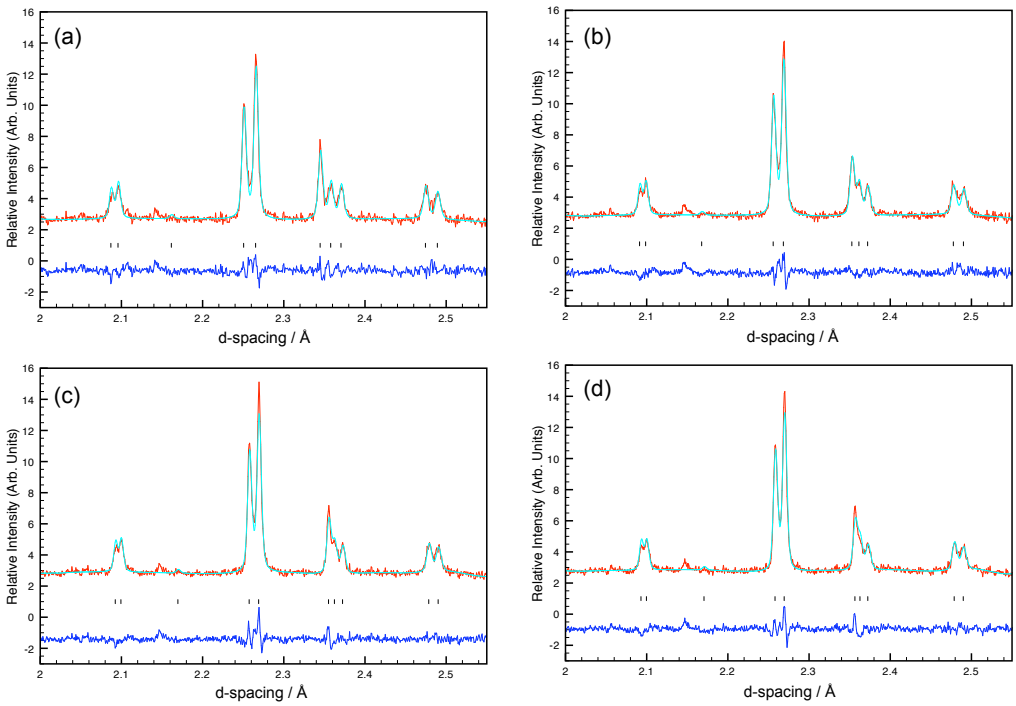

Figure 4.15: Rietveld profiles of the superlattice regions of KNN-3 refined in space group $P2_1ma$, obtained from NPD data obtained at (a) RT, (b) 200 °C, (c) 220 °C and (d) 240 °C. The peak near d = 2.15 Å is from the vanadium can used in the experiment, and is present is most of the following diffraction patterns. wRp = (a) 3.97%, (b) 3.89%, (c) 3.91% and (d) 3.94%.

the distortion (normalised to the average bond length) decreases with increasing temperature. Thirdly, the NbO_6 octahedra show the greater change as a function of temperature, compared to the NaO_{12} polyhedra. For example, from RT to 200 °C, the magnitude of the distortion parameter decreases by approximately 40%, whereas this is 15% and 3% for the $Na(1)O_{12}$ and $Na(2)O_{12}$ polyhedra, respectively.

Table 4.2: Na-O bond lengths for KNN-3 (phase Q) at different temperatures. Data are obtained from refinement of NPD data. Only bond lengths less than 3 Å are shown, and * denotes that no bond shorter than 3 Å was present. Superscript numbers show the number of symmetry-equivalent bond lengths, if any.

Temp. / °C	Site	Na-O Bond Lengths / Å			
		O1	O2	O3	O4
25	Na1	2.413(14)^2, 2.607(15)	*	2.813(9)^2, 2.974(11)^2	2.340(8)^2, 2.965(11)^2
	Na2	*	2.510(14), 2.530(12)	2.514(8)^2, 2.675(9)^2	2.687(7)^2
200	Na1	2.484(12)^2, 2.590(12)	*	2.803(9)^2, 2.957(12)^2	2.362(11)^2, 2.959(9)^2
	Na2	*	2.506(10), 2.570(10)	2.526(12)^2, 2.700(9)^2	2.708(7)^2
240	Na1	2.440(12)^2, 2.676(10)	*	2.817(8)^2, 2.948(10)^2	2.375(7)^2, 2.967(8)^2
	Na2	*	2.564(10), 2.618(11)	2.587(8)^2, 2.665(7)^2	2.654(8)^2

Table 4.3: Nb-O bond lengths for KNN-3 (phase Q) at different temperatures. Data are obtained from refinement of NPD data. 'e' and 'a' are used to denote equatorial and axial bonds, respectively.

Temp. / °C	Nb-O Bond Lengths / Å					
	O1^e	O2^e	O3^e	O4^e	O5^a	O6^a
25	1.864(4)	1.880(4)	2.106(3)	2.137(3)	1.969(4)	1.987(4)
200	1.897(5)	1.899(5)	2.084(4)	2.097(4)	1.978(4)	1.982(5)
240	1.904(4)	1.956(4)	2.055(3)	2.059(3)	1.983(6)	1.976(6)

Table 4.4: Δ_d distortion parameter for KNN-3 at different temperatures for the (six-coordinated) NbO_6 and (twelve-coordinated) NaO_{12} polyhedra. All values are obtained from Rietveld refinement of NPD data.

		$10^4\ \Delta_d$	
Temperature / °C	**NbO_6**	**$Na(1)O_{12}$**	**$Na(2)O_{12}$**
25	26.7	102.8	101.6
200	15.8	87.5	98.3
240	7.5	87.0	96.2

4.4.2. Phase G

The Rietveld profile for KNN-3 at 260 °C produces a satisfactory fit, with wRp = 5.83%, when refined in space group $P2_1ma$, as shown in Fig. 4.16. However, a more detailed analysis of the superlattice region, and consequently the M- and R-points, reveals that a second phase (G) may also be present, as marked with an asterix. The second phase (G) was later determined to most likely have the tetragonal $I4/mmm$ space group, determined from analyses of the NPD data and symmetry modes. M, R and T-points were introduced in Chapter 3, where a brief overview of each was given.

Determining the structure of phase G is made more challenging owing to its co-existence with phase Q. For example, questions such as 'does the R-point relate to phase Q or G?' are not straightforward to answer and require more careful consideration than in a dataset for a phase pure sample. Nonetheless, data for KNN-3 obtained at 260 °C, were refined to the $P2_1ma$ space group, giving a reasonable level of fit, as shown in Fig. 4.16(a). (It is also worth noting that a poorer fit of the $(111)_p$ subcell peak is observed when compared to data at slightly lower temperatures). The presence of a "non-indexed" peak at this temperature suggests that either a lowering

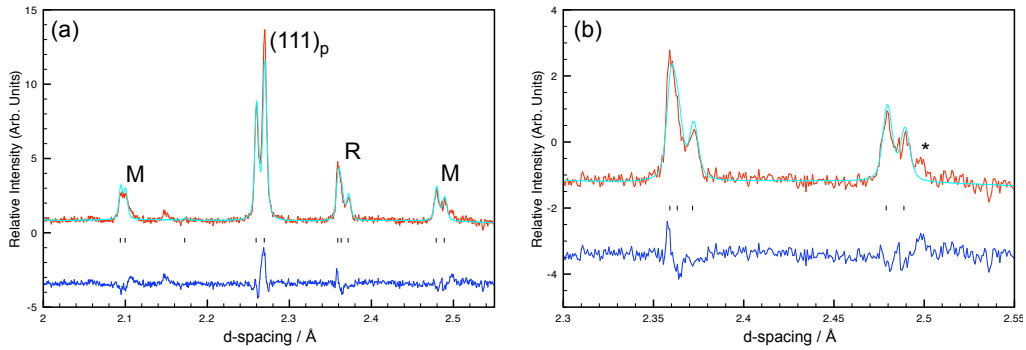

Figure 4.16: Portions of the Rietveld profile (NPD) of KNN-3 obtained at 260 °C and refined in space group $P2_1ma$. The R- and M-points and subcell peak are labeled in (a), while (b) shows a close-up of one M- and R-point, where it can be seen that the M-point is not fully indexed, as shown with by *. wRp = 4.34%.

of the symmetry is observed or a second phase is also present. It would be unlikely for the former to account for this observation, as higher-temperature phases generally show greater symmetry. In a subsequent step, data obtained at 280 and 300 °C were also analysed, and an *increase* in the intensity of this peak was observed, as well as a corresponding decrease in the goodness of fit (when refined exclusively to the $P2_1ma$ space group). This increase in intensity is shown in Fig. 4.17, and suggests that the relative fraction of a second phase is increasing with temperature.

As phase Q exhibits peaks corresponding to both M- and R-points, it is at first *assumed* (albeit incorrectly, see later) that the second phase (G) must also contain both M- and R-points. If both M- and R-points are *assumed* to be present, then the logical option is that phase G belongs to the non-polar space group *Pnma*. This assignment is based on work proposed by Howard and Stokes, in which they show the group-subgroup relationships for a number of space groups.[31] Out of the 15 possible space groups proposed, 14 of them contain either or both of the R_4^+ and M_3^+ irreducible representations, which mediate the NbO_6 octahedral tilting. It will, however, be shown that *Pnma* is not the correct assignment of phase G, and that

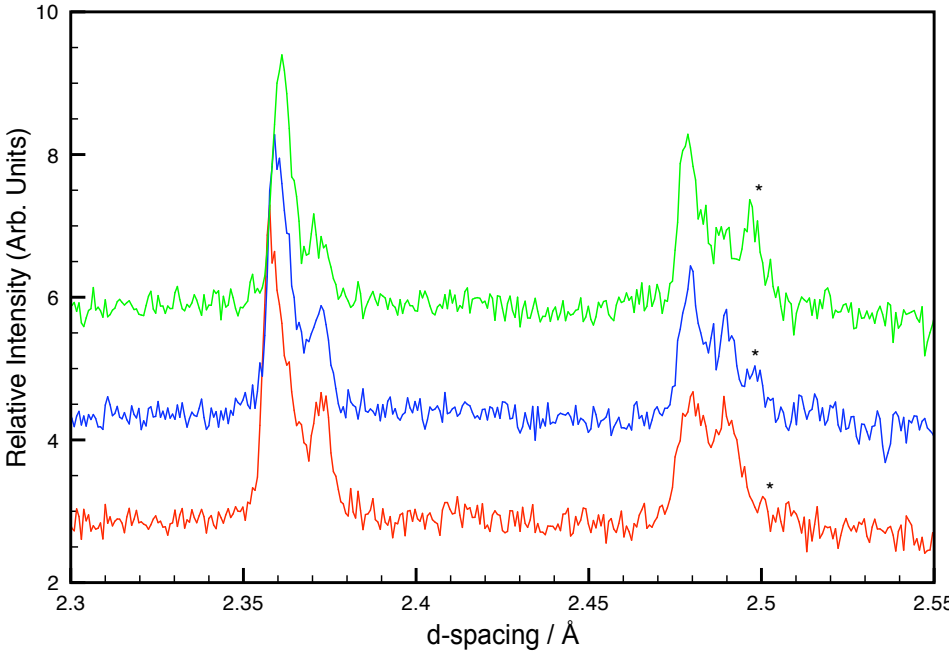

Figure 4.17: Portions of the powder patterns (NPD) of KNN-3 obtained at 260 °C (red), 280 °C (blue) and 300 °C (green). The "non-indexed" peak is denoted with *.

higher-symmetry tetragonal models are the most likely. There is no evidence to suggest that phase G is of lower symmetry than tetragonal. It is worth noting that this is difficult to reliably determine owing to the simultaneous presence of phase Q. If tetragonality is imposed, there are two possible space groups to be considered: $P4_2/nmc$ and $I4/mmm$, in which the former contains both M- and R-points and the latter only the M-point. Additionally, a phase with the R-point present but no M-point, such as $I4/mcm$, can be ruled out, as phase G necessitates the presence of the M-point, as shown by the peak at d = 2.49 Å in Fig. 4.17.

Attention was then focused on tetragonal models with cell metrics of $2a_p \times 2a_p \times 2a_p$, the minimum required to index the patterns, which contained both M- and R-points. More specifically, the M_3^+ and R_4^+ modes were required, as these are needed for the specific case of octahedral tilting. In fact, they have been shown to be present for some of the high-temperature phases of $NaNbO_3$.[32] Using ISODISTORT,[33] the only space group with point group $4/mmm$ containing both distortion modes is $P4_2/nmc$. Only the primitive cells contained both the 'required' distortion modes. $P2_1ma$ plus $P4_2/nmc$ two-phase Rietveld refinements were found to give the best fit to the data at

280 - 340 °C, suggesting that the latter may be a good model for phase G. It is worth noting that this can be considered as the 'standard' model for the Glazer tilt system $a^+a^+c^-$. The Rietveld profile for KNN-3 at 300 °C is shown in Fig. 4.18, along with corresponding crystallographic data given in Appendix C. A good fit is obtained in this two-phase refinement, with $\chi^2 = 2.41$ and wRp = 3.63%, suggesting that this *may* be the correct assignment.

In a subsequent step, the diffraction patterns (note, *not* the Rietveld refinements) obtained at temperatures between 280 and 340 °C were analysed further, with particular attention focused on the superlattice regions. Fig. 4.19 shows an expansion of these regions, highlighting the changes occurring in the superlattice peaks arising from the presence of M- and R-point distortion modes. As Fig. 4.19 shows, the intensity of the peak assigned to the R-point *decreases* relative to that of the M-point, as the temperature increases. It was also noted earlier that as the temperature increases, the relative phase fraction of G increases and that of Q decreases. By combining these two observations, it can be concluded that *the intensity of the peak corresponding to the R-point decreases as the fraction of phase Q also decreases*. This is an interesting observation, as it can now be suggested that phase G does not necessarily contain the R-point, *i.e.*, the peak corresponding to the R-point may be present solely because of phase Q, and phase G needs only the M_3^+ distortion mode. Using ISODISTORT, a search over all special *k* points (relating to the Brillouin zone) showed that *I*4/*mmm* (cell metrics $2a_p \times 2a_p \times 2a_p$) was the simplest model with the presence of the M_3^+ mode and no R_4^+ or T_4 modes, corresponding to the Glazer tilt system $a^+a^+c^0$. It is worth noting that the primitive cell, with space group *P*4/*mmm*, indexed both the M- and R-points in the diffraction patterns. As the search was for structures that gave rise to the M-point but not the R-point, this space group was ruled out. It could be considered, however, that the *P*4/*mmm* phase may be present exclusively, since it indexed both points. However, the 'splitting' in the $(111)_p$ subcell peak is not accounted for in this model, indicating that it may not be the correct assignment.

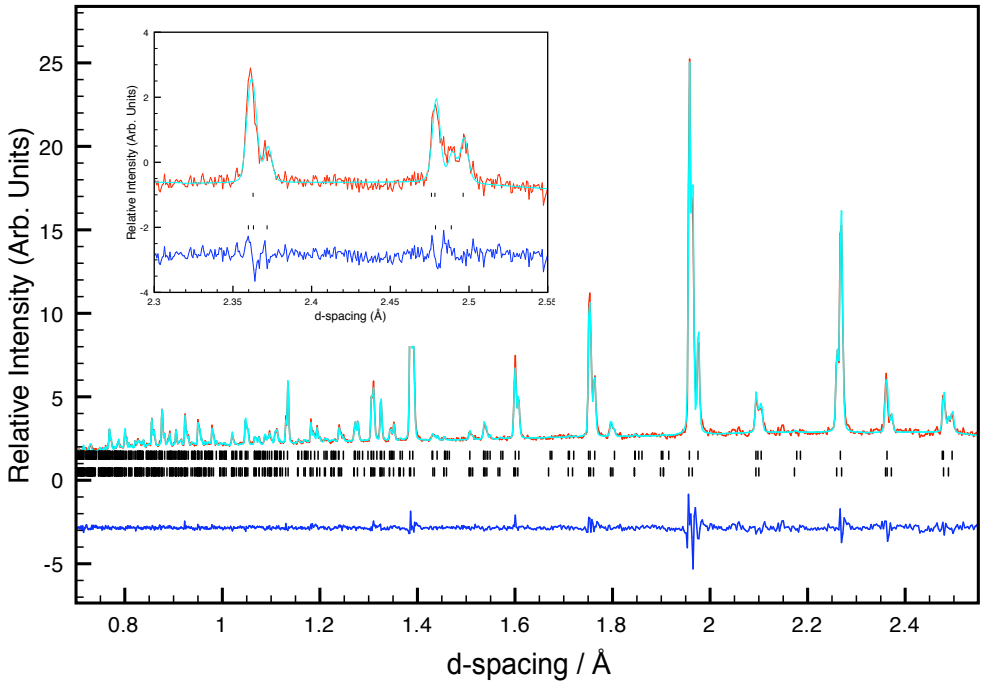

Figure 4.18: Rietveld profile (NPD) of KNN-3 obtained at 300 °C, with expansion of the M- and R-point region (inset), refined in space groups $P2_1ma$ (lower tick marks) and $P4_2/nmc$ (upper tick marks). Phase fraction $P4_2/nmc$ = 42%, wRp = 3.63%.

Further multiphase Rietveld refinements were carried out for all datasets in the temperature range 280 to 340 °C, to confirm if this was the correct assignment, and, if so, how the relative phase fractions changed. The Rietveld profiles are shown in Fig. 4.20. At 280, 300, 320 and 340 °C, the relative fraction of phase G increased, giving values of 21, 41, 56 and 58%, with the fraction of phase Q decreasing accordingly.

Interestingly, phase G has been suggested as being polar in some of the initial work by Ahtee and Glazer.[9] Polar tetragonal space groups are those with point groups 4 or 4*mm*. Initially, Ahtee and Glazer determined this phase had the $a^-b^+c^+$ tilt system, belonging to space group *Pnmm*. However, as one axis was noticeably longer than the others, they concluded that parallel cation displacements must be present along this

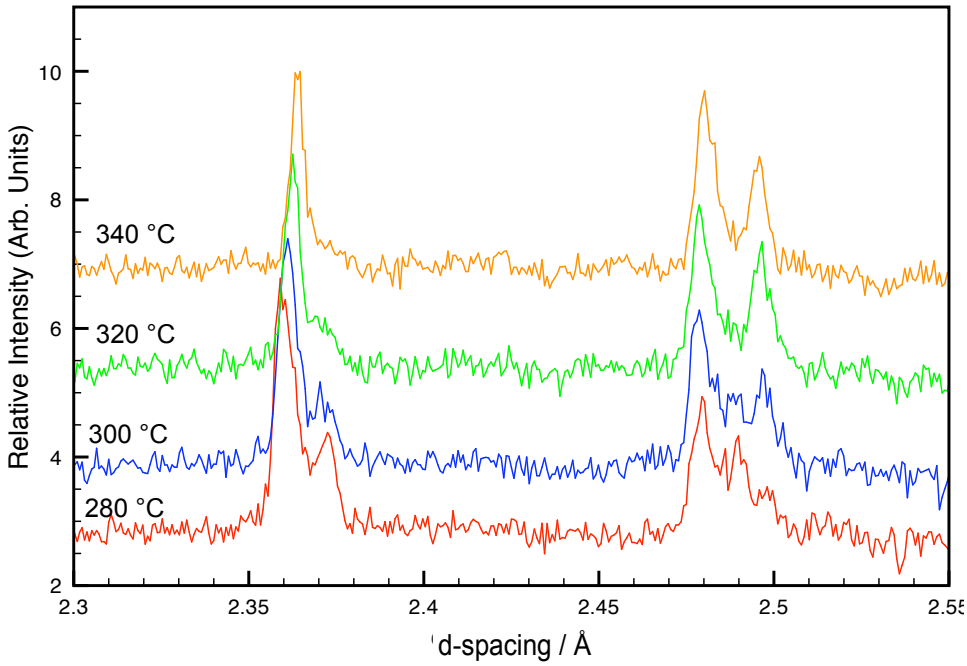

Figure 4.19: Portions of the NPD data obtained at various temperatures. It can be seen that the intensity of the peak assigned to the R-point decreases (d = 2.37 Å) relative to that of the M-point (d = 2.49 Å), as temperature increases.

axis. A similar result is observed for the data presented in this work. The *c* axis is significantly longer than *a* or *b* (7.90 and 7.83 Å, respectively), suggesting that cation displacements may be present along [001]. The *I*4*mm* space group possesses the necessary M_3^+ distortion mode and no R_4^+ mode and has cell metrics of $2a_p \times 2a_p \times 2a_p$. Consequently, a multiphase Rietveld refinement was performed for the dataset at 280 °C using the $P2_1ma$ and *I*4*mm* models. As the 'principal' difference between the *I*4/*mmm* and *I*4*mm* space groups is that cation displacements along [001] are allowed (resulting in the removal of a mirror plane) in the latter, only slight differences were expected in the goodness of fit of the refinement. Fig. 4.21 shows the Rietveld profile, with corresponding crystallographic data given in Appendix C. As the figure shows, this was a correct prediction - no discernable differences can be seen between the Rietveld profiles for $P2_1ma$ with *I*4/*mmm* versus $P2_1ma$ with *I*4*mm*, as shown by comparison of Figs. 4.20 and 4.21. For the $P2_1ma$ and *I*4*mm* joint refinements of data obtained at 280, 300, 320 and 340 °C, the relative fraction of phase G increased,

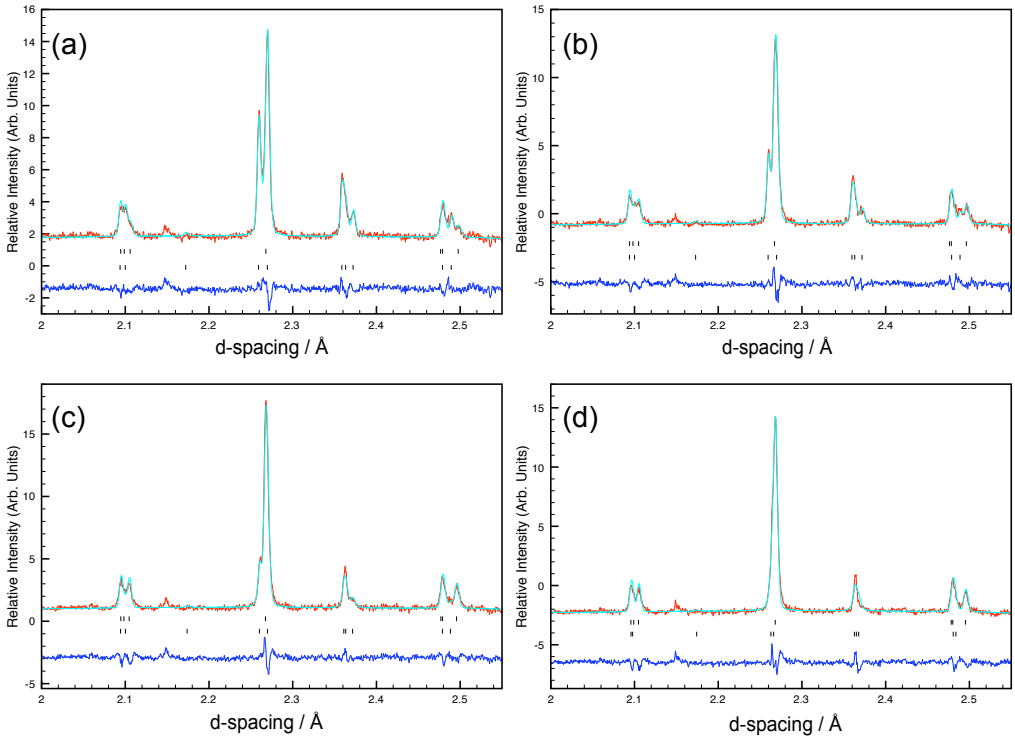

Figure 4.20: Rietveld profiles of KNN-3 obtained from refinement of NPD data at different temperatures. (a) 280 °C, (b) 300 °C, (c) 320 °C and (d) 340 °C. All data were refined to the $P2_1ma$ and $I4/mmm$ space groups (lower and upper tick marks, respectively). Phase fractions are given in the text. wRp = 4.01%, 3.96%, 3.92% and 3.99%, respectively. The small peak at approximately 2.15 Å is attributed to vanadium from using the vanadium can used in the experiment.

giving values of 23, 43, 59 and 61%, with the fraction of phase Q decreasing accordingly. These values are, unsurprisingly, very similar to those obtained for the $P2_1ma$ and $I4/mmm$ joint phase refinements. Unfortunately, it is *not* possible to determine which, if either, of the two tetragonal phases is the correct assignment, though the unusual anisotropy in the *a* versus *c* parameters supports the polar option.

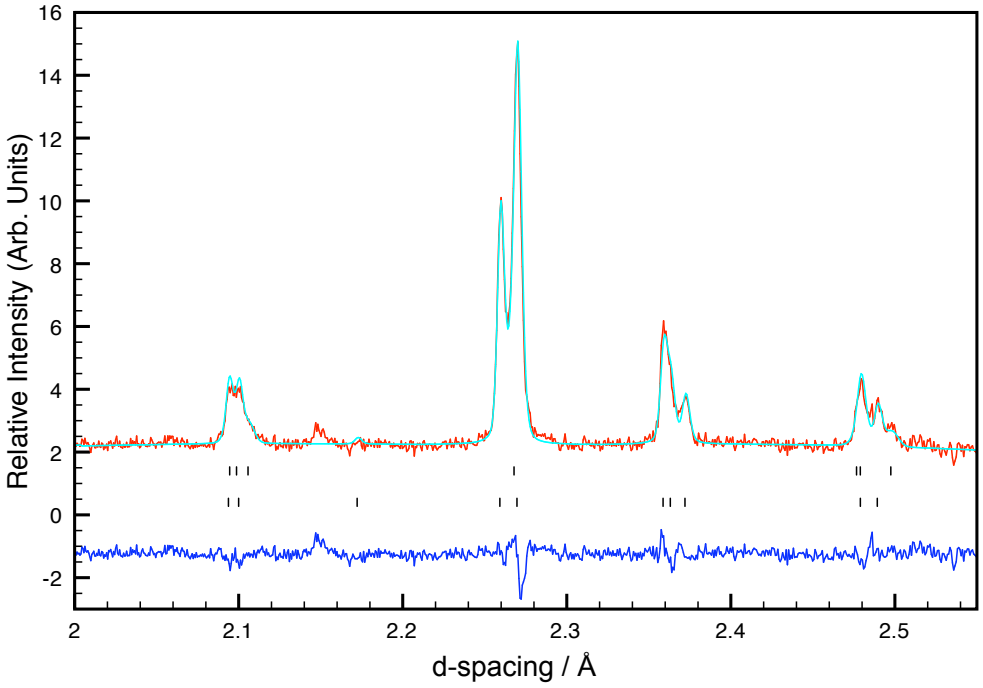

Figure 4.21: Rietveld profile (NPD) of KNN-3 obtained at 280 °C showing the superlattice region, refined in space groups $P2_1ma$ (lower tick marks) and $I4mm$ (upper tick marks). wRp = 3.59%.

Consequently, it cannot be determined, from diffraction data alone, which of the two space groups, $I4/mmm$ or $I4mm$, is the correct assignment. To complement this work, DFT calculations were performed for the two tetragonal phases to determine their (a) initial energies, and (b) energies after structural optimisation. The $I4mm$ structure gave the slightly lower energy (after optimisation) of the two by approx. 0.004 eV/f.u.. This value is relatively small when compared to some of the energy differences between the high temperature phases of $NaNbO_3$,[32] and so it cannot be concluded that one is 'preferred' over the other based on a calculation of internal energy (see Chapter 3). The best way to distinguish between the polar and non-polar options would be using physical property measurements. Second harmonic generation (SHG) measurements have been shown to be effective in distinguishing polar and non-polar phases, and, consequently, this would possibly be the best technique to use to accurate assign the space group of phase G (although this may be made more challenging owing to the presence of (the polar) phase Q).

NPD data obtained for KNN-3 at 360 °C, however, contained an additional, 'broad' reflection in the superlattice region, not too dissimilar to the peak assigned to the T_4 mode in previous work on $NaNbO_3$.[32] Glazer[7] and Thomas[12] have both previously suggested that a phase transition occurs around this temperature. In light of these observations, it is believed that the presence of this additional peak is indicative of a phase change having occurred. As no one consistent 'notation' has been assigned to this phase, *i.e.*, a letter, it is denoted here as phase T, not to be confused phases T1 or T2 of $NaNbO_3$.

4.4.3. Phase T

All data presented in this section were obtained from NPD of KNN-3. At temperatures above 360 °C, an additional peak can be seen in the superlattice region, which is believed to be similar to the peak arising from the T_4 mode in $NaNbO_3$.[32] This additional reflection is not indexed with a $2a_p \times 2a_p \times 2a_p$ cell metric, and as such, a $4a_p$ expansion was applied along each crystallographic axis independently. However, this was not able to index the observed reflection. Consequently, a $6a_p$ expansion was also considered. In a $2a_p \times 2a_p \times 6a_p$ structure (note, at this point, the lengths are not describing a specific crystallographic axis, *i.e.*, the $6a_p$ repeat unit could be along a, b or c), the M-, R- and T-points are all present, as shown in Chapter 3. The M- and R-points each have a fixed *k* value of (1/2, 1/2, 0) and (1/2, 1/2, 1/2), respectively. The R-point, therefore, results in a doubling of the unit cell. However, for the T_4 mode, there are two possible values of *k*, as observed for $NaNbO_3$, (1/2, 1/2, 1/3) and (1/2, 1/2, 1/6). The former will result in a tripling of the unit cell along c, whereas the latter results in a 6-repeat unit.

Both T_4 modes are allowed in the cell (determined using ISODISTORT), and as such, the $6a_p$ unit could be caused by (a) the T_4 k = (1/2, 1/2, 1/6) mode, or (b) the simultaneous presence of the R_4^+ and T_4 k = (1/2, 1/2, 1/3) modes about the same axis, where the R_4^+ doubles the cell and the T_4 mode causes an additional tripling. There are, in fact, two peaks indexed by the T_4 mode - one at 2.29 Å and the other at 2.43 Å (note, this is similar to phase R of $NaNbO_3$).[32] These peaks are indexed as (314)/(134) and (132)/(312) reflections, respectively, and it can be seen that l = 2n, *i.e.*, all l values are even. This observation is more compatible with the former T-

point, *i.e.*, k = (1/2, 1/2, 1/3), suggesting that the T_4 mode triples the unit cell along one direction, whilst the simultaneous presence of the R_4^+ causes an additional doubling. At this point, it cannot be determined if the M_3^+ distortion mode is also present about the same axis. Ahtee and Glazer proposed that, for temperatures above 360 °C, phase G underwent a series of $NaNbO_3$-like transitions,[7] *i.e.*, to phase R and S, *etc.*[34,35]

The choices of starting models for phase T were tetragonal cells (space group *P4*/*mbm*) with cell metrics $\sqrt{2}a_p \times \sqrt{2}a_p \times 6a_p$ and $2a_p \times 2a_p \times 6a_p$. The latter cell metric does not possess the three required distortion modes, whereas the former does. A reasonable level of fit was observed for the data obtained at 380 °C, although closer inspection of the M-, R- and T-point peak fits revealed that none were satisfactory, as shown in Fig. 4.22. As the figure shows, the T_4 point peak at 2.29 Å has a poor intensity match, as do both R- and M-point peaks at around 2.36 and 2.47 Å, respectively. The poor flexibility of the tetragonal model to accurately fit the data (with an emphasis on the superlattice region) suggests that a *lowering* of the symmetry may be required. The three required distortion modes are present for three types of orthorhombic cell (with the required cell metrics): a primitive $\sqrt{2}a_p \times \sqrt{2}a_p \times 6a_p$ cell, a *C*-centered $2a_p \times 2a_p \times 6a_p$ cell, and the lower-symmetry primitive $2a_p \times 2a_p \times 6a_p$ cell. For each, two possible space groups are available, with a detailed overview of each given in work by Peel *et al.*[32] Rietveld refinements in the higher-symmetry primitive and C-centered cells are shown in Fig. 4.23, where it can be seen that neither the primitive $\sqrt{2}a_p \times \sqrt{2}a_p \times 6a_p$ cells (space groups *Pnma* and *Pbam*) or the *C*-centered $2a_p \times 2a_p \times 6a_p$ cells (space groups *Cmcm* and *Cmmm*), fit both the M and R-point peaks particularly well. The *Pnma* model fits both the M- and R-point peaks poorly. The *Pbam* model poorly fits the R-point peak. The *Cmcm* model shows a poor fit and the *Cmmm* model fits both peaks 'better' than the others, although the M-point peak is still not sufficiently fitted. The next step was, naturally, to lower the symmetry further to the primitive $2a_p \times 2a_p \times 6a_p$ cells of which there were two models that possess the necessary distortion modes - *Pnma* and *Pmmn*, where the former has the $6a_p$ expansion along the *b* axis and the latter along *c*. Rietveld refinements were

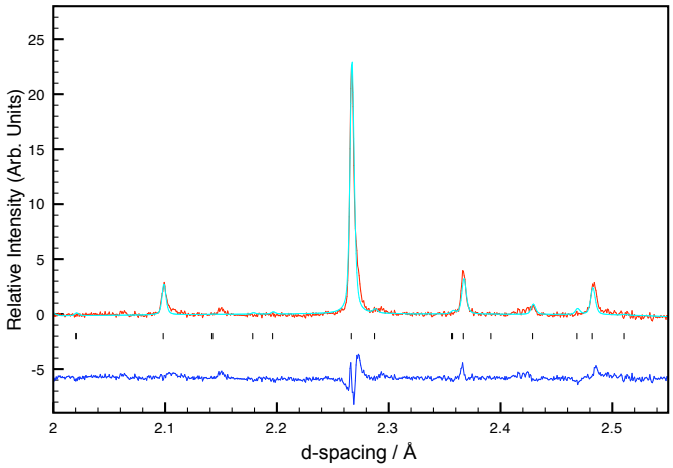

Figure 4.22: Portion of the Rietveld profile (NPD) of KNN-3 obtained at 380 °C, refined in space group *P*4/*mbm*. wRp = 5.76%. The fit of the M- and R-point peaks is noticeably poor, suggesting that the cell metrics may be incorrect.

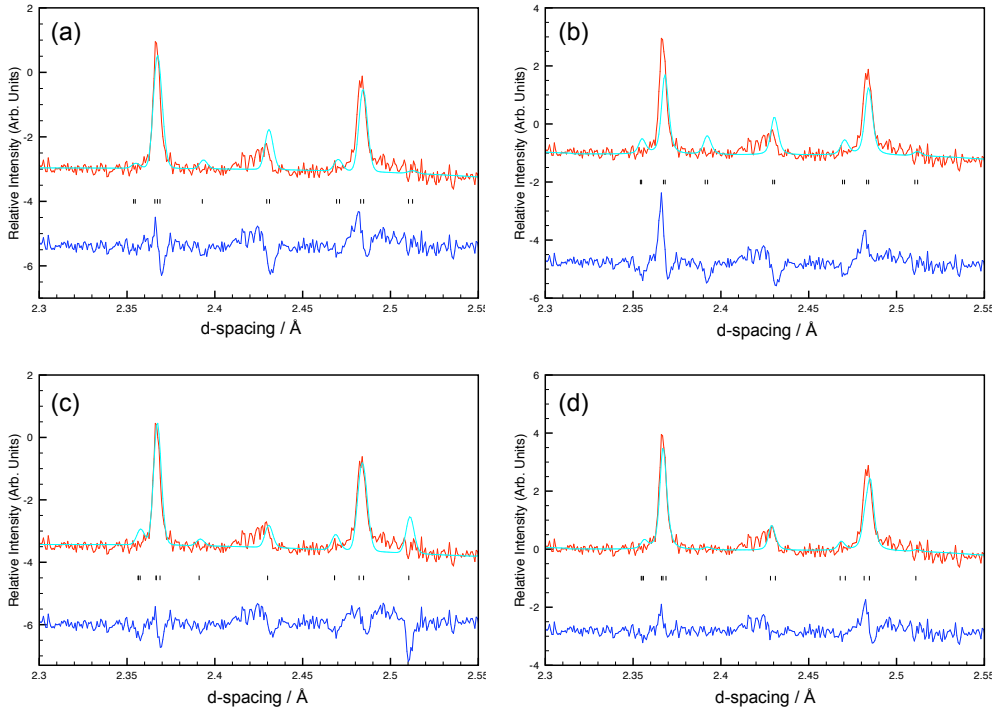

Figure 4.23: Portions of the Rietveld profiles of KNN-3 (NPD) obtained at 380 °C, showing the M-, R- and T-point peaks, when refined to the (a) *Pnma*, (b) *Pbam*, (c) *Cmcm* and (d) *Cmmm* space groups. The cell metrics and an explanation of why these space groups were chosen can be found in the main text.

performed using both space groups, for which *Pnma* produced a *marginally* better fit, as shown in Fig. 4.24. Data over the temperature range 380 to 440 °C were refined to the *Pnma* model, and the evolution of the lattice parameters (as a function of temperature) are shown in Fig. 4.25, normalised to the aristotype cell metric. It can be seen that the parameters all increase almost linearly, with no convergence shown. Crystallographic data for phase T (*Pnma*) can be found in Appendix C. The T-point peak is fit poorly in all the refinements attempted. There are three possible reasons for the broad nature of the T-point peak, both of which make accurate structural determination substantially more challenging: (i) the presence of shorter-length-scale correlations in the data set; (ii) the possibility of an incommensurate structure, and (iii) possible mixtures of the T-point distortion along more than one crystallographic axis. The second option - incommensurate modulation - is perhaps the more likely of the three, and has been reported in previous literature.[36, 37] Incommensurate modulation has been shown to sometimes occur along the 'long' crystallographic axis (*e.g.*, 4- or 6-repeat) in Na-based perovskites.[38] It is entirely possible that the structure at 380 °C requires some incommensurate modulation along the c axis (6-repeat), to account for the broad nature of the T_4-point peak. The inclusion of such effects is, at present, beyond the scope of the work presented in this thesis, although it does offer an intriguing possibility for the future.

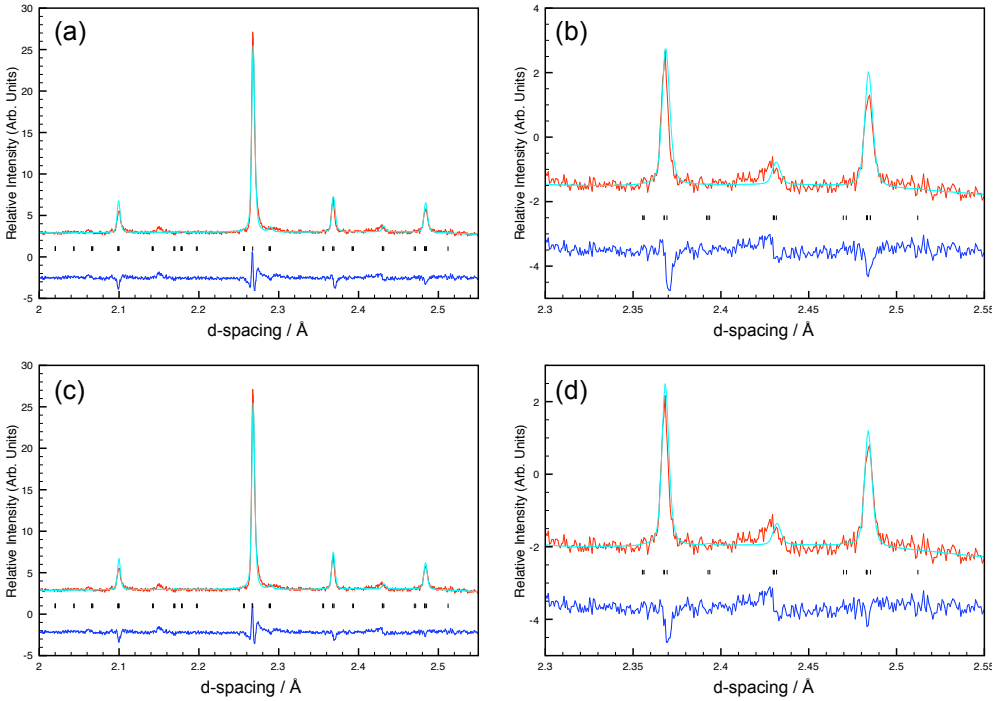

Figure 4.24: Portions of the Rietveld profiles of KNN-3 (NPD) obtained at 380 °C, refined in space groups *Pmmn* (a and b) and *Pnma* (c and d). (a and c) show the superlattice regions and (b and d) show expansions of the M-, R- and T-point peaks. wRp = 3.96% and 3.89%, respectively.

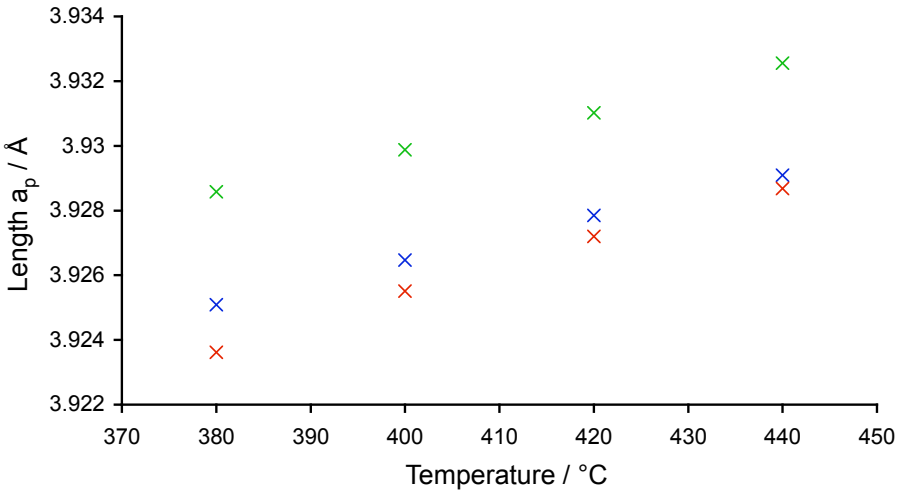

Figure 4.25: Lattice parameters as a function of temperature, normalised to the aristotype cell metric, for a sample of KNN-3. Data are obtained from Rietveld refinement of NPD data and show the *a*, *b* and *c* parameters in green, blue and red, respectively.

4.4.4. Temperature-Dependent $NaNbO_3$-like Phase Transitions

At 480 °C, the complete removal of the T-point peak is observed for KNN-3, resulting in the observation of M- and R-point peaks only. This immediately suggests that a much smaller unit cell size would be sufficient to fully index all the peaks. Results by Ahtee and Glazer suggest that KNN-3 undergoes a series of $NaNbO_3$-like phase transitions as a function of temperature.[7] The diffraction pattern of KNN-3, obtained at 480 °C, is very similar to that of $NaNbO_3$ at 540 °C, which refines well to the orthorhombic non-polar *Cmcm* space group, with cell metric $2a_p \times 2a_p \times 2a_p$. The *P*4/*mbm* phase of $NaNbO_3$ has cell metric $\sqrt{2}a_p \times \sqrt{2}a_p \times 1a_p$, which was determined to be incompatible with the diffraction data at 480 °C because of the lack of the R_4^+ mode. The natural choice was to *double* the length of the c axis to determine if a satisfactory fit could be obtained. The Rietveld profile is shown in Fig. 4.26, where it can be seen that the quality of the fit is relatively poor (again, with respect to the superlattice region), indicating that more flexibility may be required. Consequently, the symmetry was lowered to consider *C*-centered orthorhombic cells, of which models in two space groups, both with cell metric $2a_p \times 2a_p \times 2a_p$, were refined, as shown in Fig. 4.27. (There is no reason to suggest that there is a co-existence of phases in this temperature region.) The figure shows that (a) there is no T-point peak in this region, (b) the M- and R-point peaks are well-fitted, and (c) that no real differences in the fits can be seen for the two space groups: *Cmcm* and *Cmmm*. (Crystallographic data can be found in Appendix C). It is not possible to determine which is the preferred model based solely on the Rietveld refinement. However, with the slightly better goodness of fit parameters for the *Cmcm* model, in addition to the suggestion by Ahtee and Glazer[7] that the structure most likely belongs to the *Cmcm* space group, it could be proposed (somewhat tentatively, however) that *Cmcm* is most likely the correct assignment.

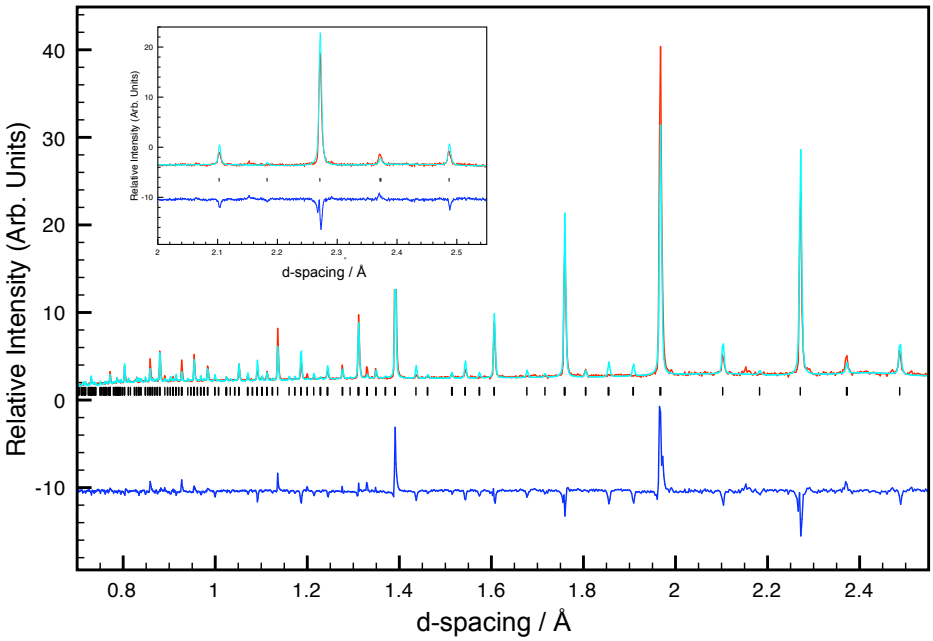

Figure 4.26: Rietveld profile (NPD) of KNN-3 obtained at 480 °C, with expansion of the superlattice region shown (inset), refined in space group *P*4/*mbm*.

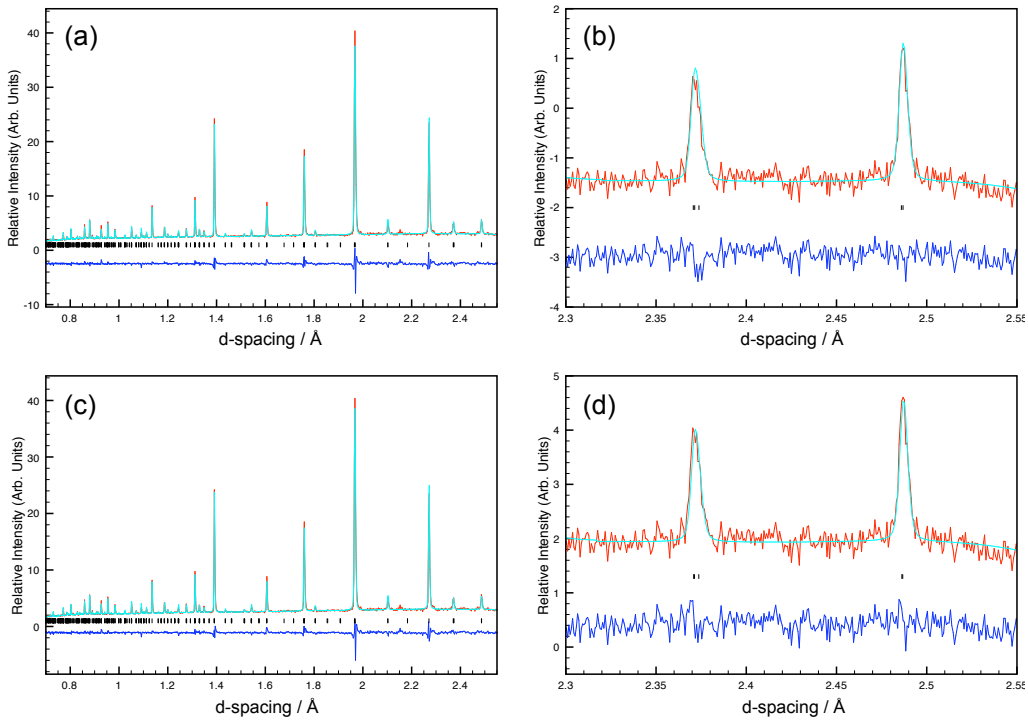

Figure 4.27: Rietveld profiles (NPD) of KNN-3 obtained at 480 °C, refined in space groups *Cmcm* (a and b) and *Cmmm* (c and d), where (b) and (d) show expansions of the M and R-point peaks. wRp = 4.87% and 4.99%, respectively.

4.4.5. Conclusions

By using complementary NPD and symmetry mode analysis we have been able to propose structures for phases G and T for KNN-3. Structures were determined using a similar convention to that outlined in Ref. 32. Accurate determination of phase G is made more challenging by its co-existence with phase Q, which causes several peaks to overlap. Unfortunately, for samples of KNN-3, 5 and 8, phase G was never formed exclusively. Three structures for phase G all gave good levels of fit to the NPD data (280 to 340 °C), space groups: $P4_2/nmc$, $I4/mmm$ and the polar $I4mm$. The former possesses the M_3^+ and R_4^+ distortion modes (irreducible representations), whereas the *I*-centred cells contain only the M_3^+ mode, relating to BO_6 octahedral tilting only (although several other modes relating to cation displacements are also present but are not the dominant distortion modes). Joint $P2_1ma$ and $P4_2/nmc$ models gave a good refinement to the NPD data, fitting both M- and R-point peaks well. However, there is no evidence to suggest that phase G *needs* the R-point, and as such, the *I*-centred cells were considered. Very good levels of fit are obtained for both models (as part of a multiphase refinement with phase Q), making it impossible to unambiguously state which is preferred. SHG measurements could be performed to determine if the phase belonged to a centrosymmetric or polar space group, which would allow one to determine if the correct assignment was $I4/mmm$ (non-polar) or $I4mm$ (polar). The difficulty in this, however, is the co-existence of the polar phase Q. It would, therefore, be difficult to suggest that phase G be polar based on this measurement alone.

The assignment of phase T was more straightforward, in that the phase was present exclusively, meaning that no overlapping peaks (from two different phases) were observed. This allowed us to conclude that phase T contained the M-, R- and T-points. The d-spacing values of the T-point peaks, coupled with their l = 2n indexing, suggested that the T_4 k = (1/2, 1/2, 1/3) point was present, rather than the k = (1/2, 1/2, 1/6) point. A similar procedure for structural determination was used to that outlined in Ref. 32, although the final results are noticeably less 'clear-cut.' Compared to previous work by Peel *et al*. on $NaNbO_3$,[32] the T-point peak (d = 2.45 Å) is substantially broader. It is so broad, in fact, that none of the models tested actually fit

the peak particularly well! The model with space group *Pnma* fit the M- and R-point peaks very well, yet the T-point peak was fitted to a much poorer level.

References

[1] Lines, M. E., Glass, A. M., Principles and applications of ferroelectrics and related materials, Oxford University Press, Oxford, 1977.

[2] Sakowski-Cowley, A. C., Ph.D. Thesis, University of Cambridge, 1967.

[3] Lefkowitz, I., Lukaszewicz, K., Megaw, H. D. *Acta Cryst*., 1966, **A20**, 670.

[4] Saito, Y., Takao, H., Tani, T., Nonoyama, T., Takatori, K., Homma, T., Nagaya, T., Nakamura, M., *Nature,* 2004, **432**, 84.

[5] Sakowski-Cowley, A. C., Lukaszewicz, K., Megaw, H. D. *Acta Cryst*., 1969, **B25**, 851.

[6] Shuvaeva, V. A., *Ferroelectrics,* 1993, **141**, 307.

[7] Ahtee, M., Glazer, A. M., *Acta Cryst.,* 1976, **A32**, 434.

[8] Ahtee, M., Hewat, A. W., *Acta. Cryst.,* 1978, **A34,** 309.

[9] Jaeger, R. E.; Egerton, L., *J. Am. Ceram. Soc.,* 1962, **45**, 209.

[10] Dai, Y. J., Zhang, X. W., Chen, K. P.; *Appl. Phys. Lett.,* 2008, **92**, 152904.

[11] Johnston, K. E., Tang, C. C., Parker, J. E., Knight, K. S., Lightfoot, P., Ashbrook, S. E., *J. Am. Chem. Soc.,* 2010, **132**, 8732.

[12] Zhang, N., Glazer, A. M., Baker, D. W., Thomas, P. A., *Acta Cryst.,* 2009, **B65**, 291.

[13] Glazer, A. M., *Acta Cryst.,* 1972, **B28**, 3384.

[14] Baker, D. W.; Thomas, P. A.; Zhang, N.; Glazer, A. M.; *Appl. Phys. Lett.,* 2009, **95**, 091903.

[15] Glazer, A. M., Megaw, H. D., *Acta Cryst.,* 1973, **A29**, 489.

[16] Glazer, A. M., Ahtee, M., Megaw, H. D., *Acta Cryst.,* 1972, **A28**, 179.

[17] Yuzyuk, Y. I., Gagarina, F., Simon, P., Reznitchenko, I. A., Hennet, I., Thiaudiere, D., *Phys. Rev. B.*, 2004, **69**, 114105.

[18] Johnston, K. E., Ph.D. Thesis, University of St Andrews, 2010.

[19] Chaker, C., Gharbi, W. E., Abdelmoula, N., Simon, A., Khemakhem, H., Maglione, M., *J. Physics and Chemistry of Solids,* 2011, **72**, 1140.

[20] Peel, M. D., Ashbrook, S. E., Lightfoot, P., *Inorg. Chem.*, 2013, DOI: 10.1021/ic401061t

[21] Konieczny, K., Śmiga, W., *Ferroelectrics,* 2011, **417**, 151.

[22] Clark, S. J., Segall, M. D., Pickard, C. J., Hasnip, P. J., Probert, M. J., Refson, K., Payne, M. C. Z. *Kristall*., 2005, **220**, 567.

[23] Pickard, C. J., Mauri, F., *Phys. Rev. B,* 2001, **63**, 245101.

[24] ICSD website: cds.rsc.org

[25] Konieczny, K., Śmiga, W., *Ferroelectrics,* 2011, **417**, 151.

[26] Mackenzie, K. J. D., Smith, M. E., Multinuclear Solid-State NMR of Inorganic Materials, Elsevier Science, Oxford, 2002, p 495-500.

[27] Carr, H. Y., Purcell, E. M., *Phys. Rev.*, 1954, **94**, 630.

[28] Meiboom, S., Gill, D., *Rev. Sci Instrum.*, 1958, **29**, 688.

[29] Alonso, J. A., Martínez-Lope, M. J., Casais, M. T., Fernández-Díaz, M. T., *Inorg. Chem.*, 2000, **39**, 917.

[30] Martínez-Lope, M. J., Alonso, J. A., Retuerto, M., Fernández-Díaz, M. T., *Inorg. Chem.*, 2008, **47**, 2634.

[31] Howard, C. J., Stokes, H. T., *Acta Cryst.*, 1998, **B54**, 782.

[32] Peel, M. D., Thompson, S. P., Duaod-Aladine, A., Ashbrook, S. E., Lightfoot, P., *Inorg. Chem.,* 2012, **51**, 6876.

[33] Web-based program: http://stokes.byu.edu/iso/isodistort.php Access date: 12/05/12

[34] Ahtee, M., Glazer, A. M., Megaw, H. D., *Philos. Mag.*, 1972, **26**, 995.

[35] Megaw, H. D., *Acta Cryst*., 1968, **A24**, 589.

[36] Graetsch, H. A., Pandey, C. S., Schreuer, J., Burianek, M., Muhlberg, M., *Acta Cryst.*, 2012, **B68**, 101.

[37] He, H., Tan, X., *Phys. Rev. B.*, 2005, **72**, 024102.

[38] Balagurov, A. M., Koroleva, E. Y., Naberezhnov, A. A., Sakhnenko, V. P., Savenko, B. N., Ter-Oganessian, N. V., Vakhushev, S. B., *Phase Trans.*, 2006, **79**, 163.

Chapter 5

A Crystallographic Study of the $Li_xNa_{1-x}NbO_3$ System

5.1. Introduction

For the $Li_xNa_{1-x}NbO_3$ perovskite system, the compositional diagram has been previously studied,[1] and reports are unanimous that low-level substitution causes a change from phase P to Q, as discussed in Chapter 4. However, for values beyond x = 0.1, there is a disagreement in the literature and reports are often conflicting. Chaker *et al.* proposed that phase Q is formed exclusively for values up to x = 0.15,[2] whereas Yuzyuk *et al.* have proposed that a rhombohedral phase exists in a narrow compositional region at around x = 0.12.[3] For compositions beyond x = 0.2, however, the perovskite system has not been thoroughly explored, apart from where x = 1. Lithium niobate ($LiNbO_3$, denoted LN) possesses the polar *R*3*c* space group at room temperature.[4] However, there are several reports of LN containing antisite Nb^{5+}, in which Nb^{5+} cations also occupy A-site vacancies, present due to the absence of some Li^+.[5,6] A general overview of the structure and phases of $NaNbO_3$ and their substitution can be found in Chapters 3 and 4.[7-18]

The work in this chapter will focus solely on understanding the compositional phase diagram of the LNN perovskite system over the range $0 < x < 1$, at room temperature. In Chapter 4, the conversion of phase P to Q was shown for LNN and this will not be repeated here. The compositional phase diagram will be investigated using a combination of X-ray and neutron powder diffraction and solid-state NMR spectroscopy. Firstly, the region $0.08 < x < 0.20$ will be discussed and the focus will be on two important observations: the dependence of the phase fractions on synthetic conditions, and the conversion of the metastable phase Q to a rhombohedral phase when left under ambient conditions. The annealing temperature and cooling rate are found to play an important role in determining the relative phase fractions formed, with 'harder' approaches (*i.e.*, higher annealing temperature and faster cooling rates) favouring formation of the rhombohedral phase. Secondly, the region $x \approx 0.20$ will be

discussed, where it will be shown that the rhombohedral phase can be formed exclusively. Additionally, for x > 0.25, the presence of a second rhombohedral phase is also observed using both diffraction and NMR techniques. The rhombohedral phases, which adopt the same space group, *R*3*c*, are, however, structurally and compositionally different, with one being Na-rich and the other Li-rich. The resulting phase fractions are found to be independent of the synthetic conditions used. The work described in this chapter has recently been published where some additional observations have been made regarding the compositional phase diagram,[19] and these will also be discussed in this chapter. A diagram, summarizing the different regions at which different phases are found to exist, is presented in Fig. 5.1.

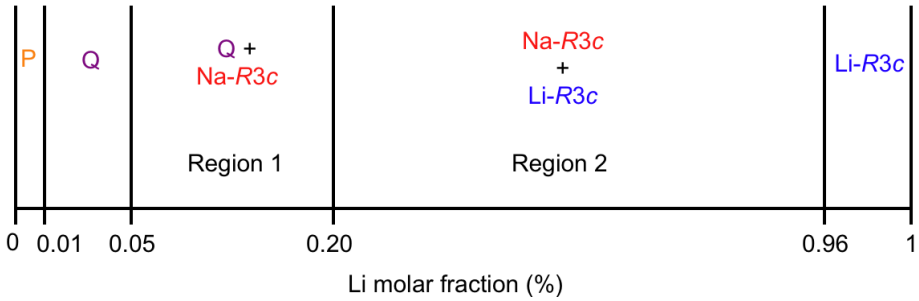

Figure 5.1: Schematic representation (not to scale) of the compositional diagram for the LNN series. Phase P denotes the centrosymmetric polymorph (space group *Pbcm*).

5.2. Solid-state NMR

Solid-state ^{23}Na (I = 3/2) NMR spectra were acquired using Bruker Avance III spectrometers, equipped with wide-bore 14.1 or 9.4 T magnets, at Larmor frequencies of 158.746 and 105.842 MHz, respectively. Samples were packed into conventional ZrO_2 (4 mm) rotors and rotated at a MAS rate of 12.5 kHz. ^{23}Na chemical shifts were referenced to 1 M $NaCl_{(aq)}$ using a secondary reference of $NaCl_{(s)}$ (δ_{iso} = 7.8 ppm). Conventional ^{23}Na MAS NMR spectra were obtained using single-pulse experiments, with pulse lengths of 1.5 and 1.9 μs, at 14.1 and 9.4 T, respectively, with recycle intervals of 5 s. All MQMAS spectra were acquired using a z-filtered pulse sequence (see Fig. 2.21). High-power pulses (of 5 and 1.5 μs with $\omega_1/2\pi$ = 100 kHz at 9.4 T and

6 and 1.9 μs with $\omega_1/2\pi$ = 95 kHz at 14.1 T) were used for triple-quantum excitation and conversion, respectively. The final 90° pulse was applied with low power (~9 kHz at both fields) to be selective for the CT. All MQMAS spectra are shown post-shearing and are all the result of averaging 192 transients for each of 80 t_1 increments of 80 μs with a 5 s recycle interval. Additional experimental details can be found in the relevant figure captions or sections.

5.4. Region I (0.08 < x < 0.20)

5.4.1. Introduction

Three different annealing temperatures were used to synthesise samples of LNN-10, 12 and 15: 850, 950 and 1050 °C. Using annealing temperatures below 850 °C was found to result in incomplete reactions, with evidence of carbonates and oxides in the samples (determined from Rietveld refinement of l-PXRD data). Fig. 5.2 shows the l-PXRD diffraction pattern of LNN-10 synthesised at 750 °C, which clearly shows that the reaction is incomplete, as evidenced by the presence of multiple non-perovskite peaks. The annealing temperature used can be manipulated to alter the relative ratios of the phases formed, with higher temperatures favouring formation of the Na-*R*3*c* phase and lower temperatures favouring phase Q. Such differences were observed for all samples of LNN-10, 12 and 15 (see Section 5.4.3). In addition, the cooling rate used also affects the relative phase fractions formed, with faster rates (referred to as fast cooling, FC) favouring formation of the Na-*R*3*c* phase while slower rates (slow cooling, SC) favour formation of phase Q. Additionally, it was observed that phase Q converts, over time, to the Na-*R*3*c* phase at ambient conditions. In samples of LNN-10, 12 and 15, phase Q was found to undergo this conversion, regardless of the initial annealing temperature and/or cooling rate used. The rates of change were investigated, and are discussed in Section 5.4.5. In the subsequent sections, the effects previously discussed are considered. However, unless stated, each effect should be considered individually. When considering composition, all the samples discussed

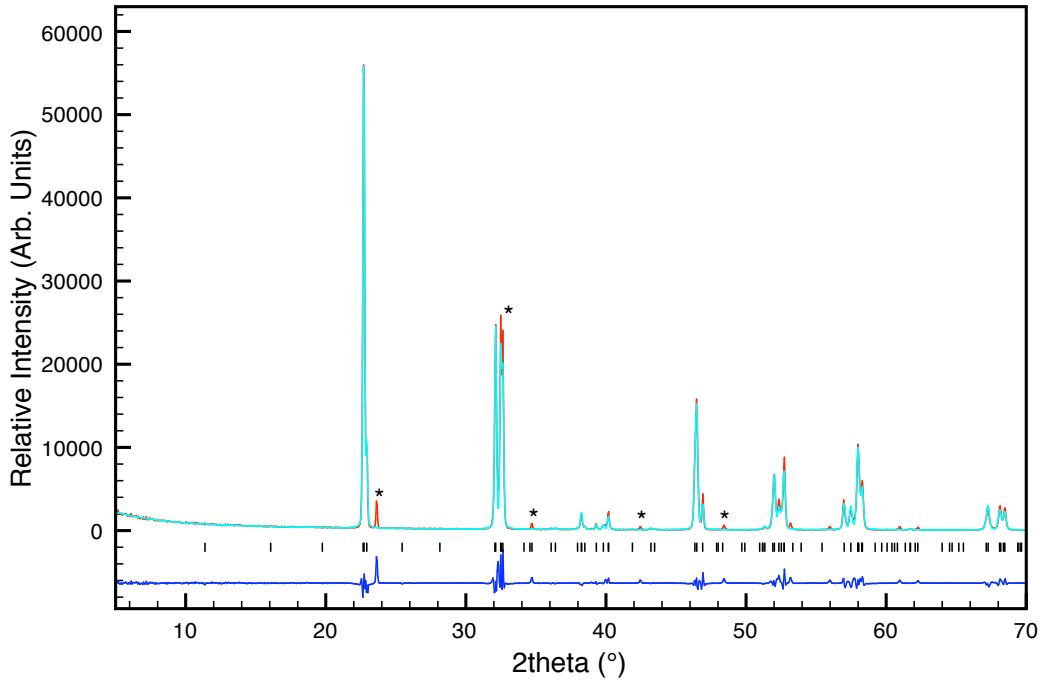

Figure 5.2: Rietveld profile (l-PXRD) of LNN-10, synthesised at 750 °C for 18 hours, refined in space group $P2_1ma$. An * denotes that a peak is not indexed by either phase Q or Na-$R3c$. The fit is noticeably poor.

were made using the same annealing temperature and cooling rate, and characterisation data recorded within 2 days of synthesis. For example, when considering annealing temperature, the cooling rate used was always the same and data were obtained within 2 days of sample synthesis (this reduces the effects of phase interconversion over time). The effects of composition and annealing temperature on the phase fractions are studied using NPD, whilst changes due to cooling rate and time at ambient temperature are studied by l-PXRD and ^{23}Na solid-state NMR spectroscopy. The different diffraction techniques used can often produce small differences in the relative phase fractions obtained from Rietveld refinement. Furthermore, samples had to be re-made a number of times in order to investigate the effects of annealing temperature, cooling rate and time at ambient temperature, leading, again, to small inconsistencies in the exact phase fractions. Consequently, when comparing results obtained from diffraction data, it is more important to focus on the trends observed and not the absolute values obtained. Fig. 5.3 shows the crystallographic structures of the orthorhombic and rhombohedral phases present in Region 1.

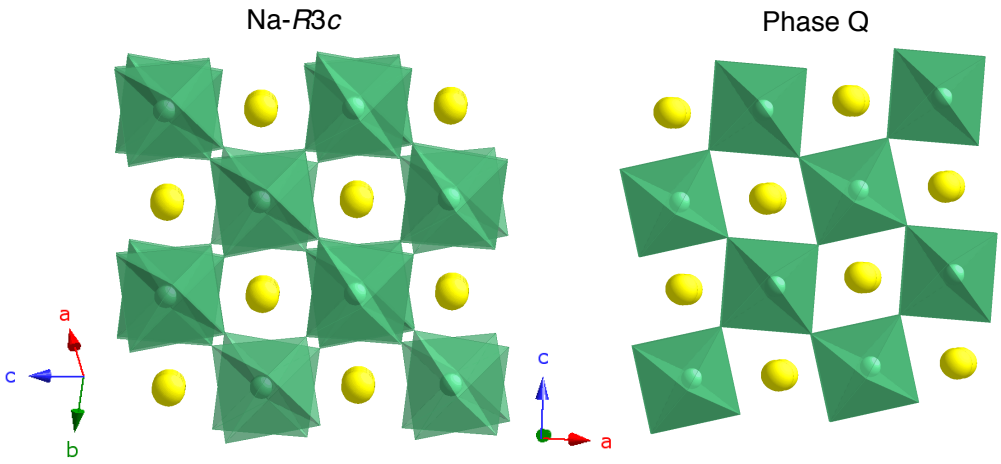

Figure 5.3: Structures of phases Na-*R*3*c* and Q showing the different NbO_6 (green polyhedra) tilting systems in the two. In Glazer notation, Q has the $a^-b^+a^-$ tilt system and Na-*R*3*c* the $a^-a^-a^-$ tilt system. Structures were determined from refinement of NPD data and can be found on the ICSD.[19]

5.4.2. The Effects of Composition

Within the compositional region $0.10 \leq x \leq 0.15$, the relative phase fractions (Q and Na-*R*3*c*) formed are found to be highly dependent upon the exact composition. The higher annealing temperatures (1050 °C) were found to favour formation of the Na-*R*3*c* phase, with lower temperatures (850 °C) favouring formation of phase Q. This observation was confirmed using Rietveld analysis of NPD data, obtained from HRPD. Table 5.1 shows the relative proportions of phase Q (%) for the three compositions studied: LNN-10, LNN-12 and LNN-15. As the table shows, for any given temperature, the proportion of phase Q decreases as the proportion of lithium used in the reaction increases. Interestingly, the largest change in phase fractions occurred between 850 and 950 °C for both LNN-10 and LNN-12 (this is difficult to

Table 5.1: Relative fractions of phase Q for three different compositions of LNN, each synthesised at three different annealing temperatures. Data are obtained from Rietveld refinement of NPD data. Values are quoted to the nearest whole number as opposed to quoting the much smaller error derived from GSAS, better reflecting the experimental error and not the fitting error.

Temperature (°C)	LNN-10 (% Q)	LNN-12 (% Q)	LNN-15 (% Q)
850	86	47	31
950	31	6	0
1050	19	2	0

compare to LNN-15 owing to the complete removal of phase Q when synthesised at 950 °C). Fig. 5.4 shows the superlattice regions of the Rietveld NPD profiles for LNN-10, 12 and 15, where it can be seen that the fraction of phase Q decreases with increasing Li content. Crystallographic data and goodness of fit parameters can be found in Appendix D.

Rietveld refinement of LNN-20 (synthesised at 1050 °C) confirmed the presence of a phase pure sample, with the data refining well to the Na-*R*3*c* model. The data, shown in Fig. 5.5, confirm that phase Q has not been formed at all (and it will be shown in Section 5.4.3 that it is not present when synthesised at 850 °C). Corresponding crystallographic data can be found in Appendix D.

Using Rietveld analysis, attempts were made to determine the fractional occupancy of the A- site for phases Na-*R*3*c* and Q, *i.e.*, the proportion of Li^+ and Na^+ on this site. However, this is more challenging for phase Q, owing to the smaller (if any) relative phase fraction (for LNN-12, 15 and 20), with large errors being observed. As such, no values for phase Q are reported here. The A-site occupancies for the Na-*R*3*c* phase as a function of composition are given in Table 5.2, where it can be seen that the composition of the phase matches well with the reactant stoichiometry. These results corroborate the changes observed in lattice parameters as a function of composition, as shown in Fig. 5.6. Overall, this represents a decrease in the unit cell size (see Appendix D for lattice parameters obtained from refinement) for samples of LNN-10,

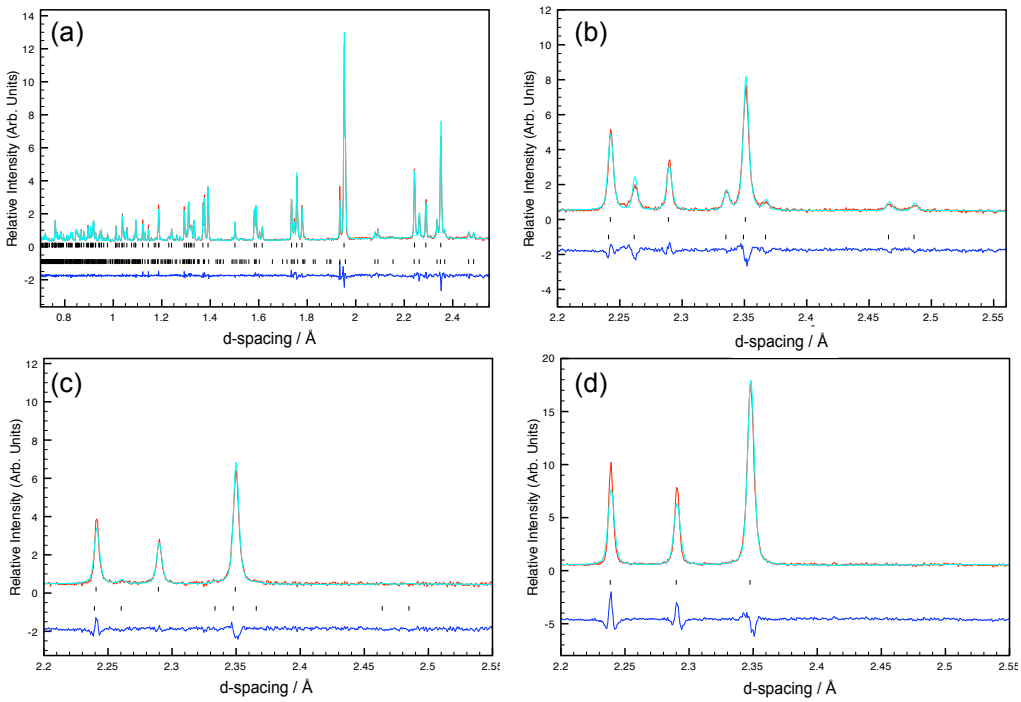

Figure 5.4: Portions of the Rietveld profiles (NPD) of (a and b) LNN-10, (c) LNN-12 and (d) LNN-15, refined in space groups $P2_1ma$ and Na-$R3c$ (lower and upper tick marks, respectively, and used throughout unless otherwise stated). LNN-15 (d) is refined in space group Na-$R3c$. All samples were synthesised at 950 °C for 18 hours. Corresponding crystallographic data and goodness of fit parameters can be found in Appendix D.

12, 15 and 20, respectively. This is an expected result in light of the data obtained for the A-site fractional occupancies of the Na-$R3c$ phase: *as the reactant molar ratio of Li increases, the amount of* Li^+ *on the A-site of Na-R3c also increases, resulting in a decrease in the unit cell volume.* This decrease is because of the small ionic radius of Li^+ compared to Na^+ (0.78 and 1.02 Å respectively, in six-coordination). The results are easily explained by Vegard's law, and show that this region of the compositional diagram can be considered to be a solid solution.

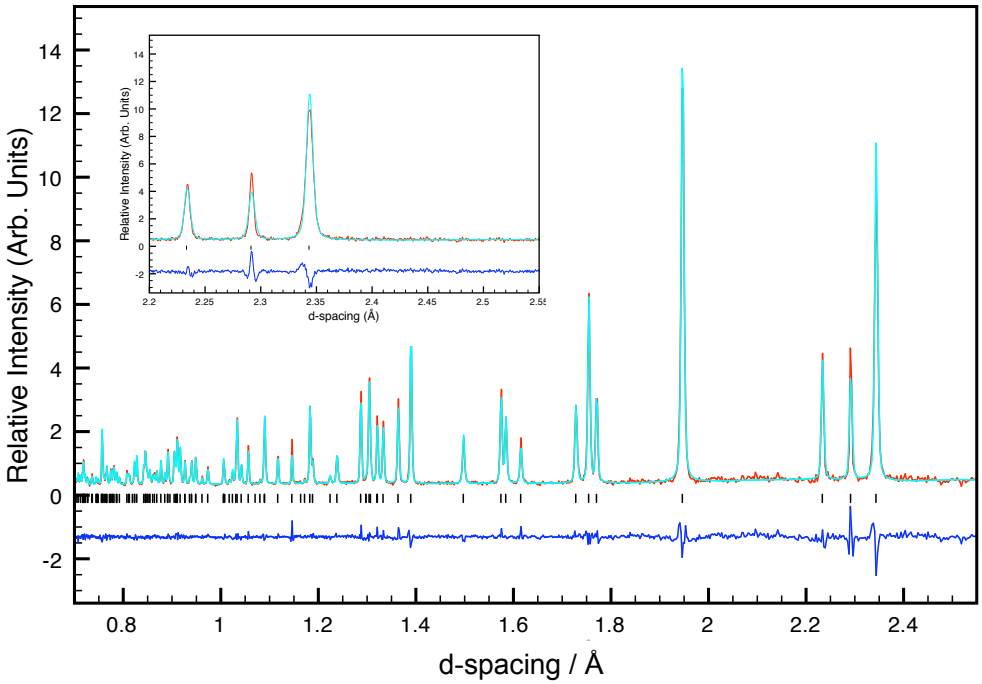

Figure 5.5: Rietveld profile (NPD) of LNN-20 (synthesised at 1050 °C) refined in space group Na-*R*3*c*, with expansion of the superlattice region also shown (inset). Corresponding crystallographic data and goodness of fit parameters are given in Appendix D.

Table 5.2: The percentages of Li on the A-site of the Na-*R*3*c* phase for different samples of LNN. All data are obtained from Rietveld refinement of NPD data, and all samples were synthesised at 1050 °C for 18 hours.

Sample	% Li A-site (Na-*R*3*c*)
LNN-10	10.9(9)
LNN-12	11.3(7)
LNN-15	15.1(7)
LNN-20	19.4(7)

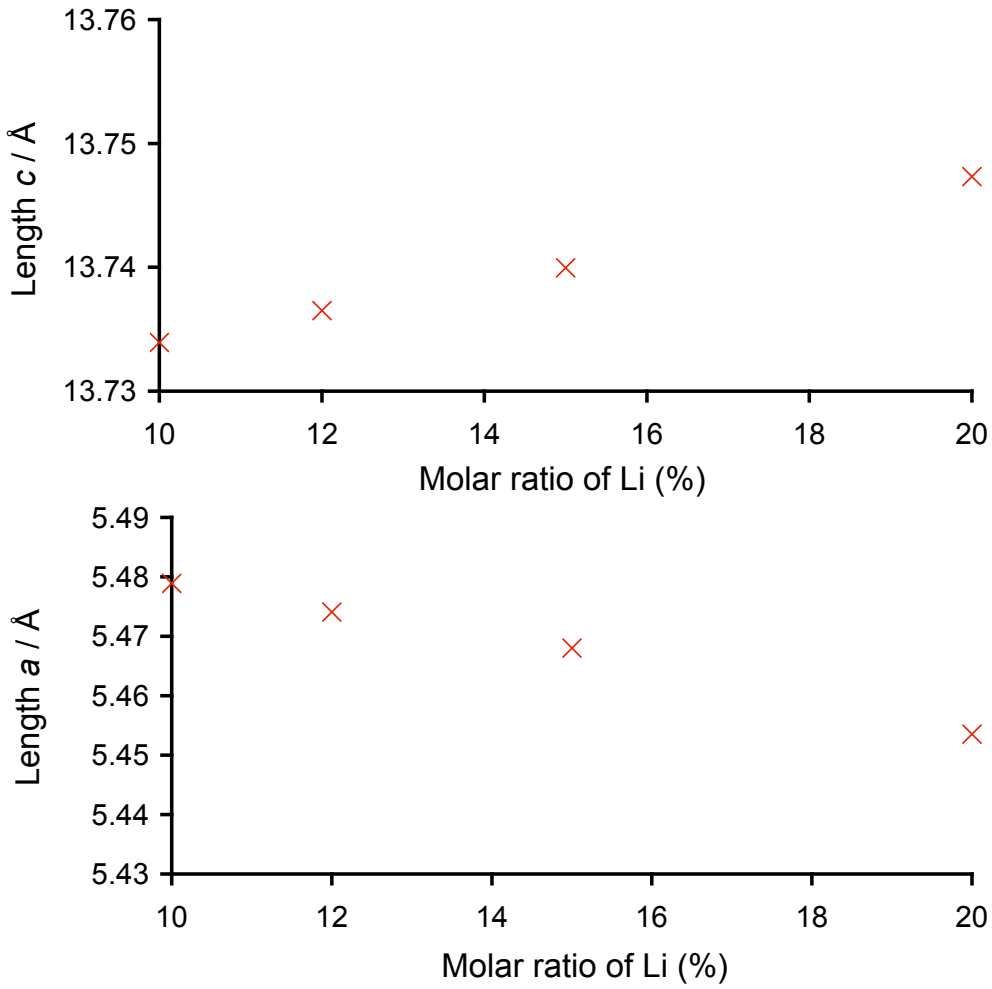

Figure 5.6: Lattice parameters for the Na-*R*3*c* phase, with data obtained from Rietveld refinement of NPD data (all samples synthesised at 1050 °C). As the reactant stoichiometry of Li increases, linear changes are observed in both cell parameters. Error bars are smaller than the data points and are therefore not shown.

5.4.3. The Effects of Annealing Temperature

Within the compositional region $0.10 \leq x \leq 0.20$, samples of LNN-10, 12, 15 and 20 were synthesised with annealing temperatures of 850, 950 and 1050 °C, and characterised using NPD and l-PXRD. As shown in Table 5.1, the annealing temperature has a significant effect on the relative phase fractions of Q and Na-*R*3*c* observed. The Rietveld profiles of samples of LNN-10 and 12 synthesised with different annealing temperatures are shown in Fig. 5.7, with corresponding crystallographic data given in Appendix D. As the Rietveld profiles in Fig. 5.7 show, the relative fraction of phase Q decreases as a function of temperature, for both LNN-10 and LNN-12. The same is also true for LNN-15, although the Na-*R*3*c* phase is formed exclusively when annealed at 1050 °C.

The Na-*R*3*c* phase was confirmed to be formed exclusively for LNN-20 when annealed at 850 °C, as shown in Fig. 5.8. It is worth noting that the atomic positional coordinates and unit cell parameters are slightly different when compared to those obtained for LNN-20 annealed at 1050 °C. This is most likely due to different diffraction techniques being used.

The A-site fractional occupancies of the two phases were determined by Rietveld refinement, to see if they changed as a function of annealing temperature, as shown in Table 5.3. However, given the size of the error bars on the numbers, no definitive conclusions can be drawn about changes as a function of temperature.

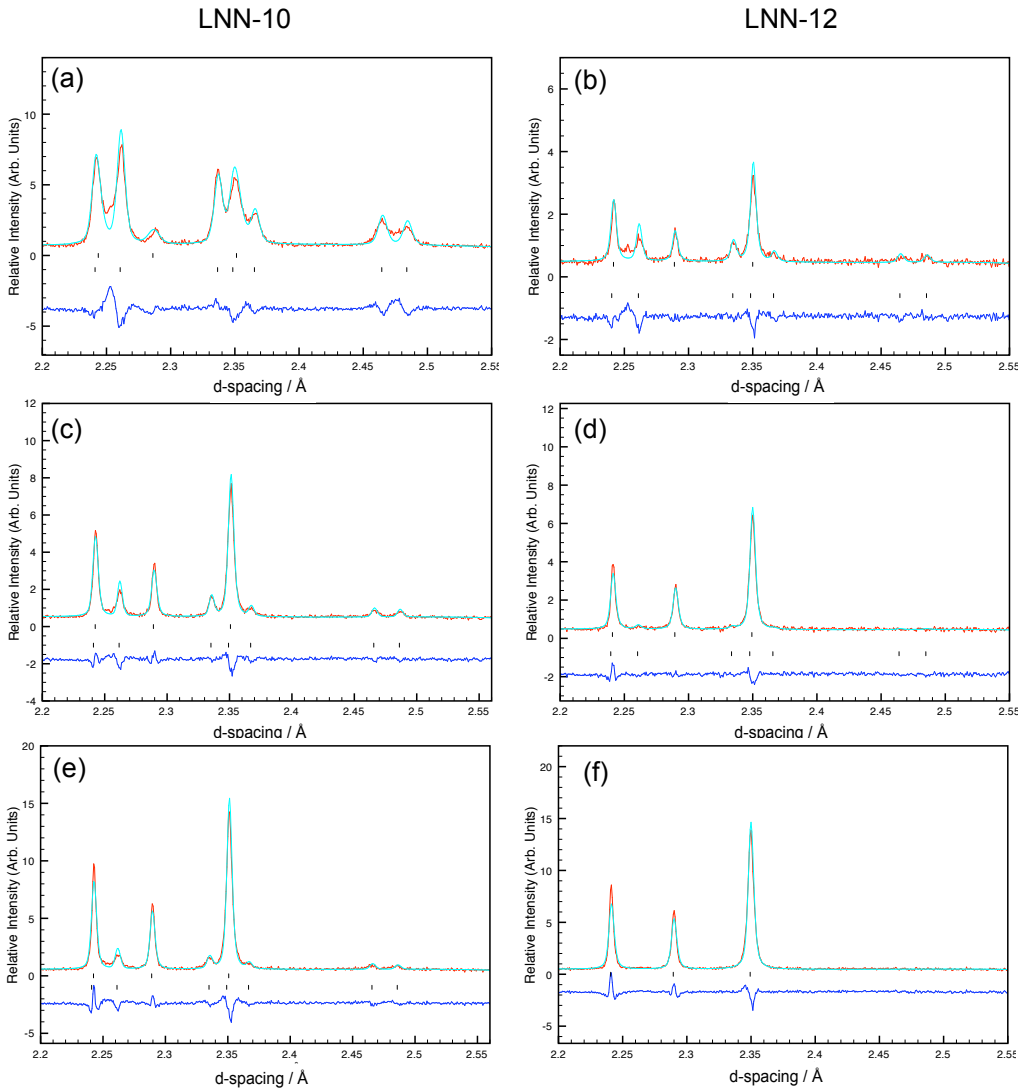

Figure 5.7: Superlattice regions of the Rietveld profiles (NPD) of LNN-10 and LNN-12, refined in space groups $P2_1ma$ and Na-$R3c$ (lower and upper tick marks, respectively). For each composition, three samples were made, with annealing temperatures of (a and b) 850 °C, (c and d) 950 °C and (e and f) 1050 °C. Note, LNN-12 (1050 °C, f) was refined in space group Na-$R3c$ only.

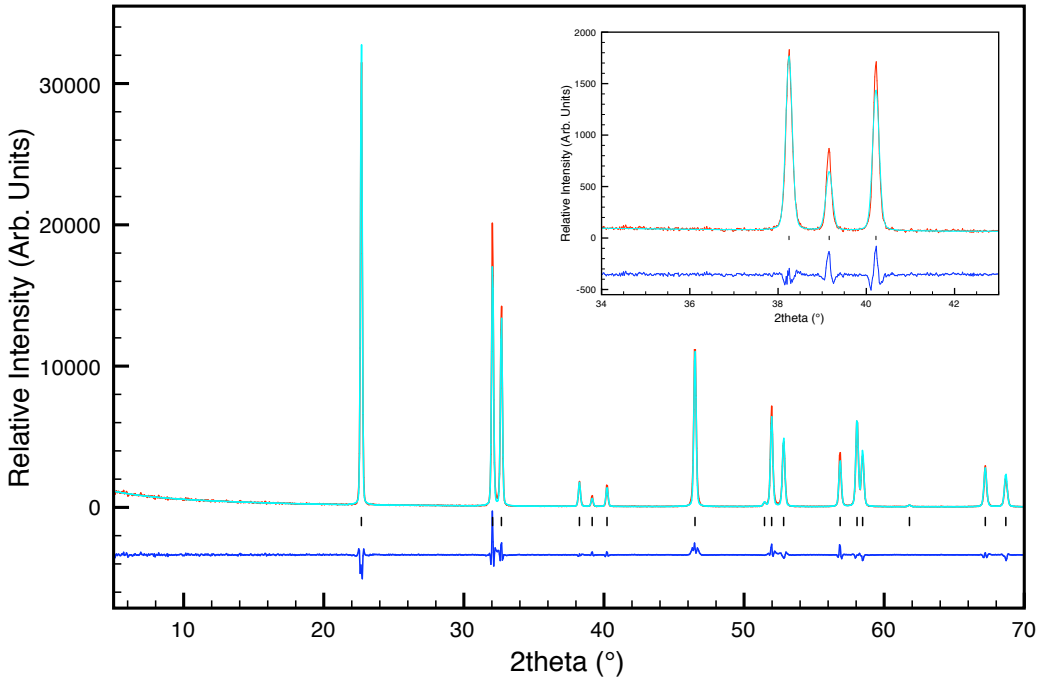

Figure 5.8: Rietveld profile (l-PXRD) of LNN-20 (synthesised at 850 °C), refined in space group Na-*R*3*c*, with expansion of the superlattice region also shown (inset). Crystallographic data and goodness of fit parameters are given in Appendix D.

Table 5.3: Percentages of Li on the A-site for two different compositions of LNN, with each annealed at three different temperatures. The % Li on the A-site of the Na-*R*3*c* matches the reactant stoichiometry well, although the large errors for phase Q make the data difficult to interpret. All data are obtained from Rietveld refinement of NPD data.

Sample	Annealing Temp. / °C	% Li A-site (Na-*R*3*c*)	% Li A-site (Q)
LNN-10	850	10.0(17)	10.1(16)
	950	10.3(10)	11(3)
	1050	10.9(9)	11(4)
LNN-12	850	11.3(8)	10(3)
	950	11.9(8)	10(5)
	1050	11.3(7)	N/A

5.4.4. The Effects of Cooling Rate

Cooling rate was found to affect the relative phase fractions formed for samples of LNN-10, 12 and 15. 'New' samples were made to determine the effects of cooling rate and characterised using l-PXRD (*i.e.*, different samples to those used for NPD experiments due to time restraints - see Section 5.4.5 for an explanation). Two different cooling rates were employed: fast-cooling (FC) in which the sample cooled at an average rate of 15 °C/min (*i.e.*, left in air) and a slower-cooling (SC) rate in which samples cooled at 2 °C/min. Fig. 5.9 shows the Rietveld profiles for two samples of LNN-10 cooled at different rates. From the figure, it can be seen that a greater proportion of the Na-*R*3*c* phase is formed when using the faster cooling rate, and formation of phase Q is favoured when using the slower rate. Similar observations were made for a number of samples characterised by l-PXRD, as shown in Table 5.4 where the relative phase fractions of the Na-*R*3*c* phase are given for samples with different compositions and synthesised with different annealing temperatures and cooling rates. It is unexpected that the slower cooling rate favours the formation of phase Q and not Na-*R*3*c*, given that Na-*R*3*c* *may* be the more thermodynamically-stable of the two (see Section 5.4.5). However, by considering the results presented in Chapters 3 and 4, it has been shown that $NaNbO_3$[20] and $K_{0.03}Na_{0.97}NbO_3$ (phases P and Q, respectively) both show complex high-temperature phase behaviour, with several transitions occurring for both, and the latter also showing regions of phase co-existence.

If the high-temperature region of the phase diagram is so complex, then it may be possible that there is an 'easier' pathway (*i.e.*, a lower energy barrier) to phase Q, which may result in its preferential formation when cooled at the slower rate. It is worth stressing that the observations presented in this section still merit further investigation and that the conclusions drawn are still preliminary. Ideally, high temperature *in-situ* diffraction experiments would be performed for samples of LNN-3 (phase Q), LNN-20 (Na-*R*3*c*) and LNN-10 (phase mixture), to gain additional insight into the observations made here.

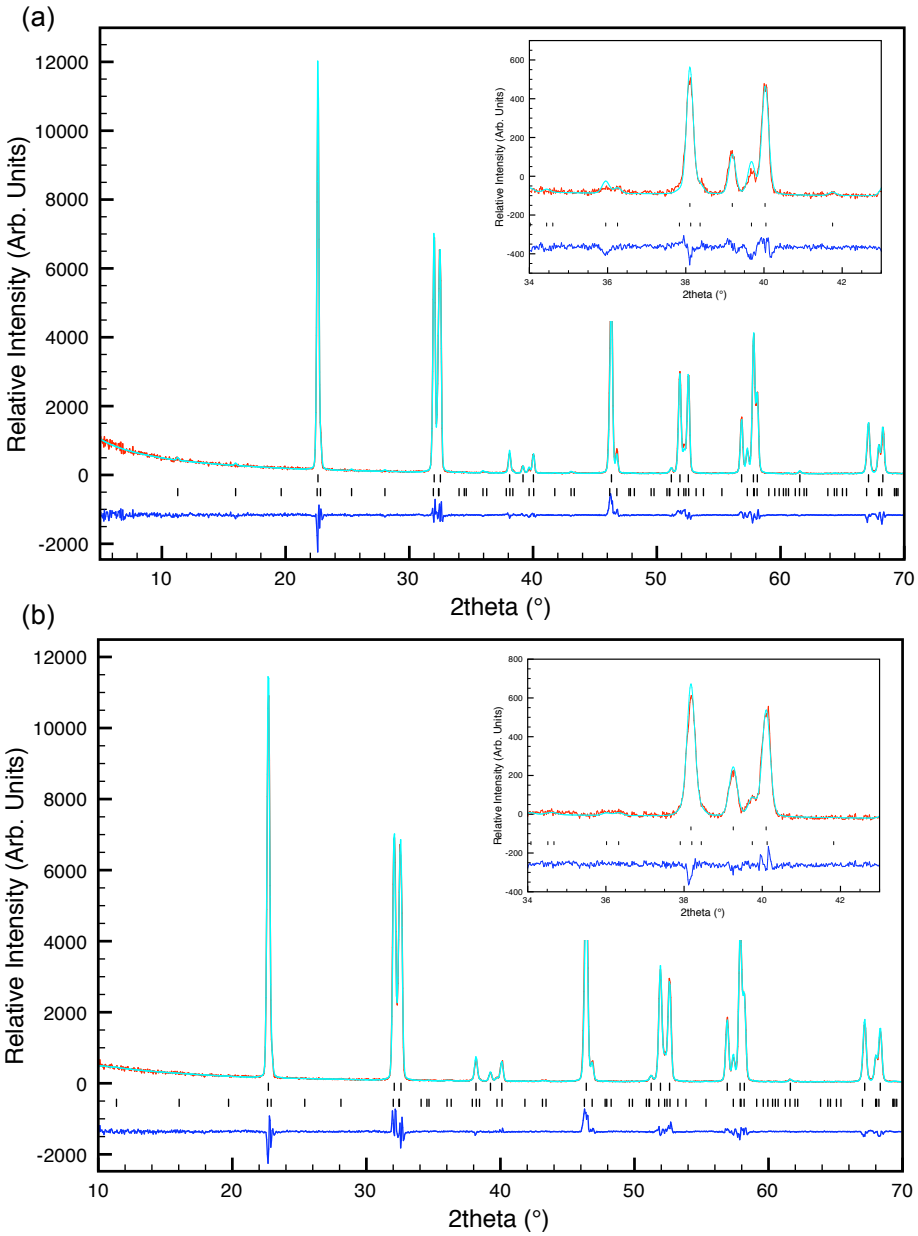

Figure 5.9: Rietveld profiles (l-PXRD) of LNN-10 (synthesised at 1050 °C) where (a) is slow-cooled and (b) is fast cooled, refined in space groups $P2_1ma$ and Na-$R3c$ (lower and upper tick marks, respectively). Expansions of the superlattice regions are also shown (insets). wRp = 9.50 and 9.02%, respectively with $P2_1ma$ phase fractions of 30 and 17%, respectively.

Table 5.4: Relative fractions of the Na-*R*3*c* phase for different compositions of LNN, with samples annealed at different temperatures and cooled at two different rates. All data are obtained from Rietveld refinement of l-PXRD data.

Composition	**Annealing Temp / °C**	**Slow-cooled % Na-*R*3*c***	**Fast-cooled % Na-*R*3*c***
LNN-10	850	31.5(6)	37.8(5)
	1050	70.4(5)	83.1(4)
LNN-12	850	54.8(5)	69.7(5)
	950	91.28(19)	97.31(18)
	1050	~0	~0

Interestingly, the changes in phase fractions resulting from manipulation of the cooling rate are noticeably less significant than those arising from changes in composition and/or annealing temperature. For example, it was shown in Table 5.1 that increasing the reactant molar ratio of Li from 10 to 15% could result in the fraction of phase Q falling from 86 to 31% or 31 to 0%, when annealed at 850 and 950 °C, respectively. It can also be seen that when increasing the annealing temperature from 850 to 1050 °C, phase Q may change from being the majority phase to a minor one. However, as Table 5.4 shows, the effects of cooling rate are less significant, with an approximate 10% reduction in the relative fraction of phase Q when going from slower to faster cooling.

5.4.5. Phase Interconversion

An additional factor was found to affect the relative proportions of phases Q and Na-*R*3*c* present in a sample - time. When samples were left under ambient conditions, *e.g.*, in a sample vial in air at room temperature, it was found that the relative proportion of phase Q decreased over time. This observation was first made by chance, when a sample of LNN-12 was re-analysed using l-PXRD approximately 12 months after its synthesis. Initially, phase Q was present with 45% abundance, whereas the Na-*R*3*c* phase was determined to be present exclusively after this time period, with the corresponding XRD data shown in Fig. 5.10. As the Figure shows, both phases are present initially (the dataset was obtained 1 day after the sample was made), yet only Na-*R*3*c* is present in the second dataset, acquired 12 months later. Data were then re-acquired to see if the same observation was made, and it was later confirmed to be correct.

^{23}Na solid-state NMR spectroscopy was subsequently used to determine if a similar observation could be made. ^{23}Na MQMAS has been shown to be an excellent probe in studying the local structure and disorder of $NaNbO_3$.[21] Firstly, the ^{23}Na z-filtered MQMAS spectra of the two "end member" structures (Q and Na-*R*3*c*) were obtained, followed by a sample containing a mixture of the two. These spectra were obtained from LNN-3, LNN-15 and LNN-12, respectively, and are shown in Fig. 5.11. As the Figure shows, the spectrum of LNN-3 contains two resonance assigned to the two chemically-distinct ^{23}Na sites, as expected for this polymorph (see Chapter 4). The spectrum of LNN-15 shows only 1 resonance/ridge, suggesting that (a) only one crystallographic ^{23}Na site is present, or (b) there are unresolved resonances, *i.e.*, they are overlapped. The presence of only one crystallographic ^{23}Na site is the most logical choice because only one site is present in the Na-*R*3*c* model. Broadening of the lineshapes is observed as a result of a distribution of NMR parameters, *i.e.*, small changes in the local environment caused by substitution. The NMR parameters extracted from the three MQMAS spectra shown are given in Table 5.5.

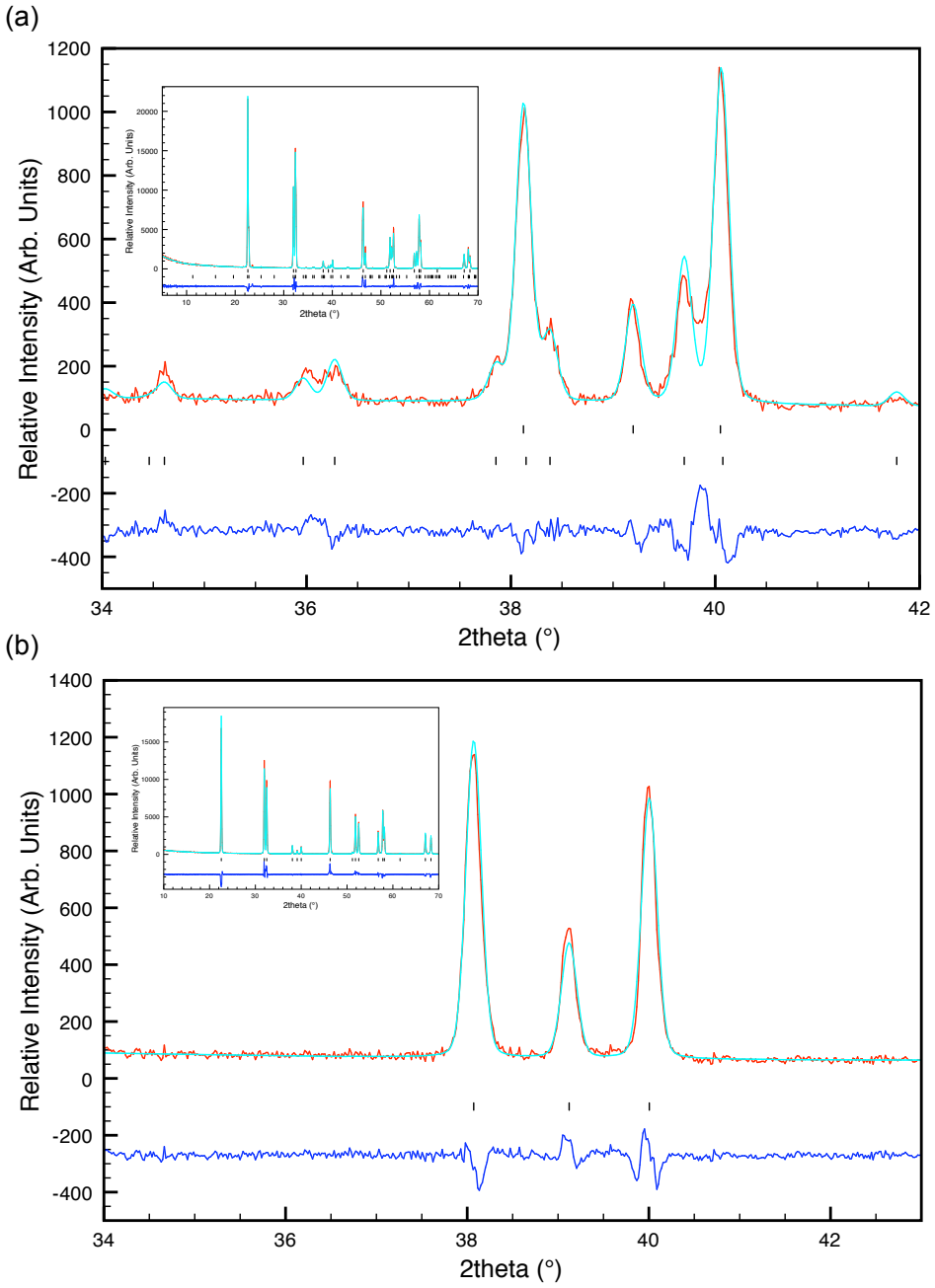

Figure 5.10: Superlattice regions of the Rietveld profiles (l-PXRD) for LNN-12 (synthesised at 850 °C), refined in space groups (a) $P2_1ma$ and Na-$R3c$ (lower and upper tick marks, respectively) and (b) Na-$R3c$ only. Full profiles are shown as insets. Data were recorded (a) 1 day and (b) approximately 12 months after the sample was synthesised. Crystallographic data and goodness of fit parameters are given in Appendix D. Despite the goodness of the fit, the reduction in the number of peaks is clearly evident.

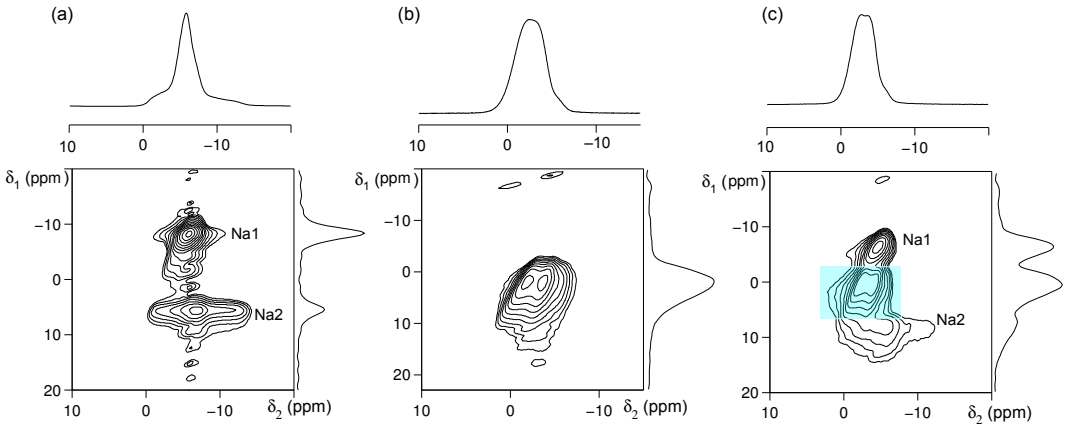

Figure 5.11: ^{23}Na (14.1 T) z-filtered MQMAS NMR spectra of (a) LNN-3, (b) LNN-15 and (c) LNN-12, where (a) and (b) show the "end members" Q and Na-*R*3*c*, respectively, and (c) shows a mixture of the two. MAS spectra are also shown. The MQMAS spectra are the result of averaging 144 transients for each of 100 t_1 increments of 80 μs, with a 5 s recycle interval. A blue box is used to highlight the 'Na-*R*3*c*-ridge' in (c).

Table 5.5: Average ^{23}Na NMR parameters extracted from the spectra shown in Fig. 5.11. See main text for an explanation regarding the use of P_Q and not C_Q.

Sample	Site	$\langle\delta_{iso}\rangle$ (ppm)	$\langle P_Q\rangle$ / MHz
LNN-3	Q-Na1	–4.6(5)	1.1(1)
	Q-Na2	–0.6(5)	2.3(1)
LNN-15	Na-*R*3*c*-1	–0.8(5)	1.6(1)
LNN-10	Q-Na1	–3.7(5)	1.1(1)
	Q-Na2	0.1(5)	2.2(1)
	Na-*R*3*c*-1	–1.2(5)	1.5(1)

It is worth noting that the quadrupolar product, P_Q, is given and not the quadrupolar coupling constant, C_Q. By comparing the isotropic shifts and quadrupolar products of the "end member" materials (*i.e.*, pure phase), it is straightforward to assign the resonances for the spectrum of LNN-12 where a mixture of phases is present. It should be noted, however, that subtle differences could arise in the isotropic shifts when considering the resonances corresponding to phase Q for different compositions of LNN. That is to say, phase Q in LNN-12 will have a higher concentration of Li^+ than LNN-3, and this may well result in differences in the isotropic shifts due to small changes in the local structure. With these resonances assigned, it is then straightforward to analyse any further spectra to determine if any changes occur as a function of time.

^{23}Na z-filtered MQMAS NMR spectra were then obtained for LNN-10 (synthesised at 1050 °C) over a four week period[*], as shown in Fig. 5.12, with the structures of the two phases shown in Fig. 5.3, although these will be discussed in more detail later. The corresponding MAS spectra are also shown in the Fig. 5.12. As the time between synthesis and acquisition of the spectra is increased, it can be that the relative fraction of phase Q decreases (spectra are normalised to the Na-*R*3*c* resonance). This observation is most readily made when comparing the intensity of the resonance corresponding to the Na1 ('sharp') site. This data supports the observation made when analysing the l-PXRD data of LNN-12, discussed previously. Unfortunately, due to the partially-overlapped resonances, it is difficult to accurately determine the relative phase fractions from integration of the resonances, and as such, absolute phase fractions are determined from Rietveld refinement, as shown in Figs. 5.13 and 5.14. The same sample was studied using l-PXRD to determine how the fraction of phase Q changed. As the Rietveld profiles show, the relative proportion of phase Q decreases as the time after synthesis increases. It is worth noting here, that due to the small fraction of phase Q after 1 week, the atomic positional coordinates were constrained to match the values obtained initially (1 day after synthesis), whereas a full refinement was obtained for the Na-*R*3*c* phase (owing to its higher abundance).

[*] This 4-week period was part of the initial investigation. Subsequent data were obtained over longer periods of time.

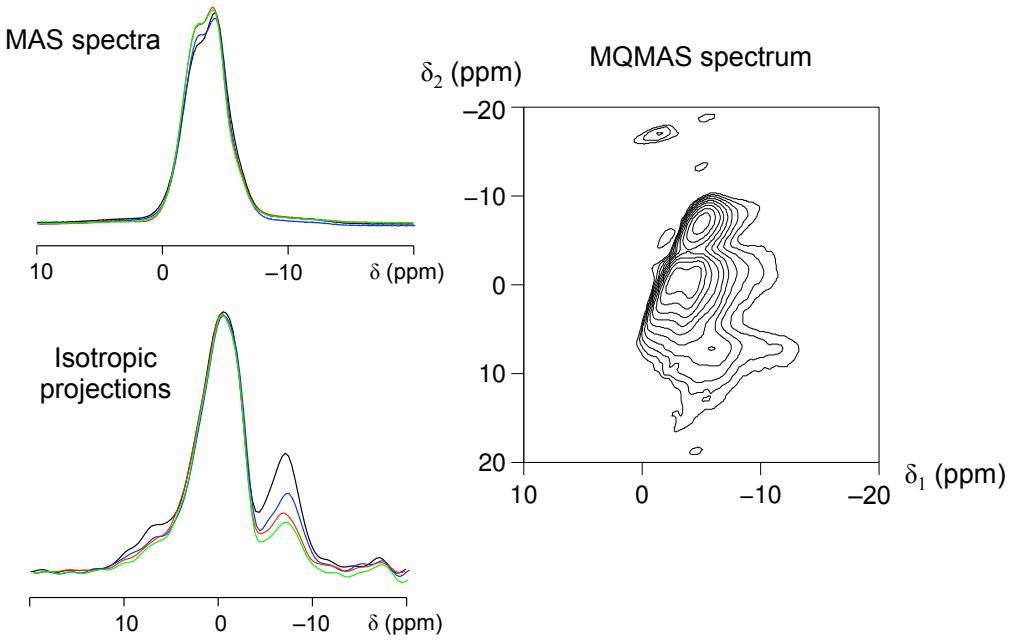

Figure 5.12: ^{23}Na (14.1 T) NMR spectra of LNN-10 (synthesised at 1050 °C). The isotropic projections obtained from z-filtered MQMAS experiments confirm the gradual reduction of phase Q. The black line is the spectrum obtained 1 day after synthesis, the blue line 1 week, the red line 2 weeks and the green line 4 weeks. The MQMAS spectrum was obtained 1 day after sample synthesis and is result of averaging 144 transients for each of 100 t_1 increments of 80 μs, with a 5 s recycle interval.

The evolution of the Na-*R*3*c* phase fraction is shown in Fig. 5.14, over a 16 week period (for LNN-10), in which it can be seen that the proportion of this phase increases over time; conversely, the fraction of phase Q decreases over time. Note that the rate of change is not linear. Instead, the fraction of Na-*R*3*c* increases at a faster rate initially (0 to 3 weeks), and then this rate decreases over the subsequent weeks. Between 0 and 3 weeks, the fraction of Na-*R*3*c* increases from approximately 70 to 92%, whereas between weeks 4 and 16 this only increases to approximately 97%.

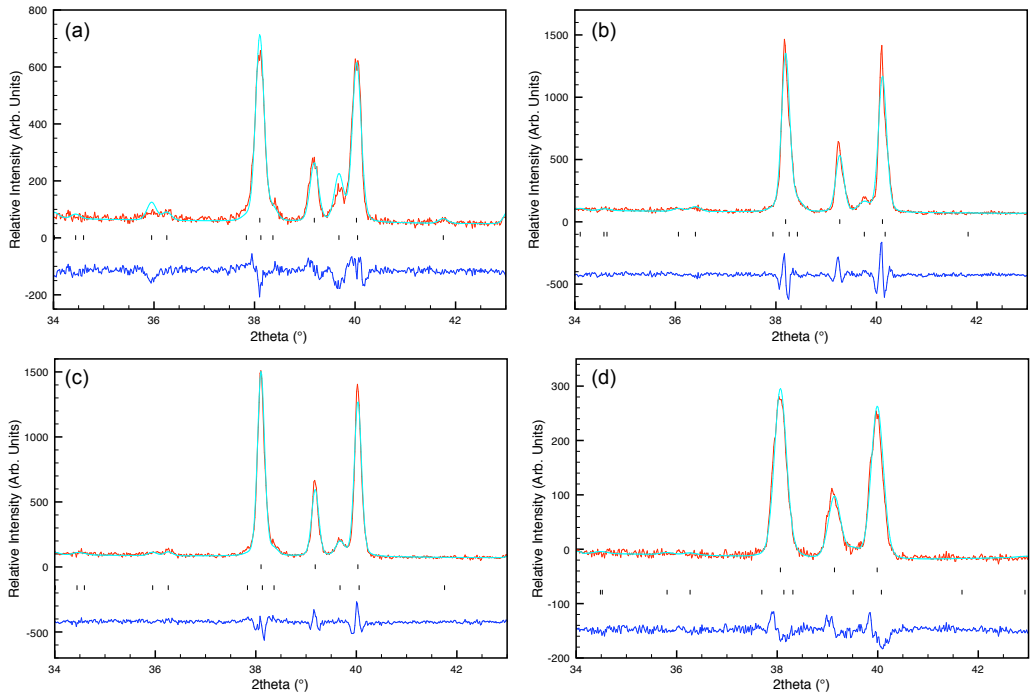

Figure 5.13: Rietveld profiles (l-PXRD) showing the superlattice regions of LNN-10 (synthesised at 1050 °C, SC), refined in space groups $P2_1ma$ and Na-$R3c$ (lower and upper tick marks, respectively). Data were obtained (a) 1 day, (b) 1 week, (c) 3 weeks and (d) 12 weeks after synthesis of the sample. Corresponding crystallographic data and goodness of fit parameters are given in Appendix D.

In light of the observation that several samples have different relative phase fractions (Q and Na-$R3c$), it needs to be determined if (a) phase Q 'degrades' into something else, or (b) phase Q undergoes a phase transition to Na-$R3c$ under ambient conditions.[24] Similar observations have been previously reported, in which phase one phase undergoes a conversion to another over time under ambient conditions.[22] Analysis of the diffraction data (l-PXRD) revealed that there was no evidence for an additional polymorph or impurity phase, *i.e.*, all peaks in the diffraction data were indexed by the two models. Additionally, the ^{23}Na NMR spectra (both MAS and MQMAS) showed no signs of a ^{23}Na-containing impurity. It is worth noting here that NMR spectra should be sensitive to the presence of any amorphous phases, unlike

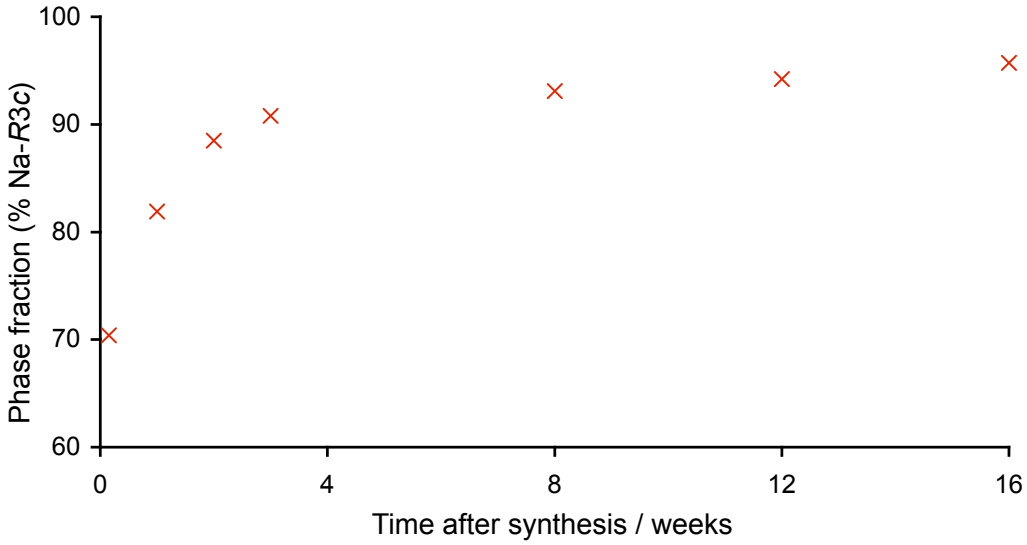

Figure 5.14: Relative abundance of Na-*R*3*c* in a sample of LNN-10, plotted as a function of time after synthesis. The error bars derived from GSAS are smaller than the data points and are therefore not shown.

XRD patterns where these may remain undetectable, although no evidence for any such phases were observed. In a subsequent step, an Al_2O_3 standard was added to samples of LNN-10 and several quantitative measurements were made over a period of a few weeks. It was confirmed that the absolute amount of LNN (*i.e.*, the total combined amount of Q and Na-*R*3*c*) remained unchanged, relative to the amount of Al_2O_3, although the relative fraction of phase Q fell by approximately 15% and the amount of Na-*R*3*c* increased by the same amount. By considering these three observations, it was concluded that phase Q undergoes a crystal-to-crystal phase transition under ambient conditions. In light of the observations made, it can be suggested that *phase Q is metastable with respect to Na-R3c at ambient temperature.*

As the previous results have shown, the rate of change from phase Q to Na-*R*3*c*, *i.e.*, the reaction kinetics, could be considered as being relatively slow. As was shown in previous studies,[20] phases Q and N of $NaNbO_3$ have very similar energies. (It is worth noting here that phase N of $NaNbO_3$ is isostructural with the Na-*R*3*c* phase of LNN, and that phase Q of both $NaNbO_3$ and LNN are isostructural). This work, centred on a DFT study, showed how the relative (internal) energies of the various

phases of $NaNbO_3$ are all very similar (both ambient and high-temperature). In fact, phases Q and N (of $NaNbO_3$) differed only by approximately 0.6 kJ/mol. Kinetic factors could also contribute to the transition being relatively slow. For example, substitution of the smaller Li^+ cation for Na^+ in the Na-*R*3*c* phase may induce lattice strain in the structure, whereby a kinetic barrier to the transition state may be present, meaning that the process may be slower. In a subsequent step, several samples of LNN-10 and 12 were synthesised using different annealing temperatures and cooling rates, to determine if either showed faster rates of phase conversion compared to the LNN-10 sample previously discussed, and the results are shown in Fig. 5.15.

In addition to the relative proportions of the phases being determined from refinement of l-PXRD data, complementary ^{23}Na z-filtered MQMAS NMR spectra were also obtained to determine how the relative proportions changed. It is worth noting here, however, that the NMR spectra do *not* strictly provide information on the relative phase fractions but on the *ratio of ^{23}Na in each phase*. Determining the relative phase fractions from NMR data would, therefore, require the fractional occupancies of Na^+ and Li^+ to be known (although those determined from NPD could be assumed to be correct). The 'initial' MQMAS spectra of each sample are shown in Fig. 5.16. For samples of the same composition annealed at different temperatures (*e.g.*, LNN-10 synthesised at 850 and 950 °C), there is very little difference in the NMR parameters obtained. For LNN-10, $\langle\delta_{iso}\rangle$ = –4.1(5) and –0.3(5) ppm for Na1 and Na2 in phase Q, respectively (labeled on Figure), with corresponding P_Q = 1.1(1) and 2.4(1) MHz, respectively, and δ_{iso} = –1.6(5) ppm and P_Q = 1.5(1) MHz for the resonance corresponding to the Na-*R*3*c* phase. For LNN-12, these values do not change (assuming 0.5 ppm and 0.1 MHz errors in δ_{iso} and P_Q, respectively). By comparing the isotropic projections obtained from increasing the time between sample synthesis and spectral acquisition, it can be seen that the relative intensity of the resonances corresponding to phase Q decrease over time. This can be seen more easily by considering the isotropic projections of these spectra, as shown in Fig. 5.17.

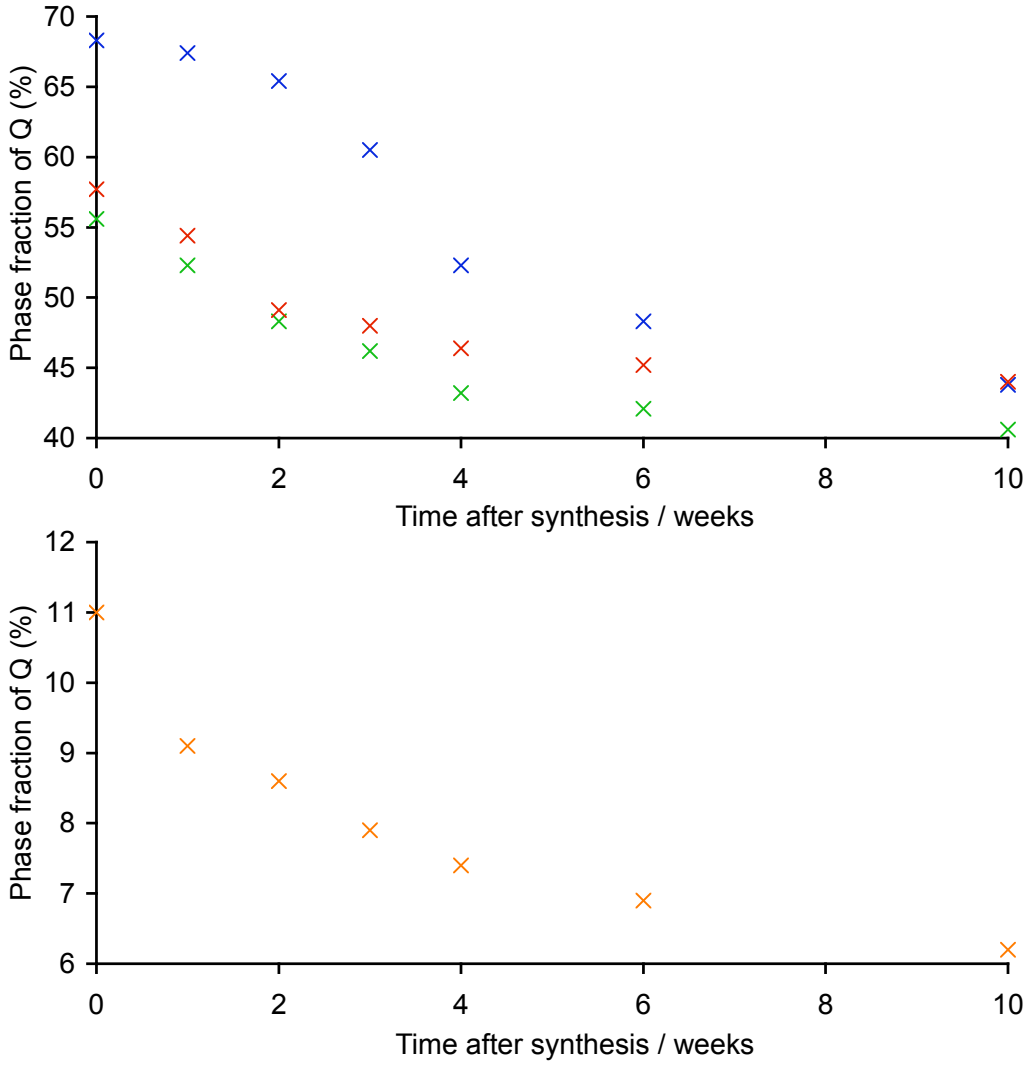

Figure 5.15: Changes in the relative fractions of phase Q over time for LNN-10 annealed at 850 and 950 °C (blue and green points, respectively), and LNN-12 annealed at 850 and 950 °C (red and orange points, respectively). All values are obtained from Rietveld refinement of l-PXRD data. All samples were prepared using the slower cooling rate.

When the Q:Na-*R*3*c* ^{23}Na content ratios are compared, as the time between synthesis and spectral acquisition increases, it can be seen that the proportion of ^{23}Na in phase Q *decreases* relative to that in Na-*R*3*c*. This observation is made for all the samples investigated, as shown in Fig. 5.18. From the figure, two important observations can

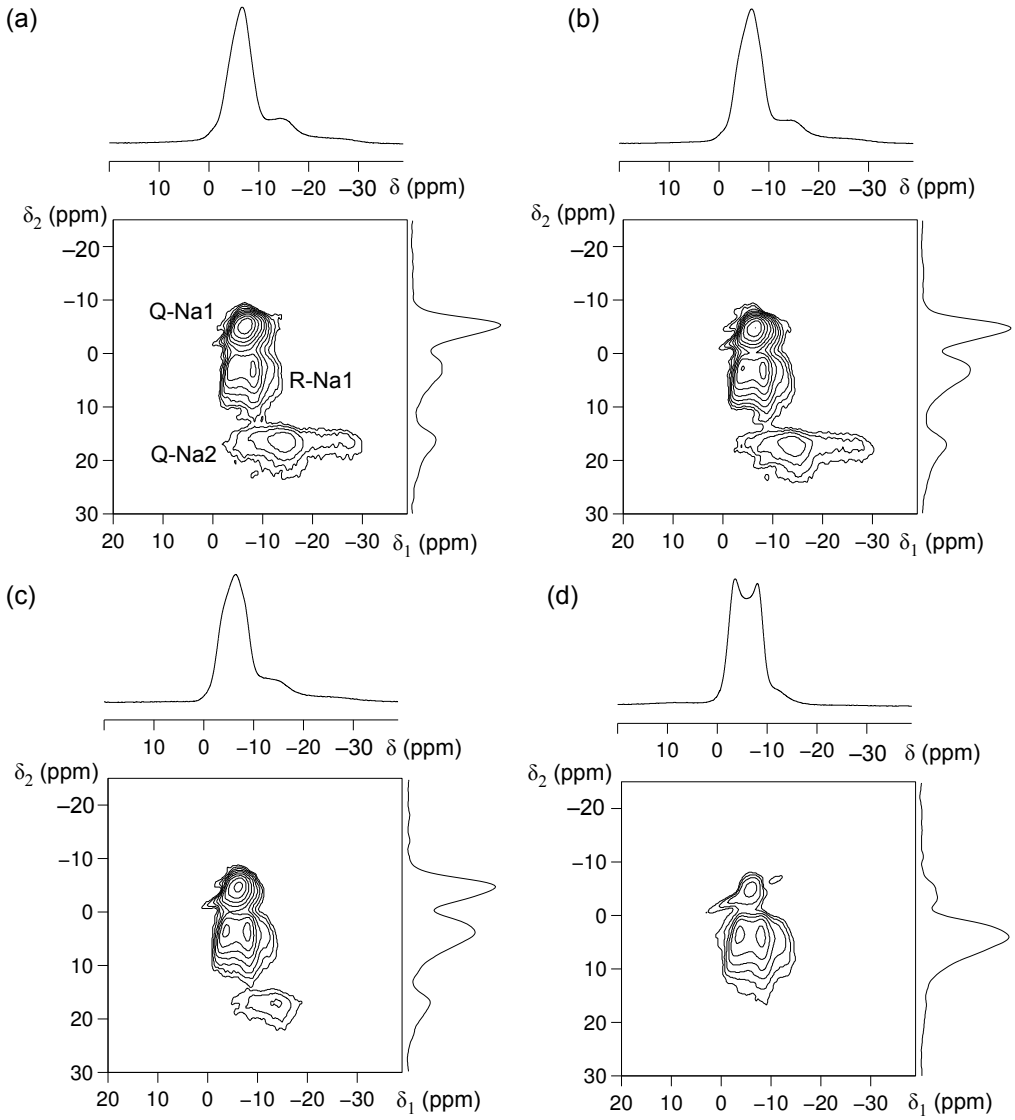

Figure 5.16: ^{23}Na (9.4 T) z-filtered MQMAS NMR spectra of (a) LNN-10 synthesised at 850 °C, (b) LNN-10 synthesised at 950 °C, (c) LNN-12 synthesised at 850 °C and (d) LNN-12 synthesised at 950 °C. Corresponding MAS spectra are also shown. All spectra were acquired between 1 and 2 days after sample synthesis. The ridges corresponding to phase Q are labeled (Q-Na1 or 2) and the rhombohedral phase (R-Na1). The MQMAS spectra are result of averaging 144 transients for each of 100 t_1 increments of 80 μs, with a 5 s recycle interval.

be made. Firstly, the Q:Na-*R*3*c* ratio of ^{23}Na content decreases as the time is increased, and, secondly, that the rate of change is greatest in the 'initial' period of 1 to 40 days. A similar observation was made when considering the XRD data, in which the greatest change (*i.e.*, fastest rate of conversion of phase Q to Na-*R*3*c*) occurred in the initial 0 to 4 week period. However, from the NMR data alone, it cannot be unambiguously determined which sample (*i.e.*, composition and annealing temperature) shows the fastest rate of phase interconversion.

By considering results obtained from XRD and ^{23}Na NMR jointly, an additional observation can be made. The sample with the lowest initial proportion of phase Q (LNN-12 annealed at 950 °C) *may* actually show the fastest rate of conversion to Na-*R*3*c*. From the XRD data, it can be seen that the proportion of phase Q, for this sample, decreases from approximately 11 to 6% over a ten-week period. This is, approximately, a 50% reduction in the amount of phase Q. For the remaining samples,

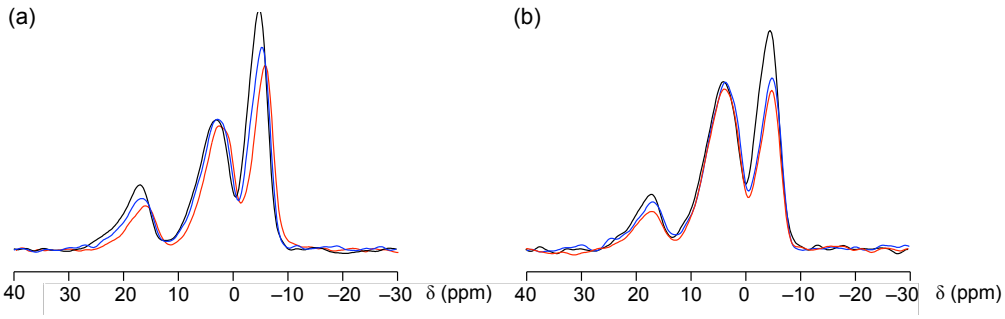

Figure 5.17: ^{23}Na (9.4 T) isotropic projections obtained from z-filtered MQMAS NMR spectra for (a) LNN-10 synthesised at 950 °C and (b) LNN-12 synthesised at 850 °C. The projection in black was obtained either 1 or 2 days after sample synthesis, with the projections blue and red acquired approximately 6 and 10 weeks later, respectively. The isotropic projections are normalised to the 'central' resonance (corresponding to Na-*R*3*c*) to clearly show the reduction in intensity of the other resonances.

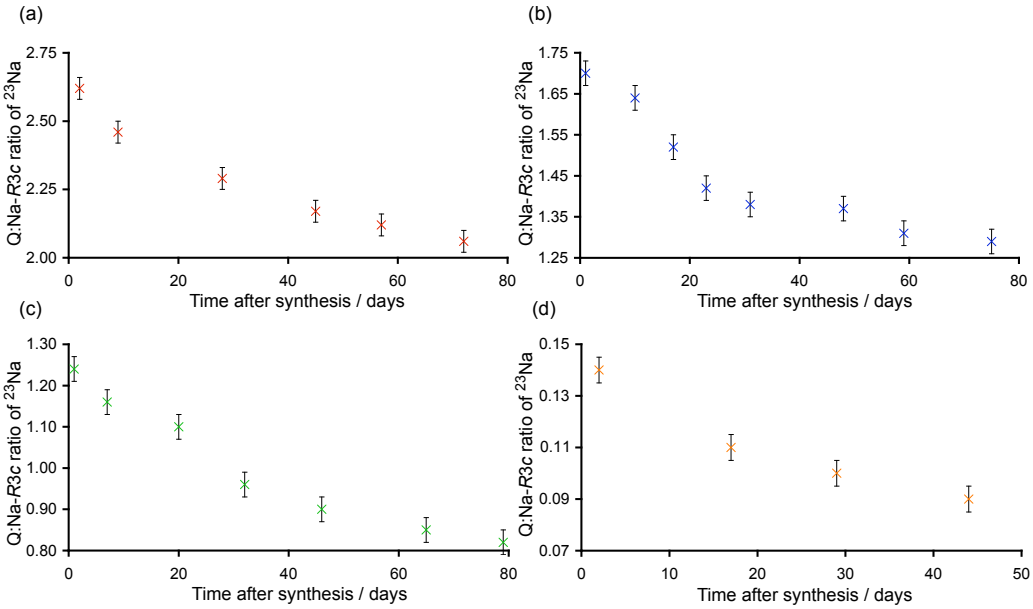

Figure 5.18: Q:Na-*R*3*c* ^{23}Na ratios for (a) LNN-10 synthesised at 850 °C, (b) LNN-10 synthesised at 950 °C, (c) LNN-12 synthesised at 850 °C and (d) LNN-12 synthesised at 950 °C. All values are obtained from integration of the resonances in the isotropic projections obtained from ^{23}Na (9.4 T) z-filtered MQMAS NMR spectra. The x-axis in each graph refers to the time between synthesis of the sample and spectral acquisition. Experimental details for the NMR spectra are given in Fig. 5.17. Due to uncertainty in integrating the resonances, *i.e.*, error, 'generic' errors bars of approximately 2% are given. The error bars, therefore, do not represent definitive quantitative values.

the proportion of phase Q falls from approximately 68 or 56% to 40 or 45%, respectively, over a ten week period, giving reductions in the amount of phase Q of approximately a third. From the ^{23}Na NMR data, shown in Fig. 5.18, the Q:Na-*R*3*c* ratio of ^{23}Na content falls from approximately 0.14 to 0.08 over a six week period, leading to a reduction in the amount of phase Q of approximately 43%. However, to make this conclusion, it must be assumed that the stoichiometry of both phases remains consistent as the time is increased, *i.e.*, the fractional occupancies of Na^+ and Li^+ in each phase do not change over time. There is no reason to suggest, however, that a change should be observed. If the stoichiometries were to change, this should result in as a consistent change in the lattice parameters, *i.e.*, the unit cell lengths (and

volume) would change proportionally if the amount of Na^+ or Li^+ changed in the either of the phases. From this data, it may, therefore, be *suggested* that the conversion of phase Q to Na-*R*3*c* happens at a faster rate when the proportion of the rhombohedral phase is greatest, although this is by no means an unambiguous conclusion.

5.5. Region 2 ($0.25 \leq x < 0.96$)

5.5.1. Evolution from Region 1

Samples of LNN ($0.25 \leq x \leq 0.96$) were synthesised and initially characterised using l-PXRD. Regardless of the annealing temperature (850 to 1050 °C) and cooling rate used in the synthesis, two phases were always formed, with the relative proportions of the two found to depend only upon the reactant stoichiometry, *i.e.*, the reactant Li/Na molar ratio. For both phases, the greatest crystallinity (as determined from XRD) was observed for samples annealed at the higher (1050 °C) temperature, as expected, and so samples suitable for NPD characterisation were synthesised at this temperature. The Rietveld profiles and corresponding crystallographic data and goodness of parameters can be found in Appendix D. The lattice parameters for the *Na-R*3*c* phase, obtained from these refinements, are given in Fig. 5.19 and the relative phase fractions in Fig. 5.20, to serve as a brief summary.

From the data obtained over this compositional range (Rietveld profiles and crystallographic data tables can be found in Appendix D) it can seen that the two rhombohedral phases show no significant changes in composition. In fact, the Na-*R*3*c* phase is found to contain approximately 80% Na^+ and 20% Li^+ on the A-site, regardless of reactant Li molar ratio. That is to say, *the composition of this phase appears to be independent of the reactant stoichiometry.* A similar observation is made for the second rhombohedral phase, in which the A-site consists of approximately 98% Li^+ and 2% Na^+, and these values are seen to be independent, once again, of the reactant stoichiometry. In light of this observation, the second rhombohedral phase is Li-rich and, therefore, denoted Li-*R*3*c*. The only notable change over Region 2 is the relative proportions of the two phases, as shown in Fig.

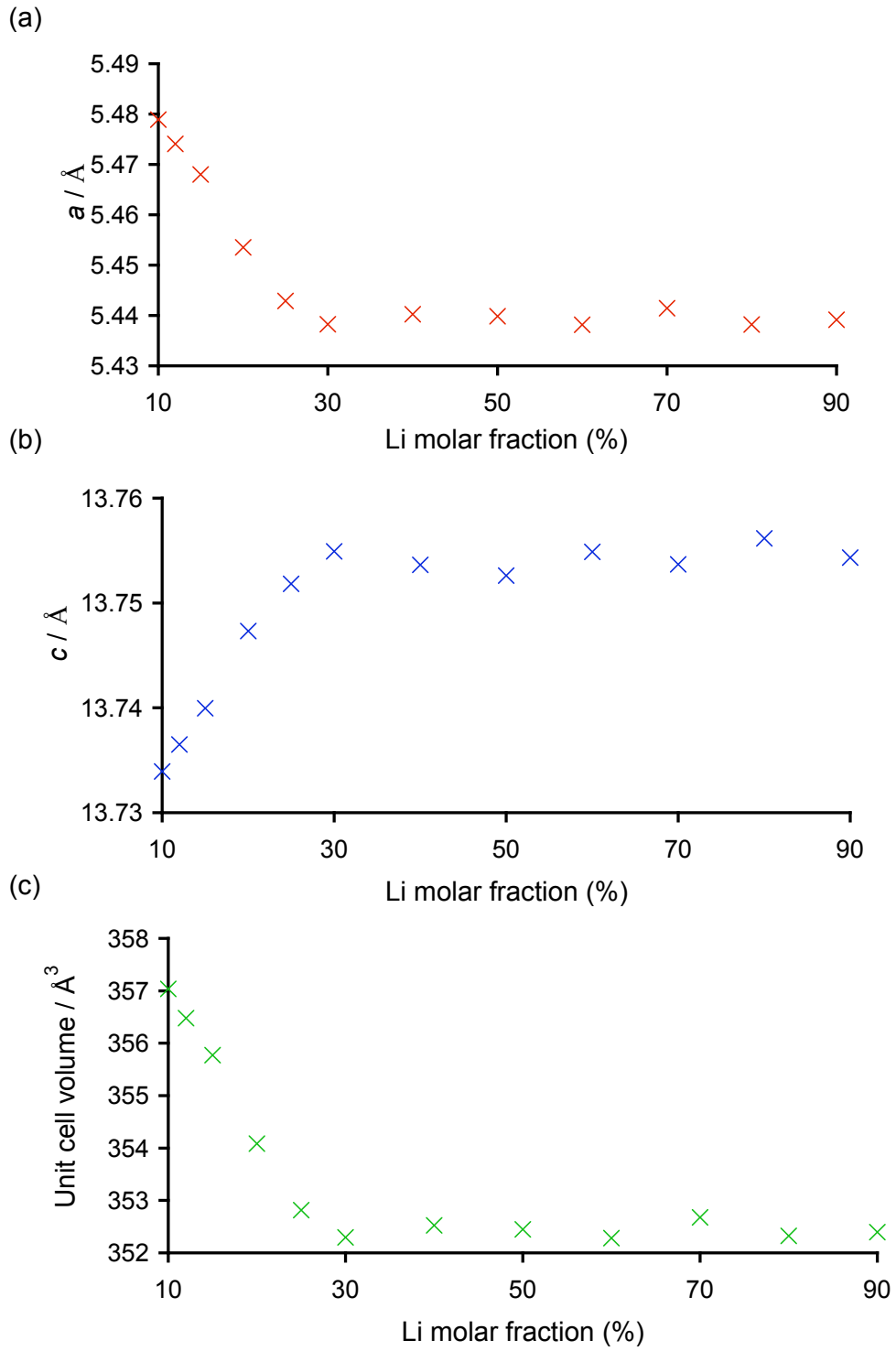

Figure 5.19: (a and b) lattice parameters and (c) unit cell volume of the Na-*R*3*c* phase as a function of the reactant Li molar ratio. All data are obtained from Rietveld refinement of NPD data. Error bars derived from GSAS are smaller than the data points and are therefore not shown.

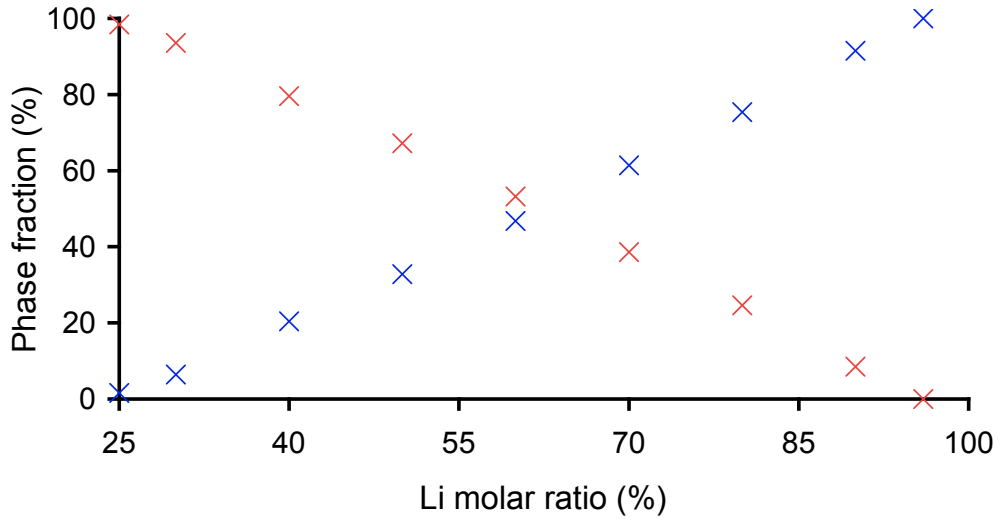

Figure 5.20: Relative fractions for phases Na-*R*3*c* (red crosses) and Li-*R*3*c* (blue crosses) as a function of reactant Li molar ratio. All values are obtained from Rietveld refinement of NPD data. Error bars are smaller than the data points and are therefore not shown.

5.20. It can be seen that as the reactant Li molar ratio increases, the proportion of Na-*R*3*c* decreases linearly and the proportion of Li-*R*3*c* increases linearly. These changes in phase fractions compensate for the changes in reactant Li molar ratio - as the molar ratio of Li^+ increases, either (i) the phases would need to incorporate more Li^+, or (ii) the proportion of Li-*R*3*c* would need to increase, with a subsequent reduction in the proportion of Na-*R*3*c*. Consequently, it can be concluded that the two rhombohedral structures show no significant changes as the reactant Li molar ratio increases (in Region 2 only). To confirm that one phase is Na-rich and the other Li-rich, ^{23}Na solid-state MAS NMR spectroscopy was used. The ^{23}Na MAS spectra of LNN-20, 60 and 90 are shown in Fig. 5.21, where two distinct resonances can be seen for LNN-60 and 90. The ^{23}Na MAS spectrum of LNN-20 shows a single resonance (labeled on Figure) which corresponds to the Na-*R*3*c* phase (single phase only). The MAS spectra of LNN-50 and 90, however, show two distinct resonances, one of which corresponds to the Na-*R*3*c* phase, and the other, which must correspond to the Li-*R*3*c* phase. It is worth noting here that these spectra do *not* directly provide information on the relative

phase fractions (like in Rietveld refinements), but on the ratio of ^{23}Na present in each phase. For LNN-60, refinement of NPD data suggests that the relative ratio of the two phases is approximately 1:1. However, from the ^{23}Na MAS NMR spectrum of this sample, it can be determined that the ratio of ^{23}Na in Na-*R*3*c*:Li-*R*3*c* is approximately 40:1. This suggests that the Na-*R3c* phase contains substantially more ^{23}Na than Li-*R*3*c*, and this value is not 'skewed' by the two phases having very different proportions. The data obtained from ^{23}Na NMR and NPD are, therefore, found to be in good agreement. The amount of Na^+ in each phase was then investigated further by refining (NPD data) the fractional occupancies of the A-site for both phases across the LNN series. The values are listed in Table 5.6, from which it can be seen that for Region 2 the proportion of Na^+ (and therefore Li^+) in each phase is relatively consistent.

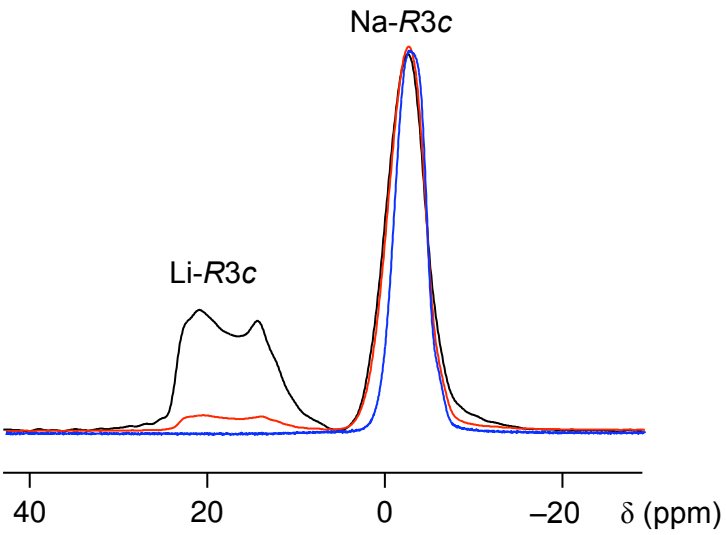

Figure 5.21: ^{23}Na (14.1 T) MAS (12.5 kHz) NMR spectra of LNN-20 (blue line), LNN-60 (red line) and LNN-90 (black line). Spectra are normalised to the resonance corresponding to the Na-*R*3*c* (labeled), and are the result of averaging 256 transients.

Table 5.6: The percentages of Na^+ on the A-sites of both Na-*R*3*c* and Li-*R*3*c* for Region 2 only. All values are obtained from Rietveld refinement of NPD data.

Composition	% Na (Na-*R*3*c*)	% Na (Li-*R*3*c*)
LNN-30	77.7(8)	0.8(19)
LNN-40	79.3(9)	1.1(18)
LNN-50	78.4(10)	1.3(16)
LNN-60	78.6(12)	3.1(14)
LNN-70	80.8(14)	2.8(11)
LNN-80	79(2)	3.2(9)
LNN-90	84(6)	3.4(9)

5.5.2. The Two Rhombohedral Structures

Structures for the two rhombohedral phases (Na-*R*3*c* and Li-*R*3*c*) are shown in Fig. 5.22, where they are obtained from Rietveld refinement of NPD data for LNN-20 and LNN-96, respectively. For the region $0.10 \leq x \leq 0.90$, the Nb-O and Na(Li)-O bond lengths are shown in Figs. 5.23 and 5.24, for each of the two phases. Both rhombohedral phases could be regarded as having either six- or twelve-coordinate A-sites. Each A-site cation has six A-O bonds shorter than 3 Å and six that are longer. For now, only the six shorter bonds will be considered, with the possibility of twelve-coordinate Na(Li) discussed later. From Figs. 5.23 and 5.24, it can seen that the Nb-O and Na(Li)-O bond lengths can be divided into two regions. Firstly, in the "solid solution" region (discussed previously), the Nb-O and Na(Li)-O bonds lengths show the greatest amount of change as the reactant Li molar ratio increases for the Na-*R*3*c* phase. The bond lengths appear to change near-linearly with an increasing value of x. Beyond this "solid solution" region the changes become significantly less noticeable and the bond lengths remain more consistent, as expected for a two-phase system.

For the Li-*R*3*c* phase, the Nb-O bond lengths (obtained from refinement of NPD data), shown in Fig. 5.24, show, unexpectedly, two distinct regions. Over the range $0.25 \leq x \leq 0.40$, the 'short' bonds decrease in the length and the 'long' bonds increase

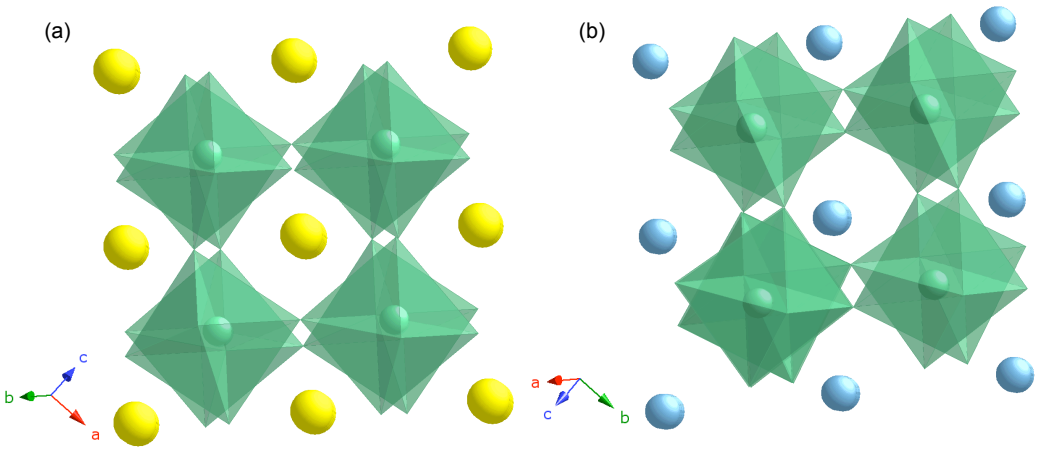

Figure 5.22: Structures for the (a) Na-*R*3*c* and (b) Li-*R*3*c* phases. The structures are obtained from Rietveld refinement (NPD) of LNN-20 and LNN-96, respectively. NbO_6 octahedra are shown as green polyhedra, Nb^{5+} cations are green and Na^+ and Li^+ cations are yellow and blue, respectively.

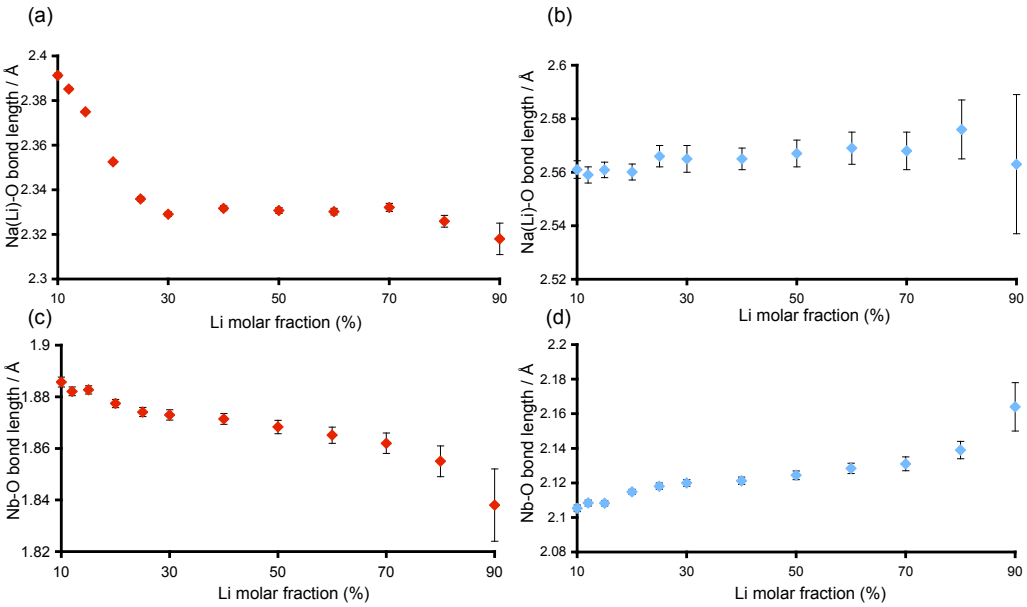

Figure 5.23: Changes in the Nb-O and Na(Li)-O bond lengths for Na-*R*3*c* as the reactant Li molar ratio increases, with values obtained from Rietveld refinement of NPD data. Assuming six-coordination of both A- and B-sites, each 'type' of bond has (a and c) three 'short' and (b and d) three 'long' bonds. Error bars, derived from GSAS, are shown.

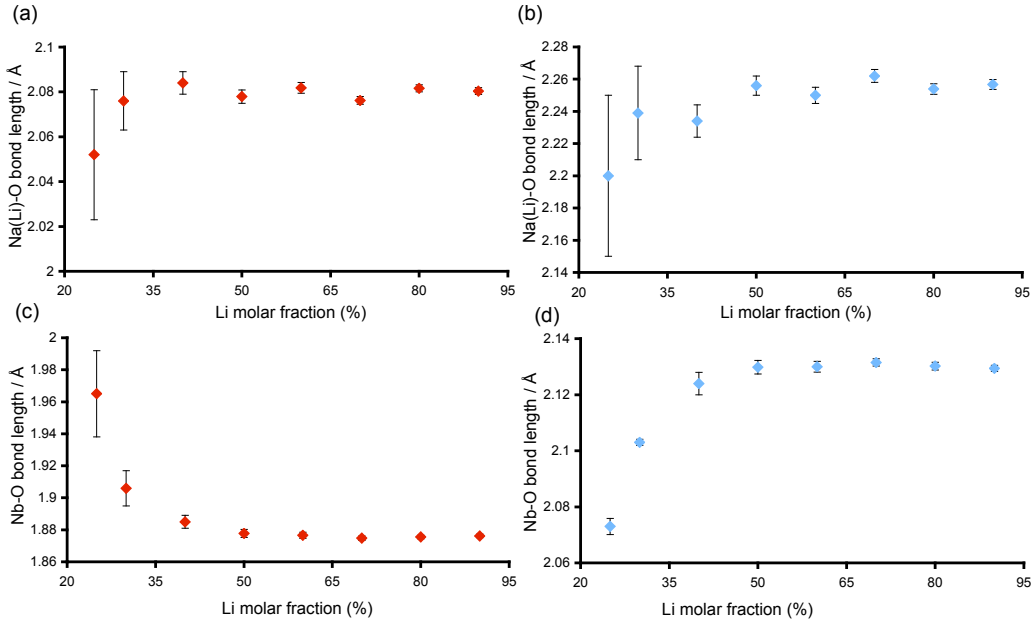

Figure 5.24: Changes in the Nb-O and Na(Li)-O bond lengths for Li-*R*3*c* as the reactant Li molar ratio increases, with values obtained from Rietveld refinement of NPD data. Assuming six-coordination of both A- and B-sites, each 'type' of atom has (a and c) three 'short' and (b and d) three 'long' bonds. Error bars, derived from GSAS, are shown.

as the value of x increases. While this change is difficult to quantify (due to the large error bars in this compositional region), the trends are more readily observed. When x > 0.40, the Nb-O bond lengths are relatively consistent and any changes are noticeably less significant than those from $0.25 \leq x \leq 0.40$. The Li(Na)-O bond lengths (both 'short' and 'long') for the Li-*R*3*c* phase do not show a similar trend to those for the Na-*R*3*c* phase. As shown in Fig. 5.24, the lengths *could* be relatively consistent across the range $0.25 \leq x \leq 0.90$. Due to the large error bars for the data at lower values of x, it is not possible to say whether one or two regions would be observed, *i.e.*, the lengths *could* change significantly over the range $0.25 \leq x \leq 0.40$ (similar to the Nb-O bonds), but this cannot be accurately determined from the data.

The reasons for the formation of two rhombohedral phases of seemingly fixed composition as a function of x ($0.30 \leq x \leq 0.90$), are still not fully understood. However, it is possible that this "region of immiscibility" arises due to the differences in the ionic radii of Na^+ and Li^+, and the potential for Li^+ to be displaced to a greater

extent than Na^+. If the two phases are (this time) assumed to have 12-coordinate A-sites (*i.e.*, all the short and longer bonds are considered), they could be regarded as adopting the perovskite structure, *e.g.*, $^{XII}A^{VI}BO_3$. For each phase, there are four sets of three distinct A-O distances. For Na-*R*3*c*, the A-O distances are 3 × 2.32 Å, 3 × 2.56 Å, 3 × 3.06 Å and 3 × 3.14 Å, and for Li-*R*3*c* these are 3 × 2.08 Å, 3 × 2.26 Å, 3 × 3.29 Å and 3 × 3.45 Å.[†] Given the A-site distortions of the two phases, it becomes understandable why this region of immiscibility is observed. However, it could be argued that the two structures (in particular Li-*R*3*c*) should be considered as having six-coordinate A-sites, given that six A-O distances in each phase are greater than 3 Å. For the Na-*R*3*c* phase, the maximum A-O distance is 3.14 Å, and so these structures are considered to be highly distorted perovskites.

5.5.3. A Possible Phase Change

In order to gain additional insight into the local structure and disorder of the two rhombohedral phases, ^{23}Na z-filtered MQMAS spectra were obtained for LNN-80 and LNN-90, as shown in Figs. 5.25 and 5.26. In each, two spectra are shown - one shows the MQMAS spectrum in its entirety and the other shows an expansion of a specific region. In the MQMAS spectra, *two* distinct resonances are observed (along with some spinning sidebands) corresponding to the Na-*R*3*c* phase (determined by comparison with the spectrum of LNN-20 which is a pure sample of Na-*R*3*c*) and another resonance which corresponds to the Li-*R*3*c* phase. The corresponding MAS spectra are also shown, which confirm that this additional resonance (labeled in figures) corresponds to the Li-*R*3*c* phase, as seen from comparison with the MAS spectra shown in Fig. 5.25. This ridge is of low intensity,[‡] and the projection onto the δ_1 axis is difficult to distinguish. This, however, supports the observations made from refinement of NPD data, in that the Li-*R*3*c* phase contains only a small proportion of Na^+ on the A-site (approximately 3%). A similar observation is made for LNN-90, in which the resonance corresponding to the Li-*R*3*c* phase is of low intensity and difficult to distinguish from the noise. Nonetheless, NMR parameters for this phase could be determined from knowledge of the δ_1 and δ_2 line positions. For both LNN-80

[†] The values given are the averages over the range $0.30 \leq x \leq 0.90$.

[‡] The 'contour' levels in the spectrum had to be lowered in order to observe this ridge.

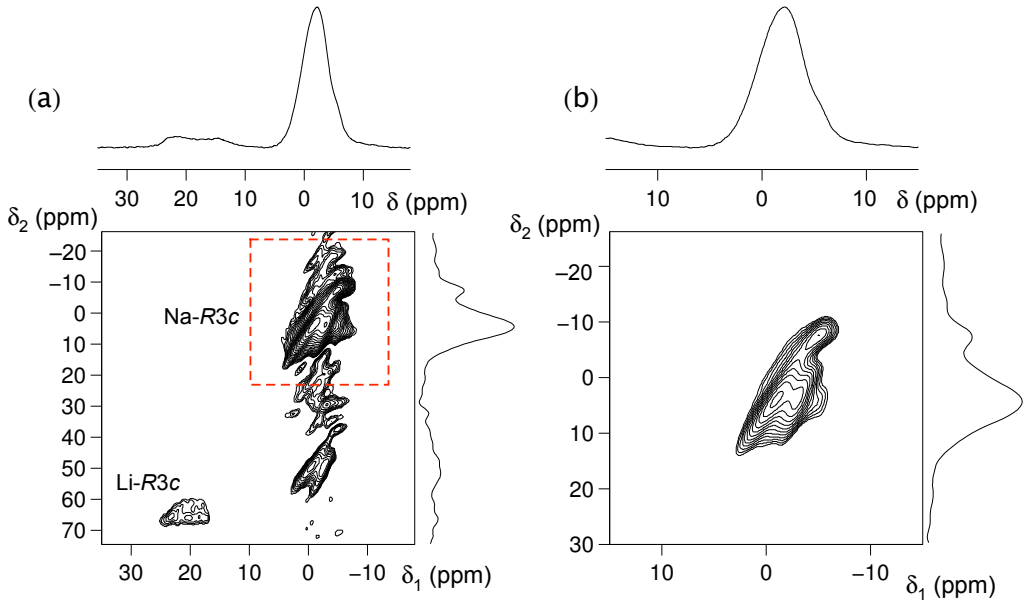

Figure 5.25: ^{23}Na (14.1 T) z-filtered MQMAS NMR spectrum of LNN-80. It can be seen that the resonance(s) corresponding to the Na-*R*3*c* phase has split into two distinct resonances. The resonance corresponding to the Li-*R*3*c* phase is also shown (labeled). The resonance(s) corresponding to the Na-*R*3*c* (highlighted in red box) are shown separately in (b). The spectra are the result of averaging 432 transients for each of 110 t_1 increments of 80 μs, with a 5 s recycle interval.

and 90, δ_{iso} = 26.4 ppm and P_Q = 2.5 MHz for the resonance corresponding to the Li-*R*3*c* phase. This is a relatively 'unusual' isotropic shift for ^{23}Na, as typical values are in the range of 15 to –15 ppm.[23] This could be because the Na^+ cations are relatively well-separated, *i.e.*, they are 'surrounded' by Li^+ in the local structure. The more interesting observation regarding the ^{23}Na MQMAS spectra of LNN-80 and 90 is that the Na-*R*3*c* phase now appears to gives rise to two distinct resonances, as shown in Figs. 5.25(b) and 5.26(b). This is an unexpected result, as refinement of diffraction data suggests this phase contains only one crystallographically-distinct Na site, and the ^{23}Na MQMAS spectrum of phase pure Na-*R*3*c* gave only one resonance. This is perhaps indicative of a phase change occurring. Here, the assumption is made that the 'extra' resonance does not correspond to an impurity phase, as there is no evidence for this in the diffraction data or ^{23}Na MAS NMR spectra, *i.e.*, no peaks or

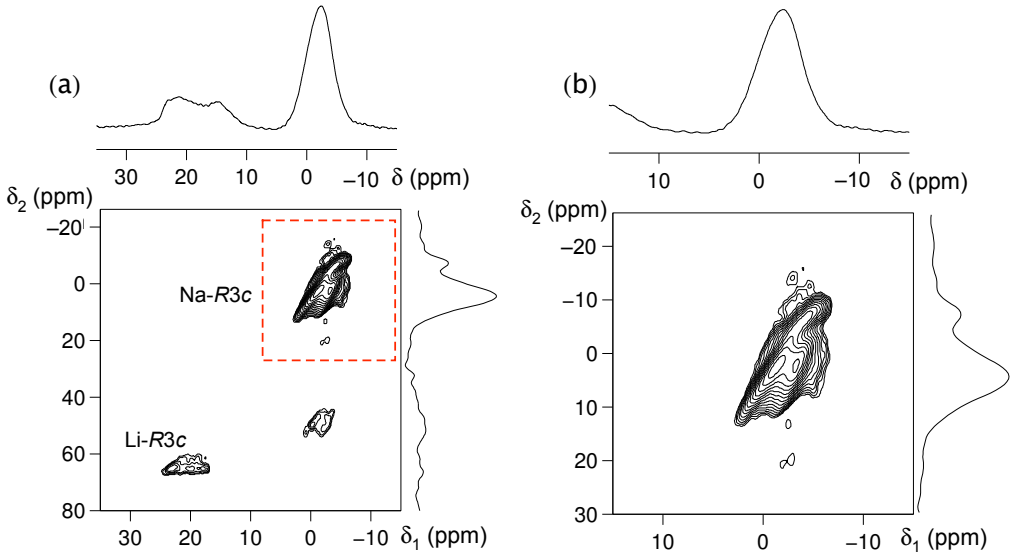

Figure 5.26: ^{23}Na (14.1 T) z-filtered MQMAS NMR spectrum of LNN-90. It can be seen that the resonance(s) corresponding to the Na-*R*3*c* phase has split into two distinct resonances. The resonance corresponding to the Li-*R*3*c* phase is also shown (labeled). The resonance(s) corresponding to the Na-*R*3*c* (highlighted in red box) are shown separately in (b). The spectra are the result of averaging 432 transients for each of 110 t_1 increments of 80 μs, with a 5 s recycle interval.

resonances are 'unaccounted' for. One possibility for this observation is that the rhombohedral (Na-)*R*3*c* phase undergoes a lowering of symmetry to the polar *R*3 space group. The NMR parameters of the two resonances in the spectrum were determined to be δ_{iso} = –0.8 ppm and P_Q = 1.4 MHz for the resonance with $\delta_1 \approx 3$ ppm, and δ_{iso} = –4.5 ppm and P_Q = 0.8 MHz for the resonance with $\delta_1 \approx -8$ ppm. It is worth noting that these resonances are relatively broad (compared to those for $NaNbO_3$ or KNN-3, for example) owing to the increased disorder in the sample from the higher proportion of Li^+. One possibility is that the symmetry is lowered locally, which is detectable using solid-state NMR but not diffraction techniques. It is possible that the 'extra' resonance arises from partial cation ordering in the structure or Na^+ clustering in the cell. These would be difficult to determine from diffraction techniques, made even more challenging by the relatively small proportion of this phase. DFT calculations of the *R*3 structure (with the model obtained from ISODISTORT) were undertaken to determine the NMR parameters for the Na^+

cations. The calculation of NMR parameters gave two distinct values, δ_{iso} values of 1.2 and –2.2 ppm. These values are not in agreement with the experimentally-observed resonances, but this could be due to disorder not being explicitly included in the calculations, *i.e.*, experimentally, the phase may contain 80% Na^+ and 20% Li^+ on the A-sites, although this disorder is difficult to include easily in DFT calculations. Subsequent refinements of LNN-80 and 90 using the (Na-*R*3) and Li-*R*3*c* models produced the same levels of fit as using both *R*3*c* models, most likely owing to the relatively small proportion of the Na-rich phase, which makes assignment of a space group more challenging.

Whilst MQMAS experiments allow the acquisition of high-resolution spectra, the technique has relatively poor sensitivity owing to inefficient excitation and conversion of MQ coherences. Satellite-transition (ST) MAS experiments also provide high-resolution spectra of quadrupolar nuclei with increased sensitivity.[24] The experiment itself is more challenging to implement than MQMAS but has the added advantages of a shorter acquisition time, This technique is, therefore, highly desirable for (a) nuclei with low natural abundance and (b) samples that contain only a small amount of the nucleus of interest. The relatively small amount of ^{23}Na in the Li-*R*3*c* phase (approx. 1-4% based on analysis of NPD data) makes STMAS an attractive technique for the study of this phase. ^{23}Na STMAS spectra of LNN-80, 90, 96 and 98 were acquired, and attention was focused on the resonance(s) corresponding to the Li-*R*3*c* phase. The STMAS spectra are shown in Fig. 5.27, where it can be seen that, for each spectrum, the isotropic projection *appears* to show at least three distinct resonances. This is, initially, a surprising result because the structures proposed from refinement of NPD data suggest that this phase contains only one crystallographically-distinct Na site. The presence of distinct resonances in the isotropic projections however, could be explained by considering the nature of the next nearest neighbour (NNN) atoms. Shown in Fig. 5.28(a) is an overlay of the projections for LNN-80 and 90, along with three labels, Na1', Na2', and

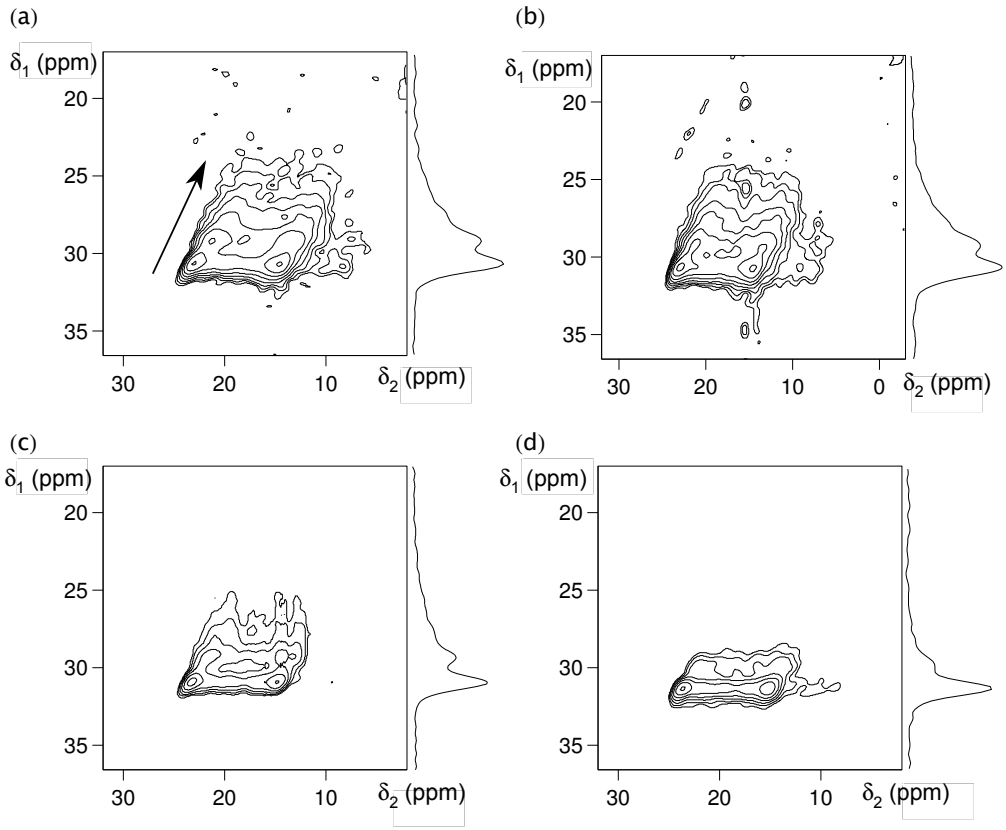

Figure 5.27: ^{23}Na (14.1 T) STMAS spectra of (a) LNN-80, (b) LNN-90, (c) LNN-96 and (d) LNN-98. All spectra were acquired with an MAS rate of 14 kHz and a 5 s recycle interval and are the result of averaging 256 transients for each of 64 t_1 increments of 134.92 μs.

Na3'.[§] In terms of peak height, it can be seen that the resonances are ordered Na1' > Na2' > Na3'. Na1' corresponds to one Na^+ cation being incorporated into the Li-*R*3*c* cell, Na2' corresponds to a second Na^+ cation being incorporated as the NNN to Na1', and Na3' corresponds to a second NNN. Statistically, there will, therefore, be less Na3' than Na2', which will in turn be less than the amount of Na1'. It is possible that there may also be a 'resonance' corresponding to Na4' and so

[§] The labels here are denoted with a prime and are not to be confused with resonances corresponding to crystallographically-distinct sites, *e.g.*, Na1 and Na2 used to denote the two Na sites in $NaNbO_3$.

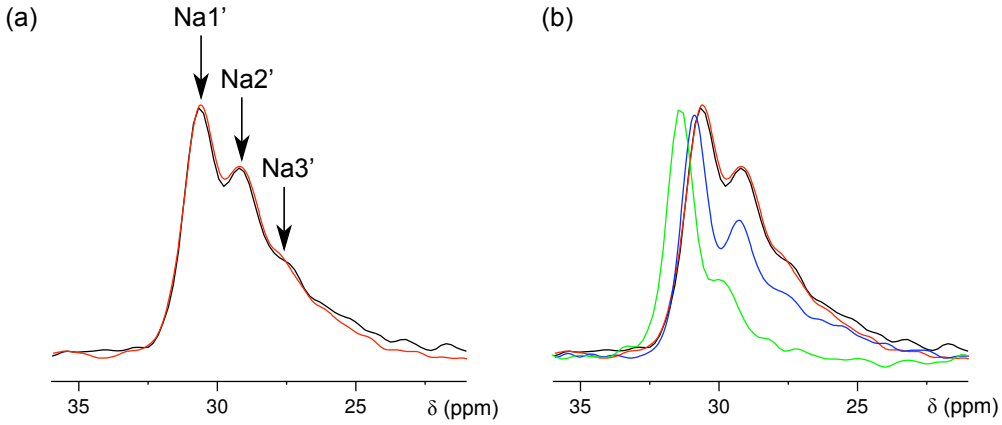

Figure 5.28: ^{23}Na (14.1 T) isotropic projections of STMAS spectra for LNN-80 (black line), LNN-90 (red line), LNN-96 (blue line) and LNN-98 (green line). Experimental details can be found in the caption of Fig. 5.33. The labels Na1', Na2' and Na3' are discussed in the main text.

forth, although this would be very difficult to distinguish owing to the low intensity.

Interpretation of the ^{23}Na isotropic projections shown in Fig. 5.28(b) reveals that there are three major differences between LNN-80, 90, 96 and 98. Firstly, as the molar ratio of Li increases, there is a shift in the peak position. This is most noticeable at compositions above LNN-90. This suggests that the composition of the phases may be changing, as this will lead to subtle differences in the local environment that will, in turn, result in different chemical shifts in the NMR spectra. The composition may not, however, change between LNN-80 and 90 as the resonances in these isotropic projections have the same chemical shift, suggesting that the solid solution limit may have been reached. Secondly, increasing the Li content from LNN-90 to LNN-96 and 98 results in a decrease in the intensity of the Na2' resonance with respect to the Na1'resonance. Thirdly, increasing the Li molar ratio from LNN-90 to 96 to 98 results in narrowing of the peak width, which would imply that less Na^+ is incorporated into the samples, *i.e.*, there is less disorder. Interestingly, the changes described above do not apply when comparing LNN-80 and 90 - the isotropic projections of these spectra show very little, if any, change, suggesting that, compositionally, they are the same, *i.e.*, the solid solution limit has been reached.

5.6. Conclusions

By using a complementary combination of X-ray and neutron powder diffraction and solid-state NMR spectroscopy, it has been possible to structurally characterise the LNN perovskite system. Within the compositional region $0.10 \leq x \leq 0.15$ (Region 1), it can be shown that two phases are formed - the orthorhombic phase Q (space group $P2_1ma$) and a Na-rich rhombohedral phase (space group $R3c$). Fig. 5.1 provides a summary of the compositional diagram for the work presented in this chapter. The relative proportions of these two phases, however, are found to be highly dependent upon the synthetic conditions used. Greater proportions of Li^+ leads to higher proportions of the rhombohedral phase being formed. Higher annealing temperatures favour formation of the rhombohedral phase also. For example, data obtained from refinement of NPD data showed that the relative fraction of $R3c$ increases (for LNN-10) from 14 to 81% when increasing the annealing temperature from 850 to 1050 °C. Within this compositional region it was also determined, from refinement of NPD data, that phase Q contains approximately 10% of Li^+ on the A-site, whereas the A-site fractional occupancies of the rhombohedral phase were determined to match the reactant stoichiometry.

Within Region 1, however, the most surprising observation was that phase Q undergoes a phase transition to the rhombohedral structure, simply by leaving the sample in air at ambient temperature. For various samples of LNN-10 and 12 synthesised under different conditions, the same observations were made. By using XRD and solid-state NMR spectroscopy, the relative reduction in the amount of phase Q (and consequently an increase in the proportion of the Na-$R3c$ phase) could be monitored. It was also shown, through use of both analytical techniques, that the fastest rate in reduction of phase Q occurred within six weeks of sample synthesis, where the rate decreased after this period. It was, therefore, very important to obtain XRD and NMR data immediately after sample synthesis, if the relative phase fractions were to be determined reliably. This observation is particularly important when attempting to make sense of the prior literature. For example, Yuzyuk reported that phase Q is present exclusively when $x = 0.02$ to 0.11 and 0.13 to 0.15, with the rhombohedral phase only present when $x = 0.12$.[23] The work presented in this chapter, however, has shown that the two phases can co-exist in the region $0.10 \leq x \leq 0.15$,

although the relative proportions are the two are highly dependent upon the synthetic conditions used and the time the sample has been left under ambient conditions. These results show that it is important to analyse samples in this compositional region immediately following synthesis. In light of the conversion of phase Q to the *R*3*c* phase, it was concluded, therefore, that phase Q is metastable with respect to the other, leading to the belief that the rhombohedral phase is the more thermodynamically stable of the two. It is important to fully investigate the nature of this phase interconversion before these samples could even be considered for commercial purposes. It should also be stressed, that to make sense of future literature regarding samples in this compositional region, the exact synthetic conditions used need to be fully described as well as, importantly, the time between synthesis and data acquisition.

Within the compositional region $0.25 \leq x \leq 0.90$ (Region 2), two rhombohedral phases are present, one Na-rich (Na-*R*3*c*) and the other Li-rich (Li-*R*3*c*). The relative phase fractions remain unaffected by annealing temperature, cooling rate and the time left under ambient conditions. The proportions of the two are affected only by the reactant Li^+ molar ratio. However, the compositions of the two phases remain unchanged across the series, such that the phase fractions are altered to compensate for the increasing reactant Li^+ molar ratio. Small changes are observed, however, in the Nb-O and A-O (A = Na, Li) bond lengths across this region, suggesting that the two phases do, at least slightly, change structurally. For example, there is the possibility of antisite Nb^{5+} cations on the A-site to account for loss of Li^+.[27] Whilst the two structures could be regarded as being distorted perovskites, the relatively large A-O bond distances in the Li-*R*3*c* phase suggest that the A-sites may only be six- or nine-coordinated, *i.e.*, not perovskite. It could be regarded as being a cation-ordered corundum structure.

References

[1] Kohori, A., Yamazoe, S., Imai, T., Adachi, H., Wada, T., *Appl. Phys. Lett.*, 2013, **102**, 112909.

[2] Chaker, C., Gharbi, W. E., Abdelmoula, N., Simon, A., Khemakhem, H., Maglione, M., *J. Physics and Chemistry of Solids,* 2011, **72**, 1140.

[3] Yuzyuk, Y. U., Gagarina, E., Simon, P., Reznitchenko, L. A., Hennet, L., Thiadière, D., *Phys. Rev. B,* 2004, **69**, 144105.

[4] Abrahams, S. C., Marsh, P., *Acta Cryst.*, 1986, **B42**, 61.

[5] Wilkinson, A. P., Cheetham, A. K., *J. Appl. Phys.,* 1993, **74**, 3080.

[6] Thomson, J. B., Small, C., Lightfoot, P., Bruce, P. G., *J. Mater. Chem.*, 1995, **5**, 1039.

[7] Lines, M. E., Glass, A. M., Principles and applications of ferroelectrics and related materials, Oxford University Press, Oxford, 1977.

[8] Sakowski-Cowley, A. C., Ph.D. Thesis, University of Cambridge, 1967.

[9] Lefkowitz, I., Lukaszewicz, K., Megaw, H. D. *Acta Cryst*., 1966, **A20**, 670.

[10] Saito, Y., Takao, H., Tani, T., Nonoyama, T., Takatori, K., Homma, T., Nagaya, T., Nakamura, M., *Nature,* 2004, **432**, 84.

[11] Sakowski-Cowley, A. C., Lukaszewicz, K., Megaw, H. D. *Acta Cryst*., 1969, **B25**, 851.

[12] Shuvaeva, V. A., *Ferroelectrics,* 1993, **141**, 307.

[13] Ahtee, M., Glazer, A. M., *Acta Cryst.,* 1976, **A32**, 434.

[14] Ahtee, M., Hewat, A. W., *Acta. Cryst.,* 1978, **A34,** 309.

[15] Johnston, K. E., Tang, C. C., Parker, J. E., Knight, K. S., Lightfoot, P., Ashbrook, S. E., *J. Am. Chem. Soc.,* 2010, **132**, 8732.

[16] Zhang, N., Glazer, A. M., Baker, D. W., Thomas, P. A., *Acta Cryst.,* 2009, **B65**, 291.

[17] Baker, D. W.; Thomas, P. A.; Zhang, N.; Glazer, A. M.; *Appl. Phys. Lett.,* 2009, **95**, 091903.

[18] Glazer, A. M., Megaw, H. D., *Acta Cryst.,* 1973, **A29**, 489.

[19] Peel, M. D., Ashbrook, S. E., Lightfoot, P., *Inorg. Chem.*, 2013, DOI: 10.1021/ic401061t

[20] Peel, M. D., Thompson, S. P., Dauod-Aladine, A., Ashbrook, S. E., Lightfoot, P., *Inorg. Chem.*, 2012, **51**, 6876.

[21] Ashbrook, S. E., Le Polles, L., Gautier, R., Pickard, C. J., Walton, R. I., *Phys. Chem. Chem. Phys.,* 2006, **8**, 3423.

[22] Troyanchuk, I. O., Karpinsky, D. V., Bushinsky, M. V., Khomchenko, V. A., Kakazei, G. N., Araujo, J. P., Tovar, M., Sikolenko, V., Efimov, V., Kholkin, A. L., *Phys. Rev. B.*, 2011, **83**, 054109.

[23] Mackenzie, K. J. D., Smith, M. E., Multinuclear Solid-state NMR of Inorganic Materials, Chapter 7, Pergamon, Cambridge, 2002.

[24] Ashbrook, S. E., Wimperis, S., *Prog. Nucl. Magn. Reson. Spec.*, 2004, **45**, 53.

Chapter 6
Final Conclusions and Further Work

The purpose of the work presented in this thesis was to provide a detailed understanding of the structural behaviour of $NaNbO_3$ and a range of A-site substituted compositions at both ambient and high temperature. Complementary NPD, XRD and solid-state NMR spectroscopy were combined to provide detailed structural characterisation over a range of length scales, and were accompanied with supporting DFT calculations.

$NaNbO_3$ undergoes several temperature-dependent phase transitions, as discussed in Chapter 3. The low- and room-temperature polymorphs (N, P and Q) have been well-characterised in previous literature, along with the higher-symmetry phases T1, T2 and U. However, phases R and S were significantly less well understood, with no unambiguous structures previously given. By using NPD and symmetry mode analysis, it was possible to propose structures for these phases. Where there were several possible structures for each phase, supporting DFT calculations and ^{23}Na MAS NMR experiments were used to gain additional insight. However, it was not possible to distinguish between different models using ^{23}Na MAS NMR spectra acquired at high temperature, and one possibility for further work would be to acquire high-temperature ^{23}Na MQMAS spectra instead. Whilst this may be challenging at high temperature, it is certainly worth attempting. The complementary DFT study performed for these models gave some unexpected results, and may benefit from the inclusion of thermal vibrations. The inclusion of these factors offers an intriguing possibility for further work but does, however, require significantly more time and computational expertise. Interestingly, NPD and XRD data obtained for phase P (ambient temperature) confirmed the presence of a single phase. However, in ^{23}Na MQMAS spectra an additional resonance was also observed, whereas ^{23}Na DOR NMR spectra showed two additional resonances. The presence of these additional resonances suggests that either (a) the structure of $NaNbO_3$ has a change in symmetry, at least locally but not observed periodically,[1] or (b) there is a second polymorph

present. The presence of a second polymorph (or lowering of the symmetry) is not detected by XRD/NPD experiments, suggesting that techniques that probe both local and periodic structure need to be combined with more conventional diffraction approaches. Further work would be needed to determine the nature of this additional polymorph. One method to achieve this is newly introduced "structure searching".[2] This would allow any (theoretical, at least) models to be determined, and subsequently NMR parameters could be calculated and compared to experiment. Structure searching would, however, require more computational time and expertise, but does offer an area of further research into $NaNbO_3$.

In Chapter 4 it was confirmed that phase Q could be formed preferentially by substituting a small amount (~2%) of K^+ or Li^+ for Na^+, referred to as KNN and LNN, respectively. The formation of phase Q was determined by both NPD and solid-state NMR spectroscopy, although results obtained from the latter provided additional information. ^{23}Na z-filtered MQMAS NMR spectra of $K_{0.02}Na_{0.98}NbO_3$ (denoted KNN-2), KNN-3, KNN-4, and KNN-5 showed three distinct resonances: two corresponding to phase Q and a third, relatively broad, additional resonance. The use of solid-state NMR has offered invaluable insight into the local structure and disorder of these materials. Complementary ^{23}Na MQMAS and DOR spectra have been used to determine that an additional phase may be formed alongside phase Q, or that phase Q (space group $P2_1ma$) may not be the correct assignment for these structures. ^{39}K MAS NMR proved challenging, owing to the poor sensitivity and longer relaxation times of ^{39}K. Nonetheless, spectra obtained at higher fields offered useful insight into the local structure. For example, the spectra appeared to show two components – one narrow and one broad, indicative of K^+ substitution onto at least two different sites (Na(K)1 and Na(K)2). Such a distinction could not be made from the X-ray data owing to the small amounts of K^+ present. ^{39}K CPMG spectra were also interpreted as possessing two distinct components – again, one narrow and one broad, consistent with the MAS spectra. Obtaining higher field ^{39}K CPMG spectra offers a possibility for future work, which may help with understanding how the potassium substitutes into the material.

In a way similar to that of $NaNbO_3$ (presented in Chapter 3), the temperature-dependent phase transitions of KNN (phase Q) were investigated using NPD and symmetry mode analysis. Again, complex phase behaviour was observed, where several space group assignments could be proposed. For example, phase G refined equally well in two space groups: *I*4/*mmm* and *I*4*mm*. An additional complication observed, however, was that phase G was found to co-exist with phase Q, which made accurate structural determination more challenging. One area for future work would be to obtain additional high-temperature diffraction data of KNN to determine if phase G could be observed exclusively. For example, by allowing longer thermal equilibration times.

In Chapter 5, the $Li_xNa_{1-x}NbO_3$ (LNN) compositional phase diagram was investigated using XRD, NPD and solid-state NMR spectroscopy. Within the region $0.02 \leq x \leq 0.08$, a single polar orthorhombic phase is formed exclusively (phase Q). Within the region $0.08 \leq x \leq 0.15$, two phases are formed depending upon the synthetic conditions: phase Q and a Na-rich rhombohedral phase, Na-*R*3*c*. From NPD data, this rhombohedral phase was determined to adopt a composition equivalent to the reactant stoichiometry. The relative proportions of theses phases were determined to be highly dependent upon annealing temperature, cooling rate and time. Samples annealed at higher temperatures showed a greater proportion of the rhombohedral phase, as did those cooled at a faster rate. Additionally, through analysis of l-PXRD data and ^{23}Na MQMAS NMR spectra, it was shown that phase Q converted into the rhombohedral phase, with the fastest rate of conversion observed in the initial 0 to 6 week period, with slower rates of conversion observed subsequently. The phase behaviour observed is, again, complex, perhaps indicating that accurate structural determination of substituted $NaNbO_3$ perovskites may require significantly more work.

For samples of LNN-70, 80, 90 and 96, some interesting, albeit preliminary, observations were made using ^{23}Na MQMAS and STMAS. Firstly, the Na-*R*3*c* phase showed two distinct resonances (only one is expected), indicating that a phase transition or lowering of the symmetry, at least locally, may have occurred. The Li-rich rhombohedral phase, Li-*R*3*c*, appears, initially, to show a distribution of NMR parameters. Further ^{23}Na STMAS experiments and supporting DFT calculations would be needed to probe the nature of this observation. As the changes appear to be

in the local structure, it is unlikely that any additional information could be gained from conventional XRD/NPD data. However, obtaining pair distribution function (PDF) data may aid in the analysis of the local structure and provide a highly complementary technique to NMR spectroscopy.

The work presented in this thesis was obtained from a multidisciplinary approach by combining XRD, NPD and solid-state NMR spectroscopy with supporting symmetry mode analyses and DFT calculations, where appropriate. It has been shown that each technique offers invaluable information that cannot be obtained from the others alone, and that further studies of niobate perovskites may yield more insight by using these combined approaches.

References

[1] Jiang, L., Mitchell, D. C., Dmowski, W., Egami, T., *Phys. Rev B.*, 2013, **88**, 014105.

[2] Pickard, C. J., Needs, R. J., *J. Phys. Condens. Matter.*, 2011, **23**, 053201.